Selection for invasive tumour cells reveals a role for MAPK signalling in cell elasticity regulation

Dominika Agnieszka Rudzka
MSc

Submitted in fulfilment of the requirements for the Degree of Doctor of Philosophy

Cancer Research UK Beatson Institute
College of Medical, Veterinary and Life Sciences
University of Glasgow

September 2017

Abstract

The metastatic spread of cancer cells is a major contributor to cancer patient deaths. In order to disseminate from one part of the body to another, invasive tumour cells must perform a complex cascade of steps. Common to several stages of the metastatic process is the ability of tumour cells to squeeze through narrow spaces. One adaptation that allows cancer cells to adjust to confined environments is a change in the cell mechanical properties, which results in diminished cell stiffness. Such an altered cellular physical property is thought to contribute to the invasive and metastatic properties of cancer cells. There is little currently known about the factors or signalling pathways that modulate cell stiffness; therefore, the identification of factors that modify tumour cell plasticity could identify potential drug targets for anti-metastasis chemotherapy.

I hypothesized that within the distributions of parameters in tumour cell line populations, it would be possible to select for cells with an augmented ability to squeeze through narrow gaps, thus highlighting factors that contributed to cell deformability. To identify factors that help cancer cells migrate through confined spaces, MDA MB 231 human breast cancer cells and MDA MB 435 melanoma cells underwent 3 rounds of selection, using tissue culture inserts with 3 μm pores. This selection approach allowed me to isolate cell populations with enhanced abilities to pass through physical constrictions, as well as augmented invasive abilities *in vitro*. Additionally, populations of small volume cells were selected from parental MD MB 231 cells by flow cytometry. By obtaining the matching cell size control, I found that increased pore invasion was not solely dependent on small cell or nuclei size. In fact, properties unique to the pore-selected invasive cells were: decreased actin cytoskeleton anisotropy and cell rigidity (Young's modulus) as determined by Atomic Force Microscopy (AFM).

To identify signalling pathways that were associated with observed cytoskeleton and elasticity changes, RNA sequencing was performed on parental, pore-selected and flow-selected MDA MB 231 cells, and parental and pore-selected MDA MB 435 cells and a stringent comparison was performed. Such an approach allowed identification of common genes, which were used for further analysis by applying GSEA. The most common gene signature was found to associate with

increased signalling through the Ras-Raf-MEK-ERK mitogen-activated protein kinase (MAPK) pathway. Blocking the activity of the MAPK/ERK pathway with two pharmacologically distinct MEK inhibitors resulted in actin stress fibre restoration, increased cell stiffness and restrained cell invasion through collagen matrices. I was able to identify, for the first time that changes in cytoskeletal organisation mediated by increased signalling through the MAPK/ERK pathway resulted in cell plasticity alterations. Therefore, drugs that block Ras-MAPK signalling would likely provide clinical benefit by reversing the effect of this signalling pathway on tumour cell plasticity and subsequently restraining migratory and invasive capabilities.

Table of Contents

List of Tables

List of Figures

Acknowledgement

First and foremost, I would like to thank my supervisor Professor Mike Olson for giving me the opportunity to work on this thesis in his laboratory and excellent supervision, support, encouragement and advice during the course of my studies. I would also like to thank my advisor Professor Laura Machesky for useful discussions and input of new ideas.

Special thanks to the research services and support staff at the Beatson who really are a huge help to us all. I would like to extend my sincere gratitude to The Beatson Institute and Cancer Research UK for funding my PhD.

My sincere thanks go to Dr. Karen Blyth and Susan Mason for their help in *in vivo* studies. Furthermore, I'd like to thank everyone who has helped me in this project and all the collaborators, especially Professor Huabing Yin and Giulia Spennati.

I would like to thank all members of our group (R17), past and present, from whom I have learned so much and for making the last four years really enjoyable. Special thanks should also go to my friends, Alessandra, Jennifer and Titziana for giving me a laugh and for the good times we spent together outside the Institute.

I would also like to thank my family for their encouragement and for helping me get to where I am today. I would especially like to thank my husband, Leszek, for all his support.

Author's Declaration

I am the sole author of this thesis. The work presented in this thesis is entirely my own unless otherwise stated.

Dominika Agnieszka Rudzka

Rudzka, D. A., J. M. Cameron, et al. (2015). "Reactive oxygen species and hydrogen peroxide generation in cell migration." Commun Integr Biol 8(5): e1074360. (Rudzka, Cameron et al. 2015)

Rudzka, D. A. and M. F. Olson (2015). "Microtrack migration: insights into 3D cell motility. Focus on "Comparative mechanisms of cancer cell migration through 3D matrix and physiological microtracks"." Am J Physiol Cell Physiol **308**(6): C434-435

Rudzka, D. A., W. Clark, et al. (2017). "Transcriptomic profiling of human breast and melanoma cells selected by migration through narrow constraints." Sci Data 4: 170172.(Rudzka, Clark et al. 2017)

Abbreviations

2D	Two-dimensional
2-DG	2-deoxyglucose
3D	Three-dimensional
ACC	Adenoid cystic carcinoma
ADP	Adenosine diphosphate
AFM	Atomic Force Microscopy
Angpt2	Angiopoietin 2
Arp2/3	Actin-Related Proteins ARP2 and ARP3
ATP	Adenosine triphosphate
BCA	Bicinchoninic acid
BM	Basement membrane
BrdU	5-bromo-2'-deoxyuridine
BSA	Bovine serum albumin
Cc	Critical concentration
cDNA	Complementary DNA
CFP	Cyan fluorescent protein
cm	centimetre
COX-2	Cyclooxygenase-2
CTCs	Circulating tumour cells
CXCL12	C-X-C motif chemokine 12
CytoD	Cytochalasin D
DAPI	4',6-diamidino-2-phenylindole
dH_2O	distilled water
DMEM	Dulbecco's Modified Eagle Medium
DMSO	Dimethyl sulfoxide
DNA	Deoxyribonucleic acid
dNTP	Deoxynucleotide
DTT	Ditiotreitol
ECM	Extracellular matrix
EDTA	Ethylenediamine tetraacetic acid
EGF	Epidermal growth factor
EGFR	Epidermal growth factor receptor
EMT	Epithelial to mesenchymal transition
ENPP1	Ectonucleotide pyrophosphatase/phosphodiesterase 1
ERK	Extracellular signal–regulated kinase
EtOH	Ethanol
ETS	E26 transformation-specific
FA	Focal adhesion

FACS	Fluorescence activated cell sorting
F-actin	Filamentous actin
FAK	Focal adhesion kinase
FBS	Fetal bovine serum
FC	Fold change
FLIM	Fluorescence-lifetime imaging microscopy
Fra-1	Fos-related antigen 1
FRAP	Fluorescence recovery after photobleaching
FRET	Förster resonance energy transfer
FS	Flow/Facs sorted/selected
g	gram
G-actin	Globular actin
GAP	GTPase-activating protein
GAPDH	Glyceraldehyde 3-phosphate dehydrogenase
GBR2	Receptor-bound protein 2
GDP	Guanosine diphosphate
GFP	Green fluorescent protein
GSEA	Gene Set Enrichment Analysis
H&E	Haematoxylin and Eosin
H1	Histone 1
H2A	Histone 2A
H2B	Histone 2B
H3	Histone 3
H3K27me^3	Trimethylation of lysine 27 in histone H3
H3K4me^3	Trimethylation of lysine 4 in histone H3
H3K9ac	Acetylation of lysine 9 in histone H3
H3K9me^3	Trimethylation of lysine 9 in histone H3
H4	Histone 4
H4K20me^1	Mono-methylation on lysine 10 in histone H4
HBEGF	Heparin-binding EGF-like growth factor
HBSS	Hanks' Balanced Salt Solution
HEPES	4-(2-hydroxyethyl)-1-piperazineethanesulfonic acid)
HLA	Human leukocyte antigen
HSD11B1	11β-Hydroxysteroid dehydrogenase type 1
JNK	c-Jun N-terminal kinases
kg	kilogram
L	Litre
LIFA	Lambert Instruments FLIM Attachment
LILRB1	Leukocyte immunoglobulin-like receptor subfamily B member 1
LIMK	LIM domain kinase

M	Molar
MAPK	Mitogen–activated protein kinase
MAPKK	Mitogen–activated protein kinase kinase
MAPKKK	Mitogen–activated protein kinase kinase kinase
MBS	Myosin-binding subunits
MEK	Mitogen-activated protein kinase
MEM/EBSS	Minimum Essential Medium with Earle's Balanced Salts
mg	milligram
ml	millilitre
MLC	Myosin light chain
MLCK	Myosin light chain kinase
MLCP	Myosin light chain phosphatase
mm	millimetre
mM	millimolar
MMPs	Matrix metalloproteinases
mW	milliwatt
MXRA8	Matrix remodelling associated 8
MYPT1	Myosin phosphatase target subunit 1
NaN_3	Sodium azide
NBD	(6-((N-(7-nitrobenz-2-oxa-1,3-diazol-4-yl)amino)hexanoyl)sphingosyl phosphocholine)
nm	nanometre
nM	nanomolar
nN	nanonewton
PAGE	Polyacrylamide gel electrophoresis
PBS	Phosphate-buffered saline
PCA	Principle Component Analysis
PCR	Polymerase chain reaction
PFA	Paraformaldehyde
Pi	inorganic phosphate
PI	Propidium iodide
PLAT	Tissue plasminogen activator
PLAU	Urokinase-type plasminogen activator
PTPRU	Receptor-type tyrosine-protein phosphatase PCP-2
PyMT	Polyoma middle T oncogene
qPCR	quantitative PCR
RIN	RNA Integrity number
RNA	Ribonucleic acid
ROCK	Rho-associated coiled-coil containing kinase
ROI	Region of Interest
rpm	Revolutions per minute

RTCA	Real-Time Cell Analyzer
Scar	Suppressor of cAMP receptor
SCC	Squamous cell carcinoma
SDS	Sodium dodecyl sulfate
Sel	Selected
SEM	Scanning electron microscopy
SEM	Standard error of mean
Ser	Serine
SRB	Sulforhodamine B
$t_{1/2}$	half time
TCA	Trichloroacetic acid
TEM	Transmission electron microscopy
TGFβ	Transforming growth factor beta
Thr	Threonine
TIRF	Total Internal Reflection Fluorescent Microscopy
TNF	Tumour necrosis factor
TNFSF15	TNF superfamily member 15
U	Unit
µg	microgram
µm	micrometre
µM	micromolar
uPA	Urokinase
v	volume
V	Volts
VEGF	Vascular endothelial growth factor
w	weight
WASP	Wiskott–Aldrich syndrome protein
WCS	Whole Cell Stain
ZEB 1/2	Zinc finger E-box-binding homeobox 1/2
β-2-M	Beta-2 microglobulin

1 Introduction

1.1 Cancer cell metastasis

Cancer cell metastasis is a complex and multistep process in which malignant cells spread from primary tumour sites to distant organs (Gupta and Massague 2006; Steeg 2006). Metastasis is one of the hallmarks of cancer, and it has been suggested that it is responsible of 90% of deaths among cancer patients. Therefore, it is very important to understand what factors drive cancer cell metastatic behaviours and to find therapeutic targets to block it (Hanahan and Weinberg 2011). In order to obtain invasive traits, cancer cells undergo many intrinsic genetic and epigenetic changes which occur in response to microenvironmental barriers (Chambers, Groom et al. 2002; Feinberg, Ohlsson et al. 2006; Bartek, Lukas et al. 2007). Such barriers can be divided into: chemical barriers, such as hypoxia, presence of reactive oxygen species, low pH; physical barriers, such as basement membrane, tensional forces; and biological barriers, such as immune surveillance and inhibitory cytokines (Chambers, Groom et al. 2002; Harris 2002; Hussain, Hofseth et al. 2003; Paszek, Zahir et al. 2005; Gupta and Massague 2006). The main consequences of an acquired invasive phenotype are reduced adhesion, increased cell motility and an ability to invade surrounding tissues. Cells which acquire such properties in primary tumours, in order to migrate from one body part to the other, perform the following cascade of steps: invasion into the surrounding environment, intravasation into the blood or lymphatic microvasculature, survival in circulation, extravasation into distant tissue, survival in the foreign tissue, and adaptation to its conditions (Figure 1-1) (Chambers, Groom et al. 2002; Fidler 2003).

1.1.1 Invasion into surrounding environment

In the first step of the metastatic cascade, cancer cells invade into the surrounding tumour-associated stroma. In order to do this, epithelial tumour cells lose the tight organisation of epithelial tissue by turning on the epithelial-to-mesenchymal transition (EMT) program (Thiery, Acloque et al. 2009). EMT leads to loss of cell polarity and disintegration of adherens and tight junctions. EMT can occur upon activation of transcription factors such as Slug, Snail, Twist, ZEB1, and ZEB2 (Thiery, Acloque et al. 2009). Some of these transcription

factors repress levels of E-Cadherin, which bond, epithelial cells together (Cavallaro and Christofori 2004). However, it has been reported that EMT is not necessary for metastasis to occur (Fischer, Durrans et al. 2015; Zheng, Carstens et al. 2015). Once tumour cells reduce their intracellular adhesiveness, they can disrupt the basement membrane (BM) which provides a specialized ECM structure underlying epithelial and endothelial cell layers, as well as a physical barrier for cancer cells (Bissell and Hines 2011). Some tumour cells are able to degrade the BM by production, secretion and activation of matrix metalloproteinases (MMPs) (Egeblad and Werb 2002; Kessenbrock, Plaks et al. 2010). In normal tissues, the expression of MMPs is tightly controlled, whereas cancer cells disturb this regulation and are able to proteolytically degrade the BM and enter the stroma (Kessenbrock, Plaks et al. 2010). Stromal tissue mainly consists of fibroblasts and myofibroblasts, endothelial cells, adipocytes, and immune cells (Grivennikov, Greten et al. 2010). Some of the components of stromal tissue have the potential to boost the metastatic capabilities of cancer cells. For example, interleukin-6 secreted by adipocytes enhance the invasiveness of breast cancer cells (Dirat, Bochet et al. 2011), while the production of chemokine CXCL12 by breast cancer associated fibroblasts increased the proliferation and migratory ability of cancer cells and promoted angiogenesis (Allinen, Beroukhim et al. 2004; Orimo and Weinberg 2006).

1.1.2 Intravasation into vasculature

Highly motile cancer cells migrate towards blood vessels due to the presence of naturally occurring chemoattractant gradients (Bockhorn, Jain et al. 2007; Leung, Xue et al. 2016). The mechanism of intravasation - entering blood or lymphatic vessels, may be augmented by overexpression of vascular endothelial growth factors which stimulate the formation of new blood vessels (Carmeliet and Jain 2011). Endothelial cells which form the neovasculature are weaker in their adjacent organisation compared to the normal vasculature, moreover they lack pericyte coverage, which makes them leakier and more likely to facilitate intravasation (Gupta, Nguyen et al. 2007). Additionally, intravasation into the blood or lymphatic vessels can be facilitated by external factors including transforming growth factor-ß (TGFß) (Giampieri, Manning et al. 2009) or epidermal growth factor (EGF) (Wyckoff, Wang et al. 2007).

1.1.3 Survival in blood circulation

Once cancer cells enter the circulation they become circulating tumour cells (CTCs) (Nagrath, Sequist et al. 2007; Pantel, Brakenhoff et al. 2008). Shedding of tumour cells into the circulation may occur in large numbers and from early stages of tumour formation, however only minority of these cells would be able to survive and form metastatic sites in distant organs (Lambert, Pattabiraman et al. 2017). In order to survive in the blood stream, CTCs must withstand many stresses related to loss of cell-matrix interaction as well as shear stress, compressive blood pressure, and immune surveillance. In the absence of adhesive supports, normal epithelial cells undergo anoikis – a form of cell death, whereas some CTCs have the ability to escape this process by triggering signalling pathways, such as the phosphatidylinositol-3-OH kinase/protein kinase B pathway (Kang and Pantel 2013). Additionally, cancer cells due to their large size (20-30 μm) may be trapped in the various capillaries (~8 μm diameter) within minutes after intravasation, therefore the time necessary to provoke anoikis process is short (Meng, Tripathy et al. 2004). Furthermore, in order to avoid being "eaten" by cells of the innate immune system, and to withstand physical hemodynamic forces, CTCs are able to become platelet-coated tumour cells called emboli. Platelets create a protective coat on the CTC surface, and in this way they increase the metastatic potential of CTCs (Nash, Turner et al. 2002; Gupta, Nguyen et al. 2007; Joyce and Pollard 2009).

1.1.4 Extravasation into distant tissue

The extravasation process enables cancer cells to escape the circulation and enter distant tissues. The vasculature at the distant site is not as leaky as the neovasculature created by tumour cells, therefore to overcome such physical barriers cancer cells secrete factors which induce vascular hyperpermeability as well as disrupting the tight endothelial organisation (Carmeliet and Jain 2011). For example, breast cancer cells secrete factors like MMP-1, MMP-2 and COX-2 which help to disturb pulmonary endothelial cell junctions in order to extravasate into the lungs (Padua, Zhang et al. 2008; Carmeliet and Jain 2011). Moreover, some cancer cells in primary tumours are able to secrete premetastatic factors like MMP-3, VEGF and angiopoietin 2 (Angpt2), which help to induce pulmonary hyperpermeability prior to cancer cell arrival to the lungs

(Weis, Cui et al. 2004; Huang, Song et al. 2009). Furthermore, once trapped in the vasculature, cancer cells have the ability to grow up to the point where they rupture the walls of the surrounding vasculature and are placed directly in the foreign tissue parenchyma (Al-Mehdi, Tozawa et al. 2000).

1.1.5 Survival and adaptation to the foreign tissue

Due to the fact that foreign tissue environments are different from primary tumour environments, cancer cells are not necessarily well adapted to their new metastatic sites. In order to overcome this issue, it was proposed that some cancer cells may release pre-metastatic signals which prepare the sites of metastasis before tumour cells start disseminating (Psaila and Lyden 2009). Once tumour cells survive in the foreign tissue, some of them may stay in a state of long-term dormancy due to limited access to blood vessels or lack of biocompatibility between cancer cells and the foreign microenvironment (Chambers, Groom et al. 2002). To escape the dormancy state and colonize the new tissue, cancer cells must have the ability to interact with the new environment, and be able to release growth and survival factors. Different tissue present different requirements for the cancer cells to be able to proliferate and create new metastatic sites, therefore it has been proposed that cancer cells present organ-specific metastatic tropism, for example breast cancer spread to bones, lungs, brain and liver, prostate cancer mostly metastasise to the bones, while melanoma cancer cells spread to the brain and lungs (McAllister, Gifford et al. 2008; Hiratsuka, Goel et al. 2011).

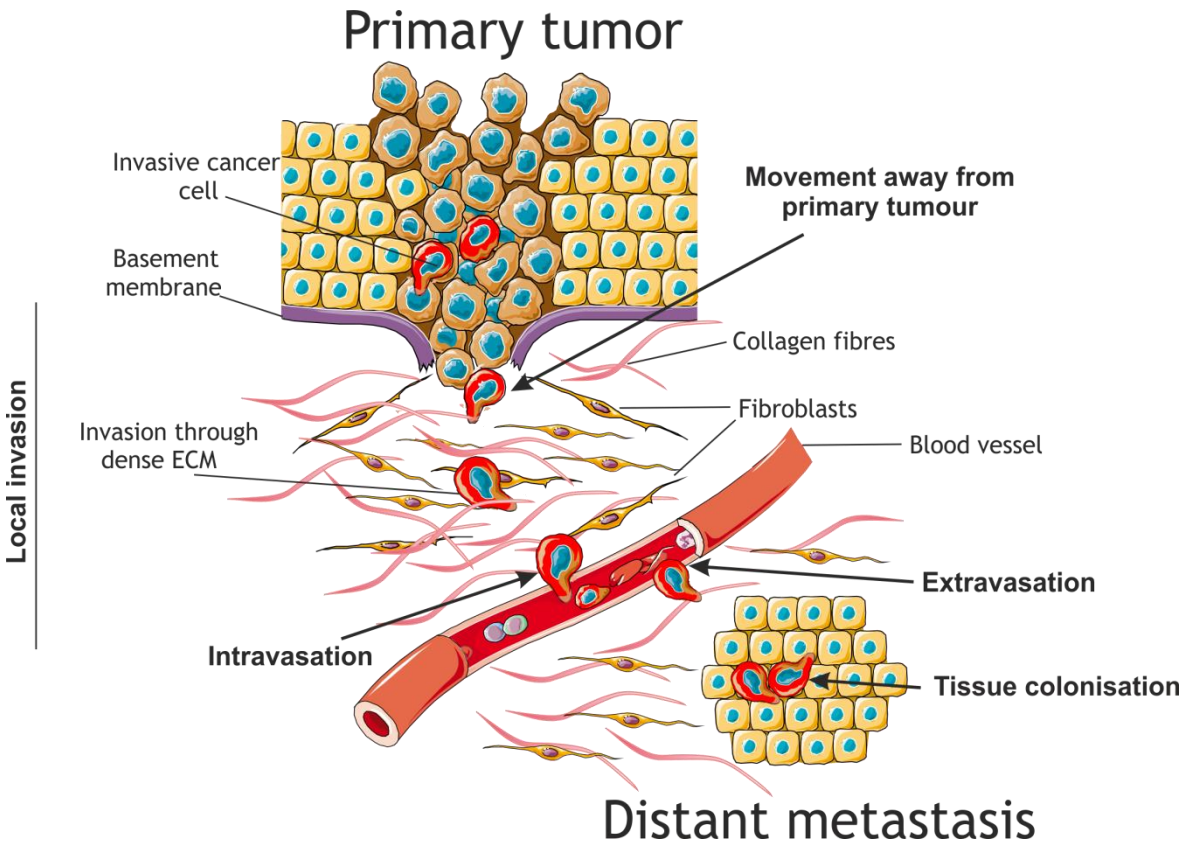

Figure 1-1 Cancer cell metastatic cascade.
The image illustrates cancer cell spread from a primary tumour to a distant site in the body. In the first step of the metastatic cascade – invasion, cancer cells lose their epithelial organisation and invade through the basement membrane into the stromal tissue and subsequently invade through its tight organisation. Stromal tissue is composed of collagen, fibroblasts, myofibroblasts, adipocytes and immune cells. In the next step, cancer cells intravasate into blood or lymphatic vessels. If cancer cells survive their journey through the circulation, they extravasate and colonize foreign tissue. Image generated using Servier Medical Art.

1.2 Cancer cell migration in confinement

The first crucial step of the metastatic cascade is invasion into the surrounding stroma. Abnormal cell migration plays a pivotal role in this step. Many mechanistic and regulatory studies of cells moving on two-dimensional (2D) substrates have been undertaken, however three dimensional (3D) cell motility is the key migration type *in vivo*. Depending on the size of spaces present in the ECM and cancer cell invasion abilities, cells can utilize different invasion modes (mesenchymal, amoeboid or collective). Cancer cells can move as individual cells or as a solid multicellular complex, or they can switch between migration types depending on the environmental properties. Such ability to change in response to varying conditions is referred to as cell plasticity. Some tracks/pores provide a path of least resistance for migrating cells, in which case cancer cells don't need to remodel the surrounding matrix to widen the matrix pore. However, to move through spaces smaller than the migrating cells, cancer cells need to remodel the ECM by proteolysis mediated by enzymes such as matrix metalloproteinases (Stetler-Stevenson, Aznavoorian et al. 1993; Friedl 2004), and/or squeeze through the tight pore structures by deforming itself (Wolf, Mazo et al. 2003).

1.2.1 Extracellular matrix confinement

Cancer cells migrating through extracellular matrix (ECM) encounter varying degrees of confinement. Spaces present in the ECM form tunnel-like tracks or pores. The size of the tracks/pores present in the extracellular environment is comparable or smaller to the diameter of migrating cells; ranging from 0.1 to 30 μm (Doerschuk, Beyers et al. 1993; Weigelin, Bakker et al. 2012). Tracks or pores exist naturally in healthy tissues, they can occur as spaces along or within blood vessels (Lugassy, Zadran et al. 2014), between muscle and nerve fibres (Weigelin, Bakker et al. 2012) or between collagen fibres (Gritsenko, Ilina et al. 2012) (Figure 1-2), or they may be created by tumour-associated fibroblasts and macrophages. As an example, it was reported that fibroblasts can create tracks in collagen/matrigel matrices by proteolytic degradation and force-mediate remodeling, leading to enhanced collective invasion of squamous cell carcinoma (SCC) cells (Gaggioli, Hooper et al. 2007). Moreover, cancer-associated fibroblasts co-cultured with adenoid cystic carcinoma (ACC) cells in microfluidic

devices created proteolytically degraded tracks within matrigel, which promoted invasion of ACC cells (Li, Jia et al. 2016). Matrix remodeling can also occur at future pre-metastatic sites, leading to pre-metastatic site formation by bone-marrow derived macrophages (Costa-Silva, Aiello et al. 2015).

Tracks/pores present in the ECM may also facilitate cancer metastasis *in vivo*, as described in numerous studies in which cancer cell migration was imaged in primary tumours. For instance, using multiphoton microscopy, it was observed that highly metastatic CFP-expressing rat mammary adenocarcinoma MTLn3 cells injected into mammary glands moved more frequently along collagen fibres compared to low metastatic GFP-expressing MTLn3 cells (Sahai, Wyckoff et al. 2005) and more importantly, metastatic MTLn3 cells were associated with higher extravasation into the lungs (Wang, Goswami et al. 2004). Similar observations were made by imaging polyoma middle T oncogene (PyMT)-derived mammary tumours, where it was observed that GFP-labelled tumour cells migrated along collagen matrix fibres and around blood vessels. Moreover, human glioma cells injected into the brain migrated through perivascular space and white matter tracks (Cuddapah, Robel et al. 2014). Additionally, melanoma cells injected intra-arterially that successfully extravasated into the brain used cerebral microvessels as the main structures for migration and proliferation (Bentolila, Prakash et al. 2016). Migration through pores present in stromal tissue also has clinical pertinence. As an example, Provenzano *et al*. showed that collagen aligned in the perpendicular orientation to the tumour boundary facilitated cancer cell invasion (Provenzano, Eliceiri et al. 2006) and such stromal collagen organization was associated with poor survival of breast cancer patients (Conklin, Eickhoff et al. 2011).

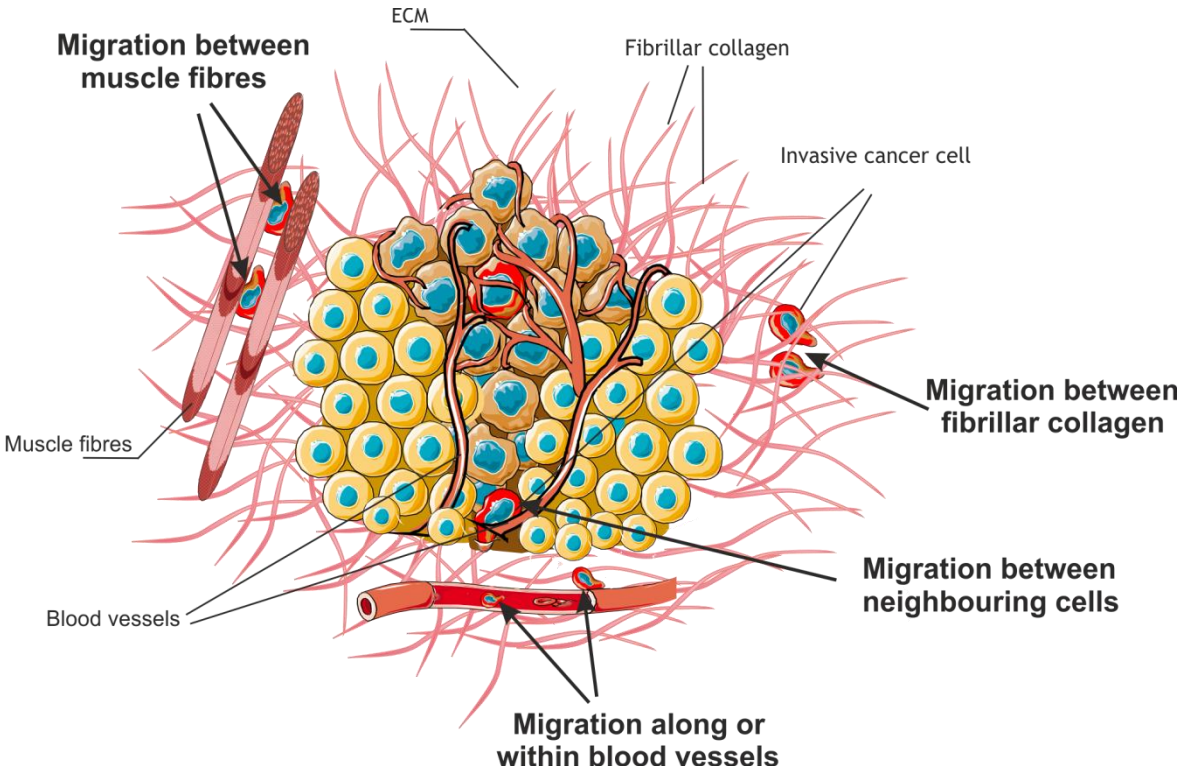

Figure 1-2 Microenvironments for confined migration *in vivo.*
The image illustrates different confined migration paths present *in vivo.* Cancer cells may migrate in spaces present between muscle fibres, along and within blood vessels, between fibrillar collagen fibres and between neighbouring cells. Image adapted from (Paul, Mistriotis et al. 2017). Image generated using Servier Medical Art.

1.2.2 Modes of cancer cell migration / invasion

The mesenchymal mode of invasion is one of the types of individual cell invasion (Figure 1-3). It occurs after completion of the epithelial to mesenchymal transition (EMT) program. It is characterized by elongated, fibroblast-like morphology with established cell polarity, and is dependent on proteolytic degradation of ECM (Friedl and Wolf 2003; Friedl 2004). Using this type of invasion, cells move relatively slowly, 0.1-1 μm/min. Such invasion mode has been detected in fibrosarcoma, glioblastoma and melanoma (Friedl and Wolf 2003; Sanz-Moreno and Marshall 2009; Thomas, Monturo et al. 2011). Mesenchymal cells employ a five-step cycle in order to migrate: pseudopod protrusion, formation of focal contacts, proteolysis of ECM, acto-myosin contraction and detachment of the trailing edge (Friedl and Wolf 2003). Protrusion occurs upon activation of Rac1 and Cdc42 GTPases, which activates the Arp2/3 complex that drives actin polymerization at the front of the cell (Ridley, Schwartz et al. 2003), (O'Connor and Chen 2013). Cells utilizing this type of migration create tracks in the ECM by using proteases, such as MMPs and plasminogen activator (uPA) (Nabeshima, Inoue et al. 2002; Tang and Han 2013). Focal adhesions provide a contact between the actin cytoskeleton and the external environment through the interaction of transmembrane proteins, such as integrins, with their extracellular ligands, and intracellular protein complexes linked to the actin cytoskeleton. Focal adhesion formation is initiated upon the binding of adhesion receptors to extracellular matrix (ECM) ligands (e.g. fibronectin, vitronectin, collagen) along the cell periphery usually at the protruding edge of a cell. Attachment of the cell to the ECM components induces clustering of integrins on the cell surface. Clustered integrins act as a platform for the recruitment of cellular proteins, such as paxillin, talin, tensin, p130Cas which provide strong linkages to the actin cytoskeleton, thereby connect cells firmly to the ECM (Nagano, Hoshino et al. 2012; Burridge and Guilluy 2016).

The amoeboid mode of invasion is the second type of individual cell invasion (Figure 1-3). It is characterized by rounded cell morphology and “a crawling” type of movement, with which cells are able to squeeze between spaces present in the ECM (Sabeh, Shimizu-Hirota et al. 2009). Cells utilizing this migration mode move at relatively high speeds, up to 4 μm/min (Friedl and Wolf 2003). Such invasion type has been observed in breast cancer, lymphoma, prostate

carcinoma, melanoma and sarcoma (Condeelis and Segall 2003; Friedl and Wolf 2003; Belletti, Nicoloso et al. 2008; Sanz-Moreno and Marshall 2009). The main features of amoeboid migration are loss of cell polarity, loose attachment to the ECM, very little to no formation of stress fibres and MMP-independent movement. Amoeboid migration is driven by cortical actin polymerization which occurs through Rho-ROCK signalling where myosin activation promotes quick remodeling of cortical actin (Sahai and Marshall 2003).

Collective modes of invasion are characterized by the migration of whole sheets, strand or tubes of cancer cells as whole structures or separated clusters (Friedl and Wolf 2008) (Figure 1-3). Such a mode of migration has been observed in breast, colorectal, melanoma cancers and other type of carcinomas (Nabeshima, Inoue et al. 1999; Hegerfeldt, Tusch et al. 2002; Wolf, Wu et al. 2007). From a mechanistic point of view, this type of migration is similar to the mesenchymal form where a leading cell degrades the ECM and creates a path for follower cells (Wolf, Wu et al. 2007). The main features of collective movement are degradation of the ECM by MMPs, maintenance of adherence junctions between cells, and coordinated action of actin cytoskeleton, acto-myosin contraction, cell polarity and cell surface receptors (Friedl and Wolf 2008).

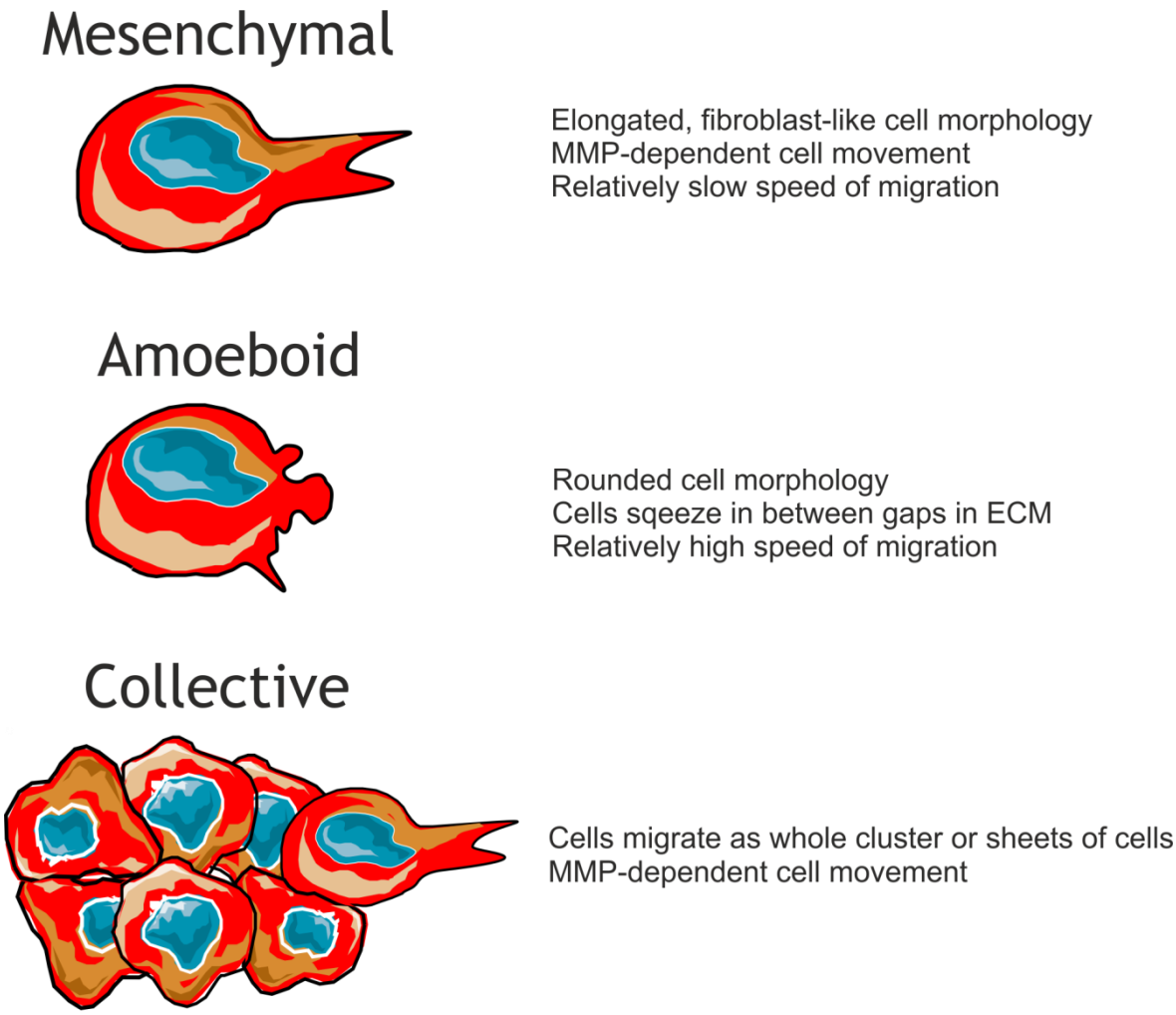

Figure 1-3 Different modes of cancer cell invasion.
The image represents three main types of cancer cell invasion: mesenchymal, amoeboid and collective. Image generated using Seriver Medical Art.

1.2.2.1 Actin cytoskeleton

Cell motility is a complex and dynamic process involving many changes in cell cytoskeleton architecture and coordination of many signalling pathways. This multistep process is initiated by external stimuli, which can be signals from neighbouring cells, extracellular matrix or diffusible factors. The main engine of cellular migration are actin microfilaments which build the cell cytoskeleton (Olson and Sahai 2009). F-actin filaments are formed by polymerization of globular monomeric actin (G-actin) subunits. Each actin filament has a positive, "barbed" end where G-actin subunits are added, and a negative "pointed" end which undergoes depolymerization. The critical concentration (Cc) of free G actin subunits determines whether the actin filament ends grow or shrink. When the polymerization and depolymerization of actin filaments is in equilibrium, the subunit concentration at the plus end is higher than the Cc, while the subunits concentration at the minus end is lower than the Cc. The maintenance of pre-existing actin filaments at equilibrium is called actin treadmilling. During this process, adenosine triphosphate (ATP)-loaded G-actin subunits associate with a positive end of the filament where over time the ATP is hydrolyzed to ADP and inorganic phosphate (Pi). The ADP-incorporated F-actin undergoes depolymerization at the "pointed" end. The ADP on released G-actin monomers is exchanged for ATP and the ATP-loaded G-actin can be re-incorporated into the positive end of F-actin (Pollard and Borisy 2003; Olson and Sahai 2009) (Figure 1-4).

There are many actin binding proteins that are associated with the assembly and disassembly of F-actin but the main players are summarized here. The Arp2/3 complex is activated by WASP/Scar proteins (Van Troys, Huyck et al. 2008), leading to nucleation of actin filaments to create a branched filament network. Gelsolins belong to a family of capping proteins, which bind and block the barbed ends of actin filaments; moreover they have F-actin severing activity (Van Troys, Huyck et al. 2008). Formins bind to barbed ends of F-actin and prevent its blocking by capping proteins; moreover they are involved in F-actin elongation (Breitsprecher and Goode 2013). Profilin is a G-actin binding protein that promotes polymerization and depolymerisation of F-actin (Nejedla, Sadi et al. 2016). ADF/Cofilin family proteins have the ability to sever F-actin filaments and to increase spontaneous polymerization (Bamburg and Bernstein 2010).

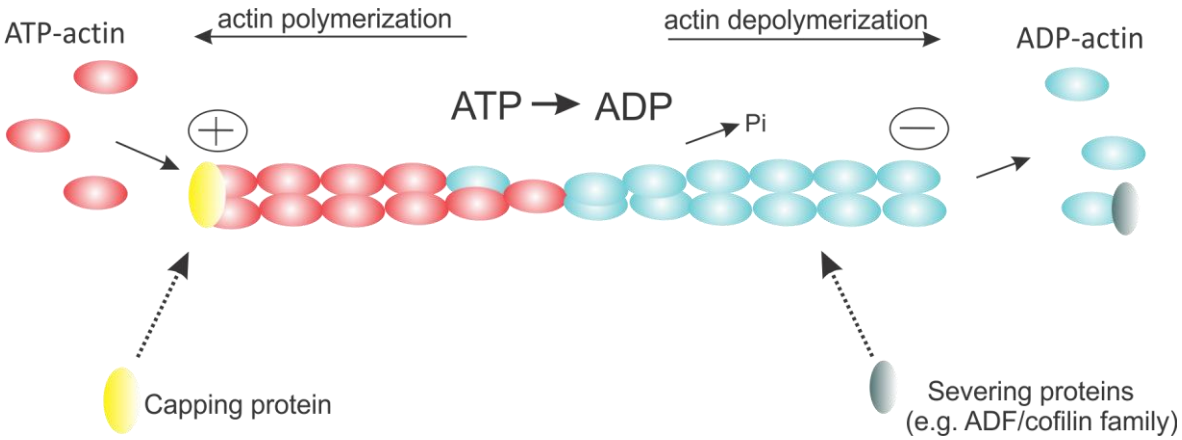

Figure 1-4 Actin filament polymerization and depolymerization.
Image illustrates actin polymerization and depolymerization process. During this process, adenosine triphosphate (ATP)-loaded G-actin subunits associate with a positive end of the actin filament where over time the ATP is hydrolyzed to ADP and inorganic phosphate (Pi). The ADP-incorporated F-actin undergoes depolymerization at the negative end.

There are many intracellular pathways that regulate the cell migration process, but Rho GTPases are known to be the key players (Figure 1-5) (Figure 1-6).

The RhoA-like cluster of proteins consist of RhoA, RhoB and RhoC GTPases which share ~85% of sequence homology and has been well studied in cell migration (Michaelson, Silletti et al. 2001). During cell migration Rho activity is associated with cell body contraction and rear end retraction and mostly known to be involved in so called amoeboid type of migration (Ridley 2015; Carlier and Shekhar 2017). Important Rho effectors are the Ser/Thr ROCK1 and ROCK2 kinases that phosphorylate myosin light chains (MLC) leading to bundling of actin fibres and clustering of integrins into focal adhesions (auf dem Keller, Huber et al. 2006; Burridge and Guilluy 2016). ROCK kinases also phosphorylate myosin-binding subunits (MBS) of the myosin light chain phosphatase (MLCP) inhibiting its activity and enhancing MLC phosphorylation (Hartmann, Ridley et al. 2015). Myosin light chain phosphorylation is also regulated by the calcium-dependent myosin light chain kinase (MLCK). ROCK kinases also phosphorylate and activate LIM kinases (LIMK1 and LIMK2) that in turn inactivate the actin-severing activity of cofilin leading to F-actin accumulation and stabilization (Oser and Condeelis 2009).

The Rac-like cluster of proteins consists of Rac1, Rac2 and Rac3 GTPases which share ~88% of homology (Jordan, Brazao et al. 1999). In cell migration, Rac GTPases are known to be involved in lamellipodia formation and membrane ruffles, and the mesenchymal type of migration characterized by elongated spindle-shaped cell morphology. A key role for Rac proteins is to induce actin polymerization in the front of migrating cells producing essential force in order to move cell forward (Eden, Rohatgi et al. 2002). Rac-dependent actin polymerization occurs via many effector proteins, which when leads to the initiation of actin polymerization. The actin-nucleating protein complex that can be indirectly triggered by Rac is the Arp2/3 complex, which is known to stimulate the formation of new actin branches, either *de novo* or at the barbed ends or sides of existing actin filaments (Goley and Welch 2006). Rac also induces the uncapping of barbed ends of actin filaments, thereby creating free ends necessary for actin assembly (Hanna and El-Sibai 2013).

The Cdc42 GTPase is known to be involved in the regulation of cell polarity and filopodia formation (Gupton and Gertler 2007). Filopodia are dynamic finger-like actin filament-bundled protrusions, which are thought to be responsible for extracellular sensing and transmitting signals back to the cell body to initiate actin polymerization. Cdc42 acts via Wiskott-Aldrich syndrome protein (WASP) leading to activation of the Arp2/3 complex (Hanna and El-Sibai 2013). Subsequently, it has been reported that mDia and IRSp53 are also downstream targets of Cdc42 and their activation leads to filopodia formation (Wu, Quondamatteo et al. 2006; Cory and Cullen 2007).

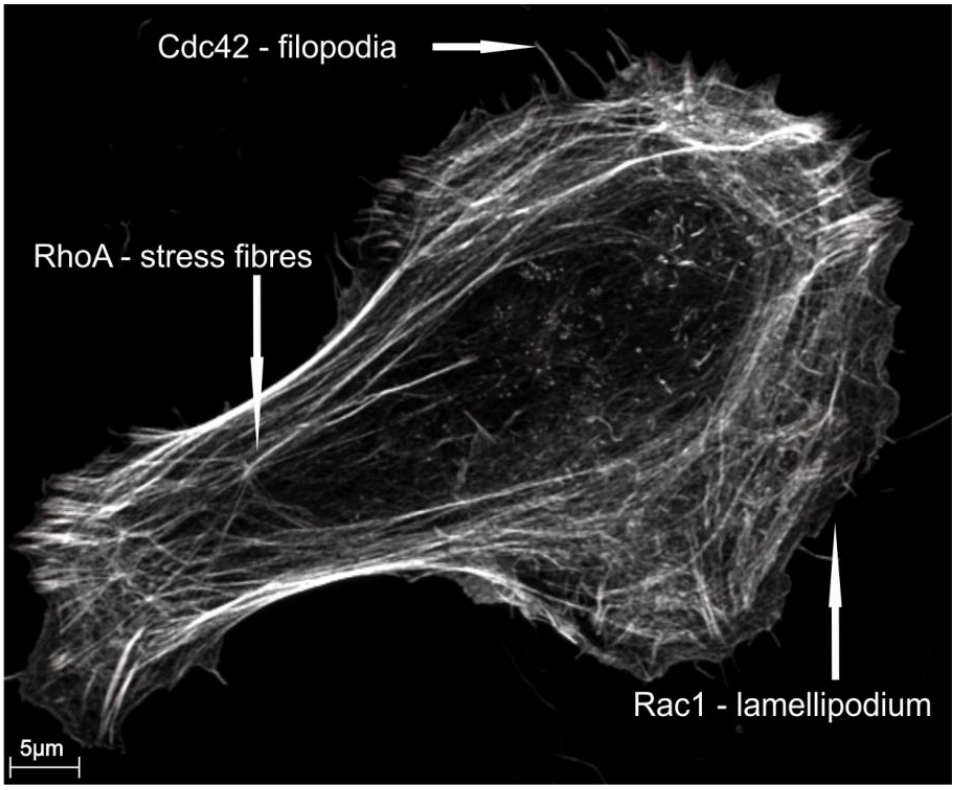

Figure 1-5 Rho GTPases and cell protrusion.
The image represents filamentous actin structures and Rho GTPase protrusion control. MDA MB 231 human breast cancer cells were fixed and stained for F-actin using phalloidin. The image was acquired on a Zeiss 880 microscope.

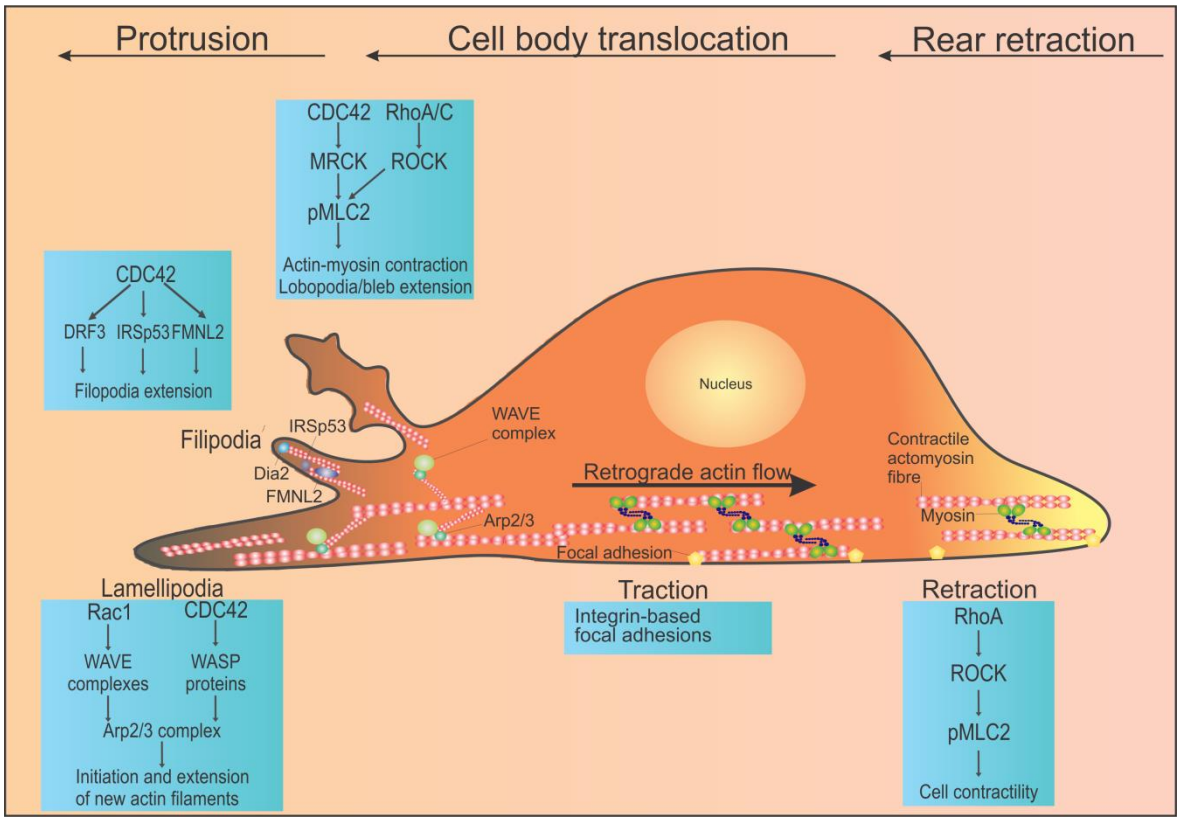

Figure 1-6 RhoGTPases and their role in organising actin cytoskeleton.
The image illustrates the downstream effectors of Rho proteins and mechanisms affecting actin in a migrating cell.

1.3 Cell elasticity

Changes in cell mechanical properties are often associated with health or disease states (Lee and Lim 2007). Diseases not only change cell biological properties, but also their physical and structural characteristics. In some diseases and pathologies, including sickle cell anaemia, spherocytosis and malaria; erythrocyte stiffening and increased viscosity have been observed and are believed to be causally linked with pathophysiological outcomes (Lee and Lim 2007). Additionally, cell mechanical changes have also been observed in cancer. For example, it was reported that cancer cells are softer compared to normal cells, and highly metastatic cancers are more easily deformed than less metastatic cancer cells (Doerschuk, Winn et al. 1990; Faria, Ma et al. 2008; Li, Lee et al. 2008). Such changes in the mechanical properties of cancer cells may play an important role in the metastatic cascade. An advantage of greater elasticity is thought to be increased cell deformability that enables passage through physical constraints to facilitate local tissue invasion and metastasis (Doerschuk, Winn et al. 1990; Cross, Jin et al. 2008). A change in cancer cell stiffness often is a result from changes in actin organisation (Li, Lee et al. 2008; Palmieri, Lucchetti et al. 2015).

The cytoskeleton plays not only an important role in creating cell shape, directing migration and invasion, but also plays a major role in regulating cell mechanical properties. The main structural components of the three types of cytoskeleton (actin, microtubule and intermediate filament) exhibit unique viscoelastic properties when measured as purified cytoskeletal preparations (Gittes, Mickey et al. 1993; Janmey, Hvidt et al. 1994; Kojima, Ishijima et al. 1994). The main determinant of cellular mechanics is the actin cortex, a rich layer of actin meshwork which lies directly beneath the plasma membrane (Bordeleau, Alcoser et al. 2014; Tao, Li et al. 2017). The actin cortex is composed of filamentous actin, myosin motors and actin-binding proteins, which undergo continuous turnover of their components during polymerization and depolymerization, cell adhesion and acto-myosin contraction processes. This continuous reorganisation allows the cells to quickly respond and adapt to external cues and biochemical signalling (Kunda, Pelling et al. 2008; Stewart, Helenius et al. 2011). The involvement of cytoskeletal components in the regulation of cell mechanical properties was demonstrated using drugs which

disrupt cytoskeletal organisation, for example latrunculins or cytochalasins. Latrunculins are toxins produced by some marine sponges which prevent actin polymerization by binding to actin monomers and preventing their re-incorporation into actin filaments (Morton, Ayscough et al. 2000). Cytochalasins are fungal metabolites which prevent actin polymerization and elongation (Goddette and Frieden 1986). Cells treated with actin-disrupting agents showed a decrease in their elastic modulus (Rotsch and Radmacher 2000; Vargas-Pinto, Gong et al. 2013).

Additionally, as well as density and length of actin filaments, the ordering of the actin filaments determinate the cell cortical mechanics. Cells with more aligned actin fibres (also called nematic or anisotropic organisation) are characterized by increased cell stiffness, while cells with more disorganised actin structure (also called isotropic organisation) are characterized by decreased cell stiffness (Gupta, Sarangi et al. 2015). Although the actin cytoskeleton is a major determinant of cell elasticity, the mechanistic pathways responsible for cell stiffness changes in cancer have not yet been identified.

There are many techniques available to study cell mechanical properties, including Atomic Force Microscopy (AFM), optical tweezers and micropipette aspiration (Addae-Mensah and Wikswo 2008).

1.4 Nuclei in confinement

As described above, confinement highly influences cell movement. Small pores present in the ECM may become challenging for a cell to pass through. In fact, cell body components like the plasma membrane, cytoplasm, small organelles and cytoskeleton are sufficiently elastic to tailor their shape and fit through available spaces (Wolf, Te Lindert et al. 2013). However, distortion of the nucleus is much more challenging. The nucleus is the largest and most rigid organelle of the cell and consequently it can become an obstacle for migrating cancer cells (Lammerding 2011; Martins, Finan et al. 2012). There were many studies done showing the importance of nuclear properties in confined migration. Using microfabricated channels with varying degree of confinement, it was reported that cells migrated with higher speed through wider channels while migration through constrictions smaller than 5 μm resulted in decreased cell speed and required stronger nuclear deformation (Fu, Chin et al. 2012; Tong, Balzer et al. 2012; Davidson, Denais et al. 2014).

1.4.1 Role of nuclear lamina in nuclear translocation

The nuclear lamina is a dense protein network underlying the inner nuclear membrane. Mammalian cells express two types of lamin; lamin A-types (lamins A and C) and lamin B-types (lamins B1 and B2) (Shimi, Pfleghaar et al. 2008). Both lamin A and B-types contribute to the overlying protein mesh that, in addition to having an impact on chromatin organization, DNA damage repair and transcriptional regulation (Shimi, Pfleghaar et al. 2008; Ho and Lammerding 2012; Solovei, Wang et al. 2013), also influences the physical properties and shape of the nucleus. The ratio of A-type lamin to B-type lamin in the nuclear lamina is proportional to tissue microelasticity. The lamina contains predominantly A-type lamins in stiff tissue, whereas B-type lamins are prevalent in the nuclear lamina in soft tissue. The nuclear mechanical response has been characterized as a combination of elastic and viscous properties with B-type lamins contributing primarily to the elastic response and A-type lamins contributing to the viscosity (Swift and Discher 2014; Swift et al. 2013). Using cell-stretching and micropipette aspiration techniques, it was reported that A-type lamins have greater influence on nuclear elasticity than B-type lamins. Mouse embryonic fibroblasts lacking lamin A and C had more deformed nuclei

and lower nuclear stiffness, while fibroblasts lacking lamin B1 had greater numbers of nuclear blebs but with physical properties that were not affected (Lammerding, Fong et al. 2006; Mitchell, Denais et al. 2015). In terms of confined cell migration, some studies reported that cells with decreased levels of lamin A/C migrated faster through constrictions smaller than the size of the nucleus (Harada, Swift et al. 2014). In contrast, increased expression of lamin A/C resulted in an opposite effect, it impaired the migration rate of neutrophils through micron-scale constrictions (Rowat, Jaalouk et al. 2013). Loss of lamin A/C expression did not affect nuclear size but rather nuclear translocations through small constrictions. Thus, nuclear stiffness may adjust to the structure of extracellular environment during cell migration through changes in lamin gene expression and contribute to cancer metastasis. Indeed, it has been observed that lamin gene expression was deregulated in many cancers (Hutchison 2014).

1.4.2 Role of chromatin in nuclear translocation

Besides lamins, the nuclear interior also plays a significant role in nuclear rigidity. Chromatin fibres occupy most of the nuclei space and, despite a major role in regulating genetic processes, such as transcription, there are also studies suggesting that it may affect the mechanical properties of the nucleus and subsequently alter cell migration. Chromatin fibres consist of DNA, proteins and RNA. DNA, in order to fit inside a small nucleus, is wrapped around histone octamers called nucleosomes, which are built of two copies of each histone protein: H2B, H2A, H3, and H4 and a linker DNA creating a “beads on a string”-like structure (Dahl, Engler et al. 2005; Bhaumik, Smith et al. 2007; Pajerowski, Dahl et al. 2007). To create higher-order chromatin structure, nucleosomes can interact with linker histones like H1 and other non-histone proteins (Bustin, Catez et al. 2005). All histones have a positively charged N-tail which sticks out from the surface of the chromatin and provides many lysine and arginine residues which can undergo post-translational modifications, such as methylation, acetylation, phosphorylation, ubiquitination, sumoylation or ADP ribosylation. Such modifications can modify DNA-histone interactions and affect the level of chromatin compaction (Luger, Mader et al. 1997; Kouzarides 2007; Kusch and Workman 2007). During interphase, chromatin can be found in two states: euchromatin and heterochromatin. Euchromatin is lightly condensed and actively transcribed, while heterochromatin is a tightly packed, and

transcriptionally silent, usually found at the periphery of the nucleus, typically associated with the nuclear lamina (Guelen, Pagie et al. 2008). Heterochromatin is subdivided into two types: constitutive heterochromatin which contains non-coding sequences and repetitive elements; and facultative form of heterochromatin which consists mainly of silenced genes, but which has the potential to be turned into transcribed euchromatin (Allis and Jenuwein 2016). Those two types of chromatin are discriminated by particular patterns of modification in the tail core of histones (Guelen, Pagie et al. 2008).

Several studies identified that chromatin structure and the level of its condensation determine nuclear size and stiffness (Gruenbaum, Margalit et al. 2005). Treatment of isolated nuclei with the chelating agent EDTA led to chromatin decondensation, nuclear swelling and decreased stiffness, while condensation of chromatin by addition of divalent cations led to nuclear shrinking and increased stiffness. (Dahl, Engler et al. 2005). Using the micropipette aspiration technique it was also reported that the nuclei of embryonic stem cells, which contained relatively lower levels of condensed chromatin, are softer compared to nuclei of differentiated cells which had more packed forms of chromatin, although nuclei of differentiated cells also expressed more lamin A and C (Pajerowski, Dahl et al. 2007; Rowat, Lammerding et al. 2008). In terms of cell migration, it was shown that directed cell migration required global chromatin condensation as it was observed by increased staining of heterochromatin marker trimethylation of Lys9 in H3 histone ($H3K9me^3$) (Gerlitz, Livnat et al. 2007). Moreover, induction of cell migration increased the levels of two other heterochromatin markers trimethylation of Lys27 in histone H3 ($H3K27me^3$) and mono-methylation on Lys10 in histone H4 ($H4K20me^1$). However the level of euchromatin markers trimethylation of Lys4 in histone H3 ($H3K4me^3$) and acetylation of Lys9 in histone H3 (H3K9ac) were not changed (Gerlitz and Bustin 2010); suggesting that cell migration is contingent on global chromatin condensation. In addition, chromatin decompaction led to decreased rates of cell migration independent of changes in transcriptional level (Gerlitz and Bustin 2010).

1.5 MAPK signalling pathway

The mitogen–activated protein kinase (MAPK) pathways control fundamental cellular processes such as proliferation, differentiation, migration and cell death. There are four distinct MAPK signalling cascades which are named according to their terminal serine/threonine kinases: ERK1/2, the c-Jun amino-terminal kinases (JNK1/2/3), p38 kinases and ERK5 (Johnson and Lapadat 2002; Roberts and Der 2007). All of the four MAPK pathways are comprised of three protein kinases and are regulated by phosphorylation cascades; MAPK is activated upon phosphorylation by mitogen-activated protein kinase kinase (MAPKK) which in turn is phosphorylated by mitogen-activated protein kinase kinase kinase (MAPKKK) (Figure 1-7). The ERK pathway is typically activated by growth factors, whereas JNK, p38 and ERK5 pathways by growth factors, stress and cytokines. Activation of MAPK pathways leads to the activation of many transcription factors such as Elk-1, ATF-2, Ets-2, thereby leading to changes in gene expression profiles (Kyriakis and Avruch 2001; Dhillon, Hagan et al. 2007). The ERK pathway is the best studied MAPK signalling pathway and it is deregulated in one-third of all human cancers (Dhillon, Hagan et al. 2007).

Various extracellular stimuli and internal processes activate the MAPK/ERK pathway. Ligand binding to receptor tyrosine kinases, for example epidermal growth factor receptors (EGFR), leads to receptor dimerization, autophosphorylation and the subsequent binding of receptor-bound protein 2 (GBR2). Such interaction recruits binding of the nucleotide exchange factor SOS at the plasma membrane. Activated SOS promotes the displacement of GDP from Ras, allowing for GTP binding and activation of membrane associated Ras. GTP-bound Ras combines with Raf and phosphorylates MEK1 and MEK2, which in turn activate ERK1 and 2 kinases. Activated ERK kinases translocate into the nucleus and activate transcription factors leading to expression of genes involved in the regulation of cell proliferation, migration, angiogenesis and survival (Chong, Vikis et al. 2003; Wellbrock, Karasarides et al. 2004; Meloche and Pouyssegur 2007; Mebratu and Tesfaigzi 2009) (Figure 1-7).

There are three human *RAS* genes designated as *H-RAS*, N-*RAS* and *K-RAS*. All of them belong to a class of proteins called small GTPases, which act as molecular switches and control the activity of many signalling pathways (Santarpia,

Lippman et al. 2012). Ras oncogenes are frequently mutated in many human cancers with the most common mutations occurring at the codons 12, 13 or 61. Such mutations lead to the formation of GTPase-activating protein (GAP)-insensitive and constitutively active Ras proteins, and consequent continuous activation of downstream effectors (Hancock 2003; Dhillon, Hagan et al. 2007).

RAF kinases are serine/threonine specific kinases. There are three members of this family, B-Raf, A-Raf and Raf1 (c-Raf) (Maurer, Tarkowski et al. 2011). Upon activation by GTP-loaded Ras proteins, Raf proteins are translocated from cytosol to the plasma membrane. The recruitment to the plasma membrane is an essential step in Raf activation (Lavoie and Therrien 2015). There is little data on A-Raf mutations in cancers. Although Raf-1 is known as a potent oncogene, B-Raf is the major player in human carcinogenesis. B-Raf is frequently mutated in various human cancers, most frequently in melanoma, malignant thyroid and colon carcinomas (Maurer, Tarkowski et al. 2011). The most common B-Raf mutation occurs at codon 600, leading to valine (V) being substituted by glutamate (E) (Davies, Bignell et al. 2002).

Due to the fact that MAPK/ERK pathway components (e.g. Ras and Raf) are frequently mutated or overexpressed (e.g. EGFR) in human cancers, this pathway has been the subject of intense research and several inhibitors have been developed. Some of them include EGFR inhibitors such as cetuximab or gefitinib (Harari 2004), Raf inhibitors such as Vemurafenib or Sorafenib which are V600E inhibitors (Santarpia, Lippman et al. 2012) or MEK1/2 inhibitors such as Trametinib and U0126 (Santarpia, Lippman et al. 2012).

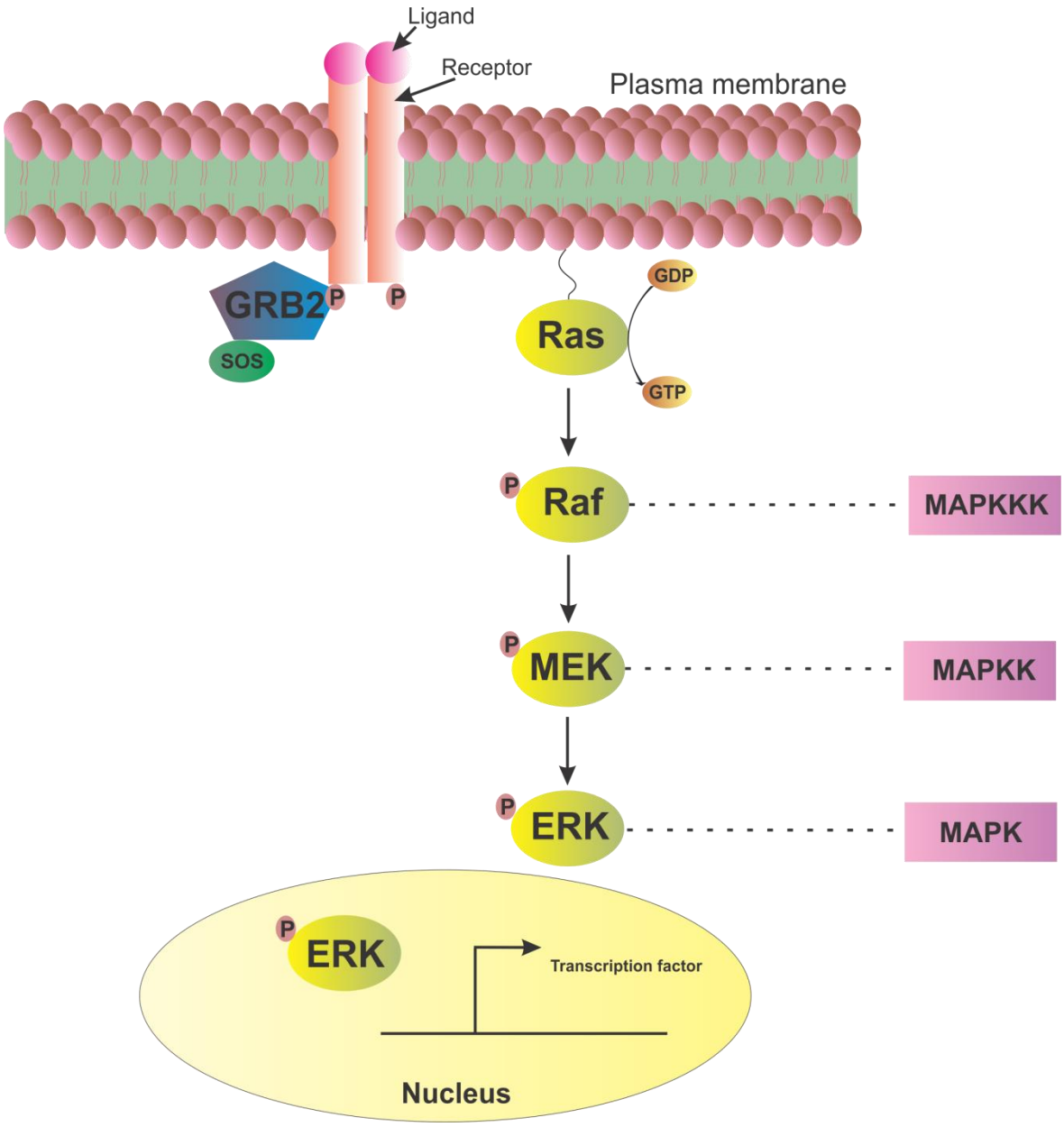

Figure 1-7 The MAPK/ERK pathway.
The MAPK/ERK pathway is the best-studied MAPK signalling pathway. The MAPK/ERK pathway involves sequential phosphorylation of three kinases: MAPK kinase kinase (MAPKKK), MAPK kinase (MAPKK) and MAPK (Kim and Bar-Sagi 2004).

1.5.1 MAPK/ERK pathway in cytoskeleton regulation

Small GTPases can be divided into members of the Ras subfamily which control cell proliferation and differentiation, and the Rho subfamily (such as Rac1, Cdc42 and RhoA) which control actin cytoskeleton organisation. Such division of GTPase functions is not always accurate as there are many studies showing that Ras proteins also have a large impact on actin organisation and the formation of adherence and tight junctions (Pollock, Shirasawa et al. 2005; Wang, Li et al. 2009). The best characterized Ras effectors are in the MAPK/ERK pathway. It has been demonstrated in many studies that the Raf/MEK/ERK pathway has profound effects on actin cytoskeleton organisation. Ras-transformed fibroblasts were characterised by the loss of stress fibres and focal adhesions, and the induction of membrane ruffling, which could be reversed by activation of RhoA (Pawlak and Helfman 2002). Furthermore, Sahai and Olson showed that sustained activation of the MAPK/ERK pathway achieved by oncogenic Ras induced transformation led to the post-translational downregulation of ROCK1 and loss of stress fibres (Sahai, Olson et al. 2001). Moreover, metastatic breast cancer cells with high levels of K-Ras and enhanced phosphorylation of ERK were characterized with disrupted stress fibres organisation and focal adhesions, and this phenotype could be restored by MEK inhibition (Choi and Helfman 2014).

1.6 Project aims

The life-threatening characteristics of particularly deadly cancers, including breast cancer and melanoma, derive principally from their metastatic dissemination. It has become increasingly apparent that cancer cells are significantly softer than corresponding normal cells, with metastatic cells typically being softer than non-metastatic tumour cells. These changes in cell mechanical properties have been proposed to play important roles in several of the steps in the metastatic process. An advantage of reduced stiffness to invasive tumour cells is increased deformability that enables cells to pass through physical constrictions to facilitate invasion. Therefore, acquiring detailed understanding of the mechanisms that contribute to elasticity changes will help to identify potential drug targets to block tumour cell dissemination. Although the actin cytoskeleton is known to be a major determinant of cell elasticity, there is little currently known about the factors or signalling pathways

that modulate cell stiffness. Therefore, the aim of this project was, firstly, to isolate invasive cancer cells with enhanced deformability that enabled them to migrate through constrained environments, and secondly, to identify regulators of cell elasticity and assess their contributions to tumour cell invasion.

2 Materials and methods

2.1 Materials

2.1.1 Antibodies

Table 2-1 List of primary antibodies.

Antigen	Species	Supplier	Catalogue Number
BrdU	Mouse	BD Bioscience	347580
FAK (pY397)	Mouse	BD Bioscience	611722
GAPDH	Mouse	Millipore	MAB374
H3K27me^3	Rabbit	Millipore	07-449
HLA	Mouse	Abcam	ab70328
Lamin A/C	Rabbit	Santa Cruz	sc-7292

Table 2-2 List of secondary antibodies.

Antigen	Supplier	Catalogue Number
Alexa Fluor 594 goat anti - mouse	Life Technologies	A11032
Alexa Fluor 594 goat anti - rabbit	Life Technologies	A11037
Alexa Fluor 680 goat anti - rabbit	Life Technologies	A21076
Goat anti-mouse DyLight 800	Thermo Fisher Scientific	SA5-35521

2.1.2 Plasmids

Table 2-3 List of plasmids.

Plasmid	Source
H2B-GFP	Addgene #11680
H2B-mCherry	Addgene #20972

2.1.3 Primers

Table 2-4 List of primers.

Primer	Supplier	Species	Catalogue Number
GAPDH	QIAGEN	Human	QT00079247
ENPP1	QIAGEN	Human	QT00094787
HBEGF	QIAGEN	Human	QT00000455
HSD11B1	QIAGEN	Human	QT00030296
LILRB1	QIAGEN	Human	QT00024920
MXRA8	QIAGEN	Human	QT00202790
PLAT	QIAGEN	Human	QT00075761
PLAU	QIAGEN	Human	QT00013426
PTPRU	QIAGEN	Human	QT00005677
TNFSF15	QIAGEN	Human	QT00041965
ß-2-M	QIAGEN	Mouse	QT01149547

2.1.4 Kits

Table 2-5 List of kits.

Kit	Supplier	Cataloque number
Amaxa Cell Line Nucleofactor kit V	Lonza	VCA-1003
CellTiter-Glo Luminescent Cell Viability Assay	Promega	G7570
Nuclei EZ Prep Nuclei Isolation kit	Sigma	NUC101
Qiagen RNasy Mini Kit	Qiagen	74104
Quantitect Reverse Transcription kit	Qiagen	205311

2.1.5 Buffers and solutions

Table 2-6 List of buffers and solutions.

Buffer/Solution	Recipe
4% PFA	4 % paraformaldehyde in PBS
1% SDS lysis buffer	1% SDS, 50 mM Tris pH 7.5
Cacodylate buffer (0.1 M, pH 7.4)	4.28 g Sodium Cocadylate, 25 g $CaCl_2$, 2.5 ml 0.2 N hydrochloric acid, make up to 200 ml with dH_2O
Loading Buffer (6x)	3 ml 1 M Tris, pH 6.8, 1.47 g SDS, 0.85 g DTT, 7.35 ml glycerol, 14.2 ml dH_2O and bromophenol blue (few grains)
PBS	170 mM NaCl, 3.3 mM KCl, 1.8 mM Na_2HPO_4, 10.6 mM H_2PO_4
Phosphate Buffer (0.1 M, pH 7.2)	36 ml $Na_2HPO_4.2H_2O$ (17.8 g in 500 ml), 14 ml $Na_2HPO_4.H_2O$, 50 ml dH_2O (13.6 g in 500 ml)
TBS-T	20 mM Tris - HCl pH 7.5, 136 mM NaCl, 0.1% Tween 20

2.1.6 Reagents and chemicals

Table 2-7 List of reagents and chemicals.

Reagent/Chemical	Supplier	Catalogue Number
10x MEM media	Thermo Fisher Scientific	21430020
2-deoxyglucose	Sigma	D8375
Acetic acid	Sigma	71251
Albumin standard (2 mg/ml)	Thermo Fisher Scientific	23209
Alexa Fluor™ 488 Phalloidin	Thermo Fisher Scientific	A12379
Bicinchoninic acid	Sigma	B9643
Bovine Serum Albumin	Thermo Fisher Scientific	23209
Cellomics® Whole Cell Stain	Thermo Fisher Scientific	8403401
Copper sulphate	Sigma	C2284
Cytochalasin D	Sigma	C8273

DAPI	Sigma	D9542
Dimethyl Sulfoxide	Sigma	D2650
Dispase II (neutral protease, grade II)	Sigma	000000004942078001
Dulbecco's Modified Eagle Medium (No glutamine)	Gibco	21969-035
Fetal Bovine Serum	Gibco	10270
Glacial acetic acid	Sigma	1005706
Glutaraldehyde	Sigma	G5882
Hank's Balanced Salt Solution (HBSS)	Thermo Fisher Scientific	14065-049
L-Glutamine (200 mM)	Gibco	25030-032
Matrigel	Corning	354234
Minimium Essential Medium / Non-Essential Amino Acids (MEM/NEAA)	Thermo Fisher Scientific	11140035
Minimum Essential Medium (MEM) with Earle's Balanced Salts (MEM/EBSS) (without L - Glutamine)	GE Healthcare Life Sciences	11541871
NBD C6-sphingomyelin (60031) from Biotium	Insight biotechnology	60031
NuPAGE 4-12% Bis-Tris Gel	Life Technologies	NP0321BOX
NuPAGE MES SDS Running Buffer (20x)	Life Technologies	NP0002
NuPAGE Transfer Buffer (20x)	Life Technologies	NP0006-1
Paraformaldehyde (16%)	EMS	15710
Penicillin Streptomycin	Gibco	15140-122
Ponceau S solution	Sigma	P7170
ProLong® Diamond Antifade Mountant	Thermo Fisher Scientific	P36961
Propidium iodide	Sigma	P4170
Protein TM All Blue weight marker	Bio-Rad	1610373
Puromycin	Sigma	P8833
RNaseA	QIAGEN	1007885
Sodium azide	Sigma	S8032
Sodium chloride	Sigma	S3014
Sodium Pyruvate	Thermo Fisher Scientific	11360070
Sulforhodamine B	Sigma	230162
SYBER Green based quantitative PCR	Thermo Fisher Scientific	F-410L
Trametinib	Medchem Express	HY-10999
Trichloroacetic acid	Sigma	T6399
Trion-X100	Thermo Fisher Scientific	28314
Trypsin (10x)	Gibco	15090-046
U0126	Cell Signalling Technology	9903S

2.2 Cell culture techniques

2.2.1 Origin, maintenance and storage of cell lines

MDA MB 231 cells are an epithelial, adherent cell line. They were originally extracted from human breast cancer metastases. MDA MB 231-luc-D3H2LN cells are derived from a spontaneous lymph node metastasis from a MDA MB 231 mammary fat pad tumour (Jenkins, Hornig et al. 2005). MDA MB 231-luc-D3H2LN cells stably express a firefly luciferase gene.

MDA MB 435 cells are an adherent, epithelial cell line, originally derived from a pleural effusion of a female breast cancer patient. MDA MB 435 cells is a melanoma cell line, however they are often mistakenly used and described as breast cancer cells. Gene expression studies showed that MDA MB 435 cells are melanoma origin, not breast cancer (Prasad and Gopalan 2015).

MDA MB 231-luc-D3H2NL and MDA MB 435 cell lines were grown in HyClone MEM/EBSS media, supplemented with 10% fetal bovine serum (FBS), 2 mM L-glutamine, 10 U/ml penicillin and 10 µg/ml streptomycin, 1% MEM/NEAA (non-essential amino acid), 1% Sodium Pyruvate. Cells were kept at 37°C with 5% CO_2 in a humidified incubator and passaged every 3-4 days as follows; culture media was aspirated and cells were washed once with PBS and subsequently incubated in 0.25% trypsin for a short time in standard tissue culture conditions. Cells were resuspended in medium and an aliquot was moved to a fresh tissue culture dish.

Human fibroblasts were kindly provided by Max Nobis (Cancer Research UK Beatson Institute). They were grown in DMEM media supplemented with 10% FBS, 2 mM L-glutamine, 10 U/ml penicillin and 10 µg/ml streptomycin. Fibroblasts were used for collagen matrix preparation for 3D cell invasion assay.

For long-term storage, frozen cell stocks were prepared by resuspending healthy cell pellets in freezing media, which consisted of 90% FBS and 10% DMSO. Subsequently, 1 ml of aliquots were transferred to cryogenic vials and stored at -80°C for 24 hours and for long-term storage in liquid nitrogen vapour phase tanks.

2.2.2 Strategy for obtaining Selected and Flow sorted cell lines

Three independent Selected (Sel) cell lines of MDA MB 231 or MDA MB 435 cells were generated as follows. Parental MDA MB 231 or MDA MB 435 cells were trypsinized and $1x10^6$ of each cell line was resuspended in 10 ml of serum free medium. The cell suspension was seeded in 7.5 cm inserts with 3 µm pore membranes (Corning®). Subsequently, the inserts were placed in 10 cm dishes containing 10 ml of serum containing medium. The plates were left for 5 days in standard tissue culture conditions to allow cells to migrate through the pores and attach to the lower chamber compartment. Afterwards, the inserts were removed, the media was changed to fresh serum containing media and the plate was placed back in the incubator. The selection strategy was repeated 2 more times as described above. In brief, each of 3 independent Selected populations of MDA MB 231 and MDA MB 435 cells were selected through 3 µm pores in 3 independent rounds of selection.

Three independent Flow Sorted (FS) populations of MDA MB 231 cells were obtained as follows. Parental MDA MB 231 cells were trypsinized and resuspended in serum containing media and sorted for small size using a BD Fusion Sorter. Subsequently, the sorted cells were kept in standard tissue culture conditions to reach the desired concentrations. Once the cells expanded, the sorted cells were subjected to 2 more rounds of independent sorting as described above. In brief, each of 3 independent Flow sorted populations of MDAMB 231 cells were sorted for small size in 3 independent rounds of sorting.

2.2.3 Tissue culture treatments

2.2.3.1 Treatment of cells with Trametinib or U0126 inhibitors

Treatment of MDA MB 231 and MDA MB 435 cells with Trametinib or U0126 inhibitors were performed as follows. Cells were seeded in culture dishes and grown overnight. Next day, 0.5 µM Trametinib or 10 µM U0126 was added and incubated for 24 hours. After incubation, cells were processed depending on the experimental requirements. Both drugs were dissolved in DMSO to 10 mM stock concentrations.

2.2.3.2 Treatment of cells with Cytochalasin D

Treatment of MDA MB 231 cells with Cytochalasin D was performed as follows. Cells were seeded in culture dishes and grown overnight. Next day, 0.5 µM Cytochalasin D was added and incubated for 2 hours. After incubation, cells were processed depending on the experimental requirements. Cytochalasin D was dissolved in DMSO to a 10 mM stock concentration.

2.2.4 Transfection of DNA plasmids

DNA plasmids, H2B-GFP, H2B-mCherry, were introduced into MDA MB 231 cells through electroporation using an Amaxa Cell Line Nucleofactor® Kit V. In brief, cells were trypsinized and $1x10^6$ of cells were centrifuged at 90xg for 10 minutes. Cell pellets were resuspended carefully in 100 µl of Nucleofactor® Solution/supplement mix (ratio 4.5:1) and subsequently 2 µg of DNA plasmid was added. The cell/DNA mix was transferred into supplied cuvettes and placed in the Nucleofactor® I Device where X-013 program for MDA MB 231 cells was applied. Thereafter, 500 µl of pre-warmed medium was added into the cuvettes and samples were gently transferred with a plastic Pasteur pipette into wells of 6-well plate containing 1.5 ml of pre-warmed medium.

2.2.5 Cell proliferation assay

Cells were seeded in triplicate at $3x10^3$ cells per well in 12-well plates. Cell numbers were measured at 24, 48 and 72 hours. Cells were trypsinized and counted using a CASY® Cell Counter.

2.2.6 Cell volume measurement

Cell volumes were calculated using the formula for the volume of the sphere, $V = \frac{3}{4}\pi r^3$. Mean diameter measurements were determined using a CASY® Cell Counter.

2.2.7 Cell adhesion assay

Cells were seeded in 96-well plate sat a density of $4x10^4$ cells in 100 µl media per well. The plates were left for 3 hours at 37°C in standard culture conditions to let cells adhere. After 3 hours of incubation, cells were washed 4 times with

PBS to remove non-adherent cells. Afterwards, 100 µl of culture medium was added to each well including control wells containing culture medium only. The number of adherent cells was measured using the CellTitre-Glo Luminescent Cell Viability Assay according to the manufacturer's instructions. Briefly, CellTitre-Glo reagent and cells were left at room temperature for 30 minutes to equilibrate. 100 µl of CellTitre-Glo reagent was added to each well. Next, plates were placed on an orbital shaker for 2 minutes and then incubated for 10 minutes at room temperature. After incubation, the content of each well was transferred to Fisherbrand white 96-well plates. Luminescent readings were made on Glomax 96 Microplate Luminometer.

2.2.8 Dispase-based cell detachment assay

Cell were seeded at $3x10^5$ cells per well in 12-well plates and left overnight in standard tissue culture conditions. Cells were washed once with PBS and 500 µl of 2 U/mg of dispase (in media) was added per well and subsequently left for 5 minutes at 37°C. 500 µl of the mix of dispase and medium was removed and cell numbers were measured. To measure the number of cells attached to the bottom of plates, 500 µl of the mix of 2 U/mg dispase and media was added and left until cells detached from the plates. The percentage of attached cells was normalized to the total number of cells.

2.2.9 Cell spreading assay

Cell spreading was measured using the xCelligence Real-Time Cell Analyzer (RTCA) system and E-plate 16. 50 µl of culture medium was added to each well and left to equilibrate for 1 hour in a standard tissue culture incubator. After incubation, the background measurement was taken before $1x10^4$ cells in 100 µl of culture media were added to each well. The plates were placed back in the RTCA analyser and measurements were taken every 3 or 5 minutes for 12 or 3 hours.

2.2.10 Transwell cell migration assay

The number of cells able to migrate through 3 µm or 8 µm pores was measured using a Transwell migration assay with 3 µm or 8 µm pore-membrane inserts. In brief, $1.2x10^5$ cells for 3 µm pore membranes and $6x10^4$ cells for 8 µm pore

membranes were resuspended in 300 µl of serum free medium. The cell suspension was added to the insert and placed in a well of 24-well plates containing 750 µl of serum full medium. The plates were left for 3 days in standard culture conditions to allow cells to migrate through the membrane and attach to the lower chamber compartment.

The number of migrated cells at the bottom of 24 well–plates was quantified using a sulforhodamine B (SRB) colorimetric assay. Briefly, after removing the inserts, 10% (w/v) of trichloroacetic acid (TCA) was added to each well to reach a final concentration of 3.3%. The cells were fixed at 4°C for 30 minutes. Cells were then washed 3 times with water, air-dried and 300 µl of 0.04% of SRB was added to each well and incubated for 30 minutes at room temperature. Afterwards, the SRB solution was removed; the wells were washed 3 times with 1% (v/v) acetic acid and air-dried. Subsequently, 250 µl of 10 mM Tris (pH 10.5) was added into each well and the plates were placed on a shaker for 15 minutes. Afterwards, 200 µl of the well content was transferred to 96-well plates and absorbance was measured on a spectrophotometer at 490 nm.

2.2.11 Individual cell migration assay

Cells were seeded in 12-well plates at a density of $5x10^3$ cells per well. Next day, the plates were placed in a Nikon TE 2000 Time Lapse Microscope set in an incubation chamber at 37°C with 5% CO_2. The plates were left for 1 hour to let cells adjust to the conditions of the chamber. Bright field images were taken every 15 minutes for 22 hours with a 10x objective. Migration velocity, accumulated distance and Euclidean distance were measured using Manual tracking and Chemotaxis plugins in ImageJ. Cells were tracked for 45 frames and dividing cells were not included.

2.2.12 3D cell invasion assay

3D collagen invasion assay was performed according to the protocol described by Timpson *et al.* (Timpson, Mcghee et al. 2011).

2.2.12.1 Preparation of collagen I from rat tails

Collagen was prepared from approximately 12-14 adolescent rat tails. Rat tails were washed with 70% ethanol, the skin was removed and the tendons were detached from the core of the proximal region of the tail using toothed forceps. The tendons were kept in 70% ethanol in a petri dish to keep it hydrated. Next, the tendons were extracted for 48 hours in 1.5 L of 0.5 M acetic acid by stirring at 4°C. Next day, the extract was centrifuged at 7500xg for 30 minutes and the supernatant was placed in a cooled 2 L beaker. Next, 10% (w/v) of NaCl was added to the supernatant and stirred for 30 – 60 minutes. The supernatant was centrifuged again at 10,000xg for 30 minutes. This time the supernatant was removed and the precipitate was dissolved in 0.25 M acetic acid and stirred for 24 hours at 4°C. In the next step, two dialysis tubes ~40 cm long were cut and microwaved for 1 min in dH_2O. A knot was tied at the bottom of the tubes, the collagen was poured inside and the tubes were closed avoiding making air bubbles. Subsequently, the collagen was dialyzed against 6-8 changes of 6 L ~17.5 mM acetic acid (changed twice daily, 1 ml of glacial acetic acid per litre of cold water). The dialyzed collagen was centrifuged at 30,000xg for 1.5 hours, the supernatant was removed and placed in the sterile bottle. The collagen solution was adjusted to 2 mg/ml concentration using 0.5 M acetic acid. The collagen was stored at 4°C.

2.2.12.2 Preparation of 3D matrix with embedded fibroblasts

25 ml of ice-cold collagen (approximately 2 mg/ml) was mixed with 3 ml of 10x MEM media and approximately 3 ml of 0.22 M NaOH was added until the collagen turned orange (pH = 7.2). $1x10^6$ fibroblasts were trypsinized and centrifuged at 400xg for 5 minutes. Fibroblasts were resuspended in 3 ml of FBS and immediately added to 25 ml of ice-cold rat tail collagen then mixed and stirred. 2.5 ml of collagen/fibroblast mix was plated per 35 mm dish as quickly as possible. The collagen/fibroblast mix was left to set in standard culture conditions for 30 minutes. Afterwards, 1 ml of fibroblast growth media was added and the collagen/fibroblast matrix was detached from the side of the dish using a pipet tip. Next day, fresh media was added and then changed every other day for approximately 8 days until the collagen matrix fitted in a well of 24-well dish. Once the collagen disks reached the desired size, they were

incubated with culture media and puromycin at a final concentration of 5 µg/ml (2 ml per dish) for 2 days to remove the fibroblasts. Afterwards, the collagen disks were washed twice with PBS for 10 minutes each.

2.2.12.3 Seeding cells on top of collagen matrix disks

Contracted collagen plugs were placed in 24-well plates. $1.5x10^5$ cells in 1 ml of culture media was seeded on top of the collagen disk and left for 2 days in standard culture conditions to let the cells adhere. After 2 days, matrix disks were moved onto grids.

2.2.12.4 Transferring collagen disks onto grids for cell invasion

Prior to use, stainless steel grids were cut to create a tripod and autoclaved. Each grid was placed in a 6 cm dish and growth media was added to reach the level above the grid. Collagen disks were placed on top of the grid and media was aspirated to create an air-liquid interface, to ensure that only the bottom of the matrix was in contact with the media. The media was replaced every other day for 8 days. After 8 days of invasion, the plugs were fixed in 4% PFA.

2.2.12.5 Fixation of collagen disks

The collagen disks were transferred onto a flat surface and cut in half. Two halves of the matrix were lifted with a scalpel and transferred to 4% PFA/PBS solution and fixed overnight. The fixed disks were horizontally paraffin-embedded and 4 µm sections were cut and stained with haematoxylin and eosin (H&E) by the Beatson Histology Service. Stained collagen disks were imaged by Beatson Histology Service using the Leica Biosystem software. The invading distance of the cells was measured using ImageJ software.

2.2.13 Plasma membrane fluidity determination using Fluorescence Recovery after Photobleaching (FRAP)

$2x10^5$ cells were seeded on 35 mm glass bottom dishes and left overnight in standard tissue culture conditions. Next day, cells were washed twice with HBSS media followed by staining with NBD-sphingomyelin at 4 µM for 10 minutes in room temperature protected from light. Cells were then rinsed and observed in HBSS media.

Evaluation of membrane fluidity was obtained by measuring lateral diffusion of NBD-sphingomyelin by FRAP. All experiments were performed on a Zeiss 880 confocal microscope. In all experiments, a 60x oil immersion objective was used. For the photobleaching, a 488 nm laser was used, set to 100% laser power. Images were set to 510 x 200 pixels and speed 12 for a sufficient speed scanning. The zoom factor was set to 2 to avoid bleach during acquisition. For bleaching a region of interest (ROI1), a circle of 24 pixels was defined on the apical cell body membrane. In order to perform quantification, two other regions of interests were drawn around the cell (ROI2) and a random non-fluorescent region, also referred to as background (ROI3). Mobile fraction and $t_{1/2}$ were quantified using Easy FRAP software. The fluorescence intensity was normalized using a full scale normalization method. In order to extract quantitative information from the curves, double term fitting exponential equations were used.

2.2.14 Nuclei volume measurement

In order to quantify nuclei volumes, cells were fixed and stained with DAPI as described for the Immunofluorescence assay. In order to measure nuclei volumes, z-stack sections of DAPI-stained nuclei were taken on a Zeiss 710 confocal microscope. The obtained z-stack sections were then fed into Volocity Software. The program allowed 3D image analysis based on the fluorescence signal obtained by the confocal microscope.

2.2.15 Nuclei isolation

Nuclei were isolated using Nuclei EZ Prep Nuclei Isolation kit. In brief, $1x10^6$ cells were seeded in 10 cm dishes and incubated overnight in standard tissue culture conditions. After incubation, cells were washed twice with 10 ml of ice cold PBS and harvested with 4 ml of lysis buffer provided with the kit using a bladed cell scraper. The entire cell lysates were transferred to 15 ml tubes, vortexed briefly and set on ice for 5 minutes. Next, the lysates were centrifuged for 5 minutes at 400xg at 4°C. The supernatants were aspirated and the nuclei pellets were resuspended in 500 µl of lysis buffer, vortexed, topped up with 3.5 ml of lysis buffer and the washing step was repeated. After the final wash, the supernatants were aspirated and the isolated nuclei were processed for further experiments.

2.2.16 DNA cell cycle analysis with propidium iodide (PI)

For the cell cycle analysis, cells were trypsinized and $1x10^6$ cells were centrifuged at 1000 rpm for 5 minutes followed by a PBS wash. Subsequently, the cell pellets were resuspended in 300 µl of PBS and then 400 µl of 70% EtOH was added. The cell suspensions were vortexed, the volumes increased to 1.5 ml with 70% EtOH and stored at 4°C for 24 hours. The samples were centrifuged at 1000 rpm and washed twice with 2 ml of PBS each. The pellets were resuspended with 500 µl of PBS containing 50 µg/ml propidium iodide and 125 µg/ml RNaseA followed by 1 hour incubation at room temperature in the dark. After the incubation, the samples were centrifuged at 1000 rpm for 3 minutes, resuspended in 300 µl of PBS and then transferred to flow cytometry tubes. The samples were analysed on a BD FACSCalibur™ machine.

2.2.17 Cellular protein extraction

2.2.17.1 Cell lysate preparation

Cells were grown to the desired concentration and lysed to extract proteins. After placing cell culture dishes on ice, the medium was aspirated and cells were washed twice with ice-cold PBS. SDS lysis buffer (1% SDS in 50 mM Tris pH 7.5) was added to the culture dishes and the monolayer of cells were scraped using a cell lifter. Lysates were then transferred to a Qiagen Qiashredder column, which homogenized the samples, filtering out insoluble debris and reducing viscosity. The filtrates were centrifuged at 14,000 rpm for 1 minute and transferred to 1.5 ml Eppendorf tubes and centrifuged at 14,000 rpm for 15 minutes at 4°C to pellet any existing debris. The supernatants were transferred to fresh Eppendorf tubes and the protein concentrations were determined using the BCA assay. Samples were stored at -20°C.

2.2.17.2 Protein concentration determination

Total protein concentration of cell lysates was determined using a bicinchoninic acid assay (BCA assay), also known as the Smith assay. Protein standards - 0.08, 0.1, 0.2, 0.4, and 1 mg/ml - were prepared using 2 mg/ml bovine serum albumin stock solution by diluting it in the lysis buffer. To measure the concentration, 10 µl of blank solution (in triplicate), standards and samples (in duplicate) were

added to Greiner Bio One 96-well plates. 200 µl of developing solution (50:1, bicinchoninic acid:copper sulphate solution) was added to each well, and the plates were incubated at 37°C for 45-60 minutes. The absorbance of each well was measured using a Molecular Devices Microplate at 562 nm reader. Protein concentration was calculated from standard curves.

2.2.17.3 SDS polyacrylamide gel electrophoresis

SDS-polyacrylamide gel electrophoresis (PAGE) was used to separate proteins based on their molecular weight. NuPAGE Bis-Tris 4-12% gradient gels were used. Protein samples were diluted in SDS lysis buffer and 6x loading buffer added to reach the desired concentration. The samples were boiled for 5 minutes at 95°C. After boiling, samples were centrifuged briefly, left to equilibrate to room temperature and then loaded onto the gel along with Precision Plus Protein™ All Blue weight marker. Bis-Tris gels were run in tanks containing 1 x NuPAGE MES buffer at 160 V for approximately 1.5 hour. Subsequently, gels were used for western blotting.

2.2.17.4 Western blotting

Proteins were transferred to Protran™ nitrocellulose membrane in a Bio-Rad Mini Trans-Blot® Cell. Proteins were transferred in tanks containing 1x NuPAGE Transfer Buffer with 20% methanol. Prior to transfer, nitrocellulose membranes were pre-wet in transfer buffer. Whatman papers and sponges were also pre-wet and stacked with the gel and membrane. All transfers were run at 100 V for 1 hour using an ice pack in the apparatus. After transfer, the membranes were stained with Ponceau red solution to confirm equal loading of proteins. The stain was washed off with distilled water, and the membranes were blocked in 5% (w/v) milk powder or 3% BSA (depending on the antibody's manufacturer instruction) in TBS-T for 1 hour at room temperature. Primary antibodies were diluted in blocking buffer to the desired concentration and incubated at 4°C overnight. After incubation, the membranes were washed three times for 10 minutes each in TBS-T and subsequently incubated with secondary antibody, which had been diluted 1:10000 in blocking buffer, for 60 minutes at room temperature. Once blots were washed in TBS-T three times, they were rinsed in

dH_20 and protein bands were visualised using a LI-COR Odyssey® system. Protein bands were quantified using Image Studio Lite version 5.2.

2.2.18 Gene expression studies

2.2.18.1 RNA isolation and RT-qPCR

RNA was isolated using the Qiagen RNasy Mini Kit according to manufacturer's instructions. RNA concentration and purity was determined using a NanoDrop 2000 spectrophotometer. To perform quantitative RT-qPCR, complementary DNA (cDNA) was prepared using the Quantitect Reverse Transcription kit. In the first step, genomic DNA was eliminated by performing the following reaction; 2 µl of gDNA Wipeout Buffer was added to 1 µg of RNA and nuclease-free water to reach a total volume of 14 µl. The mixtures were incubated at 42°C for 2 minutes in a water bath and in the next step kept on ice. Subsequently, reverse-transcription mix consisting of 1 µl of reverse transcriptase, 4 µl of RT buffer and 1 µl of RT primer mix was added and the solutions were incubated at 42°C for 15 minutes in a water bath and then at 95°C for 5 minutes in a thermal cycler.

The cDNA samples were diluted 5 times with nuclease-free water and standards were prepared by pooling 10 µl of each sample and diluting to the following dilutions: 0.01, 0.04, 0.2, 1.

To perform quantitative PCR (qPCR), SYBER Green based qPCR was performed in triplicate in 20 µl reaction mixtures containing 10 µl of master mix (master mix contains hot-start polymerase, SYBR green, PCR buffer, 5 mM $MgCl_2$, and dNTP mix), 6.35 µl of nuclease-free water, 2 µl of primer, and 0.15 µl ROX passive reference dye per sample. The reaction mixtures were then distributed into MicroAmp® Fast Optical 96-well plates and 1.5 µl of cDNA sample or standard was added to each well. Reaction mixtures containing water instead of cDNA template were used as controls. The plates were covered with optically transparent sealing film and run on an Applied 7500 Fast Real-Time PCR system. A melting curve for each primer was established, which was used to identify the presence of single PCR products. Data were analysed on Applied Biosystem 7500 Software 2.0.5 and the expression level of genes of interests were calculated using the ΔCt method and normalized to *GAPDH*.

2.2.18.2 RNA Sequencing

$1x10^6$ cells were seeded into 6-well plates and grown overnight. Total RNA was extracted using the RNAeasy kit (Qiagen) according to manufacturer's instructions. RNA was quantified using a Nanodrop spectrophotometer (Nanodrop Tech). The Agilent RNA ScreenTape assay and the Agilent 2200 TapeStation system were used to determine the RNA integrity number equivalent. This analysis indicated that the RNA integrity number (RIN) for all samples was ≥ 9.9. Total RNA was used to generate oligo dT-enriched libraries with the Illumina TruSeq RNA Library Preparation kit v2.0. The quality and quantity of DNA libraries were assessed using an Agilent 2100 Bioanalyzer and a Qubit (Thermo Fisher Scientific), respectively. The libraries were run on an Illumina NextSeq 500 platform using High Output 75 cycles kit (2x36 cycles, paired-end reads, single index). Next-generation RNA sequencing was carried out by the Beatson Institute Molecular Technology Service. Data were analysed by the Computational Biology department (Cancer Research UK Beatson Institute).

2.2.19 Microscopy

2.2.19.1 Fluorescence Life Time Imaging Microscopy (FLIM)

In order to obtain FLIM images, a Nikon TE 2000 inverted microscope fitted with a Lambert Instruments FLIM Attachment (LIFA) and a Yokogawa CSU22 spinning disk unit with 100x objective was used. The microscope was equipped with an incubation chamber suitable to maintain live cells and optics at constant temperature. The LIFA system was equipped with an Omicron 50 mW 445 nm laser for CFP lifetimes and a 60 mW 488 nm laser for GFP lifetimes. It is based on the frequency domain method for fluorescence lifetime imaging and allows the rapid acquisition and generation of lifetime images. Fluorescence lifetimes were measured using LI-FLIM software.

2.2.19.1.1 Chromatin condensation determination

For the chromatin condensation studies, $1x10^6$ cells were transfected with H2B fused to eGFP via its carboxy terminus and H2B fused to mCherry via its amino terminus using Amaxa Cell Line Nucleofactor® Kit V. Transfected cells were

seeded on 35 mm glass bottom dishes and left for 72 hours in standard tissue culture conditions. After 3 days, cells were imaged using FLIM microscopy.

For 2-deoxyglucose (2-DG) and sodium azide treatment experiments, cells were treated with 50 mM 2-deoxyglucose and 10 mM sodium azide 30 minutes before acquiring images. Control cells were treated with dH_20.

2.2.19.2 Total Internal Reflection Fluorescent Microscopy (TIRF)

TIRF images were taken on a Nikon Eclipse TE2000-U microscope. A 100x 1.45 NA Plan Apochromat TIRF oil objective (Nikon) was used. The microscope was equipped with a Photometrics Evolve 512 camera, which allowed illumination of GFP and RFP at 473 nm and 561 nm, respectively. Red and green fluorescence signals can be separated using a DualView DV2 emission splitter. MetaMorph software was used to control the camera shutters and light source. Samples for the imaging were prepared as follows. $0.8x10^5$ cells were seeded on 13 mm autoclaved cover slips placed in 24-well plates. The media was aspirated, cells were washed with PBS and then fixed with 4% PFA/PBS solution at room temperature for 15 minutes. Thereafter, cells were washed twice with PBS and permeabilized with 0.5% Triton X-100/PBS for 5 minutes at room temperature, washed twice with PBS and then incubated with Alexa Fluor 488 phalloidin (1:1000) for 1 hour at room temperature. After incubation, cover slips were washed twice with PBS and inverted on 7 µl of ProLong® Diamond Antifade Mountant with DAPI on glass slides. In order to quantify actin anisotropy, an ImageJ plugin called Fibril Tool was used.

2.2.19.3 Operetta High Content Imaging System

In order to determine cell morphological features, an Operetta High-Content Imaging System was used. Prior to cell imaging, cells were seeded in black 96-well plates at $2x10^4$ cells per well. The next day, media was removed and cells were fixed with 4% PFA/PBS for 15 minutes at room temperature. Cells were washed twice with PBS, permeabilized with 0.5% Triton X-100 for 5 minutes at room temperature and then washed twice with PBS. Cells were incubated with 0.15 µg/ml of DAPI for 20 minutes in room temperature followed by two PBS washes. 50 µl of 1:5000 dilution of Cellomics® Whole Cell Stain (WCS) was added

per well and incubated at room temperature for 30 minutes and subsequently washed three times with PBS. The plates were imaged on an Operetta High-Content Imaging System and the data was analysed on Columbus™ Image Data Storage and Analysis System. Cell shapes were analysed using Columbus™ Image Data Storage and Analysis System, and an enhanced set of algorithms known collectively as STAR system. The software was trained to recognise different populations of cell shapes by selecting examples of each class.

2.2.19.4 Immunofluorescence

$0.8x10^5$ cells were seeded on 13 mm autoclaved cover slips placed in 24-well plates and grown overnight. The media was aspirated, cells were washed with PBS and then fixed with 4% PFA/PBS solution at room temperature for 15 minutes. Cells were washed twice with PBS and permeabilized with 0.5% Triton X-100/PBS for 5 minutes at room temperature, washed twice with PBS and blocked with 1% BSA/PBS for 30 minutes. All primary antibodies were used at a 1:200 dilution and incubated for 2 hours at room temperature. The coverslips were washed twice with PBS before being incubated with secondary antibody for 1 hour at a 1:1000 dilution. After incubation, coverslips were washed twice with PBS, once with distilled water and inverted on 6 µl of ProLong® Diamond Antifade Mountant with DAPI on glass slides. Cells were imaged on a Zeiss 710 upright confocal microscope or Zeiss 880 confocal using a 63x oil immersion objective.

2.2.19.5 Electron Microscopy

Scanning electron microscopy (SEM) was used to visualise nuclei. Briefly, isolated nuclei were seeded on autoclaved 10 mm coverslips placed in 24-well plates and cultured overnight. The next day, media was aspirated and cells were fixed with 3% glutaraldehyde in 0.1 M phosphate buffer for 2 hours at room temperature. After fixation, cells were washed 3 times with 0.1 M phosphate buffer for 10 minutes each.

Transmission electron microscopy (TEM) was used to visualise chromatin structures. Cells were pelleted and resuspended in 3% glutaraldehyde in 0.1 M phosphate buffer for 1 hour at room temperature for fixation. After fixation, the

cells were washed 3 times with sodium cacodylate buffer for 5 minutes each. Samples were kept at 4°C until ready for processing.

All samples were processed by the Electron Microscopy Facility at University of Glasgow. Images were taken at different magnifications.

2.2.19.6 Atomic Force Microscopy (AFM)

The Atomic Force Microscopy studies were performed in collaboration with the Engineering department at Glasgow University. Cells were seeded in 3 cm petri dishes and incubated for 24 hours in standard tissue culture conditions. During the experiment, cells were kept in standard tissue culture conditions and 1% HEPES was added to the media to maintain the pH level. Cells were probed with a 4.74 µm diameter spherical bead and force of 3 nN. Indentations were performed with a constant speed of 2.5 µm/s and a z length of 3 µm. Cells were measured on the nucleus area at 5 points disposed in a square configuration of 1 µm and an average of Young's modulus value was determined per cell.

For the nuclei elasticity measurements, prior to the experiment nuclei were isolated using the Nuclei EZ Prep Nuclei Isolation kit. Isolated nuclei were seeded in 3 cm petri dishes in the lysis buffer provided with the kit. Once nuclei had attached onto the dish, AFM was performed. Nuclei were probed with a 4.74 µm diameter spherical bead and force of 3 nN. One measurement was taken per nucleus.

2.2.20 *In vivo* work

The *in vivo* work was carried out in collaboration with the Transgenic Models Advanced Technology service (Cancer Research UK Beatson Institute). All animal work was carried out under project licence (PPL70/8645) authority and with ethical approval (University of Glasgow) in line with the Animals (Scientific Procedures) Act and EU Directive.

2.2.20.1 Orthotopic injection of breast cancer cells into mammary fat pads of nude mice

Orthotopic injection of MDA MB 231 breast cancer cells into mammary fat pads of nude mice was performed as follows. Nude female CD1 mice were obtained from Charles River. Seven week old mice were injected with $1x10^6$ cells in 50 µl of 1:1 (Matrigel:PBS) into the fourth abdominal fat pad. Tumour growth was monitored over the course of study and animals were sacrificed when tumour size reached 15 mm. Mice were injected intraperitoneally with 250 µl BrdU two hours prior to sacrifice. Animals were euthanized by a Schedule 1 method using carbon dioxide inhalation. Primary tumour and organs were harvested, paraffin embedded and stained with hematoxylin and eosin (H&E) or antibodies against Human Leukocyte Antigen (HLA). Histology sample processing was performed by the Beatson Histology Service. Slides were analysed using Leica Biosystems software.

2.2.20.2 MDA MB 231 and MDA MB 435 cell injection into nude mouse tail veins

For the experimental metastasis assay, MDA MB 231 or MDA MB 435 cell lines were injected into the tail veins of nude female CD1 mice. Seven-week old mice were injected with $1x10^6$ cells in 100 µl of PBS into lateral tail veins. Mice were monitored over the course of the study. Mice were sacrificed 6.5 weeks after injection and lungs were harvested. Animals were euthanized by a Schedule 1 method using carbon dioxide inhalation. Lungs were paraffin embedded and H&E-stained by the Beatson Histology Service. Slides were analysed using Leica Biosystems software.

2.2.20.3 Histology

Paraffin-embedded tissue sections were cut and routinely stained with haematoxylin and eosin (H&E) by the Beatson Histology Service. Other standard stains performed by the Histology Service include BrdU and HLA. Serial lung sections of 4 µm thickness were cut at 50 µm intervals.

2.2.21 Statistical analysis

Statistical significance ($p<0.05$) of differential findings between experimental groups was determined by performing appropriate test using GraphPad 7.03 software. The test used in analysis is stated in the corresponding figure legends.

2.2.21.1 Principal component analysis (PCA)

Principal component analysis (PCA) is a mathematical procedure that transforms a number of (possibly) correlated variables into a (smaller) number of uncorrelated variables called principal components. It uses an orthogonal transformation to reduce a large set of variables to a small set that still contains most of the information in the large set. PCA is a technique used to identify outliers, batch effects and clusters. It's often used to make data easy to explore and visualize. PCA was quantified using R package, prcomp (https://stat.ethz.ch/R-manual/R-patched/library/stats/html/prcomp.html).
The calculation is done by a singular value decomposition of the centered data matrix not by using eigen on the covariance matrix. This is generally the preferred method for numerical accuracy. Data were analysed by the Computational Biology department (Cancer Research UK Beatson Institute).

3 *In vitro* selection of cancer cells through 3 µm pores using cell culture inserts

3.1 Rationale

Tumour cell invasion and subsequent cancer metastasis are the most difficult problems faced by cancer patients; moreover they remain one of the most poorly understood processes in cancer biology (Hanahan and Weinberg 2011). Within primary tumours, some cancer cells acquire invasive and metastatic traits that enable them to survive the complex journey from the primary site to distant organs and to colonise a foreign tissue. In the first and last steps (local invasion, intravasation, extravasation) of the metastatic cascade, cancer cells must invade into the surrounding associated stromal tissue and migrate through its dense composition (Gupta and Massague 2006). The ECM architecture provides complex scaffoldings, and many obstacles in the form of pores and narrow channels for migrating cancer cells. Therefore, acquiring detailed understanding of the mechanisms that contribute to constrained invasive adaptations will help to identify potential drug targets to block tumour cell dissemination and improve patient outcomes.

I hypothesized that within the dispersed distributions of parameters in tumour cell lines, it would be possible to select cells that were better able to squeeze through narrow gaps, thus highlighting factors that contributed to increased cell deformability. Therefore, I set up an *in vitro* selection strategy in which cancer cells were selected based on their ability to pass through narrow diameter constrictions (3 µm) that mimic the gaps in the ECM or between cells. In order to enrich for cells with enhanced abilities to pass through physical constrictions, cells were seeded on 3 µm pore-membranes in 10 cm Transwell inserts and allowed to migrate towards medium containing 10% fetal bovine serum (FBS). After 5 days, cells were collected and re-plated on the inserts twice more (Figure 3-1). In brief, each of three independent Selected populations were selected through 3 µm pores in three independent rounds of selection. In further parts of the thesis, I will refer to the original populations of cells as Parental cells and to the sub-population as Selected (Sel) cells. The study was performed on MDA MB 231-luc-D3H2LN breast cancer cells and some experiments were carried out on MDA MB 435 melanoma cancer cells.

3.2 Results

3.2.1 Selected MDA MB 231 cells are more migratory through 3 µm pores compared to Parental MDA MB 231 cells

In order to assess 3 µm pore migration capability of Parental and independent Selected MDA MB 231 cells, 6.5 mm diameter Transwell inserts with 3 µm pore membranes were used. Briefly, cells were resuspended in serum free media, seeded in Transwell inserts and subsequently incubated in standard tissue culture conditions for 3 days to allow cells to migrate towards medium containing 10% fetal bovine serum (FBS). Following incubation for 72 hours, the inserts were removed and cells that migrated through the membrane and attached to the lower-chamber compartment were fixed and stained with sulforhodamine B (SRB) to quantify migrated cells. The SRB assay is a colorimetric assay used for cell density determination based on the measurement of cellular protein content. The analysis revealed a significant increase in 3 µm pore migration of Selected MDA MB 231 cells relative to Parental MDA MB 231 cells (Figure 3-2).

3.2.2 Small size does not determine 3 µm pore migration ability of Selected MDA MB 231 cells

After discovering that Selected MDA MB 231 cells were significantly more migratory through 3 µm pores, I wanted to know if these changes were cell size dependent. To measure the size of Parental and independent Selected cell populations, the Operetta High Content Imaging System was utilised for high throughput quantification of cell morphological features, such as cell area. In brief, cells were seeded in black 96-well plates and following incubation for 24 hours, cells were fixed and stained with DAPI and Whole Cell Stain (WCS). The results showed that the majority of Selected MDA MB 231 cells had significantly smaller cell area compared to Parental MDA MB 231 cells (Figure 3-3A).

Given the possibility that cell size was a major determinant responsible for the enhanced 3 µm pore migration of Selected MDA MB 231 cells, one additional selection strategy that enabled testing of this parameter was adopted. I enriched Parental cells for small cell size by flow cytometry using a BD Cell Sorter. In brief, Parental MDA MB 231 cells were enriched for small size using

flow cytometry and subsequently seeded in serum full media and kept in standard tissue culture conditions until they reached the desired concentration. Next, flow cytometry sorting was repeated twice more for each independent Flow sorted (FS) cell population. Cell areas and cell volumes were determined for Parental, Selected and Flow sorted populations. The analysis revealed that Selected and Flow sorted cells were associated with 2D smaller cell area and 3D cell volume relative to Parental cells (Figure 3-3B,C). Cell areas were assessed using the Operetta High Content Imaging System and cell volumes were calculated from measured cell diameters.

To determine whether small size was a significant contributor to the enhanced constrained cell migration of Selected MDA MB 231 cells, 3 μm migration ability was assessed on Parental, independent Selected and independent Flow sorted MDA MB 231 cell populations using a Transwell migration assay with 6.5 mm Transwell inserts. I found that independent Selected cells were significantly more migratory through 3 μm pores compared to equivalently small Flow sorted cells and to Parental cells, but all of the cell sub-populations were equally invasive through 8 μm pores (Figure 3-3D). These results indicated that small size did not solely determine constrained cell migration ability of Selected MDA MB 231 cells.

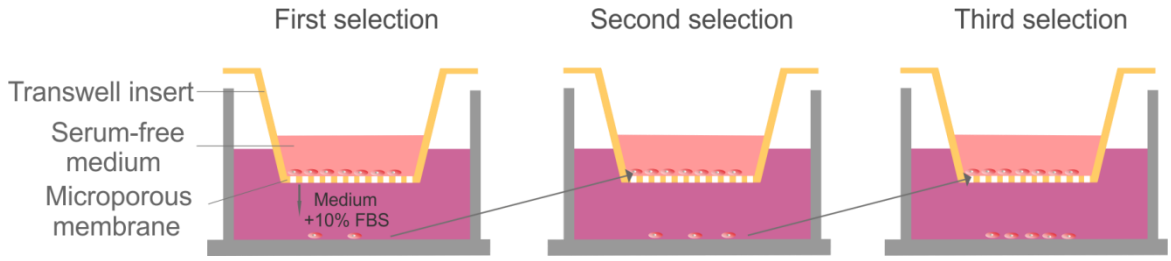

Figure 3-1 Selection strategy of cancer cells through 3 μm pore membranes.
Schematic diagram of selection strategy. Cancer cells were plated in serum-free medium in well inserts with 3 μm pores. Cells that moved towards medium containing 10% fetal bovine serum (FBS) to the bottom of the well were collected after 5 days and re-plated in the well inserts twice more to establish the selected cell populations.

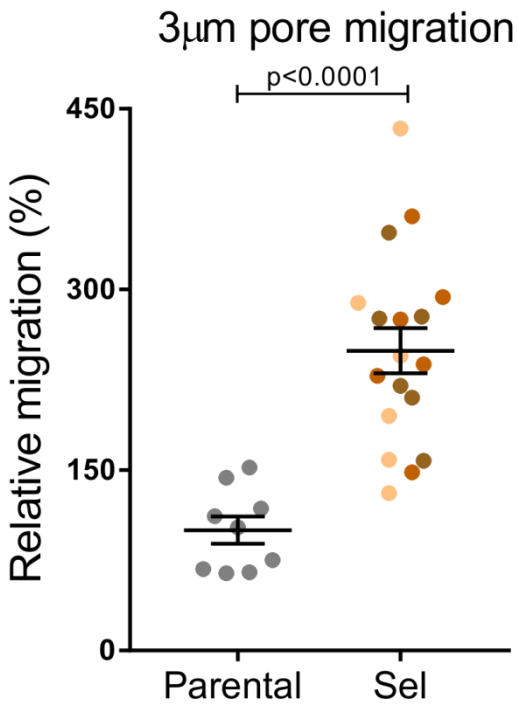

Figure 3-2 Selected MDA MB 231 cells are more migratory through 3 µm pores.
Graph represents mean (± SEM) 3 µm relative migration for Parental and independent Selected cell populations. Each dot represents an average value from n = 3 wells. Data pooled from n > 3 independent experiments. Statistical significance determined by Mann - Whitney test.

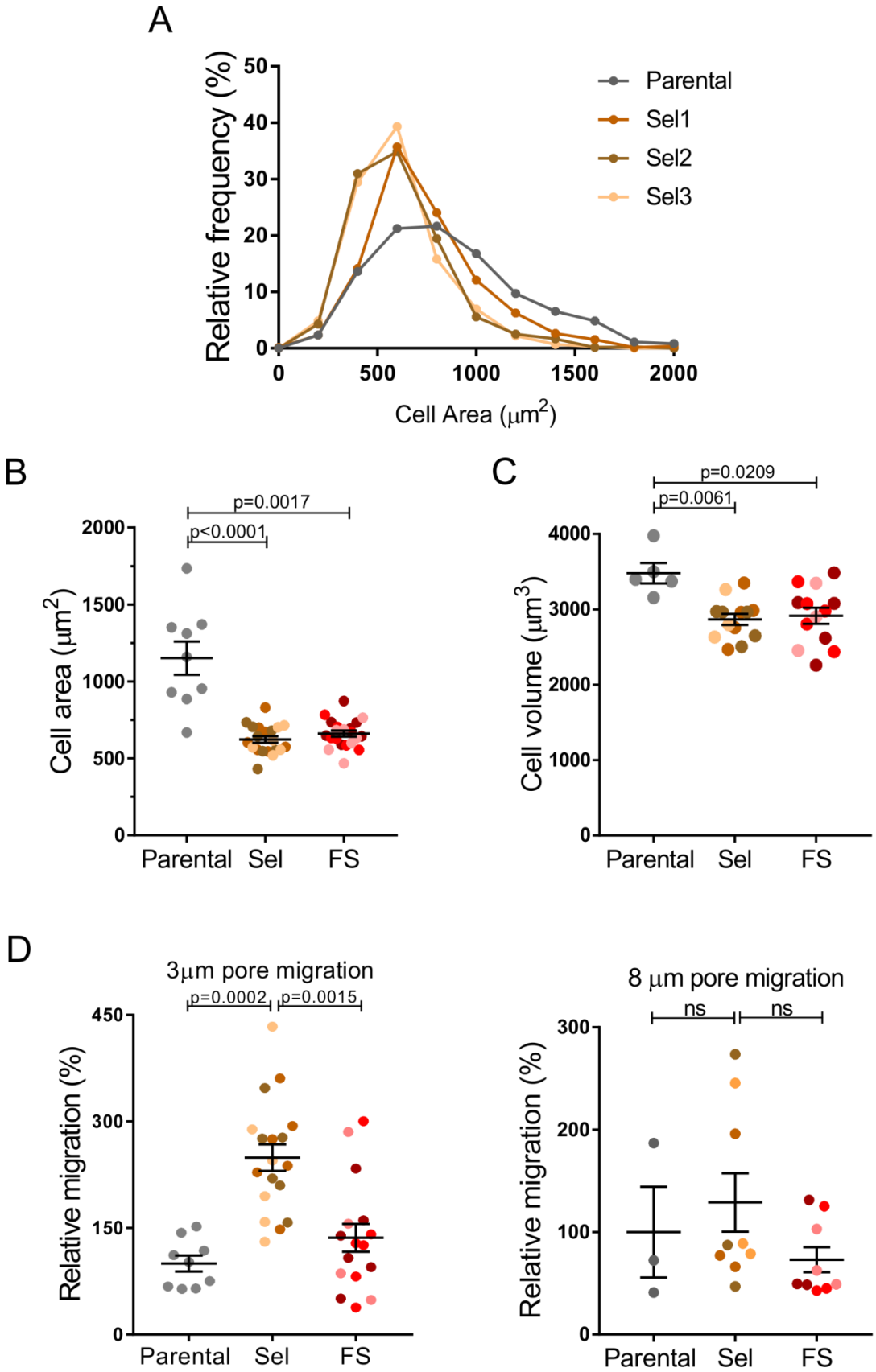
A
Relative frequency (%)
50
40
30
20
10
0
0
500
1000
1500
2000
Cell Area (μm2)
Parental
Sel1
Sel2
Sel3
B
Cell area (μm2)
2000
1500
1000
500
0
p=0.0017
p<0.0001
Parental
Sel
FS
C
Cell volume (μm3)
4000
3000
2000
1000
0
p=0.0209
p=0.0061
Parental
Sel
FS
D
3μm pore migration
Relative migration (%)
450
300
150
0
p=0.0002
p=0.0015
Parental
Sel
FS
8 μm pore migration
Relative migration (%)
300
200
100
0
ns
ns
Parental
Sel
FS

Figure 3-3 Small cell size does not determine enhanced constrained migration of Selected MDA MB 231 cells.

A) Relative frequency of cell area for Parental and independent Selected cell populations. Cell areas were determined using Operetta High Content Imaging System. B) Graph represents mean cell area (± SEM) for Parental, independent Selected and independent Flow sorted cell populations pooled from n > 3 independent experiments. Each dot represents an average value from n = 6 fields per well, from at least 200 cells per field. Cell area was determined using Operetta High Content Imaging system. C) Graph represents mean cell volume (± SEM) for Parental, independent Selected and independent Flow sorted cell populations. Cell volumes were determined by measuring cell diameter. Each dot represents an average value from n ≥ 4 measurements. Data pooled from n > 3 independent experiments. D) Left graph depicts mean (± SEM) 3 µm relative migration for Parental, independent Selected and independent Flow sorted cell populations. Right graph depicts mean (± SEM) 8 µm relative migration for Parental, independent Selected and independent Flow sorted cell populations. Each dot represents an average value from n = 3 wells. Data pooled from n ≥ 3 independent experiments. Statistical significance determined by Kruskal - Wallis followed by Dunn's multiple comparison test.

3.2.1 No difference in proliferation between Parental, Selected and Flow sorted MDA MB 231 cells *in vitro*

Before undertaking any further experiments, proliferation rates of Parental, Selected and Flow sorted MDA MB 231 cells, were checked. To assess cell proliferation rates, 30,000 cells per well were seeded in 12-well plates in triplicates. Cell number was measured after 24, 48 and 72 hours using a CASY® Cell Counter. From this, I was able to determine that there was no difference in the proliferation rates between Parental, Selected and Flow sorted MDA MB 231 cells (Figure 3-4).

3.2.2 Selected MDA MB 231 invade to a greater depth in fibroblast conditioned collagen matrix compared to Parental and Flow sorted MDA MB 231

Having determined that 3 μm pore selection enriched for cells with enhanced constrained migration properties, and that such a property was not solely dependent on cell size, the invasion of Parental, Selected and Flow sorted cells were studied in a more physiologically relevant environment. To address this, a collagen matrix invasion assay in which tumour cells moved through a dense fibroblast-conditioned collagen gel, was used. Human primary fibroblasts were mixed with rat tail collagen1 and left for a week to allow conditioning and contraction of the collagen "plug". The fibroblasts were then removed by treating the collagen disks with puromycin for 48 hours and subsequently washed twice with PBS. Once the matrices were prepared, cells were seeded on top and allowed to invade the collagen for 8 days. After this time, the collagen disks were fixed, paraffin-embedded and stained with H&E, and invasion distances were quantified using ImageJ. From this, I discovered that independent Selected MDA MB 231 cells invaded to a greater depth into the collagen relative to Parental and independent Flow sorted MDA MB 231 cells, indicating that Selected MDA MB 231 cells were more invasive *in vitro* (Figure 3-5).

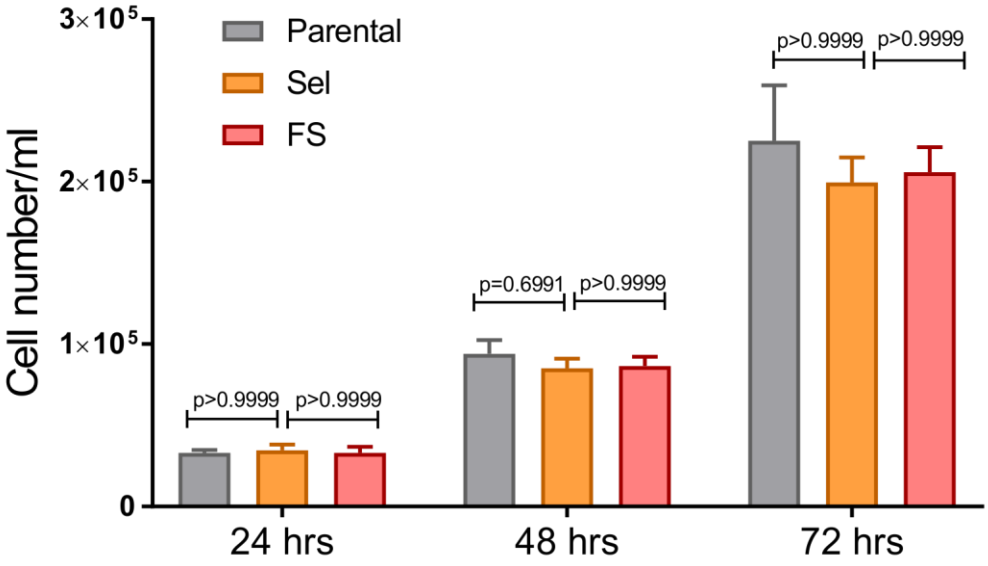

Figure 3-4 No differences in proliferation rates between Parental, Selected and Flow sorted MDA MB 231 cells.
Graph depicts mean (± SEM) cell number for Parental, Selected and Flow sorted MDA MB 231 cells measured at 24, 48 and 72 hours. Data pooled from n = 4 independent experiments. Statistical significance determined by Kruskal - Wallis followed by Dunn's multiple comparison test.

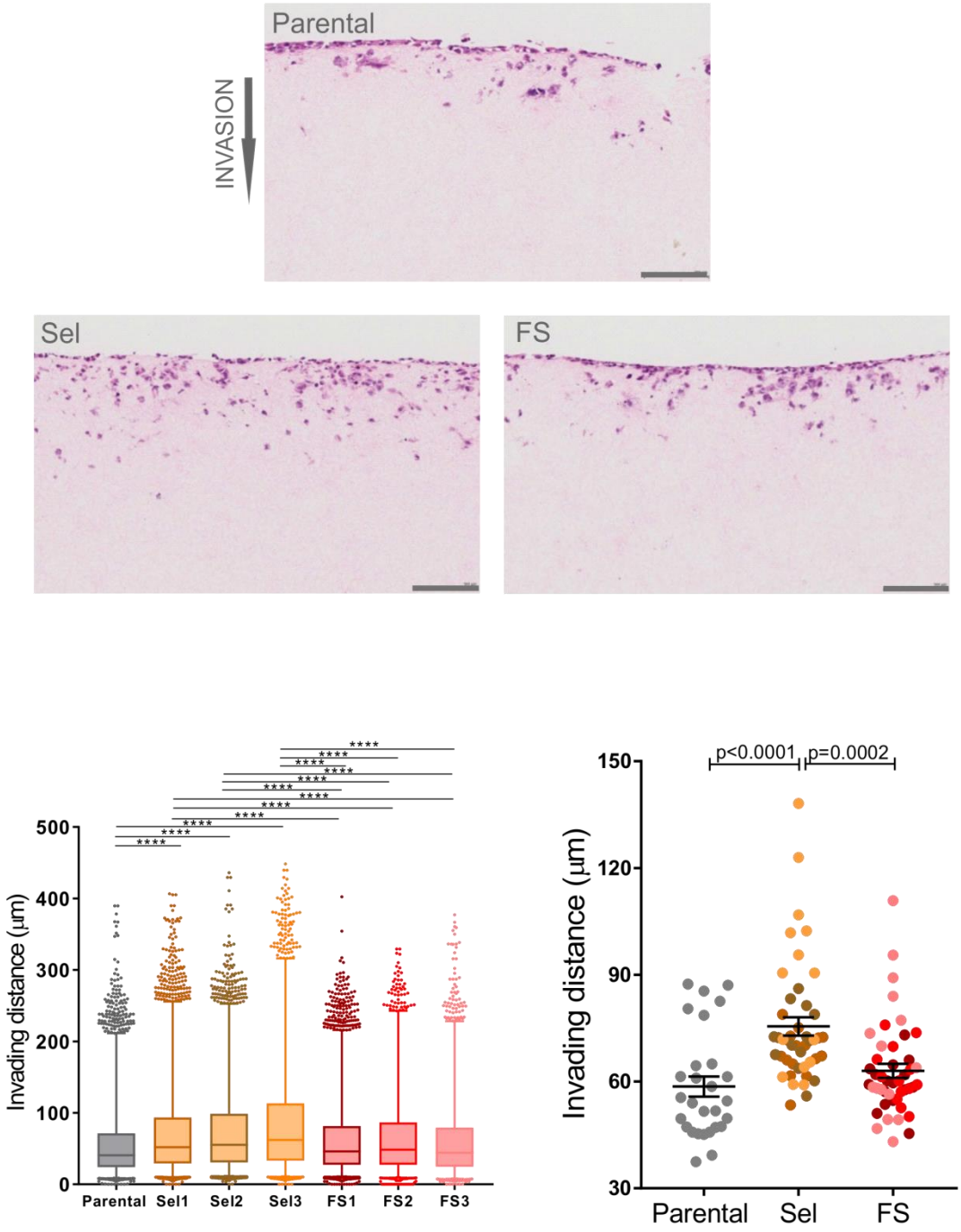

Figure 3-5 Selected MDA MB 231 cells invade to a greater depth into the collagen matrix. Representative images of invading cells into the collagen matrix showed for Parental, Selected and Flow sorted cells. Scale bar = 100 µm. Left graph depicts box and whiskers plot (1-99 percentile) representing the distance travelled by individual cells for Parental, independent Selected and independent Flow sorted populations. Data pooled from n = 3 independent experiments. Statistical significance determined by Kruskal - Wallis followed by Dunn's multiple comparison test (**** = p<0.0001). Right graph depicts mean (± SEM) travelled distance for Parental, independent Selected and independent Flow sorted cell populations. Data pooled from n = 3 independent experiments. Statistical significance determined by Kruskal - Wallis followed by Dunn's multiple comparison test.

3.2.3 Nuclear properties in constrained cell migration

3.2.3.1 Rationale

Due to the presence of narrow pores and channels in the complex architecture of the stromal tissue surrounding tumours, migration may become challenging for cancer cells. One of the biggest and stiffest cellular components, the nuclei, may become an obstacle in this process. Nuclear deformability is necessary for cells to be able to squeeze through the tight organization of the ECM (Khatau, Bloom et al. 2012). There are many factors that may dictate nuclear rigidity, such as lamin A/C, chromatin content and condensation (Lammerding 2011). The ratio of A-type lamin to B-type lamin in the nuclear lamina is proportional to tissue microelasticity. The lamina contains predominantly A-type lamins in stiff tissue, whereas B-type lamins are prevalent in the nuclear lamina in soft tissue (Swift and Discher 2014; Swift et al. 2013). Due to the strong influence that nuclear mechanical properties have been shown to have on migration through small gaps, as detailed in the introduction, I investigated several nuclear properties, including size, elasticity, lamin A/C expression, DNA content and chromatin condensation, to determine whether the nucleus was likely to be an important contributor to the invasive ability of Selected cells. All experiments described below were performed on MDA MB 231-D3H2LN cells.

3.2.3.2 Results

3.2.3.2.1 Nuclear size does not determine constrained cell migration ability of Selected MDA MB 231 cells

Having identified that small cell size did not determine the increased confined migration ability of Selected cells, nuclei size was investigated next. To measure nuclei volume, z-stack sections of DAPI-stained nuclei were taken on a Zeiss 710 confocal microscope, followed by quantification using the Volocity image analysis program. The program allowed me to fill in the fluorescent signal obtained by confocal microscopy and to determine nuclear volumes. Nuclei size measurements revealed comparable volumes for independent Selected and Flow sorted cell populations (Figure 3-6A). These results indicated that nuclear volume was not associated with differences in invasive ability of Parental, Selected and Flow sorted cells.

Moreover, isolated nuclei from each population of MDA MB 231 cells were also visualized using Scanning Electron Microscopy (SEM). The SEM images supported the previously obtained results. The results revealed smaller nuclei size of Selected and Flow sorted cells compared to Parental cells. Representative SEM images are shown in Figure 3-6B.

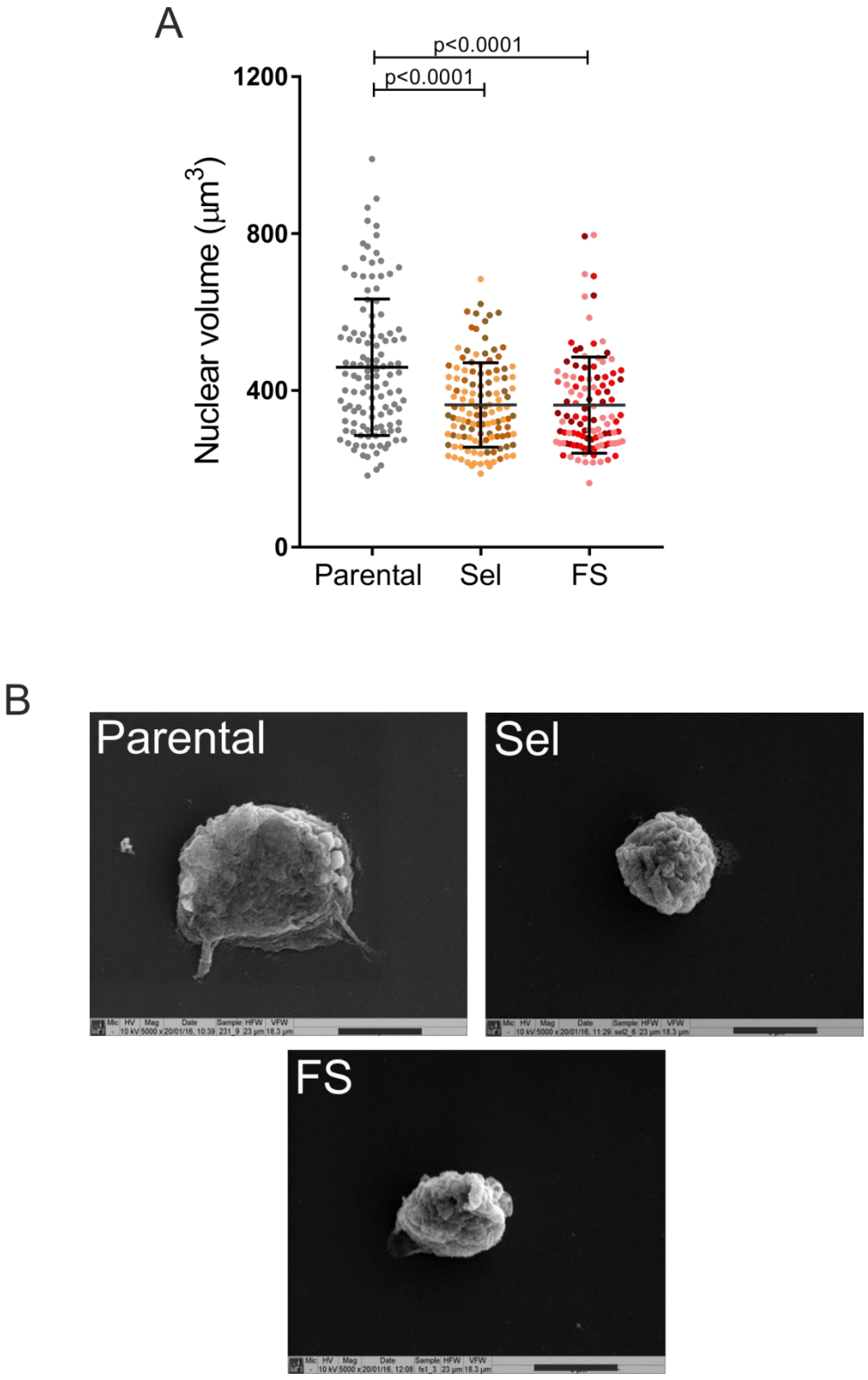

Figure 3-6 Selected and Flow sorted cells have smaller nuclear size relative to Parental cells.

A) Graph represents mean nuclear volume (± SD) for Parental, independent Selected and independent Flow sorted cell populations. Data represent individual nuclei pooled from n = 3 independent experiments. Images of DAPI-stained nuclei were taken on a Zeiss 710 confocal microscopy followed by nuclei volume determination using Volocity program. B) SEM representative images of isolated nuclei showing smaller nuclear size of Selected and Flow sorted cells compared to Parental cells. Scale bar = 5 µm. Statistical significance determined by Kruskal - Wallis followed by Dunn's multiple comparison test.

3.2.3.2.2 Selected and Flow Sorted cells have increased nuclear stiffness but the expression of nuclear lamins is diminished

After finding that nuclei volume did not determine the invasive ability of Selected cells, in the next step nuclei mechanical properties were investigated. In order to measure nuclei elasticity, a collaboration was established with the Engineering Department at Glasgow University. In the first step, nuclei were isolated using a Nuclei Isolation kit and subsequently seeded on glass bottom 3 cm petri dishes in the lysis buffer provided with the kit. Once the nuclei had settled and attached on the dish, Young's modulus values were obtained using Atomic Force Microscopy (AFM). Nuclei were probed with a 4.74 μm diameter spherical bead with a force of 3 nN and one measurement was taken per nuclei. These results revealed that Selected and Flow sorted cells had increased nuclear stiffness compared to Parental cells (Figure 3-7A).

As it was reported that nuclear deformability may depend on lamin A/C expression level as detailed in the introduction, a western blot was performed. The membrane was probed with anti lamin A/C antibody and GAPDH (Figure 3-7B). The blot showed decreased expression of lamin A/C in Selected and Flow sorted cells relative to Parental cells. The expression of Lamin B was not investigated.

3.2.3.2.1 DNA content does not determine constrained migration ability of Selected cells

As it was reported that nuclei may be a hindrance during compressive deformation using the micropipette aspiration technique (Rowat, Lammerding et al. 2006; Rowat, Lammerding et al. 2008), I wanted to investigate DNA content and its possible implication in enhanced constrained invasion of Selected cells. Firstly, DNA content was assessed by propidium iodide (PI) staining of fixed cells. PI is a commonly used dye to determine cell content/cycle. It intercalates into double-stranded DNA in proportion to DNA content. Cell cycle graphs of PI-stained cells revealed an unusual cell cycle profile for Parental cells. It suggested that Parental cells contained more DNA compared to Selected and Flow sorted cells (Figure 3-8A).

Having identified increased DNA content in Parental cells, more detailed analysis of DNA content was performed. In order to quantify chromosome number, a collaboration was established with the Welcome Trust Centre for Human Genetics in Oxford and cytogenetic analyses of Parental, independent Selected and independent Flow sorted cell populations were performed. The experiment revealed that Parental cells are largely sub-tetraploid with an average chromosome number near 70, while Selected and Flow sorted cells were near diploid (Figure 3-8B,C). This confirmed that differences in constrained cell migration ability did not depend on chromosome number or DNA content.

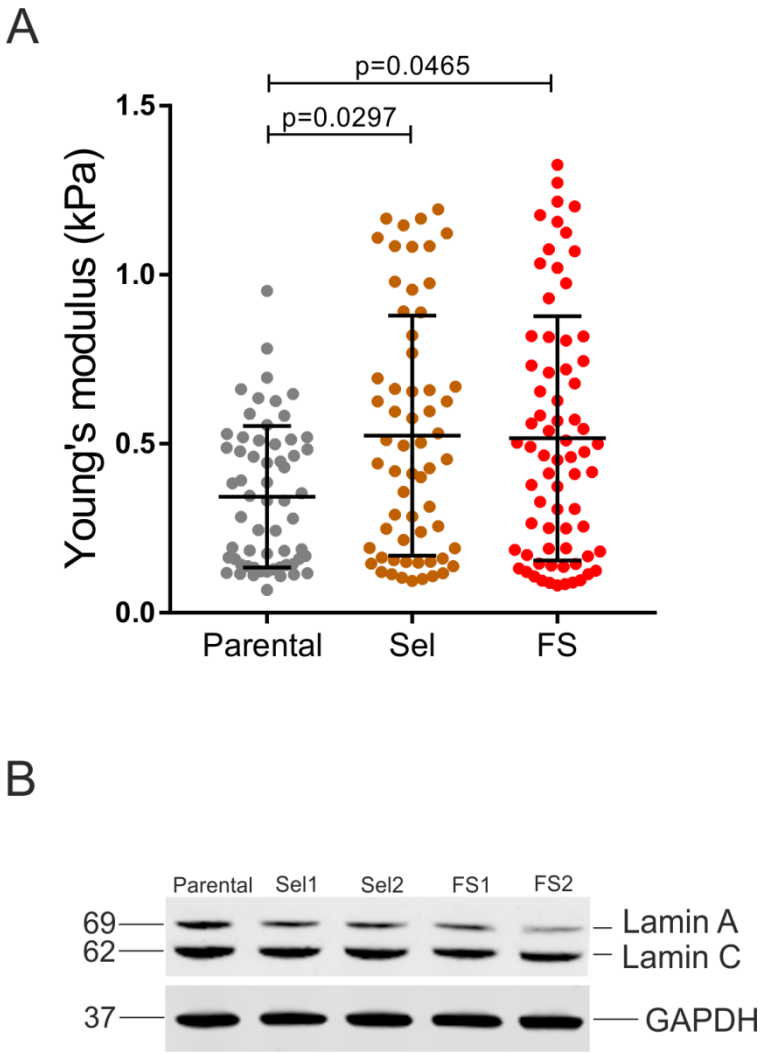

Figure 3-7 Selected and Flow sorted cells have increased nuclear stiffness but Lamin A/C expression is diminished.
A) Graph represents mean (± SD) of Young's modulus (nuclear elasticity) showing an increase of nuclear stiffness of Selected and Flow sorted cells compared to Parental. Data represent individual nuclei pooled from n = 2 independent experiments. B) Lamin A/C and GAPDH expression levels showed for Parental, two independent Selected and two independent Flow sorted cell populations. Statistical significance determined by Kruskal - Wallis followed by Dunn's multiple comparison test.

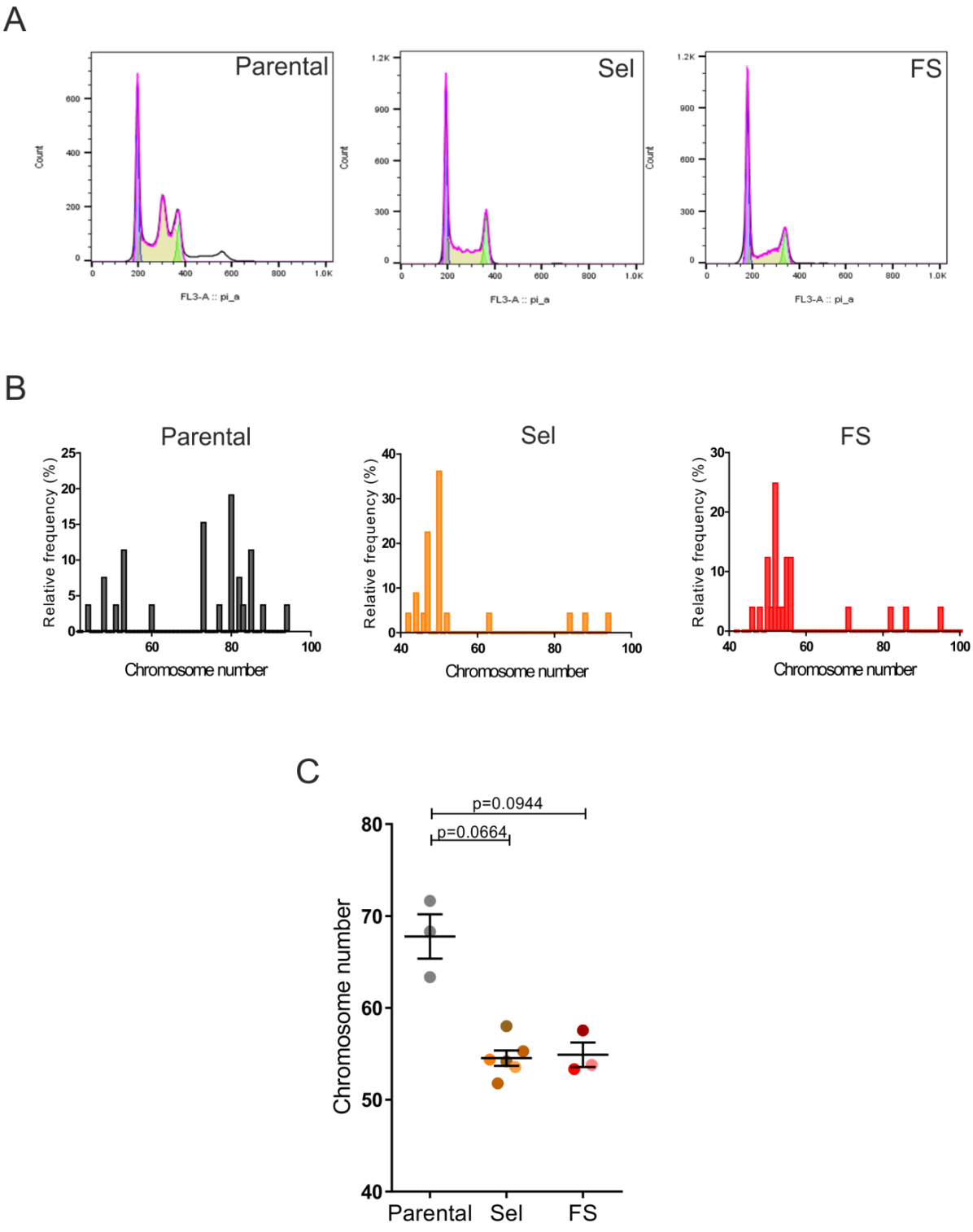

Figure 3-8 Parental cells have more DNA compared to Selected and Flow sorted cells.
A) FACS analysis showing cell cycle distribution in Parental, Selected and Flow sorted cells. B) Representative relative frequencies of chromosomes numbers for Parental, Selected and Flow sorted cell populations. C) Mean chromosome number (± SEM) determined for independent Parental, independent Selected and independent Flow sorted cell populations. Each dot represents an average value from n = 20 cells. Data pooled from n = 3 independent experiments. Statistical significance determined by Kruskal - Wallis followed by Dunn's multiple comparison test.

3.2.3.2.2 Selected and Flow sorted cells have more condensed chromatin compared to Parental cells

As discussed in the introduction, chromatin condensation plays an important role in directed cell migration. Condensation of chromatin may influence physical properties of the nucleus and its ability to pass through small pores. The organization of chromatin is determined by post-translational modification of histones tails. One of the histone modifications which is involved in repression of transcription and known to be associated with condensed forms of chromatin is a trimethylation of histone H3 at lysine 27 ($H3K27me^3$) (Kouzarides 2007). To assess chromatin condensation, cells were fixed and immunostained for the heterochromatin marker $H3K27me^3$. Immunofluorescence of $H3K27me^3$ showed a punctate pattern of staining in Selected and Flow sorted cells, while $H3K27me^3$-immunostained nuclei of Parental cells were characterized by more diffuse staining. These results suggested that Selected and Flow sorted cells might have had more condensed chromatin. Representative images of cells stained with $H3K27me^3$ antibody are shown in Figure 3-9A.

Given the possibility that chromatin compaction was a determinant of enhanced invasion of Selected cells, after finding that Selected and Flow sorted cells had increased staining of heterochromatin marker $H3K27me^3$, chromatin condensation levels were determined by applying a Förster resonance energy transfer (FRET)-based assay using Fluorescence Lifetime Imaging Microscopy (FLIM) previously described by Lleres et al. (Lleres, James et al. 2009). FRET can be used to detect protein-protein interactions in live cells and it is highly distance dependent, two proteins need to be within ~1-10 nm distance. Briefly, FLIM was used to measure FRET between histone proteins H2B fused to either GFP (donor fluorophore) or mCherry (acceptor fluorophore) in interphase nuclei. If chromatin is in a more compacted state, FRET decreases the donor fluorescence and increases the acceptor fluorescence, and by using FLIM the decreased donor fluorescence life time (time difference between fluorophore excitation and photon emission) can be measured. Fluorescence lifetimes were measured using LI-FLIM software.

In order to evaluate if changes in chromatin compaction in MDA MB 231 cells could be detected using this FLIM-FRET approach, the experiment was

performed by treating cells with 2-deoxyglucose (2-DG) and sodium azide (NaN_3). 2-DG and sodium azide treatment induces ATP depletion and leads to extensive chromatin compaction. After transfection with H2B-GFP and H2B-mCherry plasmids using Amaxa Nucleofactor Kit V, cells were incubated in standard tissue culture conditions for 72 hours to let histones incorporate into chromatin. 30 minutes before acquiring images on the FLIM microscope, cells were treated with 50 mM 2-DG plus 10 mM sodium azide or control cells with dH_2O. As a result, extensive chromatin compaction was observed, which was indicated by decreased life time of the donor fluorophore in Parental and Selected cells compared to control cells, independent of differences in DNA content (Figure 3-9B).

After validation that changes in chromatin condensation could be detected in MDA MB 231 cells, the experiment was continued to determine chromatin compaction in Parental, Selected and Flow sorted cells. Cells were transected with H2B-GFP and H2B-mCherry plasmids and left for 72 hours at standard tissue culture conditions. After 72 hours images were obtained on the FLIM microscope. The results showed that Selected and Flow sorted cells had decreased life time of donor fluorophore GFP relative to Parental cells, meaning that chromatin in those cell lines was more compacted (Figure 3-9C).

The chromatin was also visualized by transmission electron microscopy (TEM). TEM images showed more condensed material in Selected cells, which likely was more condensed heterochromatin (Figure 3-9D). These results indicated that chromatin compaction alone does not determine the invasive phenotype of Selected cells. Instead, the level of chromatin condensation correlated with small nuclei volume and chromatin content.

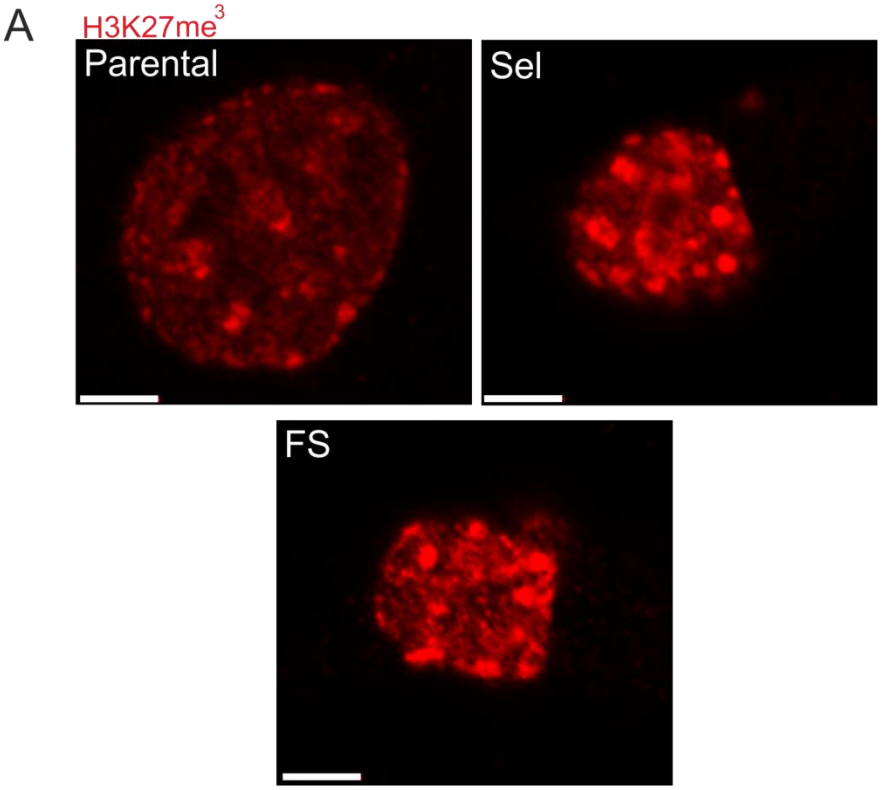
A
H3K27me3
Parental
Sel
FS

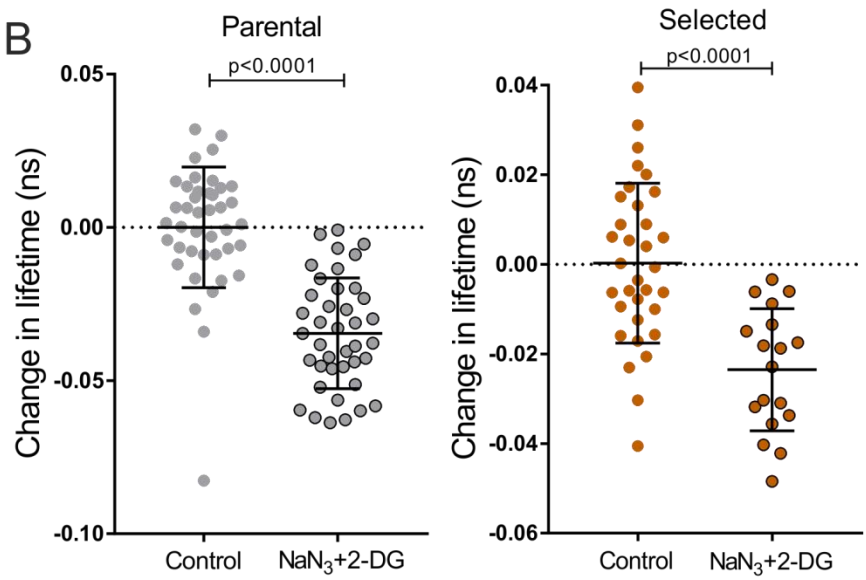
B
Parental
Selected
p<0.0001
p<0.0001
Change in lifetime (ns)
0.05
0.00
-0.05
-0.10
0.04
0.02
0.00
-0.02
-0.04
-0.06
Control
NaN3+2-DG
Control
NaN3+2-DG

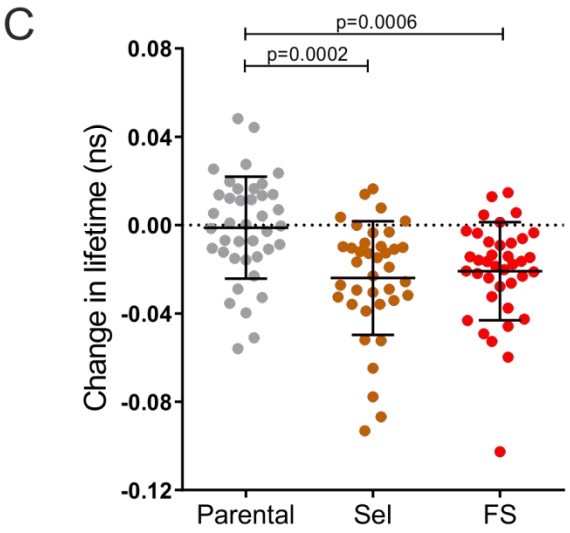
C
p=0.0006
p=0.0002
Change in lifetime (ns)
0.08
0.04
0.00
-0.04
-0.08
-0.12
Parental
Sel
FS

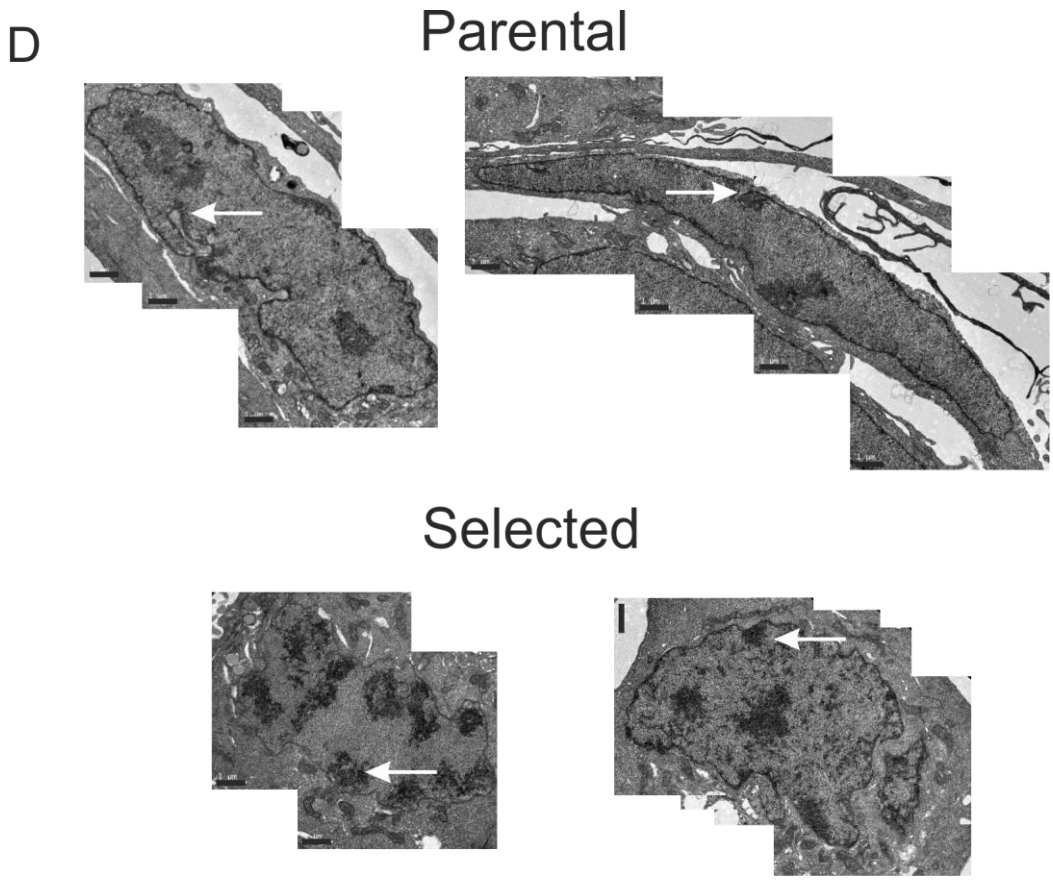

Figure 3-9 Selected and Flow sorted cells have more condensed chromatin compared to Parental cells.

A) Representative images of H3K27me^3-immunostained nuclei of Parental, Selected and Flow sorted MDA MB 231 cells. Scale bar = 5 µm. B) Left graph represents the range of changes in the fluorescence life time in Parental MDA MB 231 cells upon treatment with 2-DG and sodium azide. Right graph represents the range of changes in the fluorescence life time in Selected MDA MB 231 cells upon treatment with 2-DG and sodium azide. Data depicts individual cells pooled from n = 2 independent experiments, with mean (± SD) indicated. Statistical significance determined by Mann - Whitney test. C) Graph depicts the range of changes in the fluorescence life time in Parental, Selected and Flow sorted MDA MB 231 cells. Data depicts individual cells pooled from n = 2 independent experiments, with mean (± SD) indicated. Statistical significance determined by Kruskal - Wallis followed by Dunn's multiple comparison test. D) Representative TEM images of isolated nuclei. White arrows indicate heterochromatin. Scale bar = 1 µm.

Table 3-1 Summary of nuclear properties.

Nuclear property / Cell type	Nuclear size	Nuclear stiffness	Lamin A/C expression	Chromosome number (mean ± SEM)	Chromatin condensation
Parental	bigger	softer	higher	67.76 (2.413)	more condensed
Selected	smaller	stiffer	lower	54.53 (0.8401)	less condensed
Flow Sorted	smaller	stiffer	lower	54.89 (1.334)	less condensed
Consistency with the literature		(Harada, Swift et al. 2014)			

3.2.4 *In vitro* selection of MDA MB 435 cells using cell culture inserts

Having showed that there were cells with augmented constrained invasion capacities within MDA MB 231 Parental cell populations, I next wanted to explore this finding using another cancer cell line. For this reason, MDA MB 435 melanoma cancer cells were chosen. MDA MB 435 Parental cells were subjected to the same 3 µm selection strategy as described for MDA MB 231 cells. Three independent Selected MDA MB 435 cell populations were obtained. In order to validate Parental and Selected MDA MB 435 cells constrained migration ability, 6.5 mm Transwell inserts with 3 µm and 8 µm pore membranes were used and the Transwell migration assay was conducted. The results revealed that independent Selected MDA MB 435 cells were significantly more migratory through 3 µm and 8 µm pores, respectively compared to Parental MDA MB 435 cells (Figure 3-10).

3.2.5 No difference in proliferation between Parental and Selected MDA MB 435 cells *in vitro*

Before undertaking any further experiments, proliferation rates of Parental and Selected MDA MB 435 cells, were checked. To assess cell proliferation rates, 30,000 cells per well were seeded in 12-well plates in triplicates. Cell number was measured after 24, 48 and 72 hours using a CASY® Cell Counter. From this, I was able to determine that there was no difference in the proliferation rates between Parental and Selected MDA MB 435 cells (Figure 3-11).

3.2.6 Selected MDA MB 435 cells have smaller cell area and invade to a greater depth in fibroblast conditioned collagen matrix compared to Parental MDA MB 435 cells

After discovering that 3 µm pore selection of MDA MB 231 cells enriched for cells with smaller cell area and volume, I wanted to find out whether it was also similar for MDA MB 435 cells. In order to evaluate these possible differences, I measured cell areas and volumes of Parental and independent Selected MDA MB 435 cell populations as described for MDA MB 231 cells. The results revealed that independent Selected MDA MB 435 cells had significantly smaller 2D cell areas

(Figure 3-12A) and 3D cell volumes (Figure 3-12B), respectively, relative to Parental MDA MB 435 cells.

To evaluate the invasive behaviour of Parental and independent Selected MDA MB 435 cell populations in a more physiologically relevant environment, fibroblast conditioned collagen matrices were utilized as described for MDA MB 231 cells. Invading distances were quantified with ImageJ. The results revealed that independent Selected MDA MB 435 cells invaded to a greater depth into the collagen compared to Parental MDA MB 435 cells (Figure 3-13). These results indicated that within the Parental population of MDA MB 435 cells, there were cells with greater constrained invasive behaviours.

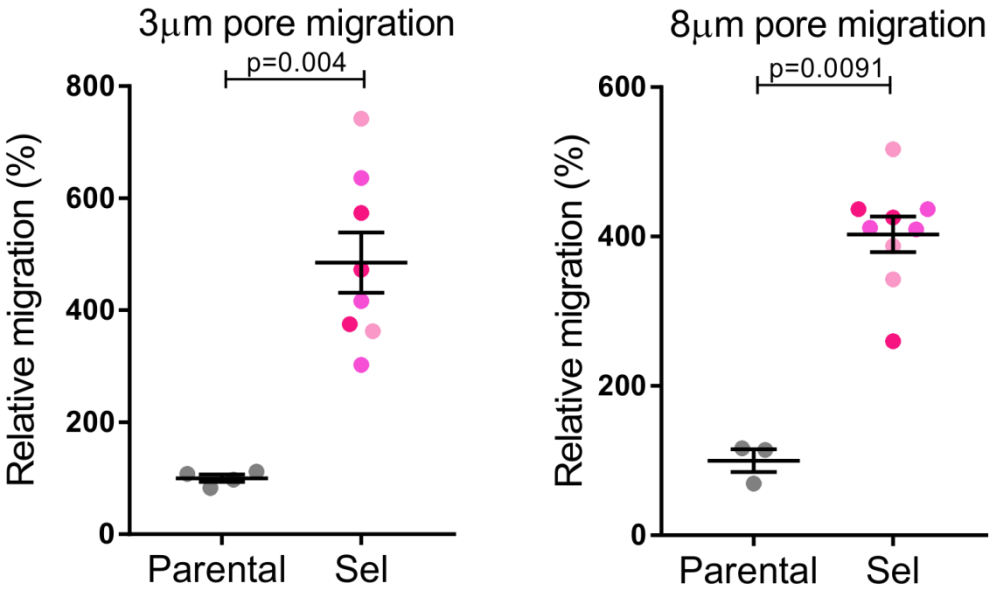

Figure 3-10 Selected MDA MB 435 cells are more migratory through 3 and 8 μm pores relative to Parental MDA MB 435 cells.
Left graph depicts mean (± SEM) relative 3 μm migration for Parental and independent Selected MDA MB 435 cell populations. Right graph depicts mean (± SEM) relative 8 μm migration for Parental and independent Selected MDA MB 435 cell populations. Each dot represents an average value from n = 3 wells. Data pooled from n ≥ 3 independent experiments. Statistical significance determined by Mann - Whitney test.

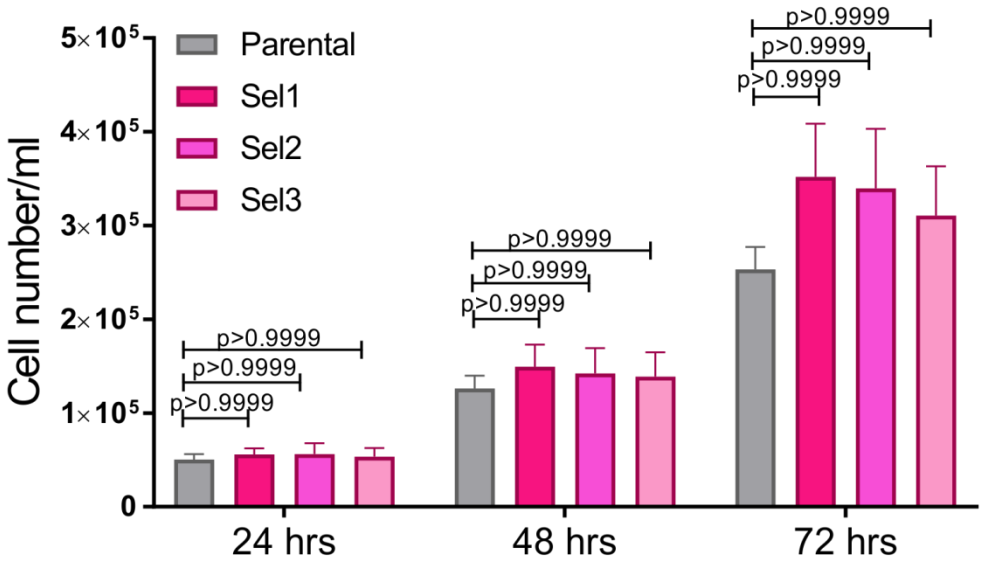

Figure 3-11 No differences in proliferation rates between Parental and Selected MDA MB 435 cells.

Graph depicts mean (± SEM) cell number for Parental and Selected MDA MB 435 cells measured at 24, 48 and 72 hours. Data pooled from n = 3 independent experiments. Statistical significance determined by Kruskal - Wallis followed by Dunn's multiple comparison test.

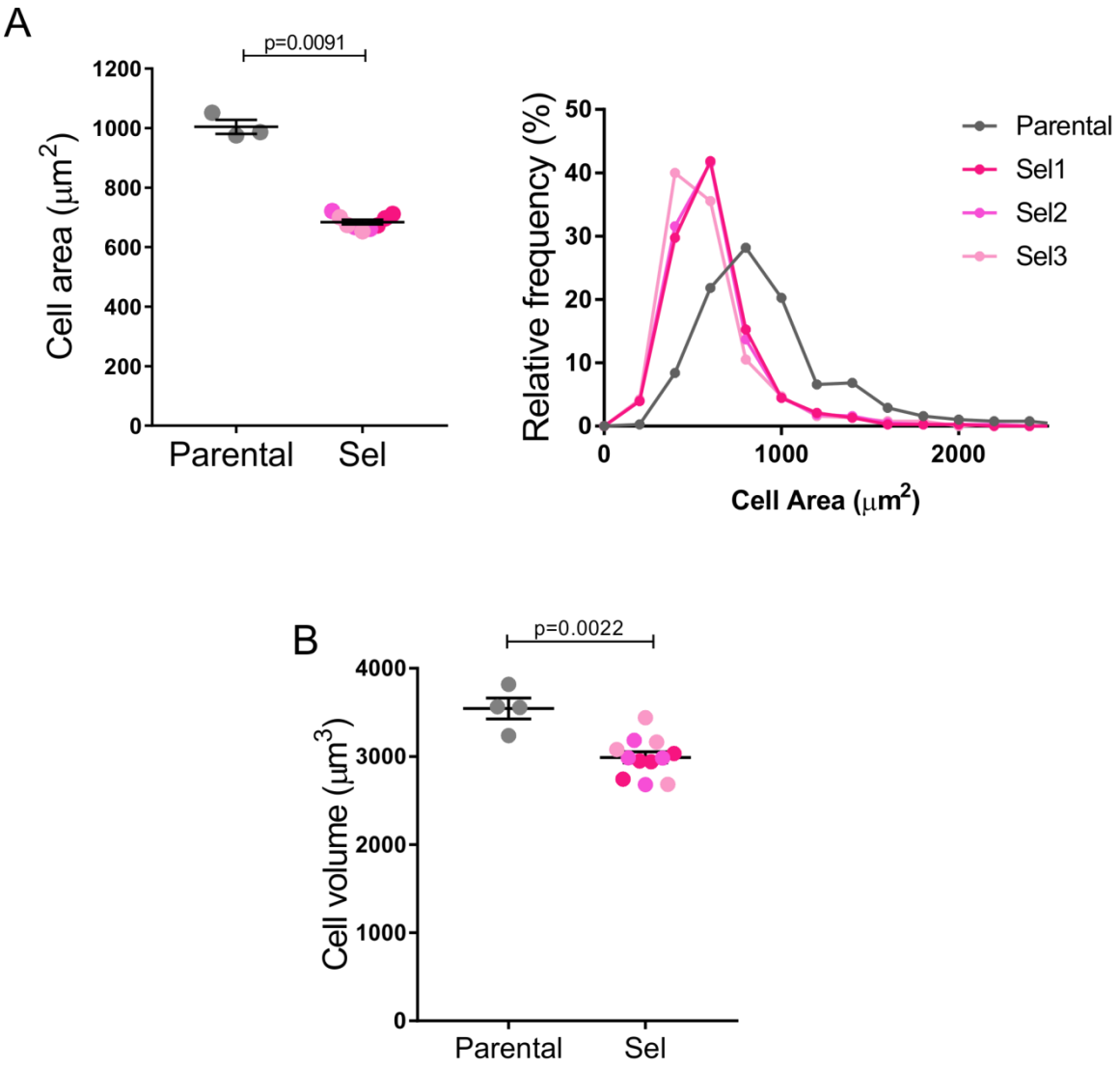

Figure 3-12 Selected MDA MB 435 cells have smaller cell size relative to Parental MDA MB 435 cells.

A) Graph depicts mean (± SEM) cell area for Parental and independent Selected MDA MB 435 cell populations. Each dot represents an average from n = 6 fields per well, from at least 200 cells per field. Data pooled from n = 3 independent experiments. Right graph depicts relative frequency of cell area for Parental and independent Selected MDA MB 435 cell populations. Cell area was determined by using Operetta High Content Imaging System. B) Graph represents mean (± SEM) cell volume for Parental and independent Selected MDA MB 435 cell populations. Cell volume was determined by measuring cell diameter. Each dot represents an average value from n = 3 measurements. Data pooled from n = 4 independent experiments. Statistical significance determined by Mann - Whitney test.

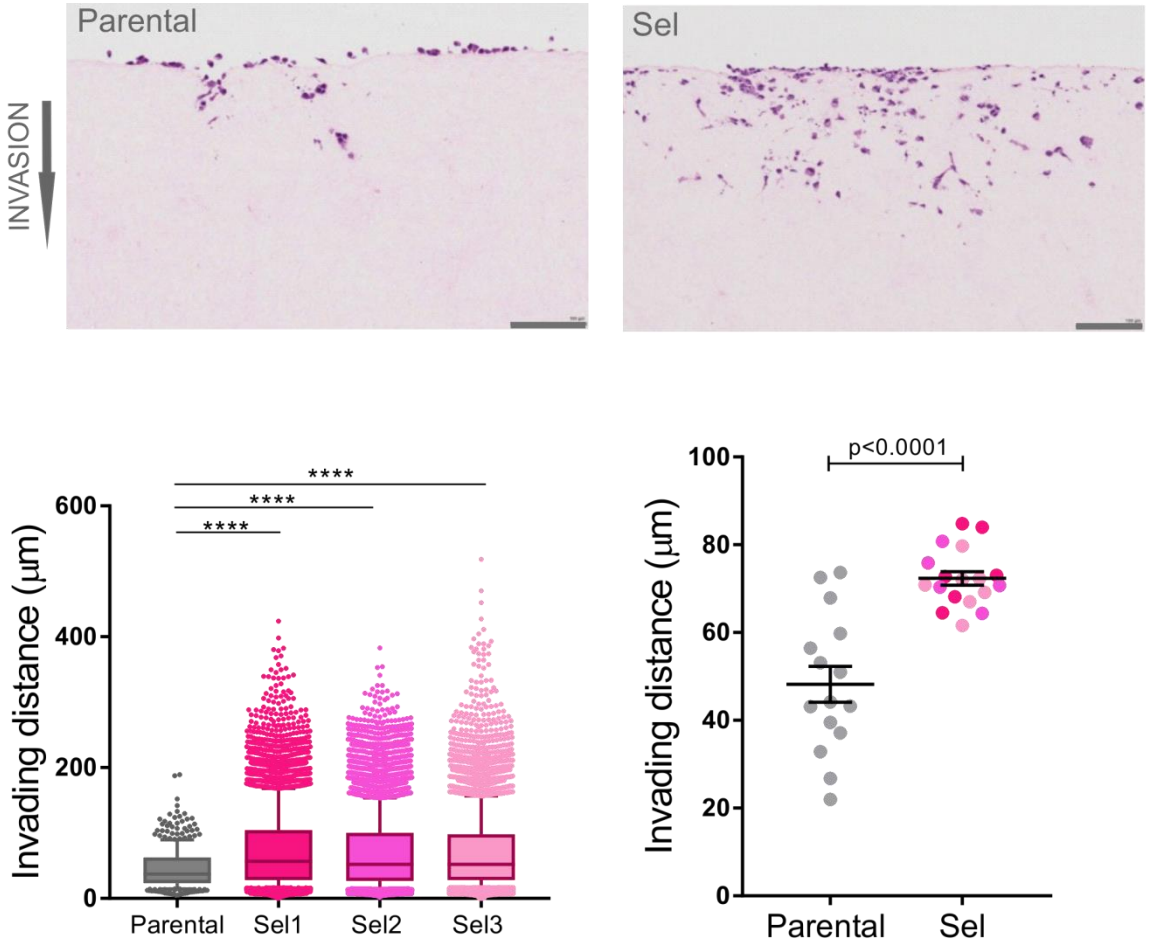

Figure 3-13 Selected MDA MB 435 cells invade to a greater depth into collagen matrix. Representative images of invading cells into the collagen matrix showed for Parental and Selected MDA MB 435 cells. Scale bar = 100 µm. Left graph depicts box and whiskers plot (1-99 percentile) representing the distance travelled by individual cells for Parental and independent Selected MDA MB 435 cell populations pooled from n = 3 independent experiments. Statistical significance determined by Kruskal - Wallis followed by Dunn's multiple comparison test (**** = p<0.0001). Right graph depicts mean (± SEM) travelled distance for Parental and independent Selected MDA MB 435 cell populations pooled from n = 3 independent experiments. Statistical significance determined by Mann - Whitney test.

3.3 Conclusions

To reveal invasive traits of cancer cells, I adopted an *in vitro* selection strategy with a successful outcome. As shown in this chapter, I have presented results indicating that the *in vitro* 3 μm pore selection strategy can be used to enrich for cells with enhanced invasive properties, as shown for MDA MB 231 and MDA MB 435 cells. By applying the 3 μm pore migration and 3D collagen invasion assays, I found that Selected cells are characterized by greater constrained invasion capacities. Additionally, to test the possibility that cell size was a major determinant for the enhanced constrained invasion of Selected cells, I adopted an additional selection strategy that allowed me to directly study this parameter. I revealed that the invasive properties by Selected MDA MB 231 cells were not solely a reflection of small cell size.

Furthermore, I have presented data showing that nuclear size did not determine the greater invasive capabilities of Selected MDA MB 231 cells. By studying nuclear mechanical properties, I showed that Selected and Flow sorted MDA MB 231 cells had increased nuclear stiffness relative to Parental cells; however this was not associated with relatively higher Lamin A/C expression. Moreover, the expression of Lamin B was not investigated. Investigation of nuclear content and chromatin condensation revealed that both of these properties also did not determine the invasive phenotype of Selected MDA MB 231 cells. However, the reduction in chromosome number correlated with decreased nuclear and cell volume; additionally the decreased chromosome number correlated with more condensed chromatin (Table 3-1).

4 *In vivo* cell properties

4.1 Rationale

Having identified enhanced invasion properties of Selected MDA MB 231 and MDA MB 435 cells *in vitro*, I next wanted to investigate their metastatic potential *in vivo*. In order to perform these experiments, a collaboration was established with the Transgenic Models Advanced Technology Service (Cancer Research UK Beatson Institute). In order to assess the aspects of cancer growth and spread of Parental, Selected and Flow sorted MDA MB 231 cells, cells were orthotopically injected into the mammary fat pads of immune-compromised mice. In addition, all isolated cell populations from both cell lines, MDA MB 231 and MDA MB 435, were injected into the tail veins of immune-compromised mice.

In order to assess *in vivo* metastatic and growth properties, there are numerous *in vivo* models available. In xenograft transplantation, human cells are inoculated into immune-compromised mice under the skin or into the organ corresponding to that from which the cancer cells were derived (orthotopic) (Khanna and Hunter 2005). A major advantage of these models is the possibility to study metastasis of human cancer cells in an *in vivo* context. Moreover, it resembles the human situation, with changes in tumour-associated vascularity, tumour-stroma interactions, gene expression patterns and metastases. On the other hand, due to the lack of a fully functional immune system, the input of the immune system to metastatic progression cannot be evaluated (Jonkers and Derksen 2007).

To study breast cancer progression, orthotropic injection of cancer cells into mammary fad pads can be utilised. This *in vivo* model allows for the assessment of tumour growth, and the metastatic progression process, from primary sites to metastasis formation. Such a transplantation model of metastatic dissemination is referred to as spontaneous metastasis (Kocaturk and Versteeg 2015). In the experimental metastasis assay, tumour cells are injected directly into the systemic circulation. Cancer cells can be injected via various routes such as lateral tail vein, intra-portal, intra-cardiac *etc*. Depending on the injection route and tropism of the tumour cells, distant metastatic sites may be manifested in different organs throughout the body (Khanna and Hunter 2005). The most

commonly used experimental metastasis assay is the injection of cancer cells into the tail vein. Such a route of cancer cell injection mostly leads to development of metastatic foci in lungs (Khanna and Hunter 2005). This transplantation model reproduces the later steps of the metastatic cascade, extravasation and organ colonisation.

4.2 Results

4.2.1 Selected MDA MB 231 cells show a trend towards enhanced tumourigenicity *in vivo* relative to Parental and Flow sorted MDA MB 231 cells

To investigate the *in vivo* properties of MDA MB 231 cells, $1x10^6$ of Parental, Selected and Flow sorted MDA MB 231 cells were injected in 50 µl PBS:matrigel (1:1) into fourth abdominal fat pads of female CD1 nude mice. Tumour measurements were taken over the course of the study, starting at the day when tumours became palpable (day 0). Tumour volumes were quantified using the formula $1/2(\text{Length} \times \text{Width}^2)$. When one of the tumours reached 15 mm in diameter, animals were sacrificed, the primary tumours and the lungs were harvested and weighed. Moreover, in order to visualise tumour growth, mice were injected with 150 mg/kg of D-luciferin in PBS prior to sacrifice. Bioluminescence images were acquired 5 min after injections in order to allow for the distribution of D-luciferin within the entire body of the animal. Images were acquired using the IVIS Spectrum Imaging System. One mouse injected with Selected MDA MB 231 cells developed a palpable tumour at day 14 and it was excluded from further analysis.

Analysis of tumour volumes and weights revealed that Selected MDA MB 231 cells injected into the mammary fat pads of immune-compromised mice showed a trend towards a slight increase of tumourigenic potential relative to Parental and Flow sorted MDA MB 231 cells (Figure 4-1) (Figure 4-2).

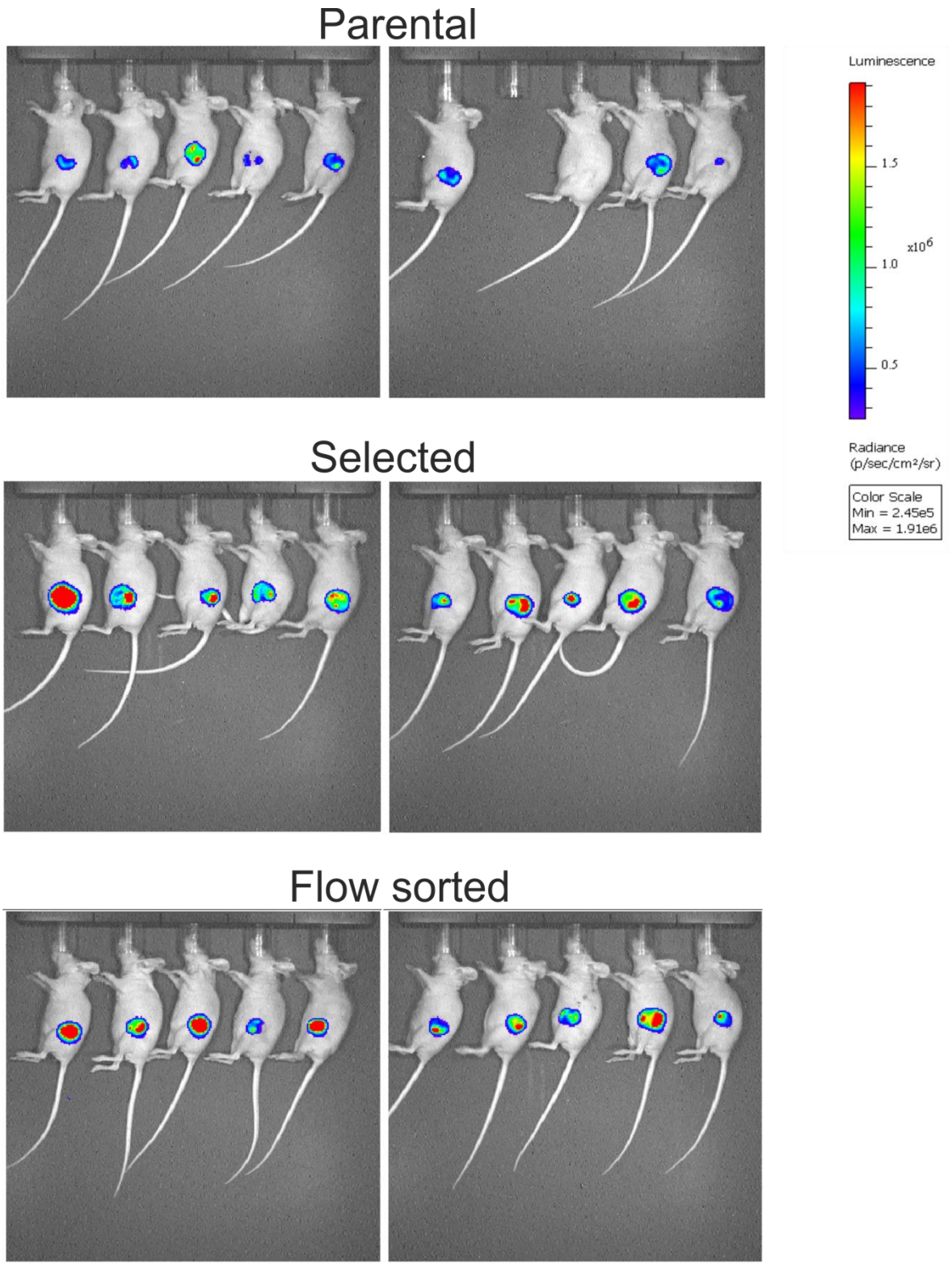

Figure 4-1 IVIS images of tumours derived from Parental, Selected and Flow sorted cells injected into the mammary fat pads of immuno-compromised mice.
Bioluminescent Parental, Selected and Flow sorted MDA MB 231 cells were injected into the mammary fat pads of nude mice and tumours size was monitored by imaging them with the IVIS Spectrum Imaging System. Images represent tumours size at day 17.

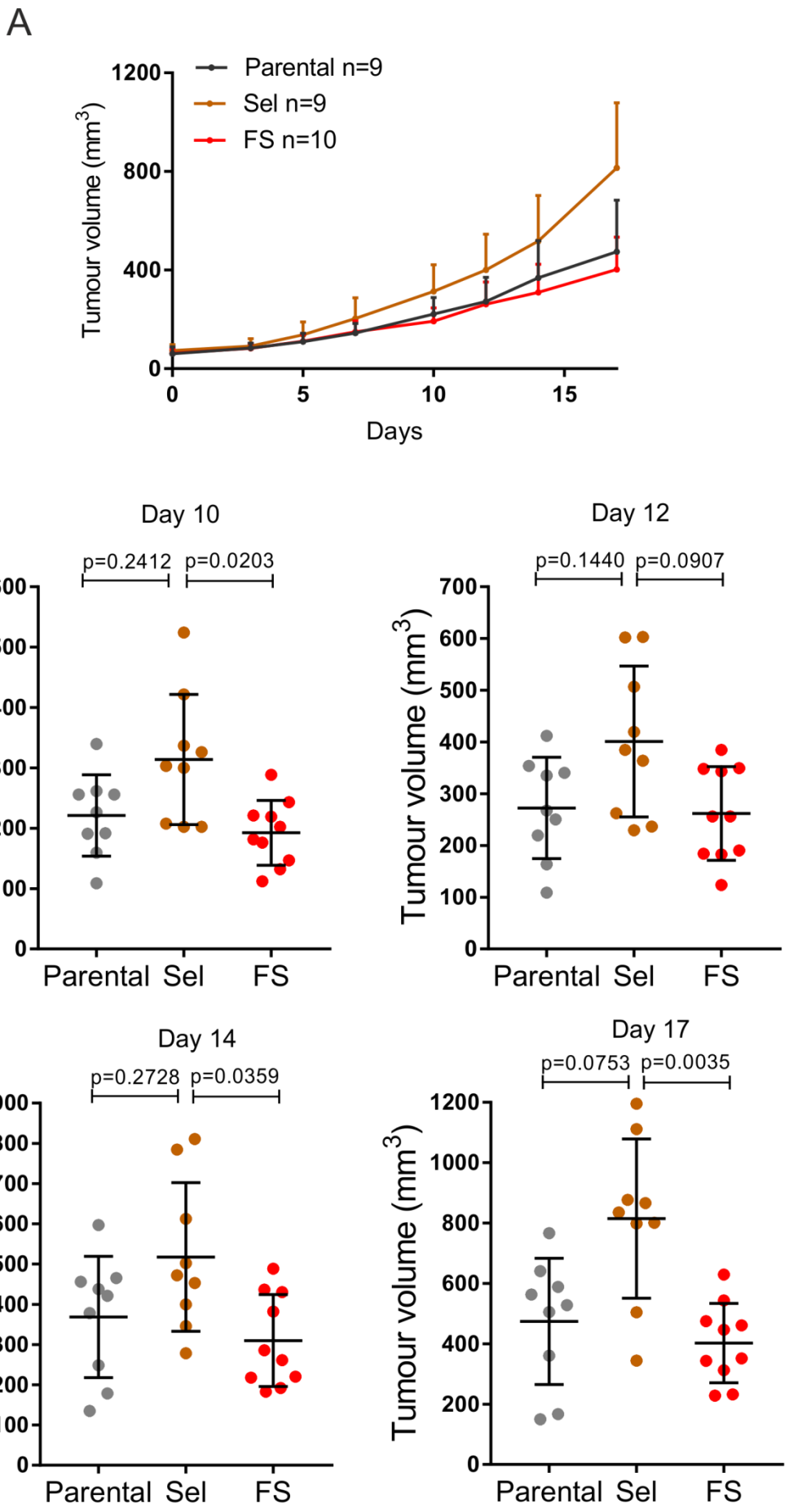
A
Parental n=9
Sel n=9
FS n=10
Tumour volume (mm3)
Days
B
Day 10
p=0.2412
p=0.0203
Day 12
p=0.1440
p=0.0907
Day 14
p=0.2728
p=0.0359
Day 17
p=0.0753
p=0.0035
Parental
Sel
FS

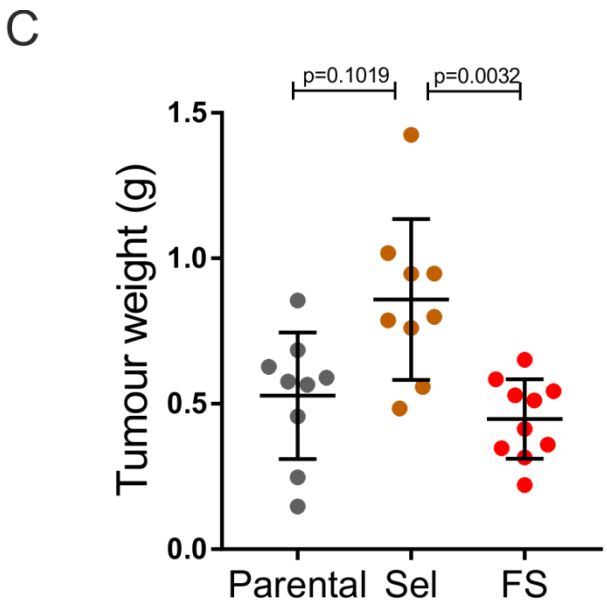

Figure 4-2 Selected MDA MB 231 cells show a trend towards an enhanced tumourigenicity *in vivo* relative to Parental and Flow sorted MDA MB 231 cells.
A) Growth curves of primary tumour volume (± SD) for tumours derived from Parental, Selected and Flow sorted MDA MB 231 cells injected into mammary fat pads. B) Graphs represent mean (± SD) tumour volume for tumour derived from Parental, Selected and Flow sorted mammary fat pad-injected cells at days 10, 12, 14, 17. C) Graph depicts mean (± SD) tumour weight for tumour derived from Parental, Selected and Flow sorted MDA MB 231 mammary fat pads-injected cells. Each dot represents data obtained from n = 1 mouse. Statistical significance determined by Kruskal - Wallis followed by Dunn's multiple comparison test.

4.2.1.1 Selected MDA MB 231 cells show a trend towards increased proliferation *in vivo* relative to Parental and Flow sorted MDA MB 231 cells

Proliferation of cells in primary tumours from mice injected with Parental, Selected or Flow sorted MDA MB 231 were determined by staining for anti-BrdU (5-bromo-2'-deoxyuridine) incorporation. Mice were injected intraperitoneally two hours prior to sacrifice, and paraffin embedded tumour section were stained with BrdU antibody. The number of BrdU-positive cells was quantified per total cell number (excluding necrotic areas) using Leica Biosystems software. Analysis of BrdU-stained tumour sections revealed that Selected MDA MB 231 cells showed a trend towards increased proliferation relative to Parental and Flow sorted MDA MB 231 cells (Figure 4-3).

Necrotic foci were quantified on H&E-stained tumour sections. Large areas of necrotic foci were seen in all tumour sections obtained from all Parental, Selected and Flow sorted cell-injected mice. The necrotic areas were quantified as a percentage necrotic area relative to total tumour area using Leica Biosystems software. The analysis revealed that there were no differences in necrotic foci between Parental, Selected and Flow sorted MDA MB 231 cells (Figure 4-3).

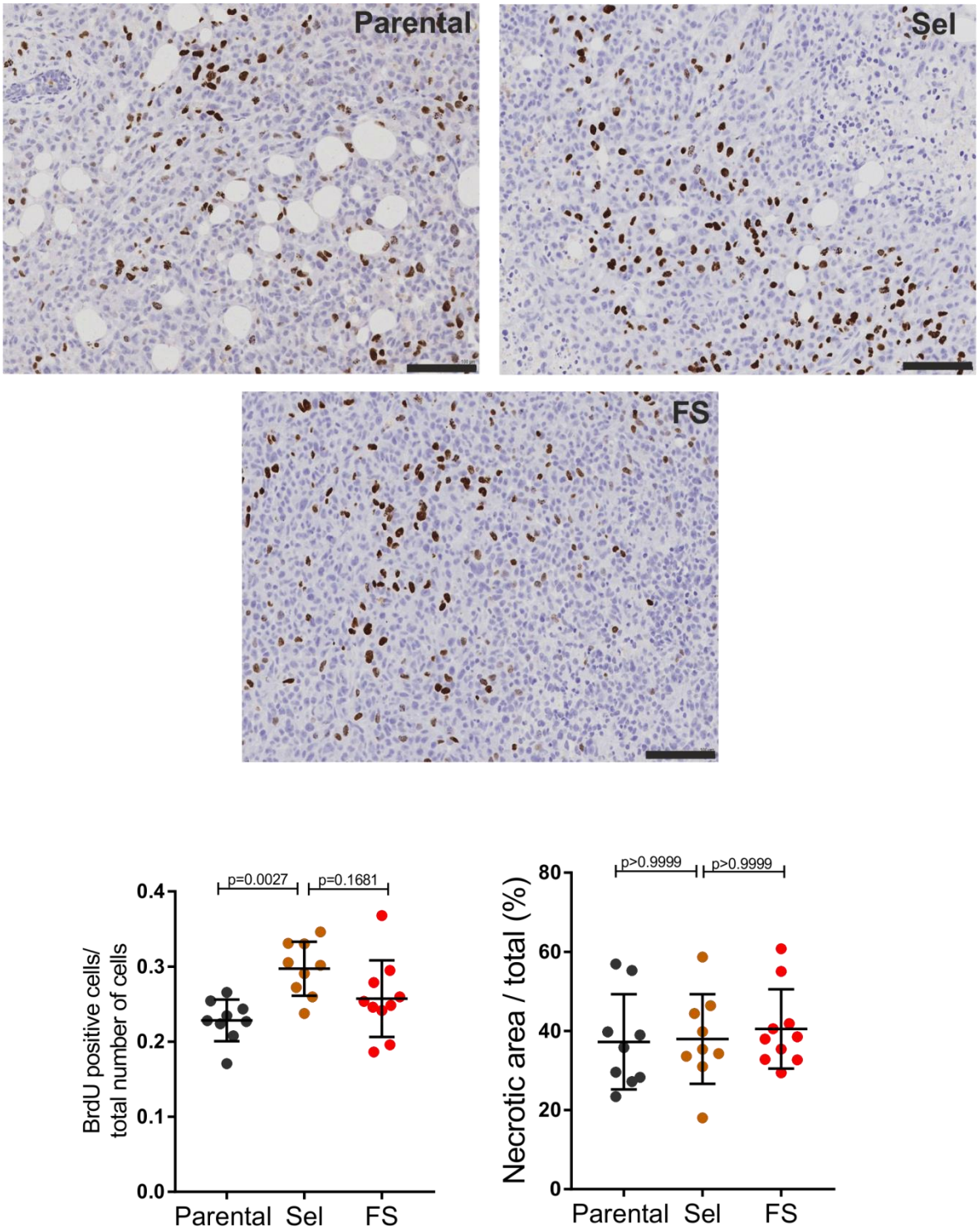

Figure 4-3 Selected MDA MB 231 cells show a trend towards increased proliferation *in vivo* relative to Parental MDA MB 231 cells.
Representative images of BrdU-stained tumour sections of Parental, Selected and Flow sorted MDA MB 231 cells. Scale bar = 100 µm. Left graph depicts mean (± SD) of BrdU-positive cells / total cells in tumour sections for Parental, Selected and Flow sorted MDA MB 231 cells. Right graph depicts mean (± SD) percent of necrotic area in tumour sections for Parental, Selected and Flow sorted MDA MB 231 cells. Each dot represents data obtained from n = 1 mouse. Statistical significance determined by Kruskal - Wallis followed by Dunn's multiple comparison test.

4.2.1.2 No visible lung metastatic sites in mice injected with Parental, Selected and Flow sorted MDA MB 231 cells

In order to detect micrometastasis in the harvested lungs of mice injected with Parental, Selected and Flow sorted MDA MB 231 cells, H&E- and Human Leukocyte Antigen (HLA)-stained sections were analysed. Analysis of H&E sections revealed no detectable micrometastasis in the lung sections.

Anti-HLA staining was used as a specific marker to detect human cells within murine lung tissue. HLA is present on most nucleated human cells. Five serial sections were prepared per mouse lung and stained with anti-HLA antibody. The staining revealed no detectable HLA-positive micrometastatic sites in the harvested lungs.

Furthermore, in order to detect human cells in murine lungs, RT-qPCR was performed. RNA was extracted from harvested lungs. Specific primers for human *GAPDH* were used and Mouse Beta-2-microglobulin (*B-2-M)* as a housekeeping reference gene. The analysis revealed no detectable tumour cell specific mRNA present in the lung tissues.

4.2.2 Parental MDA MB 231 cells show a trend towards an increase in metastatic potential *in vivo* in the experimental metastasis assay

In order to assess the metastatic potential of MDA MB 231 cells, Parental, Selected and Flow sorted cells were injected into the tail vein of immune-compromised mice. In brief, $1x10^6$ Parental and Selected cells in 100 µl of PBS were injected into the lateral tail vein of female CD1 nude mice (8 mice per condition). After 6.5 weeks, mice were sacrificed and lungs were harvested. H&E staining was performed on paraffin-embedded lung sections and lung metastasis was assessed. 5 serial sections were made per harvested lung. Analysis of H&E sections showed the presence of metastatic nodules and thickening of the alveolar septa. Analysis of metastatic score revealed that six out of eight mice injected with Parental MDA MB 231 cells developed metastatic nodules. Four out of eight mice injected with Selected MDA MB 231 cells developed metastatic foci, while three out of eight mice injected with Flow sorted MDA MB 231 cells developed metastases (Figure 4-4).

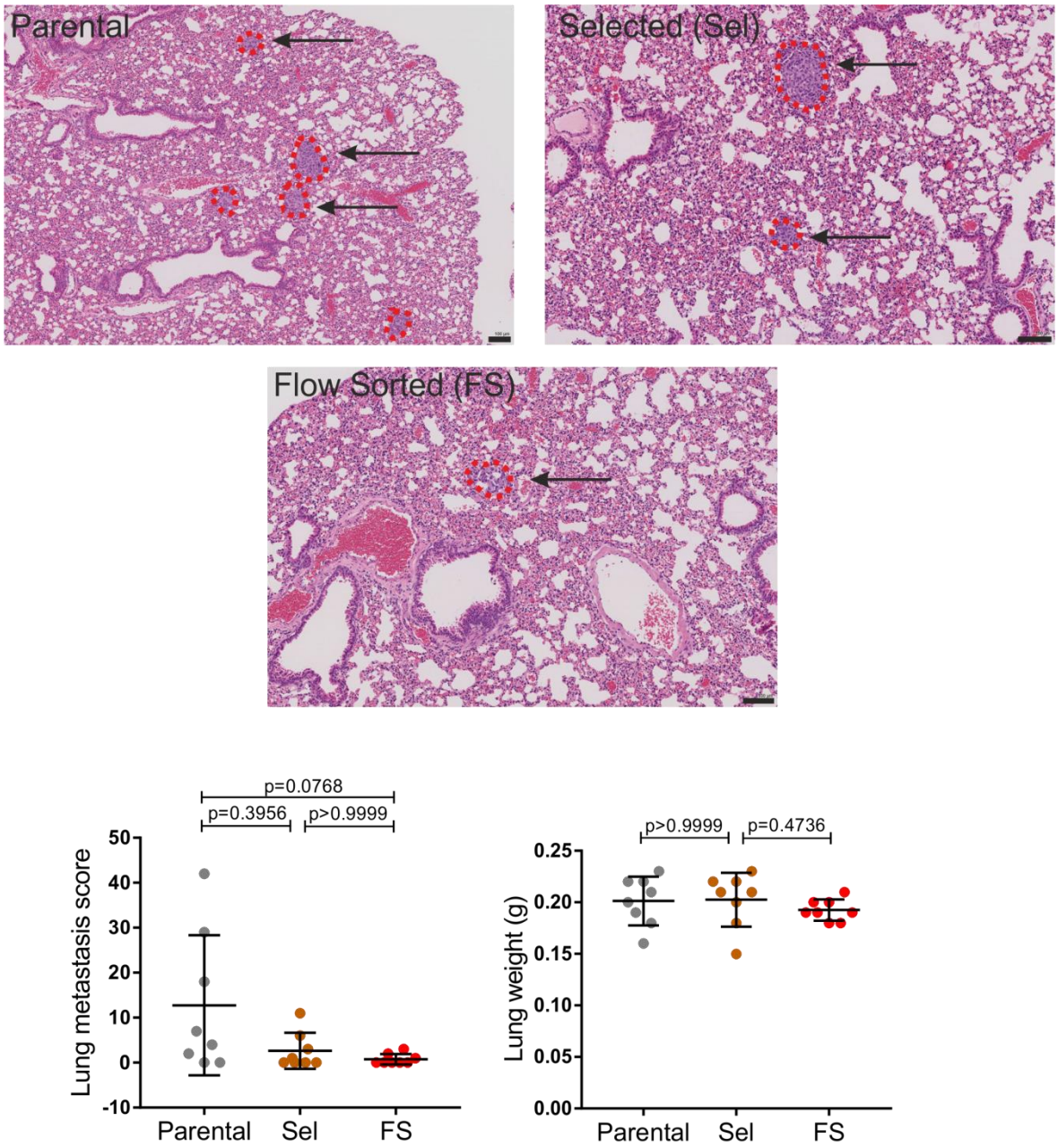

Figure 4-4 Parental MDA MB 231 cells show a trend towards an increase in metastatic potential *in vivo* in the experimental metastasis assay.
Representative H&E-stained lung sections from mice injected with Parental, Selected and Flow sorted MDA MB 231 cells showing more tumour foci in mice injected with Parental cells. Black arrows indicate metastatic nodules and green arrows indicate thickening of the alveolar septa. Scale bar 100 µm. Left graph depict mean (± SD) lung metastasis score in lungs harvested from mice injected with Parental, Selected and Flow sorted MDA MB 231 cells. Right graph depicts mean (± SD) lung weight harvested from mice injected with Parental, Selected and Flow sorted MDA MB 231 cells. Each dot represents data obtained from n = 1 mouse. Statistical significance determined by Kruskal - Wallis followed by Dunn's multiple comparison test.

4.2.3 Selected MDA MB 435 cells show a trend towards an increase in metastatic potential *in vivo* in the experimental metastasis assay

In order to assess the metastatic potential of MDA MB 435 cells, Parental and Selected cells were injected into the tail veins of immune-compromised mice. In brief, $1x10^6$ Parental and Selected cells in 100 µl of PBS were injected into the lateral tail vein of female CD1 nude mice (7 mice per condition). After 6.5 weeks, mice were sacrificed and lungs were harvested. H&E staining was performed on paraffin-embedded lung sections and lung metastasis was assessed. Analysis of H&E sections showed the presence of metastatic nodules and thickening of the alveolar septa. 5 serial sections were made per each harvested lung. Analysis of metastatic score revealed that five out of seven mice injected with Selected MDA MB 435 cells developed metastatic nodules. Three mice had 1, 2 or 3 visible tumour foci in their lungs, whereas the other two developed high numbers of metastatic foci, 16 or 18 (Figure 4-5). Furthermore, two out of seven mice developed a tumour at a lumbar region. Histopathological analysis of H&E-stained tumours revealed that the lumbar tumours consisted of injected Selected cells and that the tumour cells invaded into the muscle region (Figure 4-6). Two mice out of seven injected with Parental MDA MB 435 cells developed 3 metastatic lesions each in the lung.

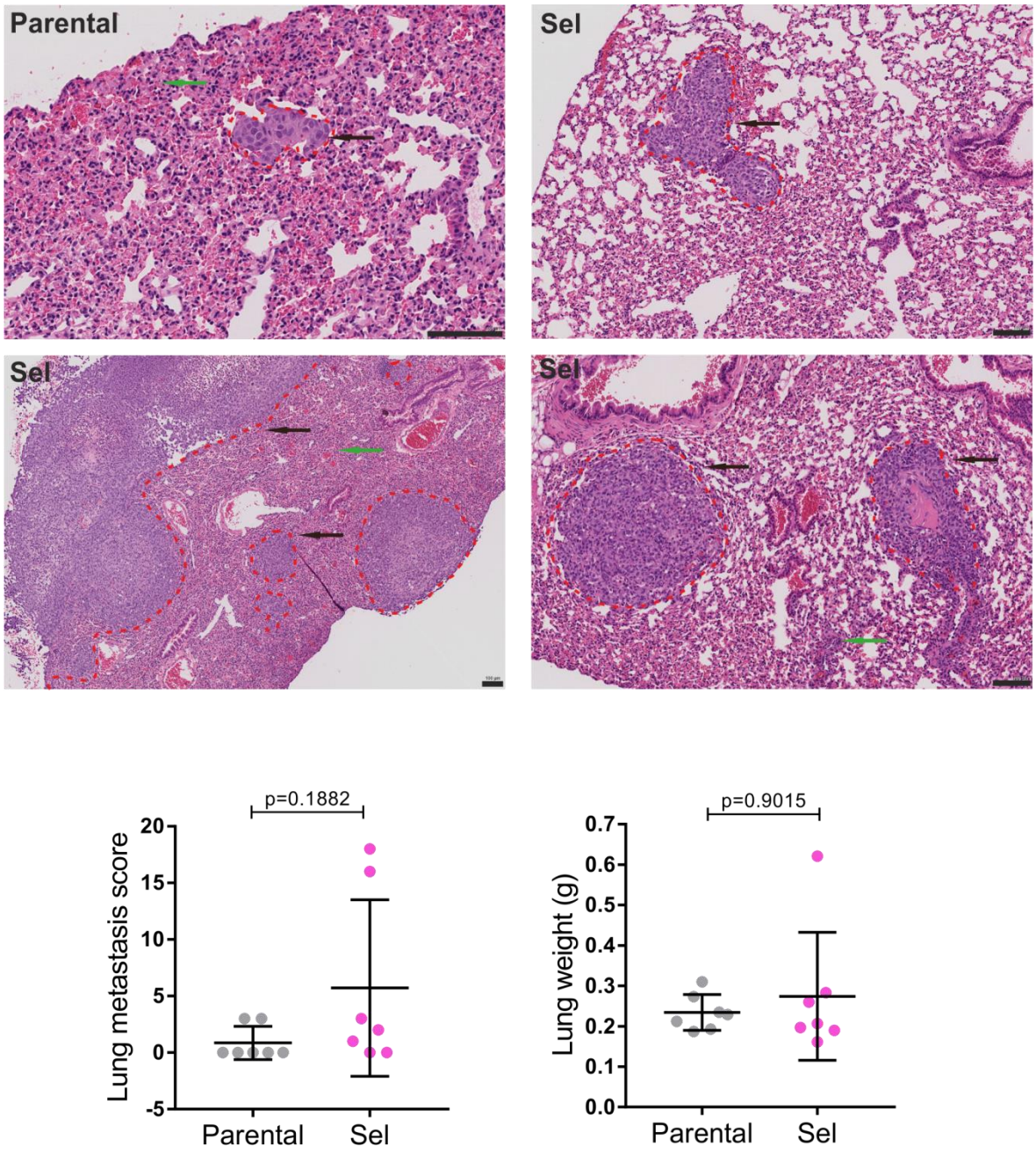

Figure 4-5 Selected MDA MB 435 cells show a trend towards an increase in metastatic potential *in vivo* in the experimental metastasis assay.
Representative H&E-stained lung sections from mice injected with Parental or Selected MDA MB 435 cells showing more tumour foci in mice injected with Selected cells. Black arrows indicate metastatic nodules and green arrows indicate thickening of the alveolar septa. Scale bar = 100 µm. Left graph depicts mean (± SD) lung metastasis score in lungs harvested from mice injected with Parental and Selected MDA MB 435 cells. Right graph depicts mean (± SD) lung weight harvested from mice injected with Parental and Selected MDA MB 435 cells. Each dot represents data obtained from n = 1 mouse. Statistical significance determined by Mann - Whitney test.

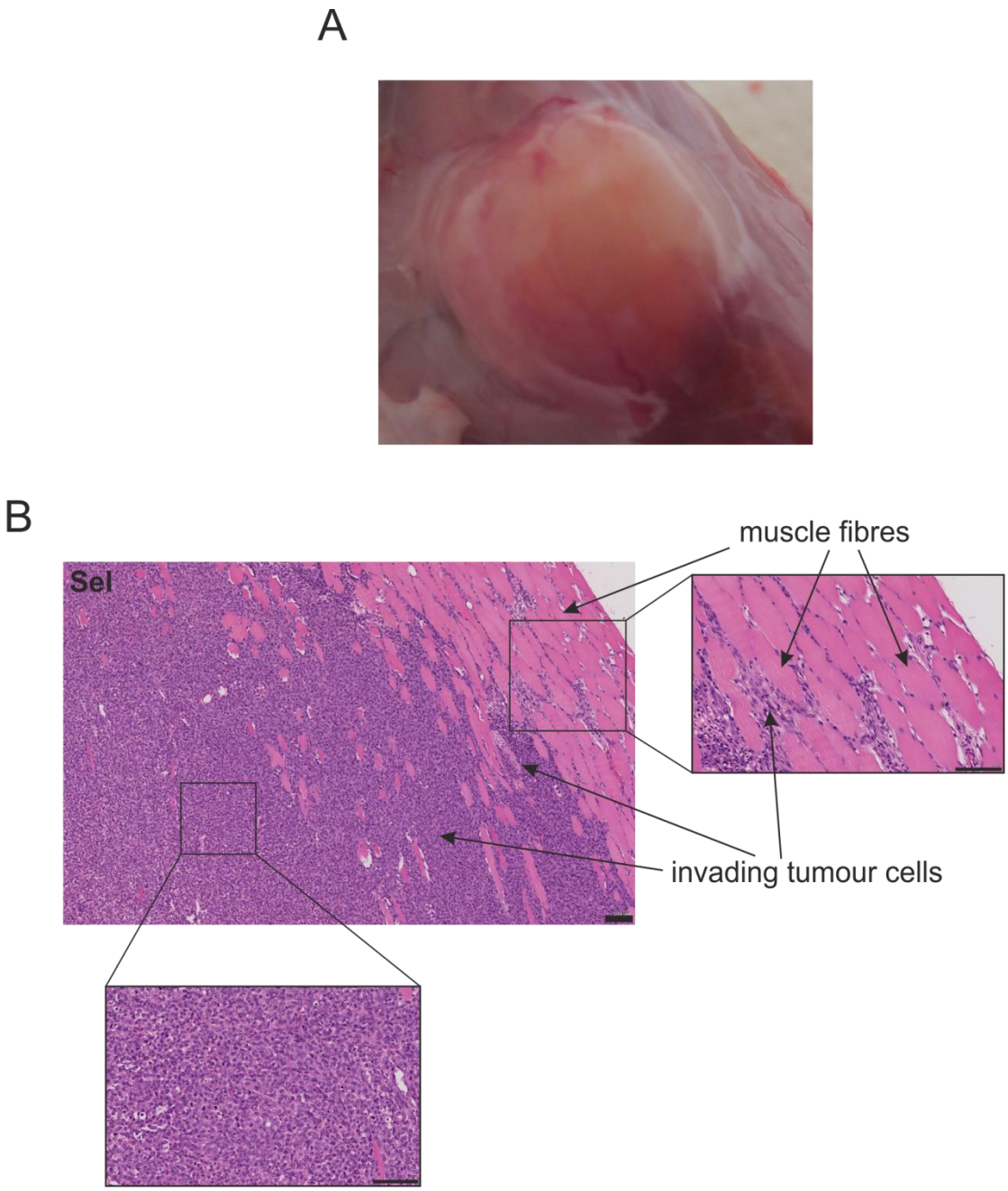

Figure 4-6 Two mice injected with Selected MDA MB 435 cells develop tumour at a lumbar region.
A) Photo showing a developed tumour at the lumbar region in mice injected with Selected MDA MB 435 cells. B) H&E staining of tumour developed at the lumbar region in mice injected with Selected MDA MB 435 cells. The image shows that the tumour consists of Selected MDA MB 435 cells and invasion of Selected cells into the muscle region.

4.3 Conclusions

In this chapter I have presented data describing the metastatic and growth potential of Parental, Selected and Flow sorted MDA MB 231, and Parental and Selected MDA MB 435 cell lines. Taking advantage of MDA MB 231 cells being breast cancer cells, their *in vivo* metastatic and growth abilities were assessed by injecting them into the mammary fat pads of immune-compromised mice and monitoring their growth over the course of the study. From this experiment, I found that Selected MDA MB 231 cells showed a trend towards increased tumourigenic potential in comparison to Parental and Flow sorted MDA MB 231 cells. Due to the short duration of the experiment, there were no metastatic foci found in the lungs in any of the injected mouse.

In order to assess the metastatic potential of Parental, Selected and Flow sorted MDA MB 231 cells, cells were injected into the tails of immune-compromised mice. The analysis of H&E-stained lung sections revealed a trend towards increased number of metastatic sites in lungs of mice injected with Parental cells. Such results are not surprising since Parental MDA MB 231-luc-D3N2LN cells are derived from spontaneous lymph node metastasis of MDA MB 231 cells and possess enhanced growth and widespread metastasis in mice (Jenkins, Hornig et al. 2005). Additionally, Parental cells due to their bigger size may lodge in pulmonary capillaries, where they formed tumours, while the smaller size of Selected and Flow Sorted cells might have reduced the number getting stuck, therefore leading to fewer tumours.

In order to assess the metastatic potential of Parental and Selected MDA MB 435 cells, cells were injected into the tail veins of immune-compromised mice. The analysis of H&E-stained lungs revealed a trend towards increased number of metastatic sites in lungs of mice injected with Selected MDA MB 435 cells. Additionally, two mice injected with Selected MDA MB 435 cells developed tumours at a lumbar region.

In conclusion, these results revealed that there were no significant differences in the metastatic or tumourigenic potential between Parental, Selected and Flow sorted MDA MB 231 cell lines and between Parental and Selected MDA MB 435 cells. Such lack of differences could be explained by the limitations of the

experimental metastatic *in vivo* model used, such as it only reproduces the later steps of the metastatic cascade, extravasation and organ colonisation, therefore the stages of the metastasis cascade might be irrelevant for this assay. Furthermore, tumours which were derived from Selected MDA MB 231 or MDA MB 435 cells may revert back to parental-like phenotype.

5 Determination of cell mechanical properties and behaviour

5.1 Rationale

A number of cellular changes occur that enable cancer cells to become invasive and metastatic; however many of the metastatic cascade steps require enhanced cell motility which is driven by a cycle of actin polymerisation, cell adhesion and acto-myosin contraction (Olson and Sahai 2009). The cell cytoskeleton plays not only a dominant role in driving cell migration and invasion, but also by creating a network of actin filaments, it shapes and provides a structural support that subsequently contributes to cell mechanical rigidity (Blanchoin, Boujemaa-Paterski et al. 2014; Grady, Composto et al. 2016). From a mechanical perspective, a cell can be considered as an elastic material that will deform if subjected to an applied external force, and which will recover its shape when the force is removed (Kuznetsova, Starodubtseva et al. 2007). As the stiffness of a material increases, more force is necessary to deform its shape, which is a reflection of the material's elasticity and can be quantitatively represented as its Young's modulus (Polacheck and Chen 2016).

Multiple studies have reported that malignant cancer cells are more easily deformed than normal cells (Cross, Jin et al. 2008; Swaminathan, Mythreye et al. 2011) and such biological adaptations of cell mechanical rigidity may facilitate cancer cell invasion and metastasis. Although the actin cytoskeleton is known to be the major determinant of cell elasticity (McPhee, Dalby et al. 2010; Ketene, Schmelz et al. 2012), the mechanistic signalling pathways and potential contributors have not been identified yet. Besides the cytoskeleton being a known cell elasticity determinant, it has been shown that lipid bilayers also possess bending and compression elasticity (Espinosa, Lopez-Montero et al. 2011). In order to investigate cell mechanical properties, Atomic Force Microscopy (AFM) was utilised. Potential contributors of mechanical properties, cytoskeleton structures and membrane fluidity, were studied as described below. Furthermore, dysregulation in cancer cell adhesiveness has been shown to facilitate cancer cell migration and invasion (Cavallaro and Christofori 2001; Yoshimura, Hamada et al. 2016). Therefore, to address the questions whether there were differences in migration, spreading and adhesion properties between

Parental, Selected and Flow sorted MDA MB 231, and Parental and Selected MBA 435 cells, a set of experiments to explore these phenotypes was performed as described below.

5.2 Results

5.2.1 Selected MDA MB 231 have reduced stiffness compared to Parental and Flow sorted MDA MB 231 cells as measured by Atomic Force Microscopy (AFM)

Given the possibility that cell mechanical properties may play an important role in enabling Selected MDA MB 231 cells to squeeze through constraining environments, the elasticity of Parental, Selected and Flow sorted MDA MB 231 cells were investigated. In order to measure cell mechanical properties, Atomic Force Microscopy was utilised in collaboration with the Engineering Department at Glasgow University. In order to perform the experiment, cells were seeded in 3 cm petri dishes and incubated 24 hours in standard tissue culture conditions prior the experiment. During the experimental procedure, cells were kept in standard tissue culture conditions and 1% HEPES was added to the media to maintain the pH level. Cells were probed with a 4.74 μm diameter spherical bead and force of 3 nN. Five measurements were taken on the nuclear area and an average of Young's modulus value was determined per cell. The results revealed that Selected MDA MB 231 cells had significantly decreased Young's modulus values relative to Parental and Flow sorted MDA MB 231 cells (Figure 5-1), suggesting that Selected MDA MB 231 cells were more easily deformed than Parental and Flow sorted MDA MB 231 cells.

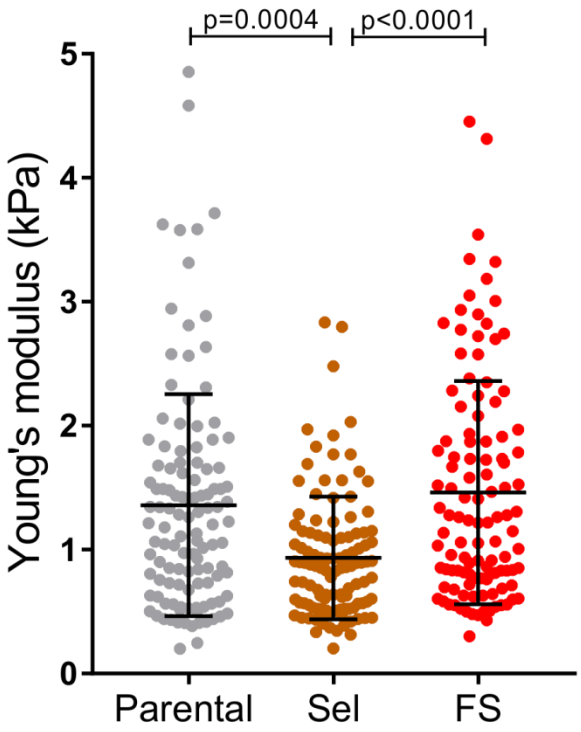

Figure 5-1 Selected MDA MB 231 cells have decreased Young's modulus relative to Parental and Flow sorted MDA MB 231 cells.
The graph depicts mean (± SD) Young's modulus measured for Parental, Selected and Flow sorted cells. Young's modulus was determined by applying AFM. Data represent individual cells pooled from n = 4 independent experiments. Statistical significance determined by Kruskal - Wallis followed by Dunn's multiple comparison test.

5.2.2 Selected MDA MB 231 cells have more isotropic actin alignment compared to Parental and Flow sorted MDA MB 231 cells

Having identified decreased stiffness of Selected MDA MB 231 cells, the organisation of the cytoskeleton, was investigated as a potential contributor of elasticity. As it has been reported that transitions from isotropic to anisotropic fibrillary actin ordering have been associated with increased cell stiffness (Gupta, Sarangi et al. 2015), actin cytoskeleton structures were visualised using a Zeiss 880 high resolution confocal microscopy. Phalloidin staining revealed that Selected MDA MB 231 cells had more ruffled-like F-actin with short actin filaments, while Parental and Flow sorted MDA MB 231 cells had longer and more aligned actin stress fibre organisation (Figure 5-2A).

In order to quantify actin alignment, an ImageJ plug-in Fibril Tool was utilised. Fibril Tool allowed quantification of fibre anisotropy. In order to be consistent with a z-plane image of stained F-actin taken for the anisotropy analysis, Total Internal Reflection Fluorescence microscopy (TIRF) images were used. TIRF microscopy allowed visualisation of fluorescent molecules within 200 nm from the cell-coverslip interface. Such location corresponded to the cortical actin position. TIRF images revealed organised long actin filaments in Parental and Flow sorted MDA MB 231 cells, while phalloidin-stained Selected MDA MB 231 cells had more diffused cortical actin staining (Figure 5-2A). Analysis of actin anisotropy showed that Selected MDA MB 231 cells had significantly decreased actin anisotropy compared to Parental and Flow sorted MDA MB 231 cells, suggesting that Selected cells had more disorganised actin organisation (Figure 5-2B).

5.2.2.1 Cytochalasin D disrupts actin structure and reduces cell stiffness

In order to determine whether the changes in cell stiffness of Parental, Selected and Flow sorted MDA MB 231 cells might have depended on difference in actin organisation, a control experiment with Cytochalasin D (CytoD) treatment was performed. CytoD is a cell permeable inhibitor that blocks actin polymerisation and elongation. First, the effect of CytoD was validated by microscopy visualisation. Cells were treated with 0.5 μM CytoD or vehicle control DMSO for 2 hours and incubated in standard tissue culture conditions. After incubation, cells

were fixed, stained with phalloidin and subsequently actin was visualised on a Zeiss 710 confocal microscopy. The images revealed that CytoD-treated cells had disrupted actin stress fibre organisation compared to vehicle-treated cells (Figure 5-3A).

After validation that CytoD disorganised actin structure, AFM measurements were performed on CytoD-treated Parental MDA MB 231 cells. Prior to the AFM measurements, cells were incubated with 0.5 μM CytoD for 2 hours, and control cells were treated with DMSO. The results revealed a reduction in Young's modulus upon CytoD treatment compared to DMSO-treated cells (Figure 5-3B).

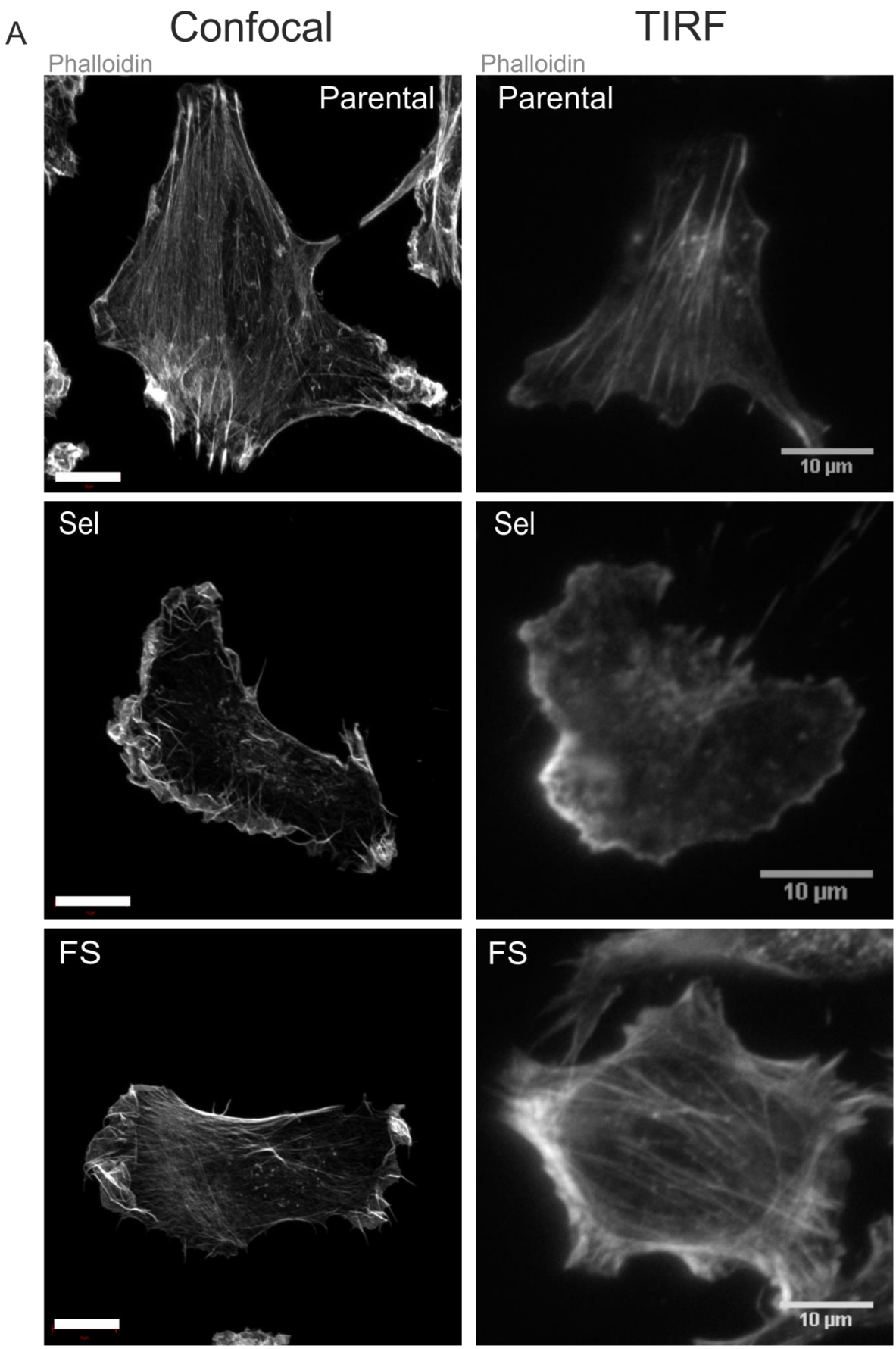
A
Confocal
TIRF
Phalloidin
Phalloidin
Parental
Parental
10 µm
Sel
Sel
10 µm
FS
FS
10 µm

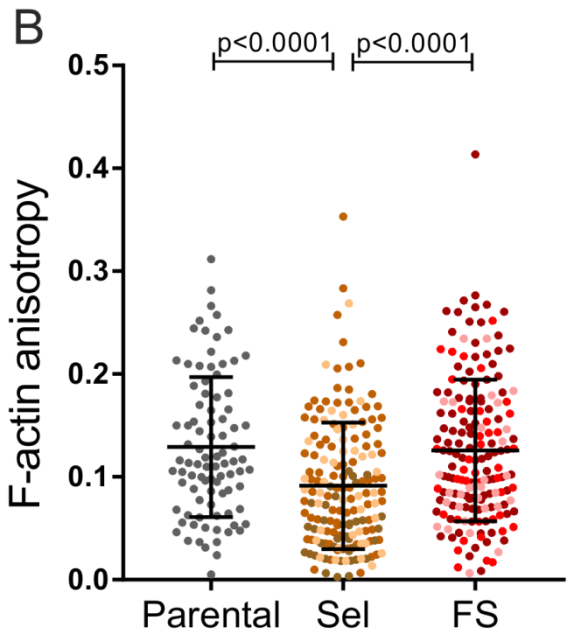

Figure 5-2 Selected MDA MB 231 cells have more isotropic actin alignment relative to Parental and Flow sorted MDA MB 231 cells.
A) Left column shows maximal projection images of phalloidin-stained cells showing F-actin structures. The images were taken on a Zeiss 880 confocal microscope. Scale bar 10 µm. Right column shows representative images of phalloidin-stained cells showing cortical actin structure. Images were taken by TIRF microscopy. Scale bar 10 µm. B) Graph depicts mean (± SD) F-actin anisotropy for Parental, independent Selected and independent Flow sorted cell populations. Data represent individual cells pooled from n = 3 experiments. Statistical significance determined by Kruskal - Wallis followed by Dunn's multiple comparison test.

A

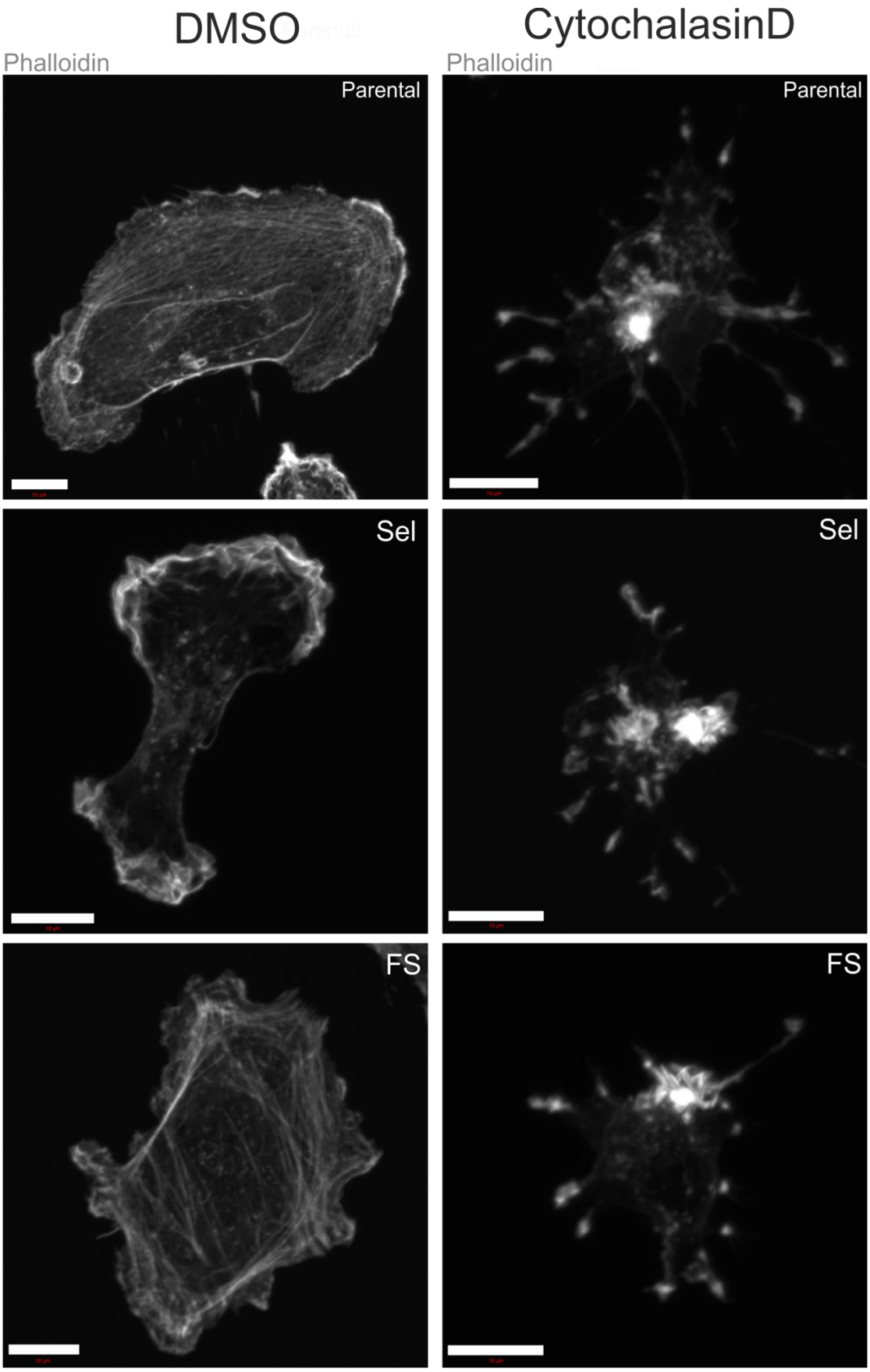
DMSO
CytochalasinD
Phalloidin
Phalloidin
Parental
Parental
Sel
Sel
FS
FS

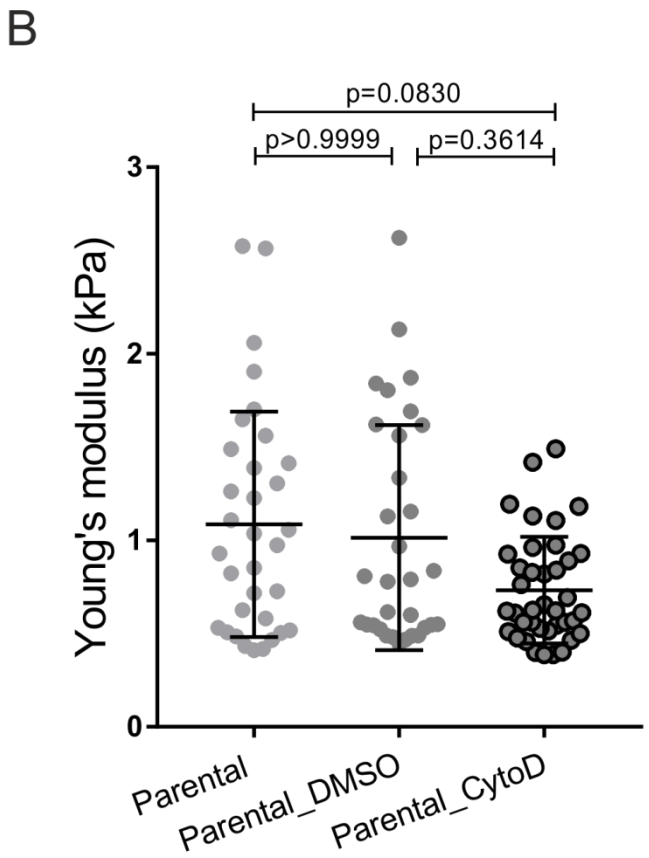

Figure 5-3 CytochalasinD treatment of Parental MDA MB 231 cells disrupts actin organisation and leads to decreased cell stiffness.
A) Representative images of phalloidin-stained Parental, Selected and Flow sorted MDA MB 231 cells treated with Cytochalasin D or DMSO. Images were taken on a Zeiss 710 confocal microscope. Scale bar 10 µm. B) Graph depicts mean (± SD) Young's modulus measured for Parental cells treated with DMSO or Cytochalasin D. Data represent individual cells from n = 1 experiment. Statistical significance determined by Kruskal - Wallis followed by Dunn's multiple comparison test.

5.2.3 Selected MDA MB 231 cells have fewer focal adhesions compared to Parental and Flow Sorted MDA MB 231 cells

Having identified a disorganised actin organisation in Selected MDA MB 231 cells and more aligned actin fibres in Parental and Flow sorted MDA MB 231 cells, the assembly of focal adhesion (FA) complexes was investigated next. Focal adhesions provide a contact between the actin cytoskeleton and the external environment through the interaction of transmembrane proteins, such as integrins, with their extracellular ligands, and intracellular protein complexes linked to the actin cytoskeleton (Burridge and Guilluy 2016). In order to visualise focal adhesions, cells were fixed and stained with pFAK antibody and subsequently visualized on a Zeiss 710 confocal microscope. The images revealed that Selected MDA MB 231 cells had fewer and less pronounced focal complexes relative to Parental and Flow sorted MDA MB 231 cells, which were characterized by more mature and larger focal assemblies (Figure 5-4A). The number of focal adhesions complexes were counted using ImageJ. Number of FA was counted per cell. The average number of focal adhesions per group was counted per cell and then normalized to the cell area, which was determined from Operetta High Content Imaging System. This revealed that Selected MDA MB 231 cells had significantly fewer focal adhesions per cell and per cell area compared to Parental and Flow sorted MDA MB 231 cells (Figure 5-4B). In terms of anti-pFAK staining, it is predominantly used for detection of tension differences. In order to reveal more differences in number of focal adhesions, antibodies against paxilin or talin could be used.

A

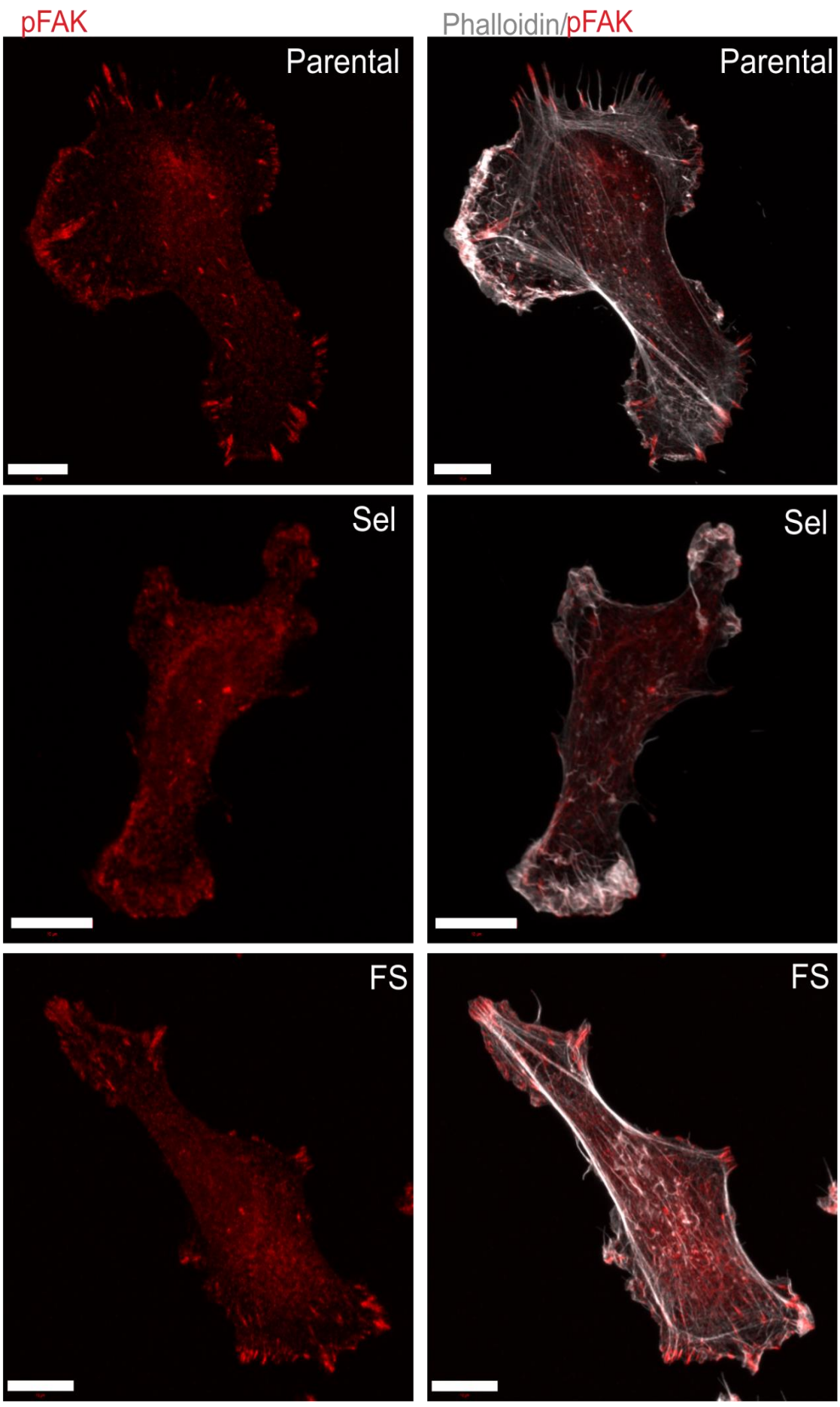

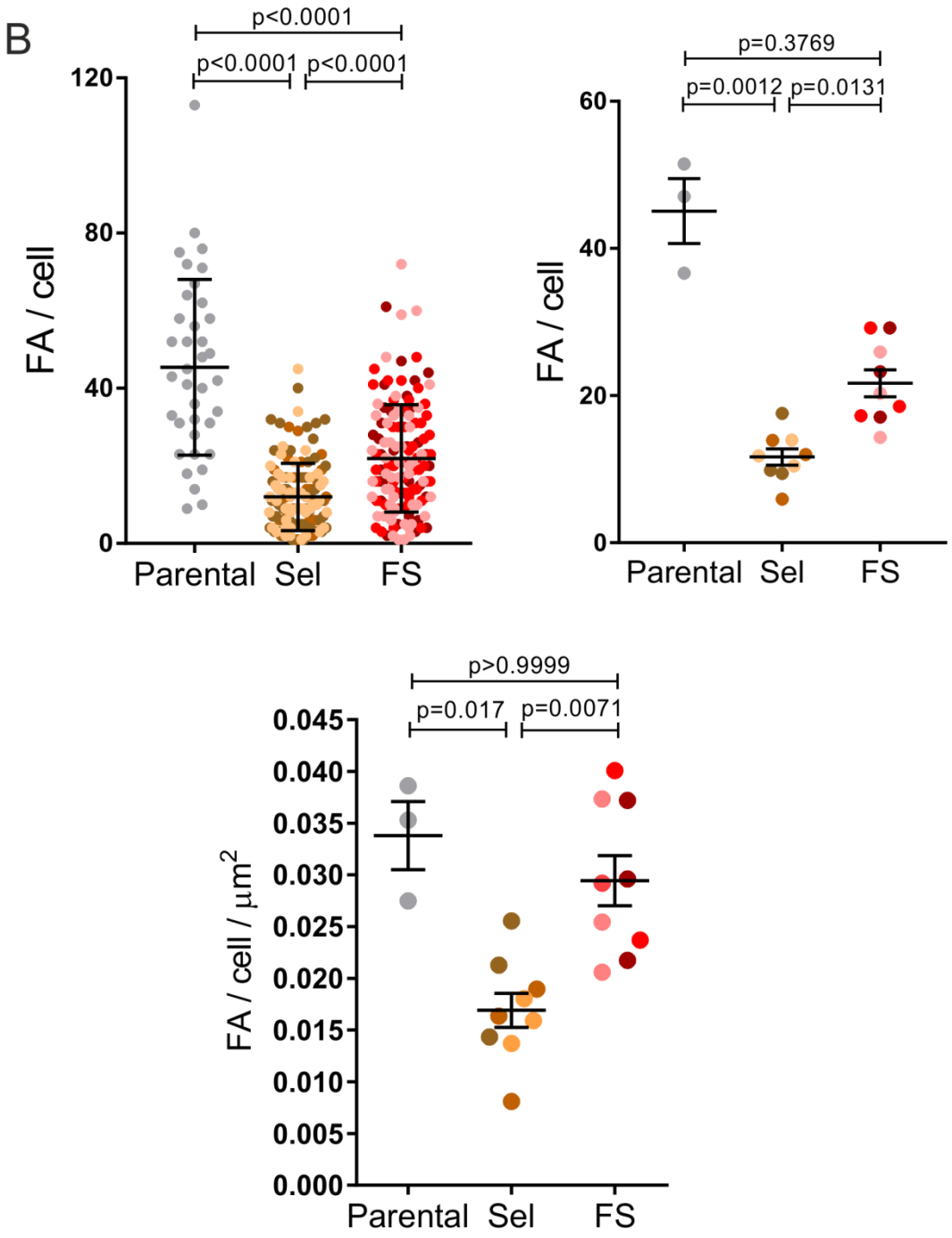

Figure 5-4 Selected MDA MB 231 cells have fewer focal adhesions relative to Parental and Flow sorted MDA MB 231 cells.

A) Representative images of pFAK-stained focal adhesions and phalloidin-stained F-actin for Parental, Selected and Flow sorted MDA MB 231 cells. Scale bar 10 µm. B) Top panel – left graph depicts focal adhesions per individual cell for Parental, independent Selected and independent Flow sorted MDA MB 231 cells. Data depicts individual cells pooled from n = 3 independent experiments, with mean (± SD) indicated. Right graph depicts mean (± SEM) focal adhesions per cell (n = 12 – 15 cells per experiment) for Parental, independent Selected and independent Flow sorted MDA MB 231 cells. Data from n = 3 independent experiments. Bottom panel – mean (± SEM) focal adhesions per cell per mean cell area (n = 12 – 15 cells per experiment) for Parental, independent Selected and independent Flow sorted MDA MB 231 cells. Data pooled from n = 3 independent experiments. Statistical significance determined by Kruskal - Wallis followed by Dunn's multiple comparison test.

5.2.4 No difference in membrane fluidity between Parental, Selected and Flow sorted MDA MB 231 cells

Given the possibility that the decreased cell stiffness of Selected MDA MB 231 cells could be due to changes in membrane fluidity, the lateral membrane diffusion of NBD-C6-sphingomyelin in cells was measured using the Fluorescence Recovery after Photobleaching method (FRAP). NBD-C6-sphingomyelin is a probe that fluorescently labels membrane fatty acid phospholipids, with excitation of the NBD group at 460 nm and emission at 534 nm (Klein, Pillot et al. 2003). In brief, a small portion of fluorescently labelled cell membrane is photobleached and then the recovery of fluorescence is imaged over time. Based on the normalized recovery curves, three parameters can be obtained: the half time ($t_{1/2}$), which is the time it takes for the fluorescence intensity to recover to half of the plateau level; immobile fraction, which is a fraction of molecules that cannot exchange between bleached and nonbleached regions; and mobile fraction, which is the fraction of recovered fluorescence.

In order to perform the experiment, cells were seeded in the glass bottom dishes and incubated for 24 hours, the next day they were stained with 4 μM NBD-C6-sphingomyelin for 10 minutes at room temperature, subsequently washed twice with HBSS medium and then imaged on the fluorescent microscopy (Zeiss 880 confocal microscopy). Bleaching was performed on a cell apical membrane (Figure 5-5A). Cells were imaged for 10 scans prior to bleaching, and then the bleaching was performed for five successive scans and then imaging of the cells for 105 scans. Data analysis was performed using Easy FRAP software. The results revealed that there were no differences in $t_{1/2}$ and mobile fraction between Parental, independent Selected and independent Flow sorted MDA MB 231 cells (Figure 5-5B,C) suggesting that there were no difference in membrane fluidity between the cell lines.

A

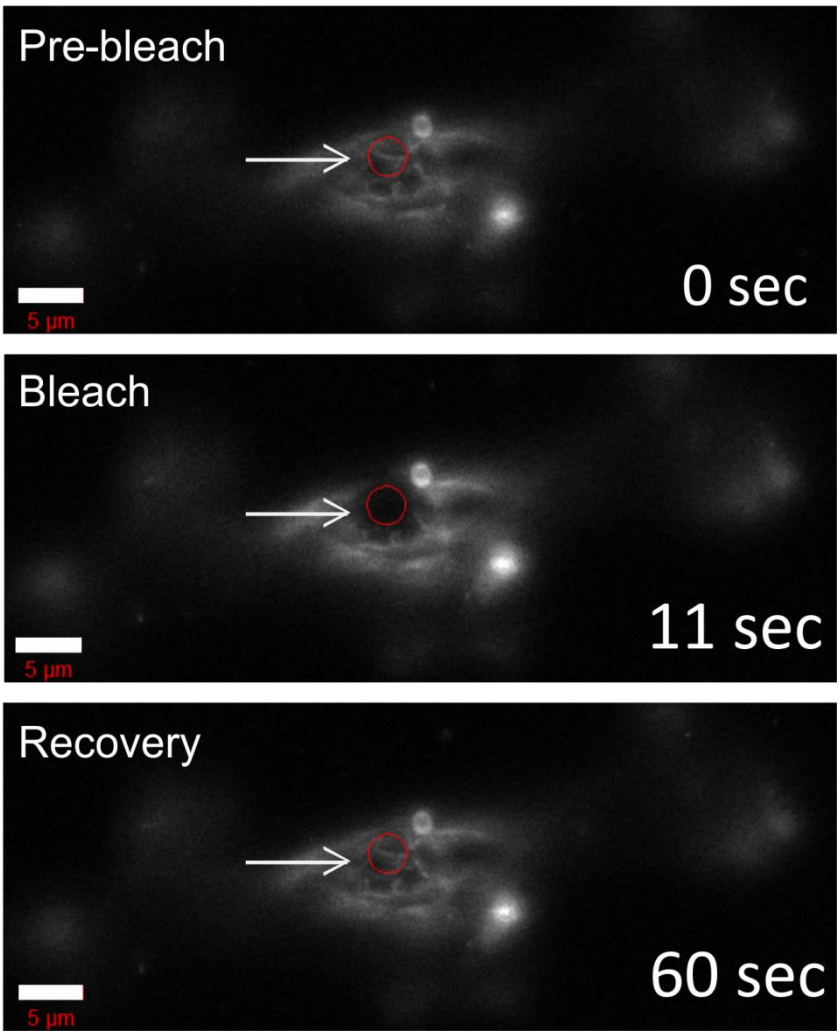

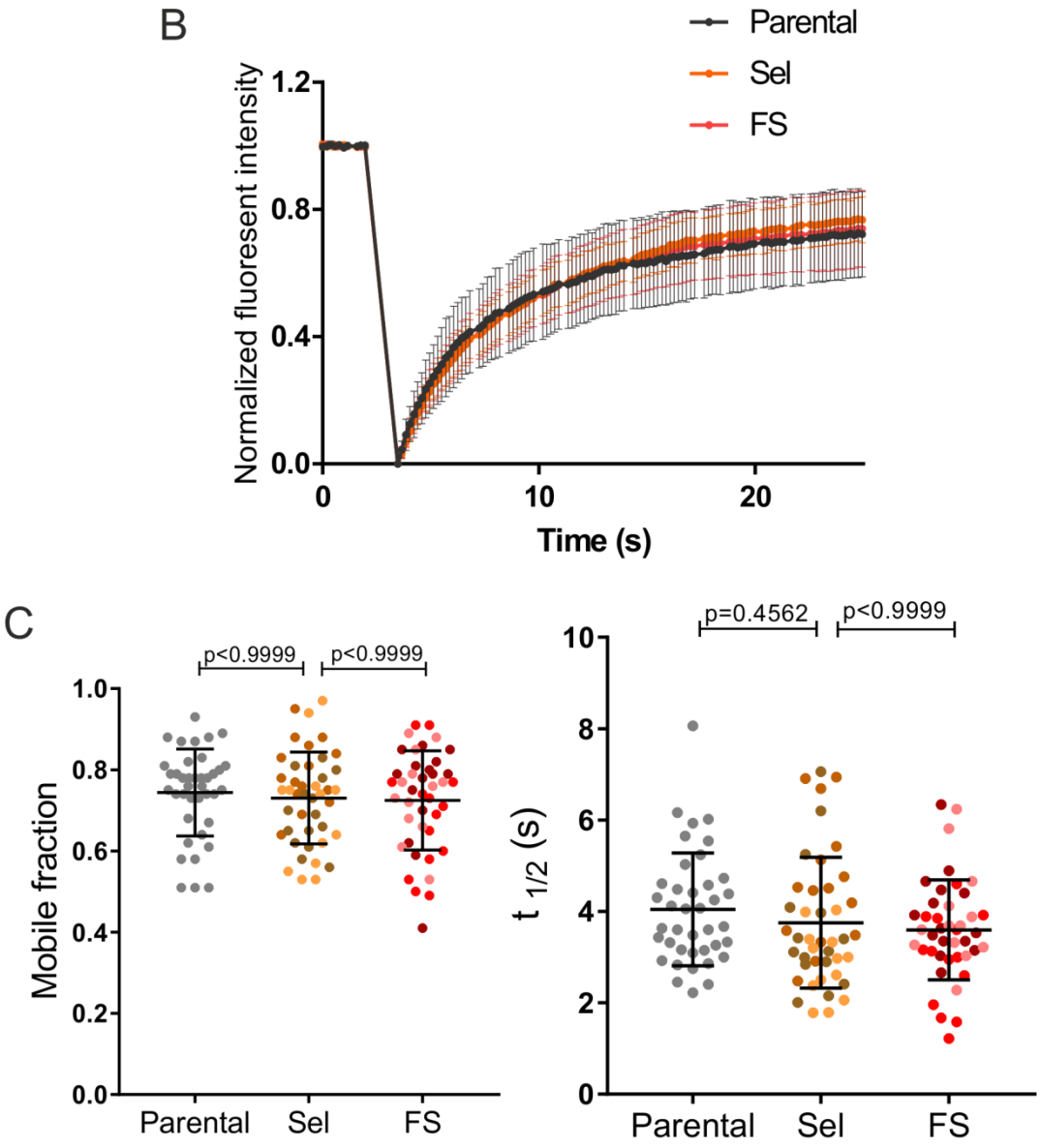

Figure 5-5 No difference in membrane fluidity between Parental, Selected and Flow sorted MDA MB 231 cells.

A) Representative images of a FRAP experiment. Cell before (0 seconds) and just after bleaching (11 and 16 seconds). White arrow indicates a bleached area on the apex of the cell. Scale bar 5 µm. B) Example of FRAP analyses curves from Parental, Selected and Flow sorted cells. C) Left graph represents mean (± SD) mobile fraction for Parental, independent Selected and independent Flow sorted cell populations. Right graph represents mean half time (± SD) for Parental, independent Selected and independent Flow sorted cell populations. Data represent individual cells pooled from n = 3 independent experiments. Statistical significance determined by Kruskal - Wallis followed by Dunn's multiple comparison test.

5.2.5 Selected MDA MB 435 cells have reduced cell stiffness, more isotropic cytoskeleton alignment and fewer focal adhesions compared to Parental MDA MB 435 cells

After finding that Selected MDA MB 231 cells had reduced cell rigidity, next, the stiffness of MDA MB 435 cells was investigated. The experiment was performed as described for MDA MB 231 cells. The results revealed that Selected MDA MB 435 cells had significantly reduced Young's modulus relative to Parental MDA MB 435 cells, suggesting that Selected MDA MB 435 cells were more elastic (Figure 5-6A).

In order to determine whether cell stiffness differences could be an effect of cytoskeleton disorganisation, phalloidin-stained cells were visualised by Zeiss 880 confocal microscopy and actin alignment was measured using an ImageJ plug-in Firbil Tool. The experiments were performed as detailed for MDA MB 231 cells. Imaging F-actin revealed cytoplasmic fibrillary structures in Parental MDA MB 435 cells while Selected MDA MB 435 cells primarily had cortical F-actin (Figure 5-6B). Using Fibril Tool to quantify F-actin anisotropy revealed that Selected MDA MB 435 cells had significantly decreased actin anisotropy relative to Parental MDA MB 435 cells (Figure 5-6C).

Having shown changes in actin organisation between Parental and Selected MDA MB 435 cells, focal adhesion complexes were also visualized and counted as described for MDA MB 231 cells. From this, I found that Selected MDA MB 435 cells had also fewer mature and smaller focal complexes relative to Parental MDA MB 435 cells (Figure 5-7). Moreover, by quantifying the number of focal complexes, I found that Selected MDA MB 435 cells had significantly fewer focal adhesions per cell and per cell area compared to Parental MDA MB 435 cells (Figure 5-7).

5.2.6 No difference in membrane fluidity between Parental and Selected MDA MB 435 cells

Membrane fluidity measurements for Parental and independent Selected MDA MB 435 cells were performed as described for MDA MB 231 cells. The results showed that there were no differences in half time and mobile fraction between

Parental and independent Selected MDA MB 435 cells indicating that there were no differences in membrane fluidity between the cell lines (Figure 5-8).

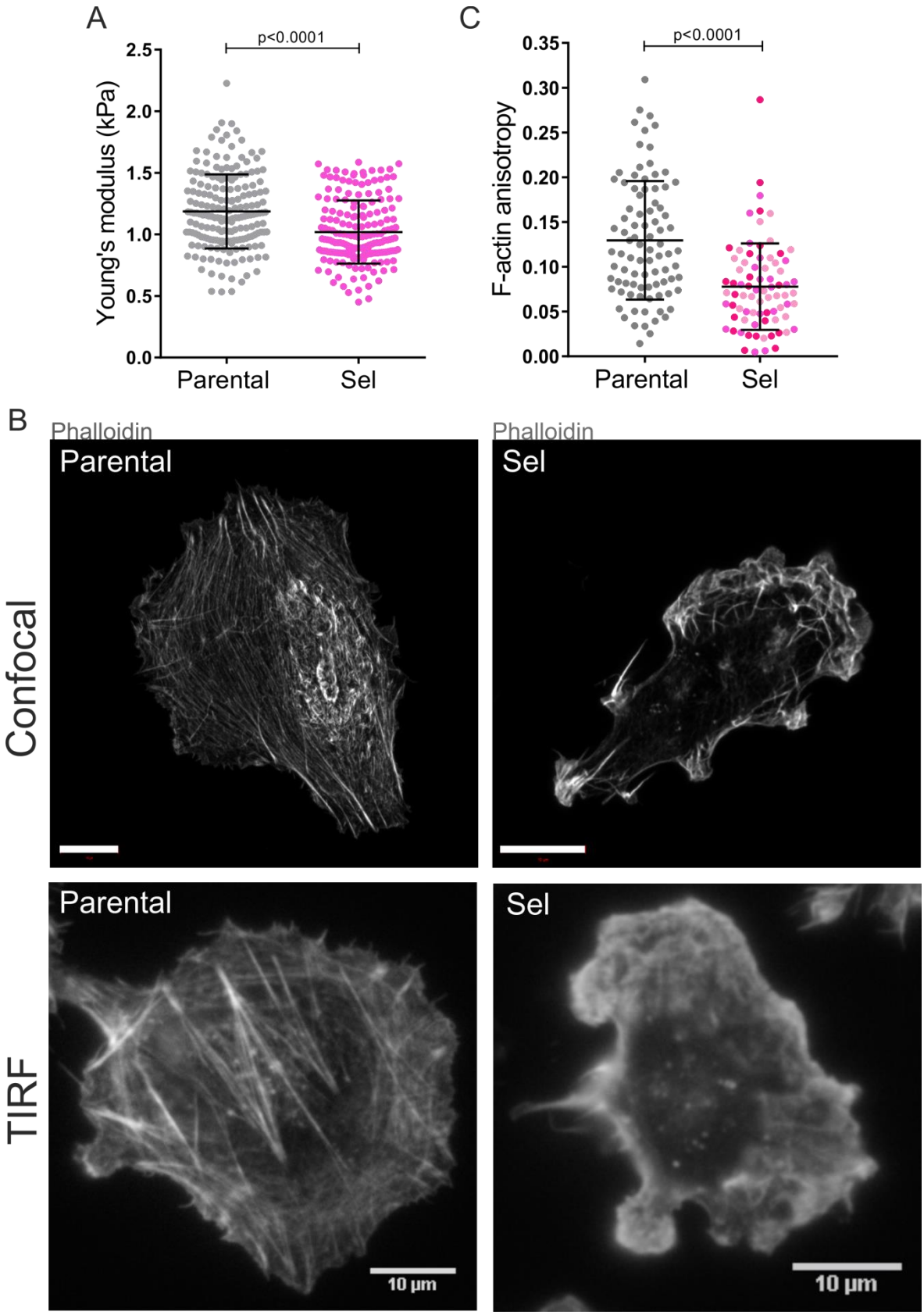
A
p<0.0001
Young's modulus (kPa)
2.5
2.0
1.5
1.0
0.5
0.0
Parental
Sel
C
p<0.0001
F-actin anisotropy
0.35
0.30
0.25
0.20
0.15
0.10
0.05
0.00
Parental
Sel
B
Phalloidin
Phalloidin
Confocal
Parental
Sel
TIRF
Parental
Sel
10 µm
10 µm

Figure 5-6 Selected MDA MB 435 cells have decreased cell stiffness and F-actin anisotropy relative to Parental MDA MB 435 cells.
A) Graph depicts mean (± SD) Young's modulus measured for Parental and Selected MDA MB 435 cells. Young's modulus was determined by AFM. Data represent individual cells pooled from n = 2 independent experiments. B) Top panel - representative maximum projection images of phalloidin-stained cells showing F-actin structure for Parental and Selected MDA MB 435 cells. The images were taken on a Zeiss 880 confocal microscope. Scale bar 10 µm. Bottom panel - representative images of phalloidin-stained cells showing cortical actin structure for Parental and Selected MDA MB 435 cells. The images were taken by TIRF microscopy. C) Graph depicts mean (± SD) F-actin anisotropy for Parental and independent Selected MDA MB 435 cell populations. Data represent individual cells pooled from n = 3 independent experiments. Statistical significance determined by Mann - Whitney test.

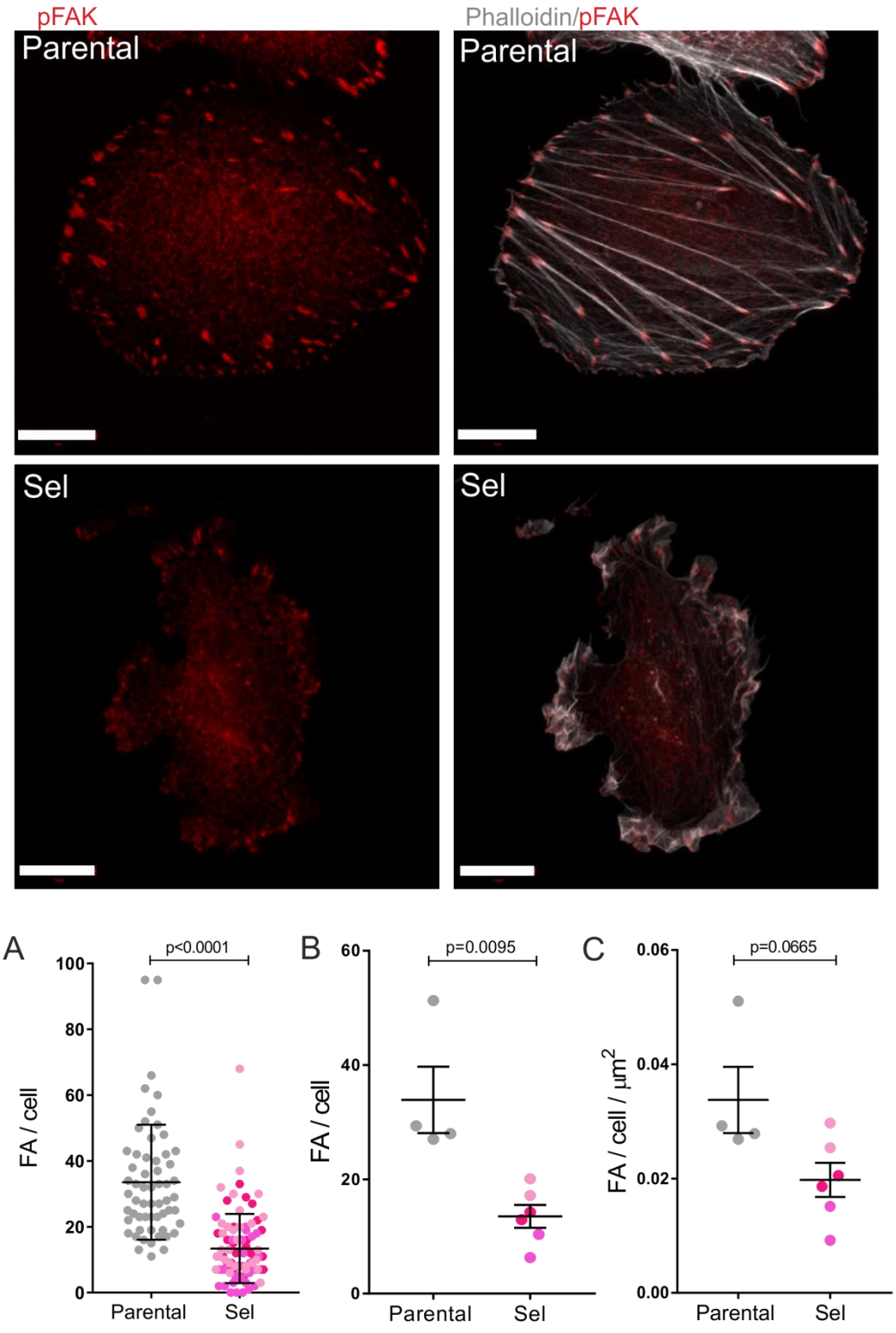

Figure 5-7 Selected MDA MB 435 cells have fewer focal adhesions relative to Parental MDA MB 435 cells.

Representative images of pFAK-stained focal adhesions and phalloidin-stained F-actin for Parental and Selected MDA MB 435 cells. Scale bar 10 µm. A) Focal adhesions per individual cell for Parental and independent Selected MDA MB 435 cells. Data depicts individual cells pooled from n = 3 independent experiments, with mean (± SD) indicated. B) Mean (± SEM) focal adhesions per cell (n = 12 – 15 cells per experiment) for Parental and independent Selected MDA MB 435 cells. Data from n = 3 independent experiments. C) Mean (± SEM) focal adhesions per cell per cell area (n = 12 – 15 cells per experiment) for Parental and independent Selected MDA MB 231 cells. Data pooled from n = 3 independent experiments. Statistical significance determined by Mann - Whitney test.

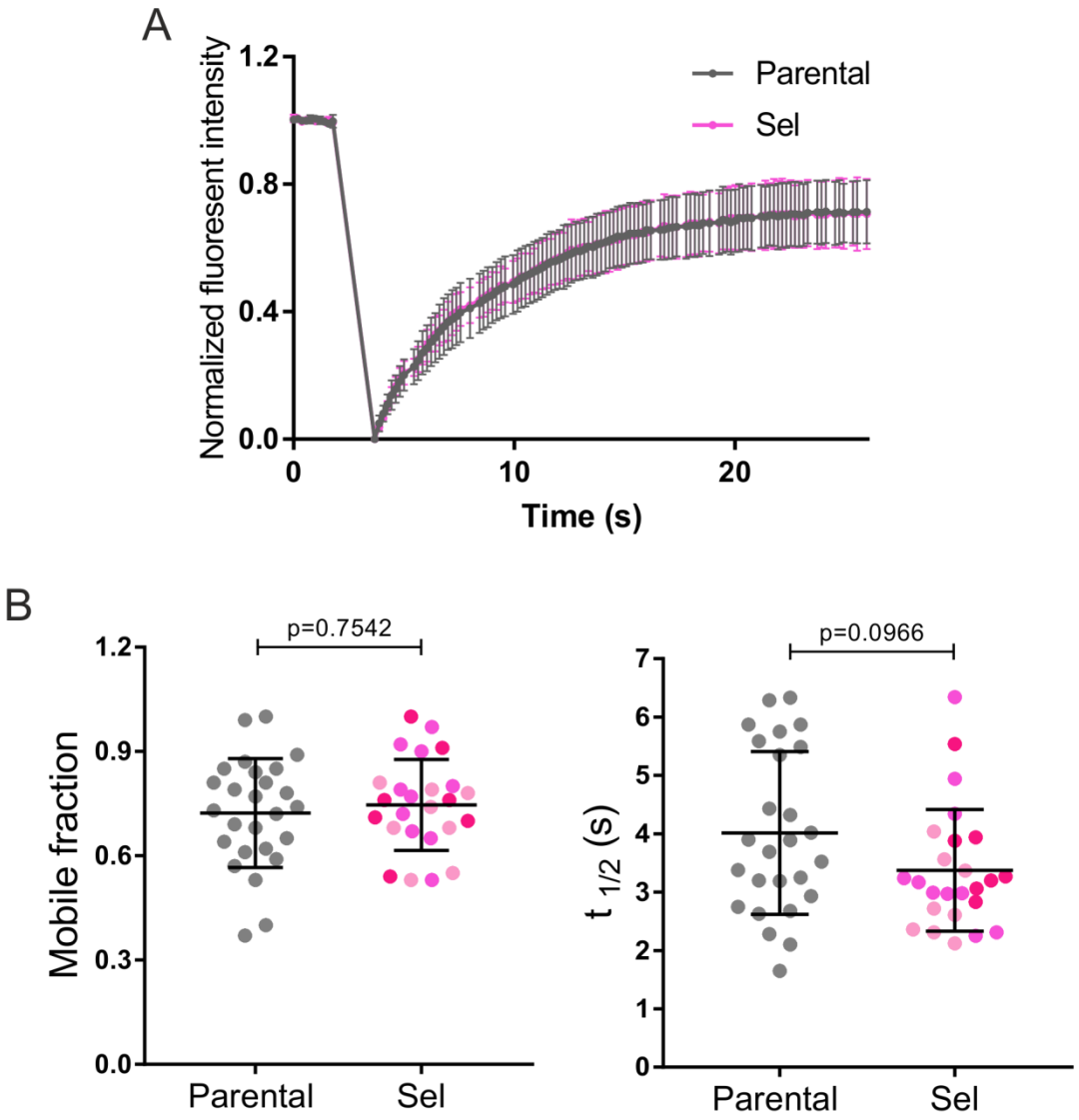

Figure 5-8 No difference in membrane fluidity between Parental and Selected MDA MB 435 cells.

A) Examples of FRAP analyses curves from Parental and Selected MDA MB 435 cells. B) Left graph represents mean (± SEM) mobile fraction for Parental and independent Selected cell populations. Right graph represents mean (± SD) half time for Parental and independent Selected MDA MB 435 cell populations. Data represent individual cells pooled from n = 3 independent experiments. Statistical significance determined by Mann - Whitney test.

5.2.7 Selected and Flow sorted MDA MB 231 cells are characterized by more elongated and less irregular cell shapes relative to Parental MDA MB 231 cells

Human cells adopt many different cell shapes which closely relate to their tissue specific functions; for example, nerve cells have many thin extensions (dendrites, axons) which allow them to send and receive electrical signals, while red blood cells have biconcave shapes that maximise oxygen absorption. In addition, embryonic non-migratory epithelial cells have the potential to convert into motile mesenchymal cells needed for tissue organisation; hence cell morphological plasticity plays an important role in organism development (Alizadeh, Lyons et al. 2016). Additionally, changes in cell shapes have been associated with disease states; for example, it has been shown that during the progression from non-invasive to invasive phenotypes, cancer cells undergo a transition from tightly packed to spindle-like cell morphology, a process known as epithelial to mesenchymal transition (EMT) (Ding, Zhang et al. 2013). The cytoskeleton is known to be the main determinant of cell shape. Due to the forces generated during actin polymerisation, acto-myosin contractility and adhesion, it generates hydraulic pressure which contributes to cell shape determination (Pellegrin and Mellor 2007; Gauthier, Fardin et al. 2011). Due to observed alterations in actin organisation and cell elasticity in Selected MDA MB 231 and Selected MDA MB 435 cells, I decided to undertake detailed analysis of cellular morphology, hence Operetta High Content Imaging System was utilised.

Cellular morphology characteristics were assessed using the Operetta High Content Imaging System. 10,000 cells were seeded in each well of black 96-well plates. Following 24-hour incubation, cells were fixed and stained with DAPI and Whole Cell Stain (WCS). Cell shapes were analysed using Columbus™ Image Data Storage and Analysis System, and an enhanced set of algorithms known collectively as STAR system. The software was trained to recognise different populations of cell shapes by selecting examples of each class. Three different cell shapes were assessed: regular, characterized by a rounded morphology; irregular, characterized by many protrusions extending at different directions; elongated cells, characterized with spindle-like shapes (Figure 5-9). The cell morphology analysis revealed that Selected and Flow sorted MDA MB 231 cells

had more elongated and regular shaped cells, and fewer irregular cell shapes relative to Parental MDA MB 231 cells (Figure 5-9B).

5.2.8 Selected MDA MB 231 cells migrated with increased speed and further distance compared to Parental and Flow sorted MDA MB 231 cells

In order to examine single cell motility parameters such as velocity, accumulated and Euclidean distances, an individual cell migration assay was utilised. To perform the assay, 5,000 cells were seeded on a 12-well plate per well. Next day, the plate was placed in Nikon TE 2000 Time Lapse Microscope and images were acquired every 15 minutes for 22 hours. Individual cells from each Parental, independent Selected and independent Flow sorted MDA MB 231 cell population were tracked for 45 frames excluding dividing cells using the Manual tracking tool in ImageJ. Migration velocity, accumulated distance and Euclidean distance were measured using the Chemotaxis plug-in in ImageJ. From this experiment, I discovered that Selected MDA MB 231 cells migrated with increased velocity, migrated with further accumulated and Euclidean distances as individual cells compared to Parental and independent Flow sorted MDA MB 231 cells (Figure 5-10).

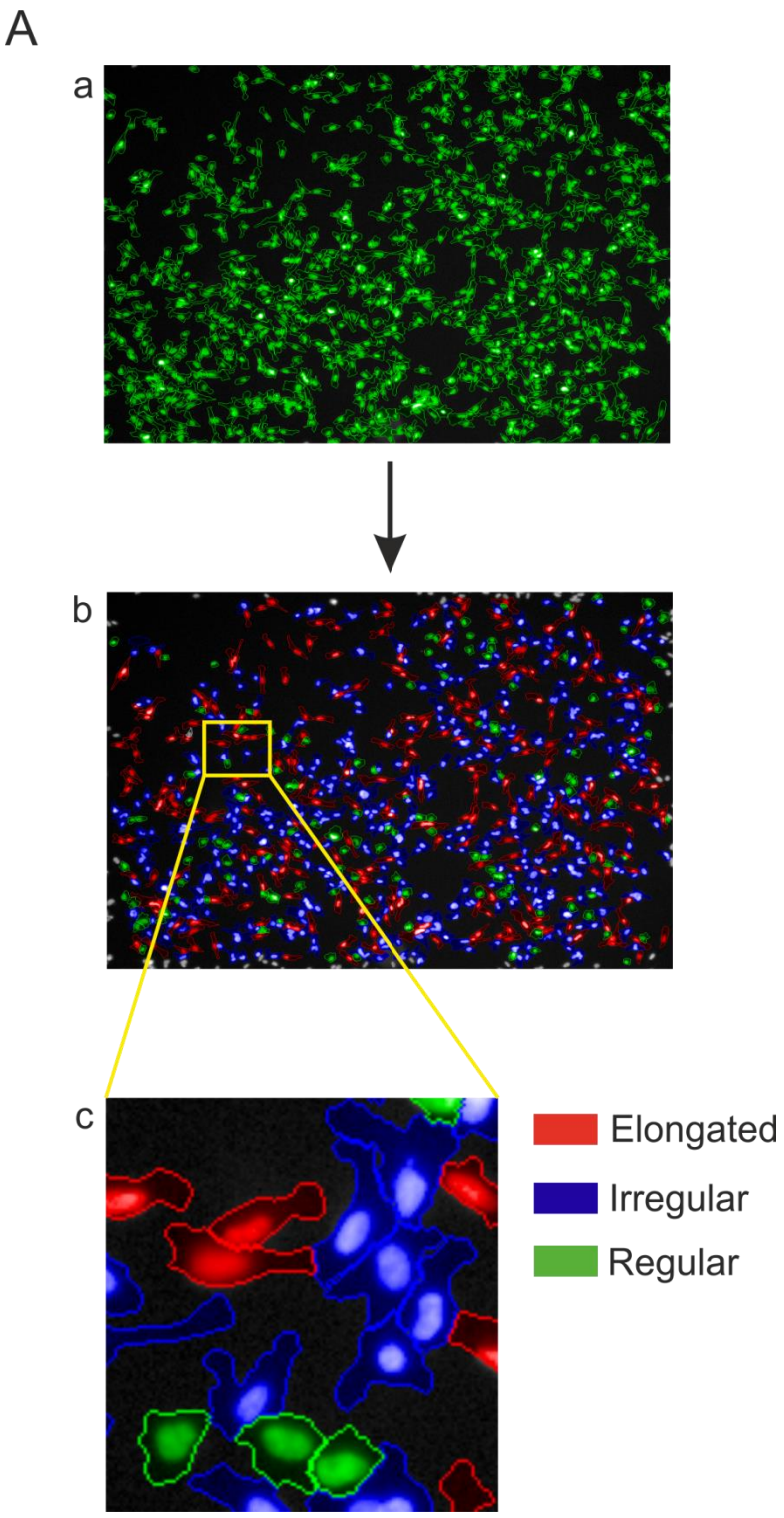
A
a
b
c
Elongated
Irregular
Regular

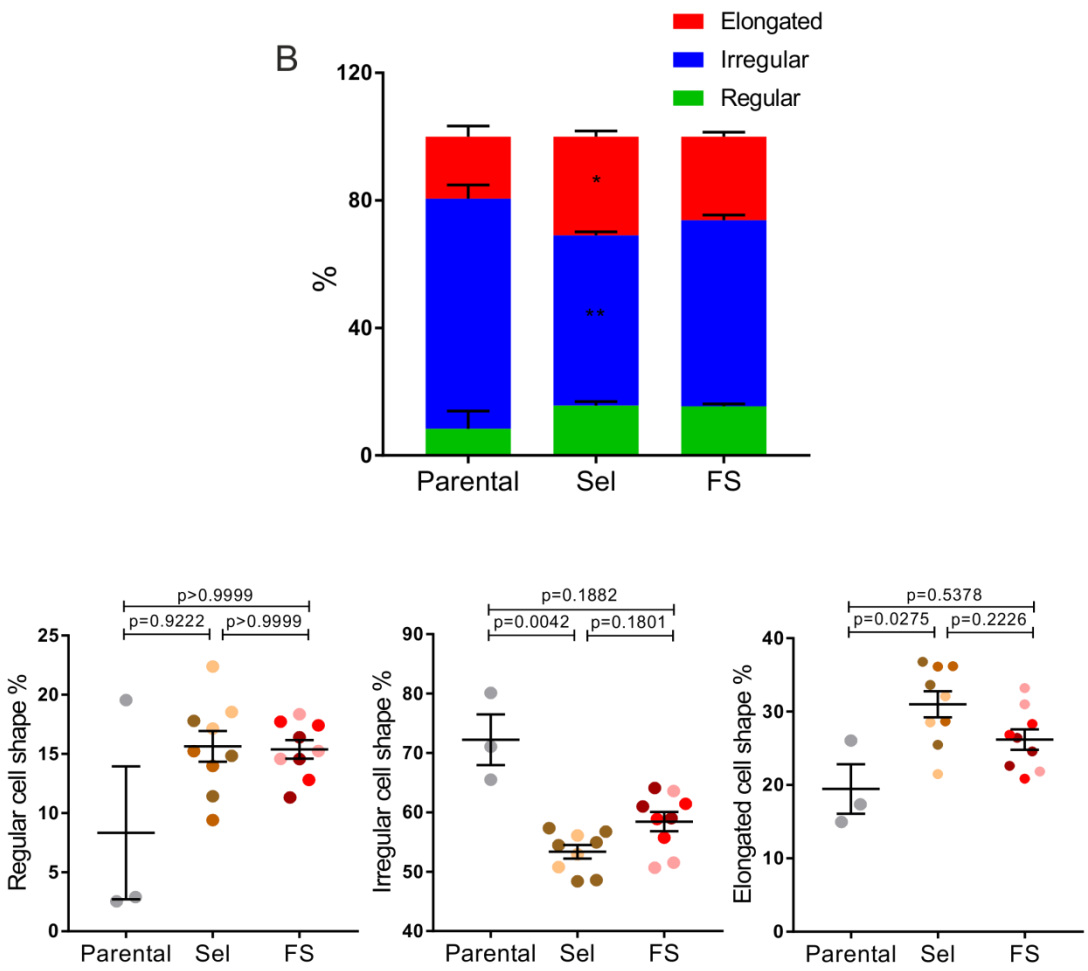

Figure 5-9 Cell shape analysis reveals that Selected and Flow sorted MDA MB 231 cells characterize with more regular and elongated, and fewer iregular cell shapes relative to Parental MDA MB 231 cells.

A) Cell morphological profiling, a) image shows Whole Cell Stain (WSC)-stained cells which were recognised by Columbus™ Image Data Storage and Analysis System, b) image depicts software training step where three cell shapes (irregular, regular and elongated) were chosen, c) image depicts three different cell shapes which were recognised by the software. B) Top panel - graph represents a mean percentage (± SEM) of elongated, regular and irregular cell shapes within Parental, Selected and Flow sorted MDA MB 231 cell populations. Bottom panel - graphs represent a mean (± SEM) percentage of regular, irregular and elongated cell shape for Parental, independent Selected and independent Flow sorted MDA MB 231 cell populations. Each dot represents an average from n = 6 fields per well, from at least 200 cells per field. Data pooled from n = 3 independent experiments. Statistical significance determined by Kruskal - Wallis followed by Dunn's multiple comparison test (* = p=0.0275, ** = p=0.0042).

A

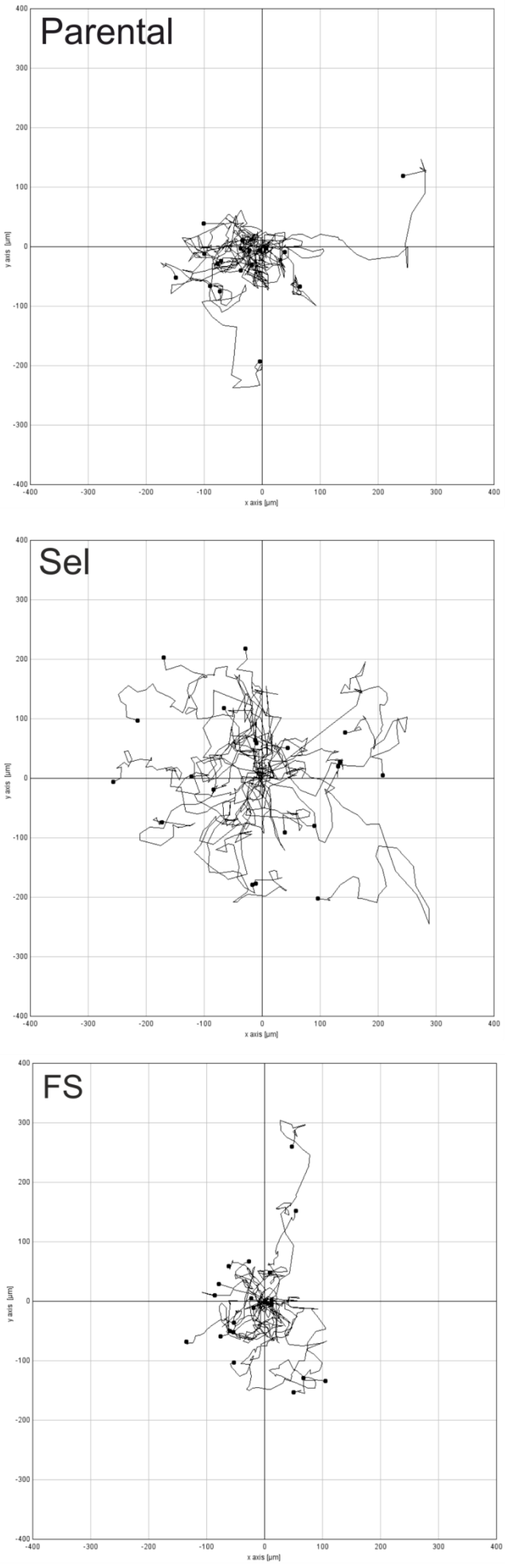
Parental
Sel
FS
y axis [µm]
x axis [µm]
400
300
200
100
0
-100
-200
-300
-400

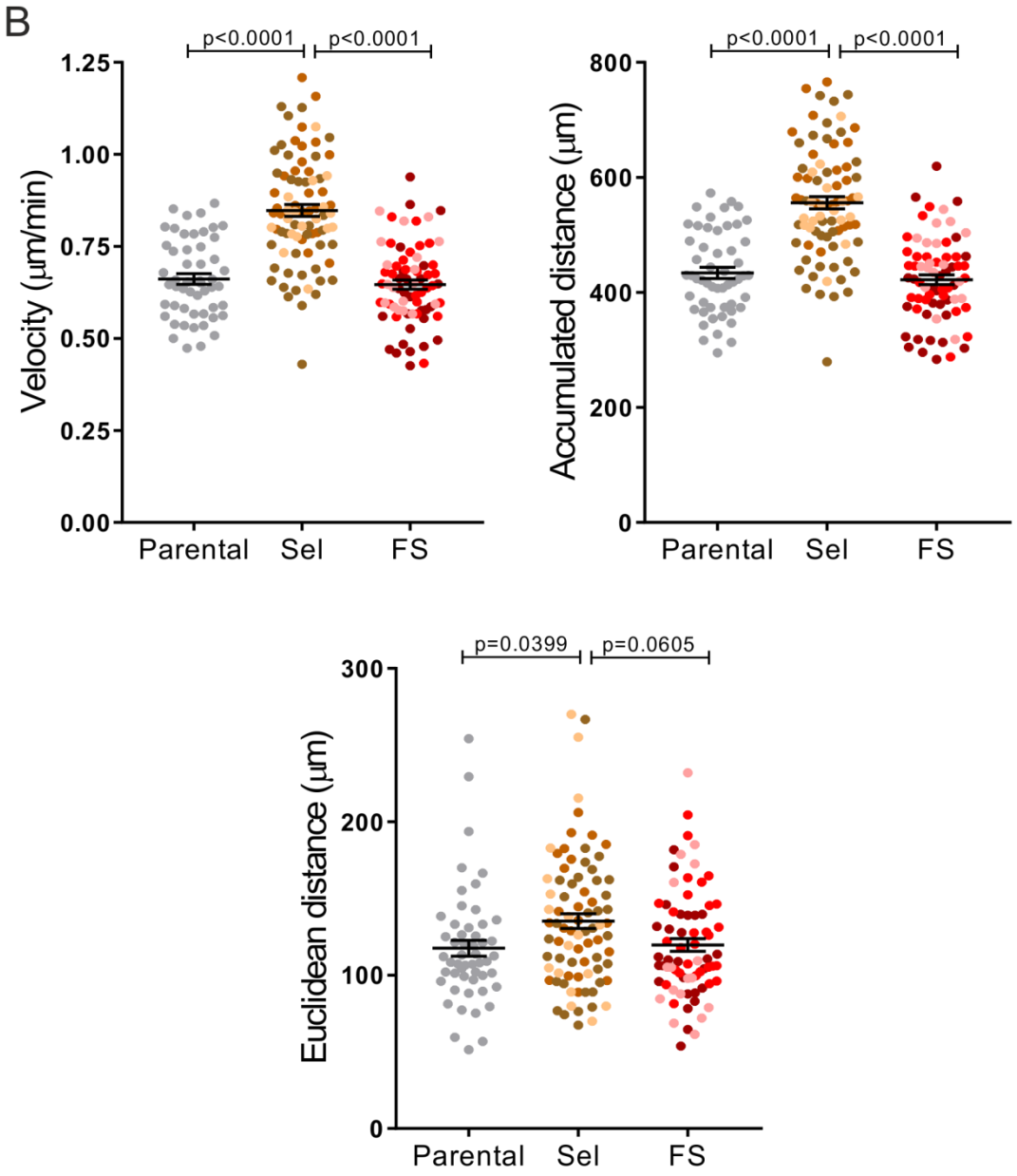

Figure 5-10 Selected MDA MB 231 cells migrate with increased velocity and travel further distances relative to Parental and Flow sorted MDA MB 231 cells when measured as individual cells.

A) Representative tracked plots for Parental, Selected and Flow sorted MDA MB 231 cells. Each track represents one cell. B) Top panel - left graph depicts mean velocity (± SEM) for Parental, independent Selected and independent Flow sorted MDA MB 231 cells. Right graph depicts mean (± SEM) accumulated distance for Parental, independent Selected and independent Flow sorted MDA MB 231 cells. Bottom panel - graph depicts mean (± SEM) Euclidean distance for Parental, independent Selected and independent Flow sorted MDA MB 231 cells. Each dot represents a mean of n ≥ 8 tracked cells. Data pooled from n ≥ 3 independent experiments. Statistical significance determined by Kruskal - Wallis followed by Dunn's multiple comparison test.

5.2.9 Selected MDA MB 231 cells have reduced cell spreading compared to Parental and Flow sorted MDA MB 231

In the next experiment, spreading properties of Parental Selected and Flow sorted cell populations using the xCelligence Real-Time Cell Analyzer (RTCA) system was investigated. The RTCA system is impendence-based and allows monitoring of cell spreading in real-time. Special plates called E-plates used in this assay have micro-electrodes integrated at the bottom of the plate that allow measurement of changes in electrical impendence across the plate due to cell spreading and a read out of this called cell index is reported. In order to perform the experiment, 10,000 cells were seeded per well and measurements were taken every 3 minutes for 12 hours. From this experiment, I found that Selected MDA MB 231 cells had significantly decreased cell spreading abilities compared to equivalently smaller Flow sorted cells and Parental MDA MB 231 cells. Due to significantly bigger size of Parental MDA MB 231 cells compared to Selected and Flow sorted MDA MB 231 cells, the measured spreading for Parental cells was much larger (Figure 5-11).

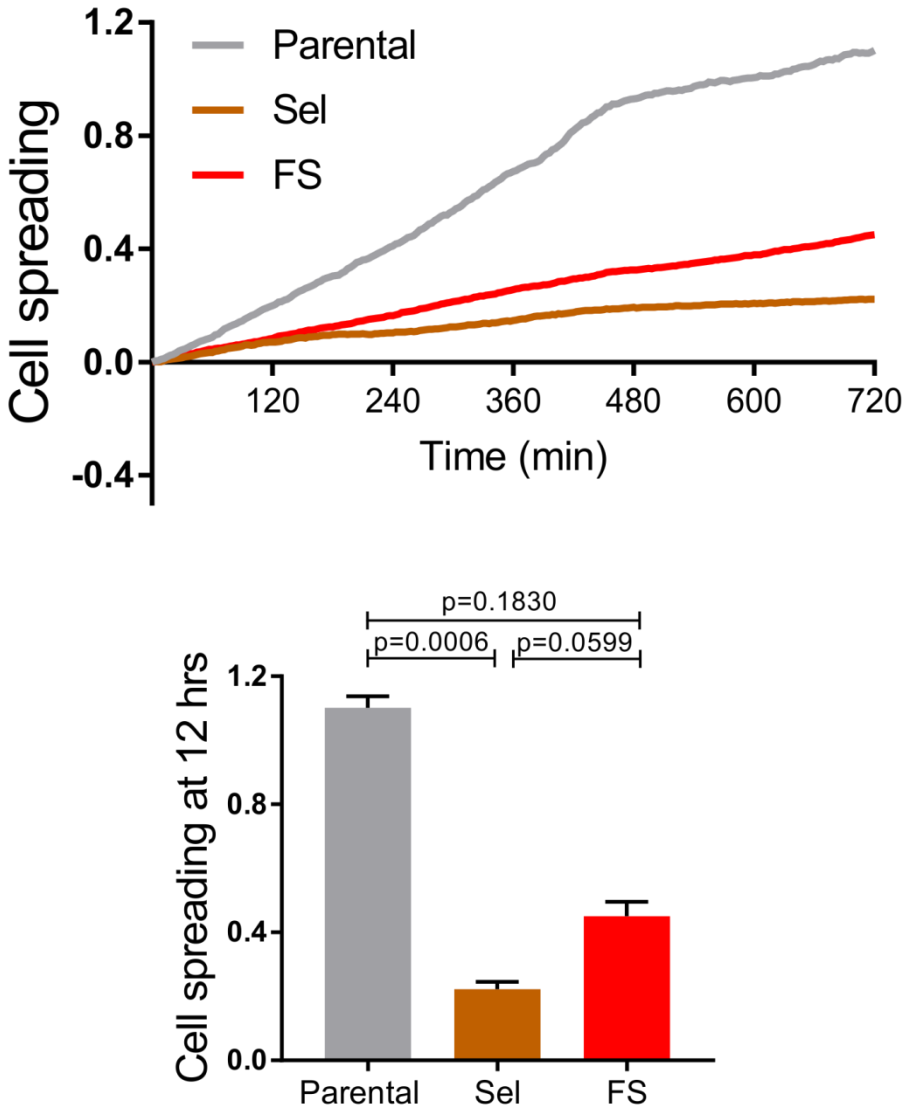

Figure 5-11 Selected MDA MB 231 cells spread less relative to Parental and Flow sorted MDA MB 231 cells.

Top graph depicts cell spreading for Parental, Selected and Flow sorted MDA MB 231 cells. The spreading was measured with the RTCA system. Bottom panel - graph depicts mean (± SEM) cell spreading at 12 hrs for Parental, Selected and Flow sorted MDA MB 231 cells. Data pooled from n = 2 independent experiments. Statistical significance determined by Kruskal - Wallis followed by Dunn's multiple comparison test.

5.2.10 Selected MDA MB 231 cells have reduced adhesion compared to Parental and Flow sorted MDA MB 231 cells

Having revealed decreased spreading properties of Selected MDA MB 231 cells, adhesion properties were explored next. Adhesion properties were investigated in two different experiments. In the first experiment, 40,000 cells per well of Parental, independent Selected and independent Flow sorted cells lines were seeded in 96-well plate and left to adhere for three hours in standard tissue culture conditions. Thereafter, non-adherent cells were washed away with PBS and cells that remained attached to the plate were measured using the CellTitre-Glo® Luminescent Cell Viability assay. The CellTitre-Glo method allowed determination of viable cells based on their ATP levels. From this experiment, decreased adhesive properties of Selected and Flow sorted MDA MB 231 compared to Parental MDA MB 231 cells were observed (Figure 5-12).

In the second experiment, dispase-based solution was used as a mild reagent for cell detachment. 300,000 cells of Parental, independent Selected and independent Flow sorted cells were seeded per well in a 12-well plate and left overnight in standard tissue culture conditions. Next, 500 µl of dispase solution was added to the plate and left for 5 minutes in the tissue culture incubator. Thereafter, 500 µl of cell suspension was removed and the number of detached cells was counted. 500 µl of disapse was added again to the plate followed by 15 minutes incubation at 37°C and subsequently the number of attached cells was counted. The percentage of attached cells was normalized to the total number of cells. From this experiment, I found that Selected and Flow sorted MDA MB 231 cells had decreased adhesion properties compared to Parental MDA MB 231 cells (Figure 5-12).

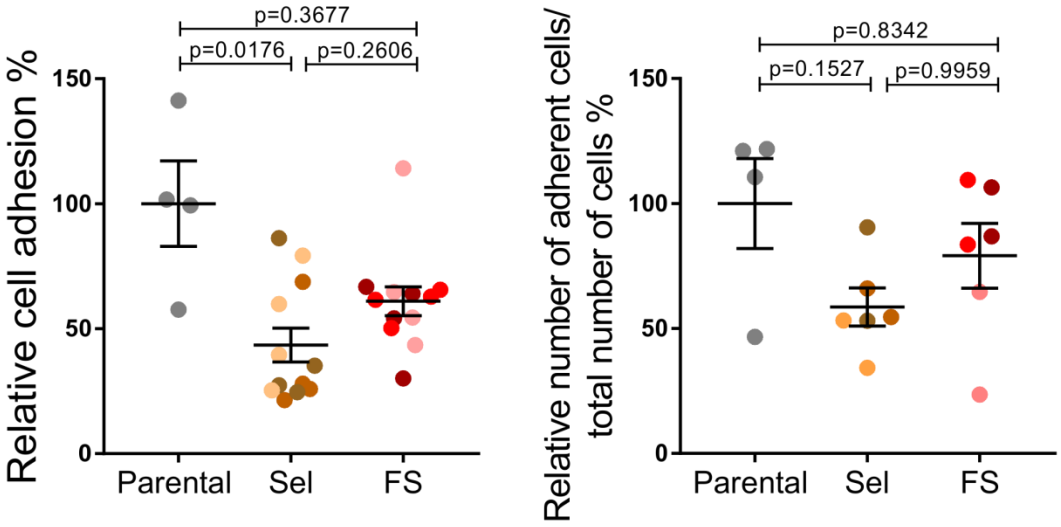

Figure 5-12 Selected and Flow sorted MDA MB 231 cells have reduced adhesion compared to Parental MDA MB 231 cells.

Left graph depicts mean (± SEM) percent of relative cell adhesion measured with CellTitre-Glo method for Parental, independent Selected and independent Flow sorted MDA MB 231 cell populations. Each dot represents an average value from n = 3 wells. Data pooled from n = 3 independent experiments. Right graph depicts mean (± SEM) percent of relative number of adherent cells measured with dispase detachment assay for Parental, independent Selected and independent Flow sorted MDA MB 231 cell populations. Each dot represents an average value from n = 3 wells. Data pooled from n = 3 independent experiments. Statistical significance determined by Kruskal - Wallis followed by Dunn's multiple comparison test.

5.2.11 Selected MDA MB 435 cells are characterized by more irregular and elongated, and fewer regular cell shapes relative to Parental MDA MB 435 cells

Cellular morphology characteristics were assessed by applying Operetta High Content Imaging System as described in detail for MDA MB 231 cells. The cell morphology analysis revealed that Selected MDA MB 435 cells were characterized by more irregular and elongated, and fewer regular cell shapes relative to Parental MDA MB 435 cells (Figure 5-13).

5.2.12 Selected MDA MB 435 cells migrate with increased speed and migrate further distance compared to Parental MDA MB 435 cells

After discovering that Selected MDA MB 231 cells migrated with increased speed and further distance compared to Parental and Flow sorted MDA MB 231 cells, individual migration assay was undertaken for MDA MB 435 cells. From this experiment, I discovered that Selected MDA MB 435 cells migrated with significantly increased velocity and further distance relative to Parental MDA MB 435 cells (Figure 5-14).

5.2.13 Selected MDA MB 435 have reduced spreading compared to Parental MDA MB 435 cells measured by the xCelligence system

In order to study cell spreading properties of MDA MB 435 cells, an RTCA system was used as described for MDA MB 231 cells. The results demonstrated that Selected MDA MB 435 cells had significantly diminished spreading properties relative to Parental MDA MB 435 cells (Figure 5-15).

5.2.14 Selected MDA MB 435 cells have reduced adhesion compared to Parental MDA MB 435 cells

After establishing that Selected MDA MB 435 cells had reduced spreading abilities compared to Parental MDA MB 435 cells, further experiments to investigate cells adhesiveness were undertaken. Cell adhesion assay and dispase-based assay were utilised as described in details for MDA MB 231 cells. The results from both experiments revealed that Selected MDA MB 435 cells had significantly reduced adhesiveness compared to Parental MDA MB 435 cells (Figure 5-16).

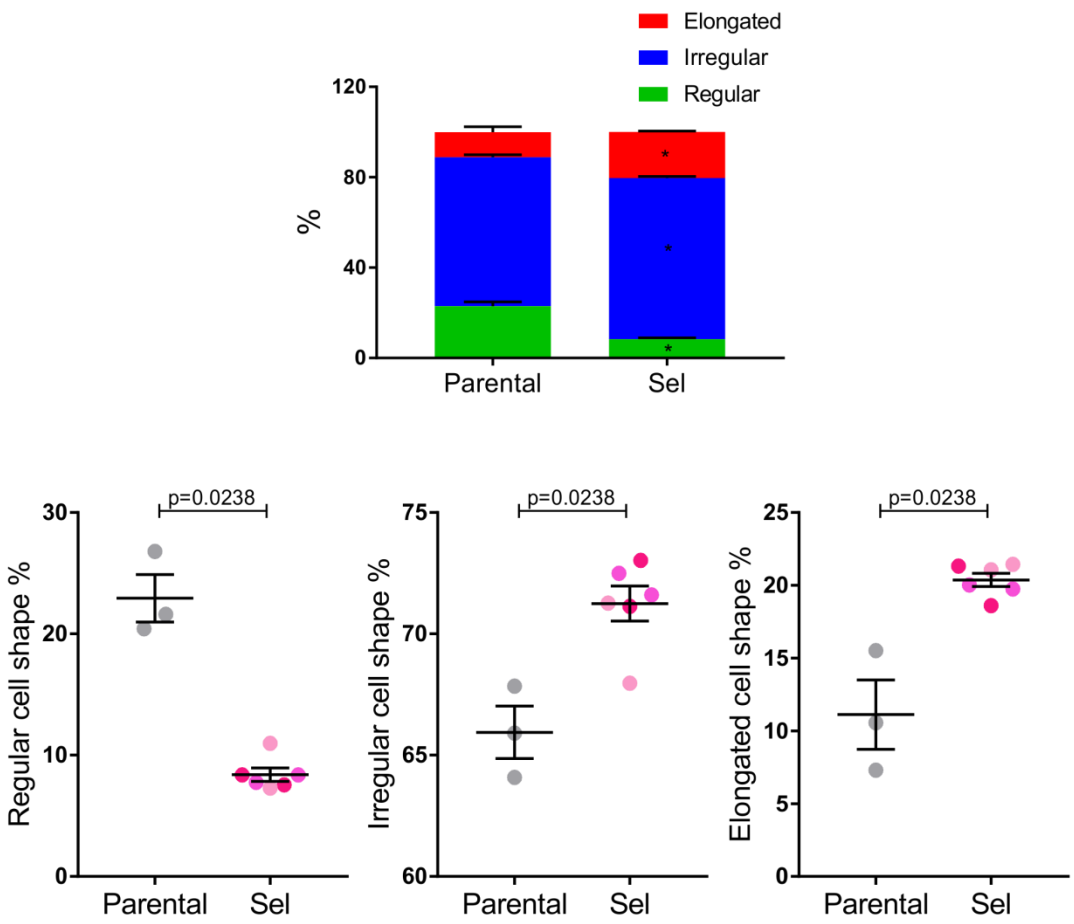

Figure 5-13 Cell shape analysis reveals that Selected MDA MB 435 cells were characterized by more irregular and elongated, and fewer regular cell shapes compared to Parental MDA MB 435 cells.

Top panel - graph represents a mean percentage (± SEM) of elongated, regular and irregular cell shapes for Parental and Selected MDA MB 435 cell populations. Bottom panel - graphs represent a mean (± SEM) percentage of regular, irregular and elongated cell shape for Parental and independent Selected MDA MB 435 cells. Each dot represents an average from n = 6 fields per well, from at least 200 cells per field. Data pooled from n = 3 independent experiments. Statistical significance determined by Mann - Whitney test (* = p=0.0238).

A

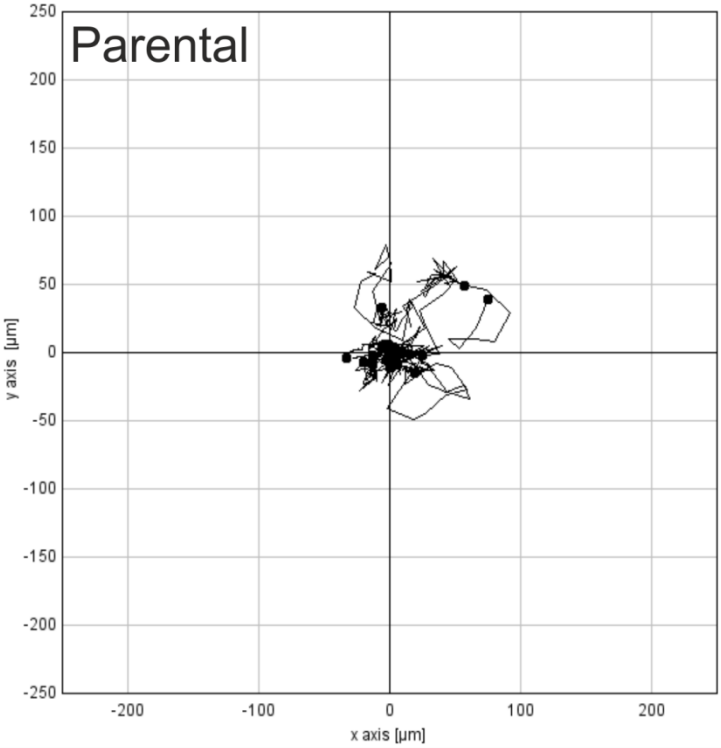
Parental
250
200
150
100
50
0
-50
-100
-150
-200
-250
y axis [µm]
-200
-100
0
100
200
x axis [µm]

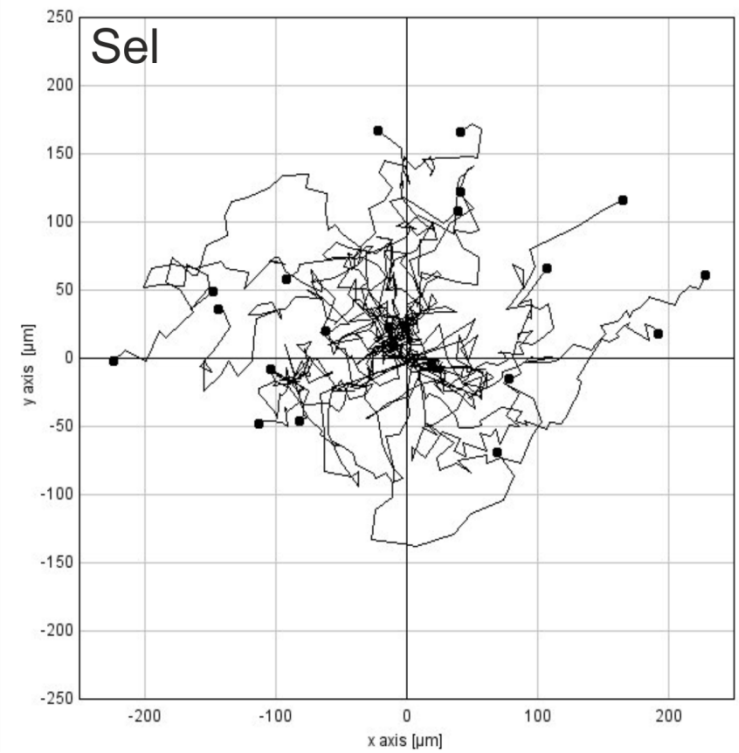
Sel
250
200
150
100
50
0
-50
-100
-150
-200
-250
y axis [µm]
-200
-100
0
100
200
x axis [µm]

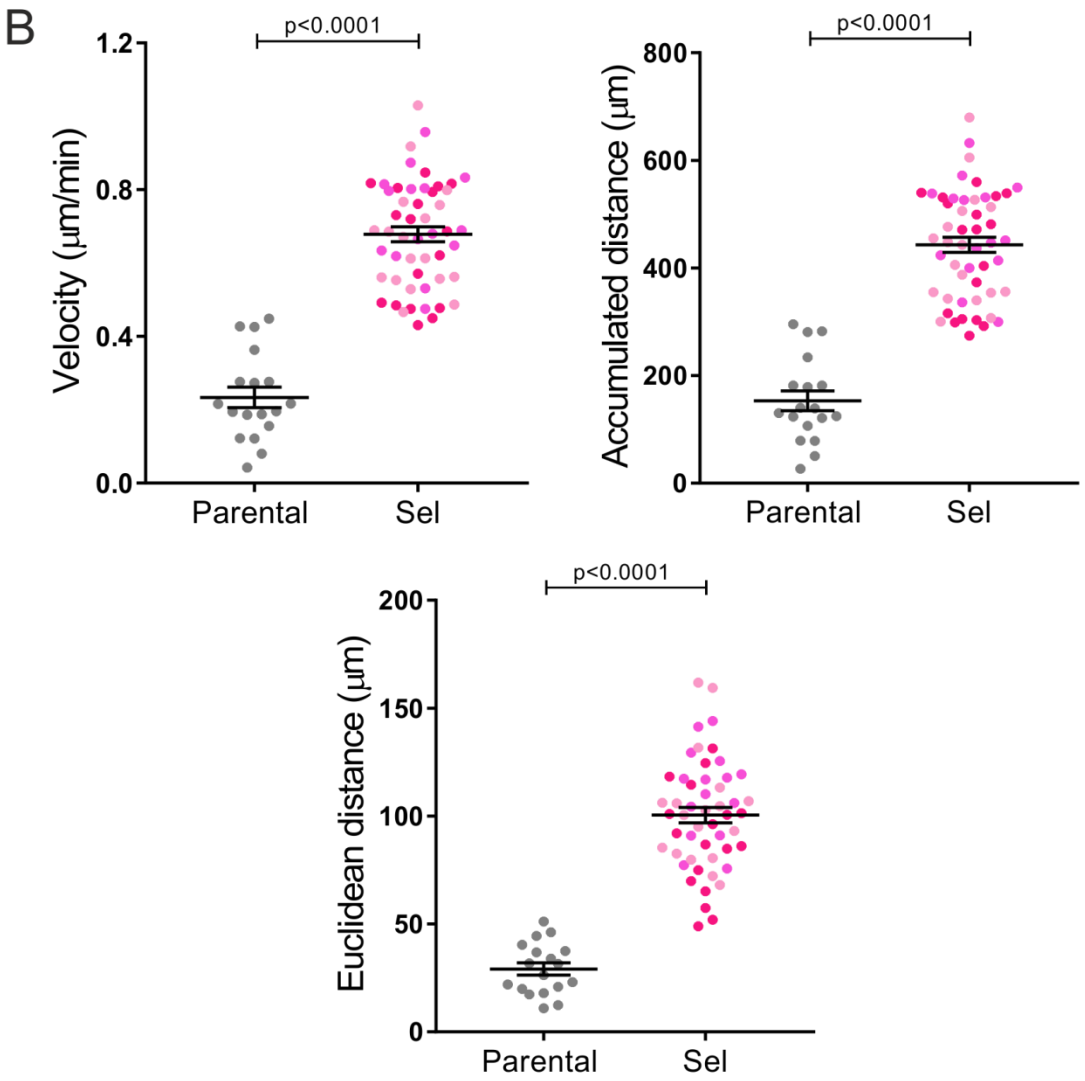

Figure 5-14 Selected MDA MB 435 cells migrate with increased velocity and further distance relative to Parental MDA MB 435 cells measured as individual cells.
A) Representative tracked plots for Parental and Selected MDA MB 435 cells. Each track represents one cell. B) Top panel – left graph depicts mean velocity (± SEM) for Parental and independent Selected MDA MB 435 cells. Right graph depicts mean (± SEM) accumulated distance for Parental and independent Selected MDA MB 435 cells. Bottom panel - graph depicts mean (± SEM) Euclidean distance for Parental and independent Selected MDA MB 435 cells. Each dot represents a mean of n ≥ 8 tracked cells. Data pooled from n = 3 independent experiments. Statistical significance determined by Mann - Whitney test.

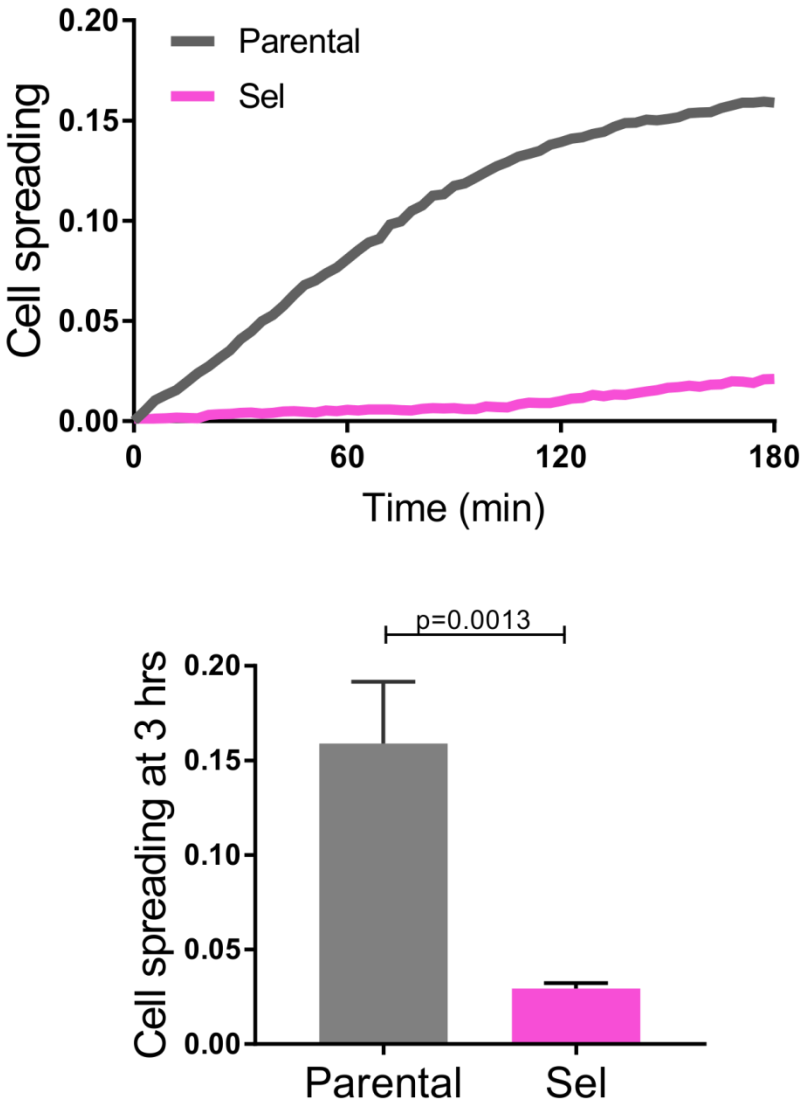

Figure 5-15 Selected MDA MB 435 cells spread less relative to Parental MDA MB 435 cells. Top graph depicts cell spreading for Parental and Selected MDA MB 435 cells. The spreading was measured with RTCA system. Bottom graph depicts mean (± SEM) cell spreading at 3 hours for Parental and Selected MDA MB 435 cells. Data for n = 2 independent experiments. Statistical significance determined by Mann - Whitney test.

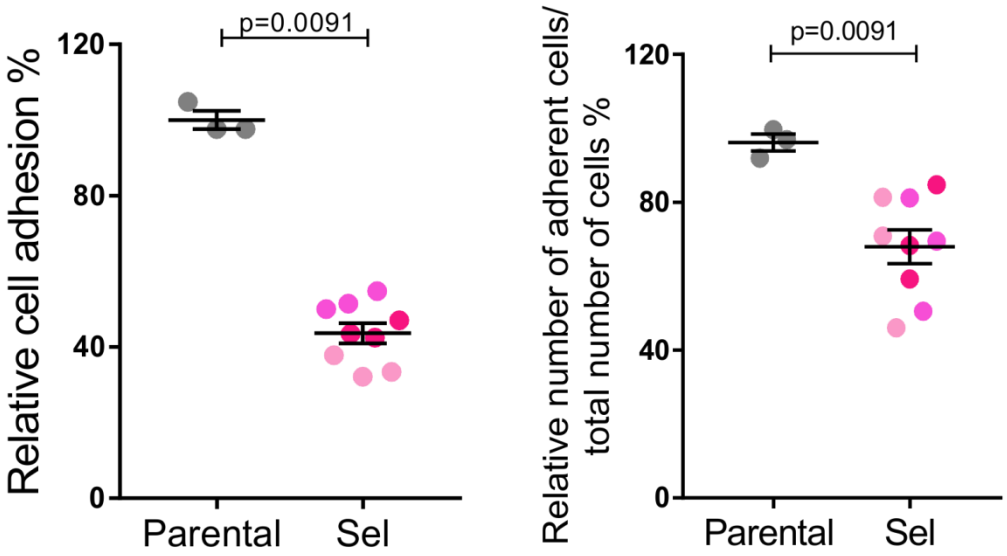

Figure 5-16 Selected MDA MB 435 cells have reduced adhesion compared to Parental MDA MB 435 cells.
Left graph depicts mean (± SEM) percent of relative cell adhesion measured with CellTitre-Glo method showed for Parental and independent Selected MDA MB 435 cells. Each dot represents an average value from n = 3 wells. Data pooled from n = 3 independent experiments. Right graph depicts mean (± SEM) percent of relative number of adherent cells measured with dispase detachment assay for Parental and independent Selected MDA MB 435 cells. Each dot represents an average value from n = 3 wells. Data pooled from n = 3 independent experiments. Statistical significance determined by Mann - Whitney test.

5.3 Conclusions

In this chapter I have investigated cell mechanical properties and two possible cell mechanical determinants – the cytoskeleton and the cell membrane. I revealed that properties unique to the pore-selected invasive cells were decreased actin cytoskeleton anisotropy and cell rigidity (Young's modulus) as determined by Atomic Force Microscopy (AFM). Additionally, changes in cell cytoskeleton organisation reflected changes in focal adhesion assembly in both pore-selected sub-populations. Observed changes in focal adhesion densities could reflect the changes in adhesion tension due to observed differences in the anti-pFAK staining applied. In order to get more insights into organisation or number of focal adhesions, staining for paxillin or talin could be utilised. Moreover, by applying FRAP and studying cell membrane fluidity, I revealed that there were no differences in membrane elasticity between MDA MB 231 and MDA MB 435 sub-populations.

Additionally, I have presented data describing *in vitro* cell properties such as cell morphology, migration, spreading and adhesion. By analysing cell shapes, I found that Selected and Flow sorted MDA MB 231 cells are characterized by increased regular and elongated, and fewer irregular cell shapes relative to Parental MDA MB 231 cells, while Selected MDA MB 435 cells have more irregular and elongated, and fewer regular cell shapes compared to Parental MDA MB 435 cells. Additionally, both pore-selected cell populations exhibited enhanced cell velocity and migrated further distance as measured with individual cell migration assays. Moreover, by studying cell spreading and adhesion properties, I revealed that Selected and Flow sorted MDA MB 231, and Selected MDA MB 435 cells spread less and have decreased cell adhesion compared to Parental cell lines.

6 RNA Sequencing reveals a Ras "signature" associated with pore-selection

6.1 Rationale

As described in previous chapters, I showed that 3 μm pore selection enriched for cells with enhanced constrained migration properties. I revealed that pore-selected MDA MB 231 and MDA MB 435 cells were more migratory through 3 μm pores, and invaded to a greater depth into collagen matrices *in vitro*. *In vivo* studies showed that Selected MDA MB 231 cells injected into the mammary fat pads of immune-compromised mice were more tumourigenic relative to Parental and Flow sorted MDA MB 231 cells. Selected MDA MB 435 cells injected into tail veins of immune-compromised mice were more invasive and metastatic relative to Parental MDA MB 435 cells. Additionally, the properties unique to the pore-selected invasive cells were decreased cell rigidity (Young's modulus) and actin cytoskeleton anisotropy. To identify signalling pathways associated with these cytoskeleton and elasticity changes that contributed to the invasive behaviour of pore-selected cells *in vitro* and *in vivo*, RNA Sequencing was performed on Parental, pore-selected and flow-selected MDA MB 231 cells, and Parental and pore-selected MDA MB 435 cells. RNA Sequencing analysis was performed in collaboration with the Beatson Institute Molecular Technology Service and obtained data were analysed by the Computational Biology department. The most common gene signature was found to associate with increased signalling through the Ras-Raf-MEK-ERK mitogen-activated protein kinase (MAPK) pathway. In order to validate whether the MAPK pathway was involved in the regulation of actin organisation and cell rigidity in Selected MDA MB 231 and MDA MB 435 cells, treatments of pore-selected invasive cells with pharmacological MEK inhibitors, such as Trametinib and U0126, were performed.

6.2 Results

6.2.1 RNA Sequencing data validation

RNA Sequencing was conducted on Parental (four replicates), Selected (two independent cell populations – Sel1 and Sel2, in triplicates each), Flow sorted (two independent cell populations – FS1 and FS2, in triplicates each) MDA MB 231 cells and Parental (four replicates), Selected (two independent cell populations – Sel1 and Sel2, in quadruplicate each) MDA MB 435 cells. RNA quality was confirmed using the Agilent RNA Screen Tape assay and the Aligent 2200 TapeStation system which revealed RNA Integrity Number (RIN) values of around 10 for both cell lines (Table 6-1). The library was run on the Illumina NextSeq platform using High Output 75 cycles kit.

For validation purposes, fold changes in gene expression derived from the number of sequence reads identified by RNA - Seq were compared with fold changes determined by quantitative reverse transcription PCR (RT-qPCR). In order to validate RNA - Seq data from MDA MB 231 cells, I selected the following genes for RT-qPCR, *MXRA8*, *ENPP1*, *LILRB1*, *TNFSF15*, *PTPRU*, *HBEGF* and compared Selected MDA MB 231 vs Parental MDA MB 231 and Selected MDA MB 231 vs Flow sorted MDA MB 231. For Selected MDA MB 231 vs Parental MDA MB 231, the fold changes from both experiments fell on a single fitted straight line with $R^2 = 0.9044$, $P = 0.0035$. For the Selected MDA MB 231 vs Flow sorted MDA MB 231, the fold changes from both experiments also fell on a single fitted straight line with $R^2 = 0.9971$, $P < 0.0001$ (Figure 6-1). In order to validate RNA - Seq data obtained for MDA MB 435, I chose the following genes *PLAU*, *PLAT*, *PTPRU*, *MXRA8*, *HBEGF* and *HSD11B1* and compared Selected vs Parental MDA MB 435. In this case, the fold changes from both experiments fell on a single fitted straight line with $R^2 = 0.97$, $P = 0.0003$ (Figure 6-2).

Table 6-1 RIN values for MDA MB 231 and MDA MB 435 cell lines.

MDA-MB-231		MDA-MB-435	
Sample name	**RIN**	**Sample name**	**RIN**
Parental1	10	Parental1	10
Parental2	9.9	Parental2	10
Parental3	10	Parental3	10
Parental4	9.9	Parental4	10
Sel1-1	10	Sel1-1	10
Sel1-2	9.9	Sel1-2	10
Sel1-3	10	Sel1-3	10
Sel2-1	10	Sel1-4	9.6
Sel2-2	8.9	Sel2-1	10
Sel2-3	9.9	Sel2-2	10
FS1-1	10	Sel2-3	10
FS1-2	10	Sel2-4	10
FS1-3	10		
FS2-1	9.9		
FS2-2	10		
FS2-3	10		

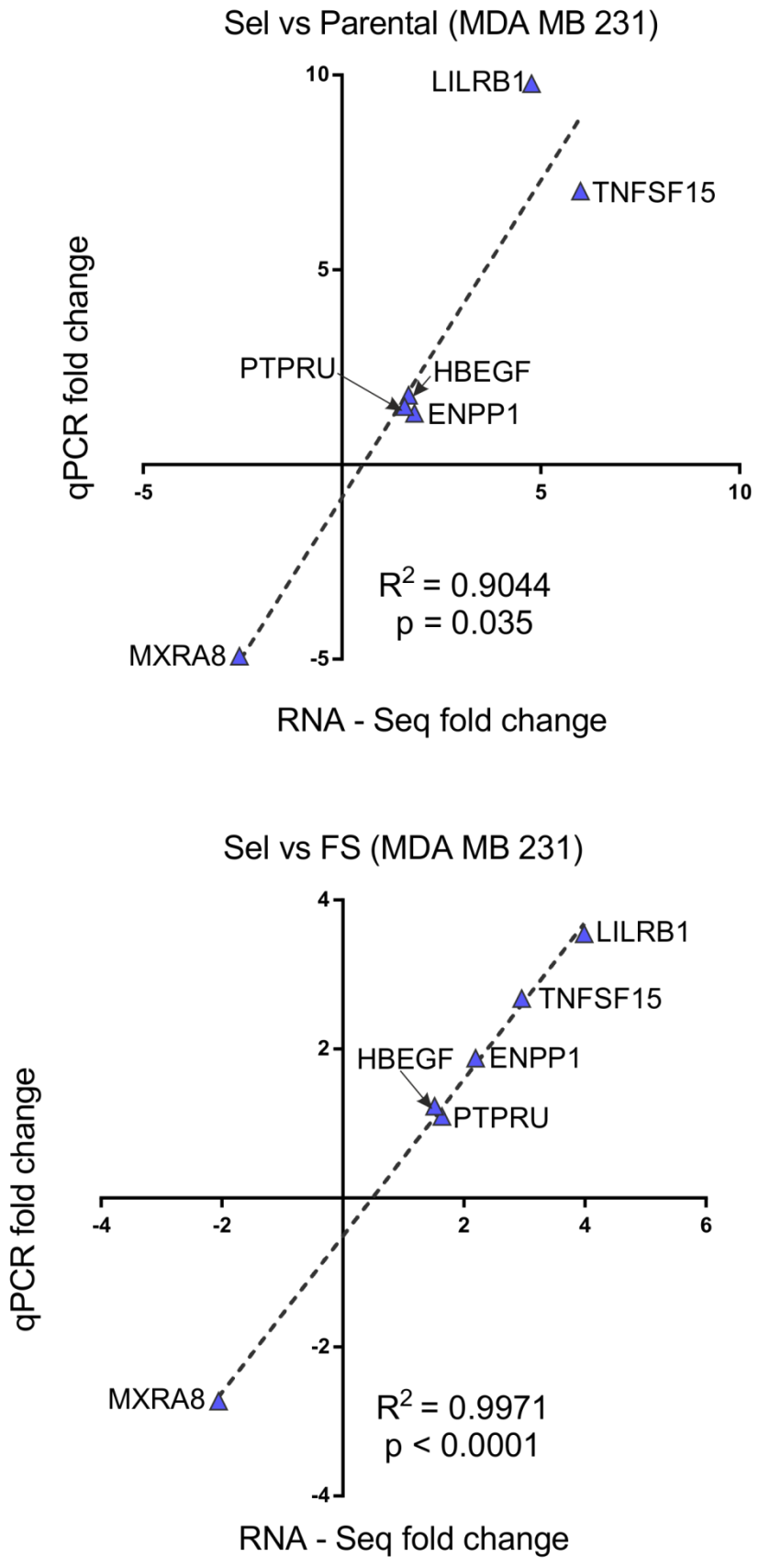

Figure 6-1 Data validation of RNA - Seq for MDA MB 231 cells.
Linear regression plots of fold change for Selected MDA MB 231 vs Parental MDA MB 231 (top) and Selected MDA MB 231 vs Flow sorted MDA MBA 231 (bottom) obtained by RNA - Seq compared to RT-qPCR (relative to *GAPDH*).

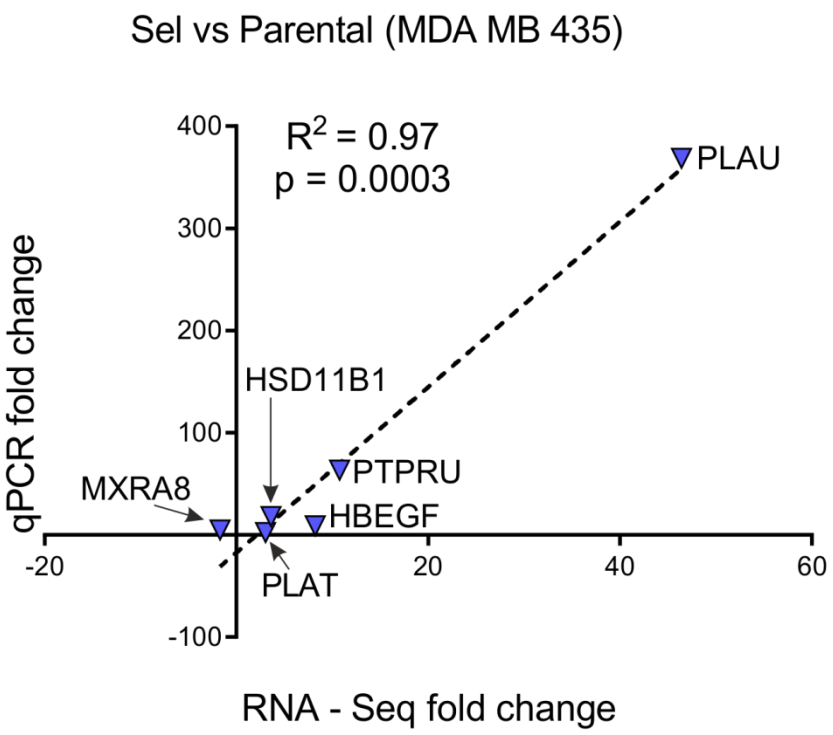

Figure 6-2 Data validation of RNA - Seq for MDA MB 435 cells.
Linear regression plots of fold change for Selected MDA MB 435 vs Parental MDA MB 435 obtained by RNA - Seq compared to RT-qPCR (relative to *GAPDH*).

6.2.2 RNA Sequencing analysis of Parental, Selected and Flow sorted MDA MB 231 cells

To obtain an overview of the differences and similarities between samples obtained from Parental, Selected and Flow sorted MDA MB 231 cells, Principle Component Analysis (PCA) was performed (Figure 6-3).

RNA sequencing data analysis revealed that the expression of 1817 genes were significantly different ($p < 0.05$) by greater than 1.5 fold change (FC) in Selected MDA MB 231 cells relative to Parental MDA MB 231 cells. Whereas, by comparing genes identified in Selected MDA MB 231 cells to Flow sorted MDA MB 231 cells, 1632 genes were significantly different ($p < 0.05$, $FC > 1.5$), of which 615 genes were common changes between the two pairwise comparisons (Figure 6-4). Bonferroni correction was not applied.

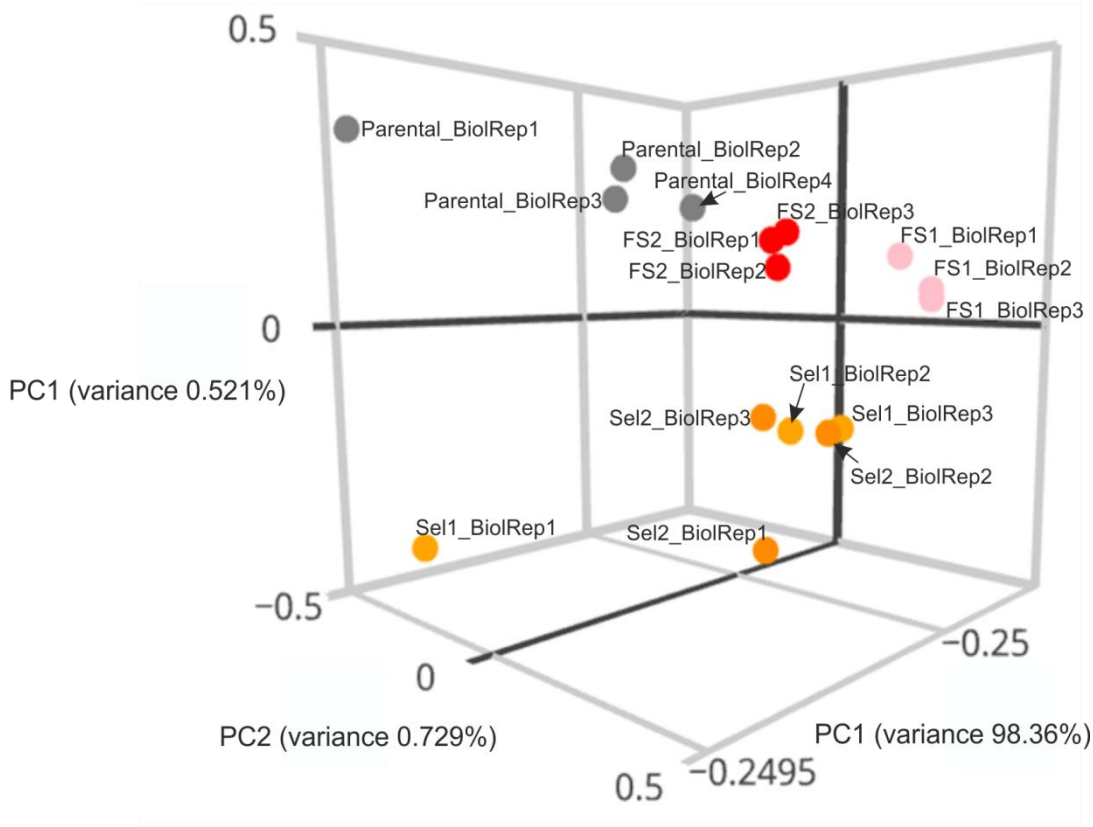

Figure 6-3 Principal component plot of RNA - Seq data obtained for Parental, Selected and Flow sorted MDA MB 231 cells.
Principal component plot of RNA - Seq data indicating the clustering together of samples obtained from Parental and Flow sorted MDA MB 231 cells, which separated from samples obtained from Selected MDA MB 231 cells.

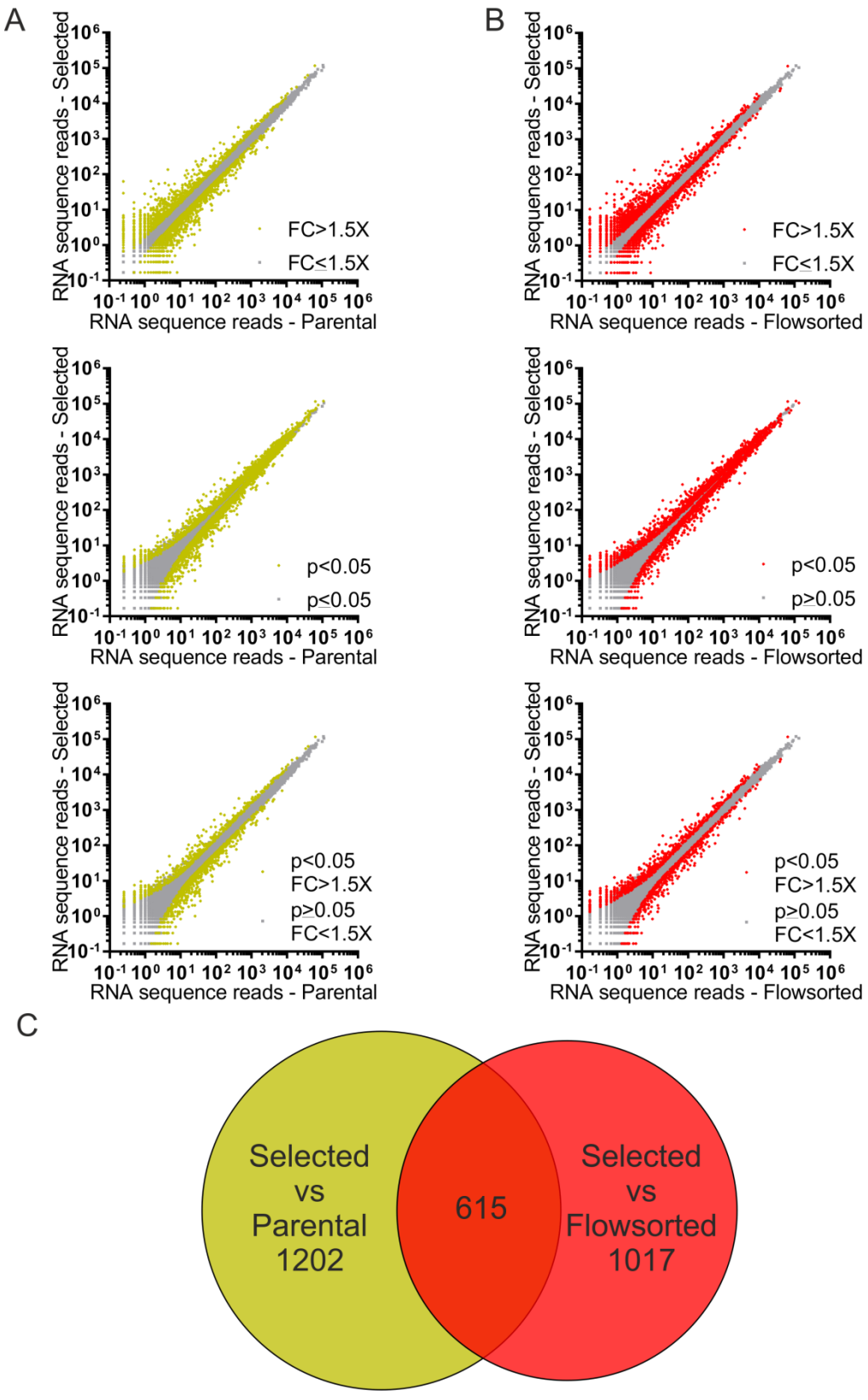

Figure 6-4 Gene expression profile of Parental, Selected and Flow sorted MDA MB 231 cells. A) Comparison of global gene expression profile of Parental MDA MB 231 and Selected MDA MB 231 cells (threshold FC > 1.5; p < 0.05). B) Comparison of global gene expression profile of Flow sorted MDA MB 231 and Selected MDA MB 231 cells (threshold FC > 1.5; p < 0.05). C) Venn diagram of gene expression changes for Selected MDA MB 231 vs Parental MDA MB 231, and Selected MDA MB 231 vs Flow sorted MDA MB 231 (thresholds of p < 0.05 and FC > 1.5).

6.2.3 RNA Sequencing analysis of Parental and Selected MDA MB 435 cells

To compare RNA Sequencing samples obtained for Parental and Selected MDA MB 435 cells, PCA was performed (Figure 6-5).

RNA sequencing data analysis of global gene expression profile revealed that the expression of 23,423 genes were identified, of which 10,876 genes were significantly changed ($p < 0.05$, $FC > 1.5$) (Figure 6-6). Bonferroni correction was not applied.

6.2.4 Comparison of gene expression data sets obtained for MDA MB 231 and MDA MB 435 cells

In order to find common genes associated with cytoskeleton and elasticity changes, the two data sets for MDA MB 231 and MDA MB 435 cells were compared. Thresholds of $p < 0.05$ and $FC > 1.5$ were used. By comparing genes changed in Selected MDA MB 231 vs Parental MDA MB 231 to genes changed in Selected MDA MB 435 vs Parental MDA MB 435, 562 genes were found to be in common, while comparison of genes sets of Selected MDA MB 231 vs Flow sorted MDA MB 231 to genes changed in Selected MDA MB 435 vs Parental MDA MB 435, 427 genes were found to be in common. More stringent comparison of three data sets, Parental MDA MB 231 vs Selected MDA MB 231 to Flow sorted MDA MB 231 vs Selected MDA MB 231 to Parental MDA MB 435 vs Selected MDA MB 435, revealed 214 genes that were common changes for pore-selected MDA MB 231 and MDA MB 435 cells (Figure 6-7).

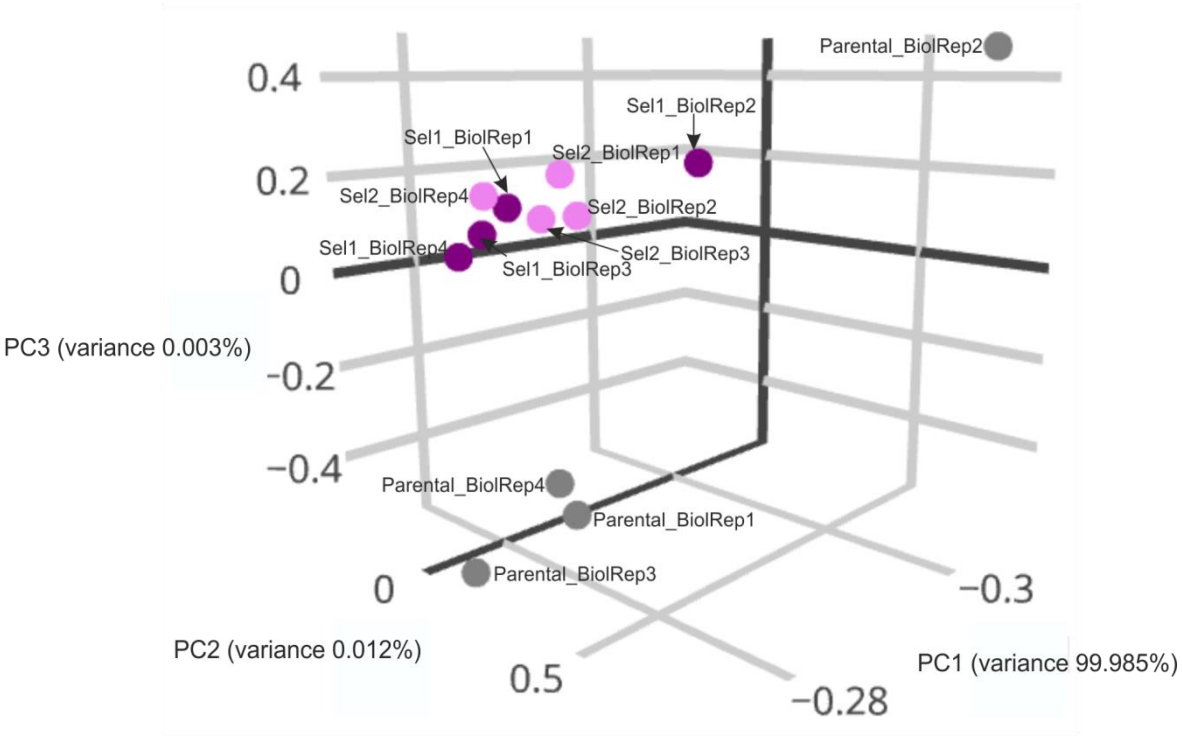

Figure 6-5 Principle component plot of RNA - Seq data obtained for Parental and Selected MDA MB 435 cells.
Principal component plot of RNA - Seq data indicating the clustering together samples obtained from Parental MDA MB 435 cells separated from samples obtained from Selected MDA MB 435 cells.

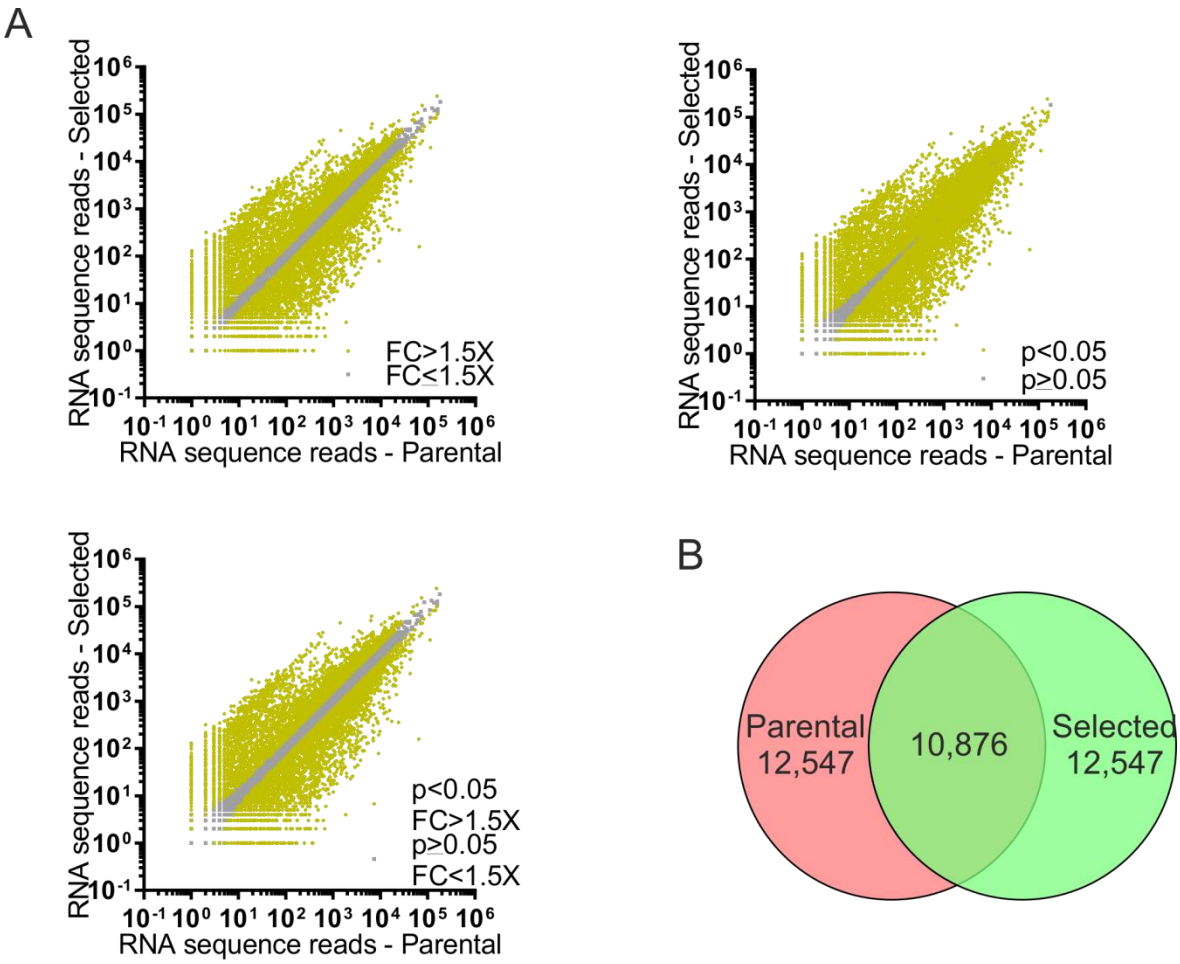

Figure 6-6 Gene expression profile showed for Parental and Selected MDA MB 435 cells.
A) Comparison of global gene expression profile of Parental MDA MB 435 and Selected MDA MB 435 cells (threshold FC > 1.5; p < 0.05). B) Venn diagram of gene expression changes for Parental and Selected MDA MB 435 cells, 10,876 genes were found to be significantly changed (thresholds of p < 0.05 and FC > 1.5).

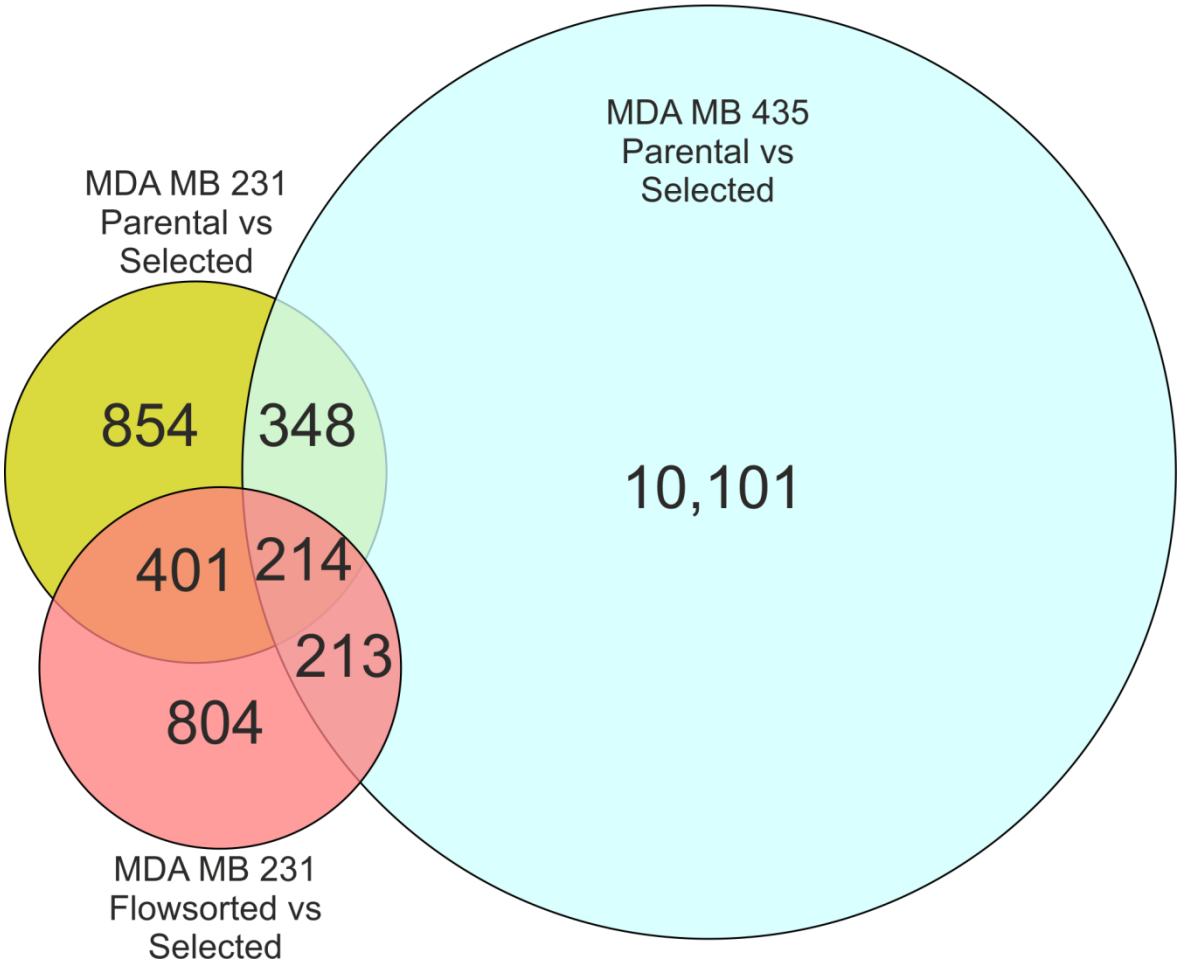

Figure 6-7 Comparison of number of overlapped genes for three data sets: Parental vs Selected MDA MB 231, Flow sorted vs Selected MDA MB 231 and Parental vs Selected MDA MB 435.

Venn diagram depicts the number of overlapping genes for three data sets, Parental vs Selected MDA MB231, Flow sorted vs Selected MDA MB 231 and Parental vs Selected MDA MB 435. Thresholds of $p < 0.05$ and FC >1.5 were used.

6.2.5 GSEA data analysis of common genes reveals increased signalling through the Ras-Raf-MEK-ERK mitogen-activated protein kinase (MAPK) pathway

The Broad Institute's Gene Set Enrichment Analysis (GSEA) algorithm was employed to identify functional patterns or pathways associated with the cytoskeleton and elasticity changes of Selected MDA MB 231 and MDA MB 435 cells. In order to identify oncogenic signatures of Selected MDA MB 231 cells, 615 genes that were identified as common genes associated with the invasive behaviour of Selected MDA MB 231 cells by comparing two data sets, (Parental vs Selected with Flow sorted vs Selected) were used as data input. GSEA of oncogenic signatures allowed identification of the 10 most significantly changed Gene Sets, of which 5 (in fact, 5 of the top 6) were associated with increased signalling through KRAS, (Figure 6-8) (Table 6-2).

In order to find common gene sets from invasive pore-selected MDA MB 231 and MDA MB 435, the 214 genes that were identified as common genes by comparing 615 genes identified in invasive MDA MB 231 cells were compared to the 10,678 genes identified as significantly changed genes in Selected MDA MB 435 cells, were used as a data input for GSEA. GSEA revealed the 10 most significantly changed Gene Sets, of which KRAS signalling alterations were commonly associated in 5 (and 4 of the top 5) (Figure 6-8) (Table 6-3). These results suggested that the identified genes in the KRAS signatures were indicative of changes in Ras/MAPK signalling being involved in the invasive behaviour of pore-selected MDA MB 231 and MDA MB 435 cells.

KRAS "signature" genes identified in the significantly changed Gene Sets associated with KRAS, Raf and MAPK signalling were used for heatmaps to depict patterns of gene expression for MDA MB 231 (Figure 6-9) and MDA MB 435 data (Figure 6-10).

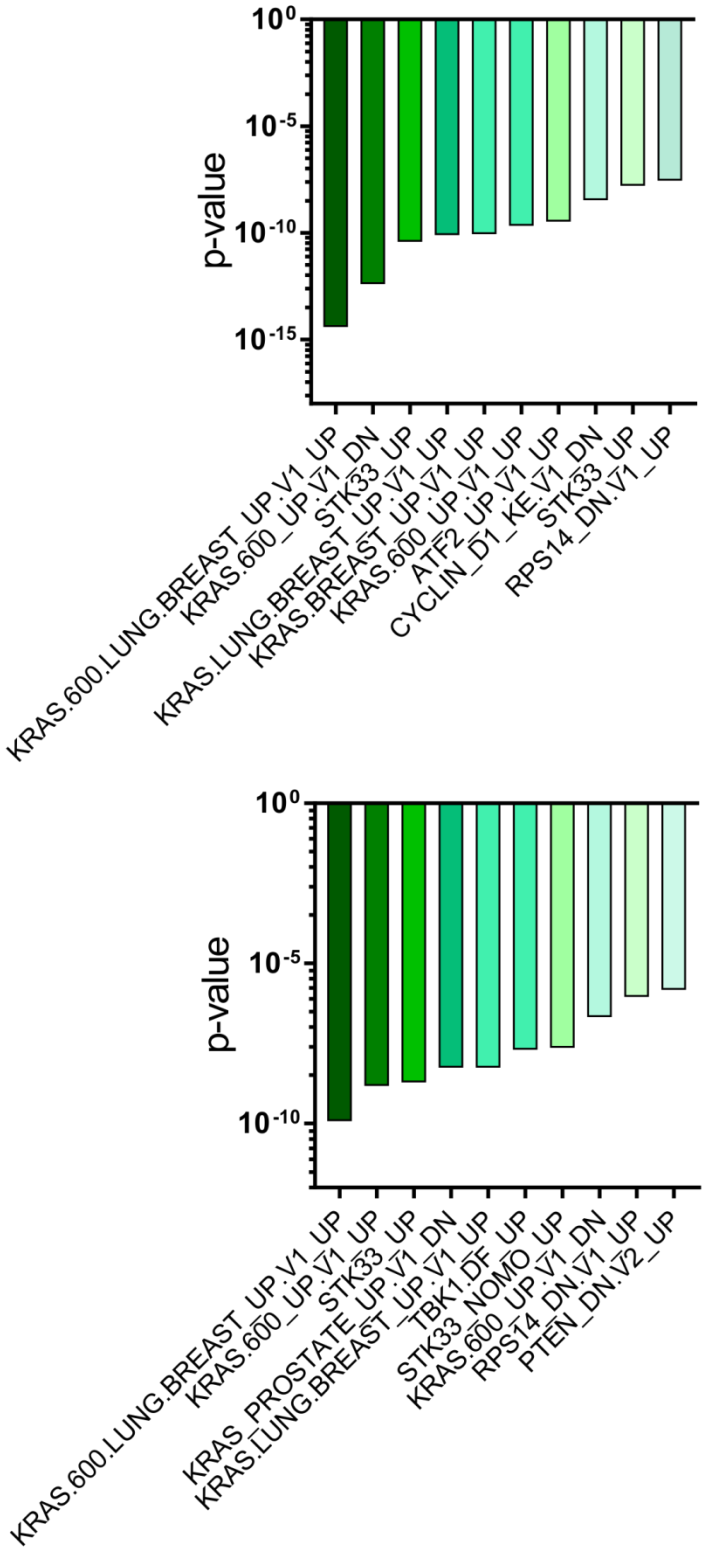

Figure 6-8 GSEA analysis reveals KRAS signalling gene signatures in pore-selected cells. Top graph depicts the 10 most significantly changed Gene Sets identified by GSEA in Selected MDA MB 231. The bottom graph depicts the 10 most common significantly changed Gene Sets identified for pore-selected MDA MB 231 and MDA MB 435 cells.

Table 6-2 GSEA identified Gene Sets.
The table represents the 20 most significantly changed Gene Sets identified for Selected MDA MB 231 cells. Data analysis was performed with GESA.

Gene Set Name	Description	Number of Genes in Overlap	p-value
KRAS.600.LUNG.BREAST_UP.V1_UP	Genes up-regulated in epithelial lung and breast cancer cell lines over-expressing an oncogenic form of KRAS gene.	23	3.95 e-15
KRAS.600_UP.V1_DN	Genes down-regulated in four lineages of epithelial cell lines over-expressing an oncogenic form of KRAS gene.	21	3.97 e-13
STK33_UP	Genes up-regulated in NOMO-1 and SKM-1 cells (AML) after knockdown of STK33 by RNAi.	19	3.8 e-11
KRAS.LUNG.BREAST_UP.V1_UP	Genes up-regulated in epithelial lung and breast cancer cell lines over-expressing an oncogenic form of KRAS gene.	14	7.91 e-11
KRAS.BREAST_UP.V1_UP	Genes up-regulated in epithelial breast cancer cell lines over-expressing an oncogenic form of KRAS gene.	14	8.67 e-11
KRAS.600_UP.V1_UP	Genes up-regulated in four lineages of epithelial cell lines over-expressing an oncogenic form of KRAS gene.	18	2.14 e-10
ATF2_UP.V1_UP	Genes up-regulated in myometrial cells over-expressing ATF2 gene.	15	3.38 e-10
CYCLIN_D1_KE_.V1_DN	Genes down-regulated in MCF-7 cells (breast cancer) over-expressing a mutant K112E form of CCND1 gene.	14	3.68 e-9
STK33_NOMO_UP	Genes up-regulated in NOMO-1 cells (AML) after knockdown of STK33 by RNAi.	16	1.63 e-8
RPS14_DN.V1_UP	Genes up-regulated in CD34+ hematopoietic progenitor cells after knockdown of RPS14 by RNAi.	13	2.85 e-8
ATF2_S_UP.V1_UP	Genes up-regulated in myometrial cells over-expressing a shortened splice form of ATF2 gene.	13	3.03 e-8
P53_DN.V1_UP	Genes up-regulated in NCI-60 panel of cell lines with mutated TP53.	13	3.22 e-8
PRC2_EZH2_UP.V1_DN	Genes down-regulated in TIG3 cells (fibroblasts) upon knockdown of EZH2 gene.	13	3.22 e-8
KRAS.LUNG_UP.V1_UP	Genes up-regulated in epithelial lung cancer cell lines over-expressing an oncogenic form of KRAS gene.	11	7.9 e-8
STK33_SKM_UP	Genes up-regulated in SKM-1 cells (AML) after knockdown of STK33 by RNAi.	15	8.88 e-8
KRAS.PROSTATE_UP.V1_DN	Genes down-regulated in epithelial prostate cancer cell lines over-expressing an oncogenic form of KRAS gene.	11	9.8 e-8
RELA_DN.V1_UP	Genes up-regulated in HEK293 cells (kidney fibroblasts) upon knockdown of RELA gene by RNAi.	11	1.39 e-7
LEF1_UP.V1_DN	Genes down-regulated in DLD1 cells (colon carcinoma) over-expressing LEF1.	12	2.07 e-7
CAHOY_ASTROGLIAL	Genes up-regulated in astrogia cells.	9	3.59 e-7
RELA_DN.V1_DN	Genes down-regulated in HEK293 cells (kidney fibroblasts) upon knockdown of RELA gene by RNAi.	10	7.46 e-7

Table 6-3 GSEA identified Gene Sets.
The bottom graph represents the 20 most significantly changed Gene Sets identified for pore-selected MDA MB 231 and MDA MB 435 cells. Data analysis was performed with GESA.

Gene Set Name	Description	Number of Genes in Overlap	p-value
KRAS.600.LUNG.BREAST_UP.V1_UP	Genes up-regulated in epithelial lung and breast cancer cell lines over-expressing an oncogenic form of KRAS gene.	13	1.2 e-10
KRAS.600_UP.V1_UP	Genes up-regulated in four lineages of epithelial cell lines over-expressing an oncogenic form of KRAS gene.	12	1.51 e-9
STK33_UP	Genes up-regulated in NOMO-1 and SKM-1 cells (AML) after knockdown of STK33 by RNAi.	12	1.91 e-9
KRAS.PROSTATE_UP.V1_DN	Genes down-regulated in epithelial prostate cancer cell lines over-expressing an oncogenic form of KRAS gene.	9	5.53 e-9
KRAS.LUNG.BREAST_UP.V1_UP	Genes up-regulated in epithelial lung and breast cancer cell lines over-expressing an oncogenic form of KRAS gene.	9	5.88 e-9
TBK1.DF_UP	Genes up-regulated in epithelial lung cancer cell lines upon over-expression of an oncogenic form of KRAS gene and knockdown of TBK1 gene by RNAi.	11	2.02 e-8
STK33_NOMO_UP	Genes up-regulated in NOMO-1 cells (AML) after knockdown of STK33 by RNAi.	11	2.32 e-8
KRAS.600_UP.V1_DN	Genes down-regulated in four lineages of epithelial cell lines over-expressing an oncogenic form of KRAS gene.	10	2.11 e-7
RPS14_DN.V1_UP	Genes up-regulated in CD34+ hematopoietic progenitor cells after knockdown of RPS14 by RNAi.	8	8.94 e-7
PTEN_DN.V2_UP	Genes up-regulated in HCT116 cells (colon carcinoma) upon knockdown of PTEN by RNAi.	7	1.5 e-6
BMI1_DN_MEL18_DN.V1_UP	Genes up-regulated in DAOY cells (medulloblastoma) upon knockdown of BMI1 and PCGF2 genes by RNAi.	7	1.65 e-6
KRAS.AMP.LUNG_UP.V1_DN	Genes down-regulated in epithelial lung cancer cell lines over-expressing KRAS gene.	7	1.72 e-6
RELA_DN.V1_UP	Genes up-regulated in HEK293 cells (kidney fibroblasts) upon knockdown of RELA gene by RNAi.	7	1.98 e-6
STK33_SKM_UP	Genes up-regulated in SKM-1 cells (AML) after knockdown of STK33 by RNAi.	9	2.12 e-6
ESC_V6.5_UP_EARLY.V1_DN	Genes down-regulated during early stages of differentiation of embryoid bodies from V6.5 embryonic stem cells.	7	5.11 e-6
ATF2_UP.V1_DN	Genes down-regulated in myometrial cells over-expressing ATF2 gene.	7	8.83 e-6
IL21_UP.V1_DN	Genes down-regulated in Sez-4 cells (T lymphocyte) that were first starved of IL2 and then stimulated with IL21.	7	8.83 e-6
LEF1_UP.V1_DN	Genes down-regulated in DLD1 cells (colon carcinoma) over-expressing LEF1.	7	9.79 e-6
ATF2_UP.V1_UP	Genes up-regulated in myometrial cells over-expressing ATF2 gene.	7	1.05 e-5
KRAS.LUNG_UP.V1_UP	Genes up-regulated in epithelial lung cancer cell lines over-expressing an oncogenic form of KRAS gene.	6	1.91 e-5

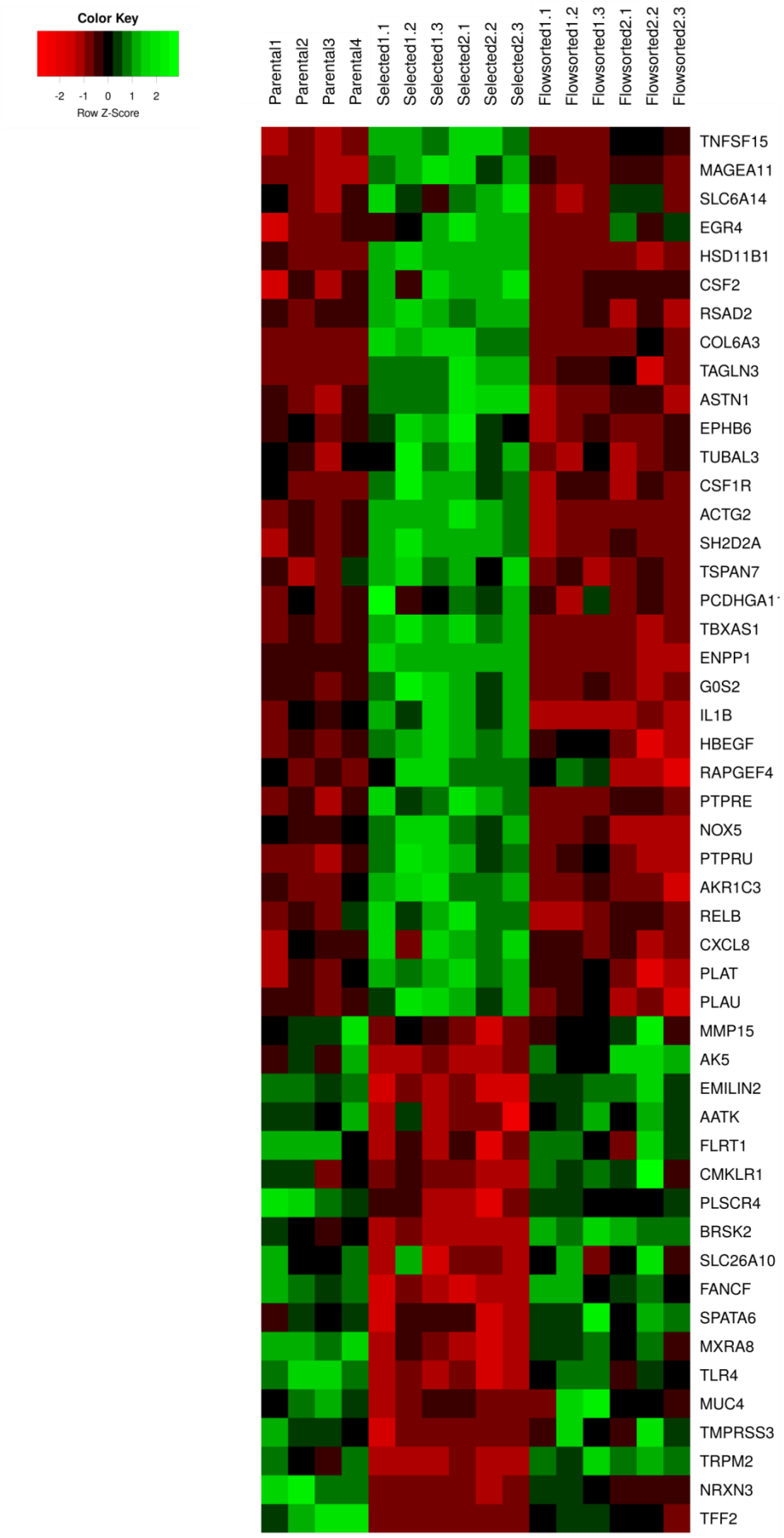

Figure 6-9 Genes identified in KRAS "signatures" for MDA MB 231 cells.
The heatmap represents 49 genes that were associated with KRAS, Raf and MAPK signalling identified by GSEA for MDA MB 231 sub-populations.

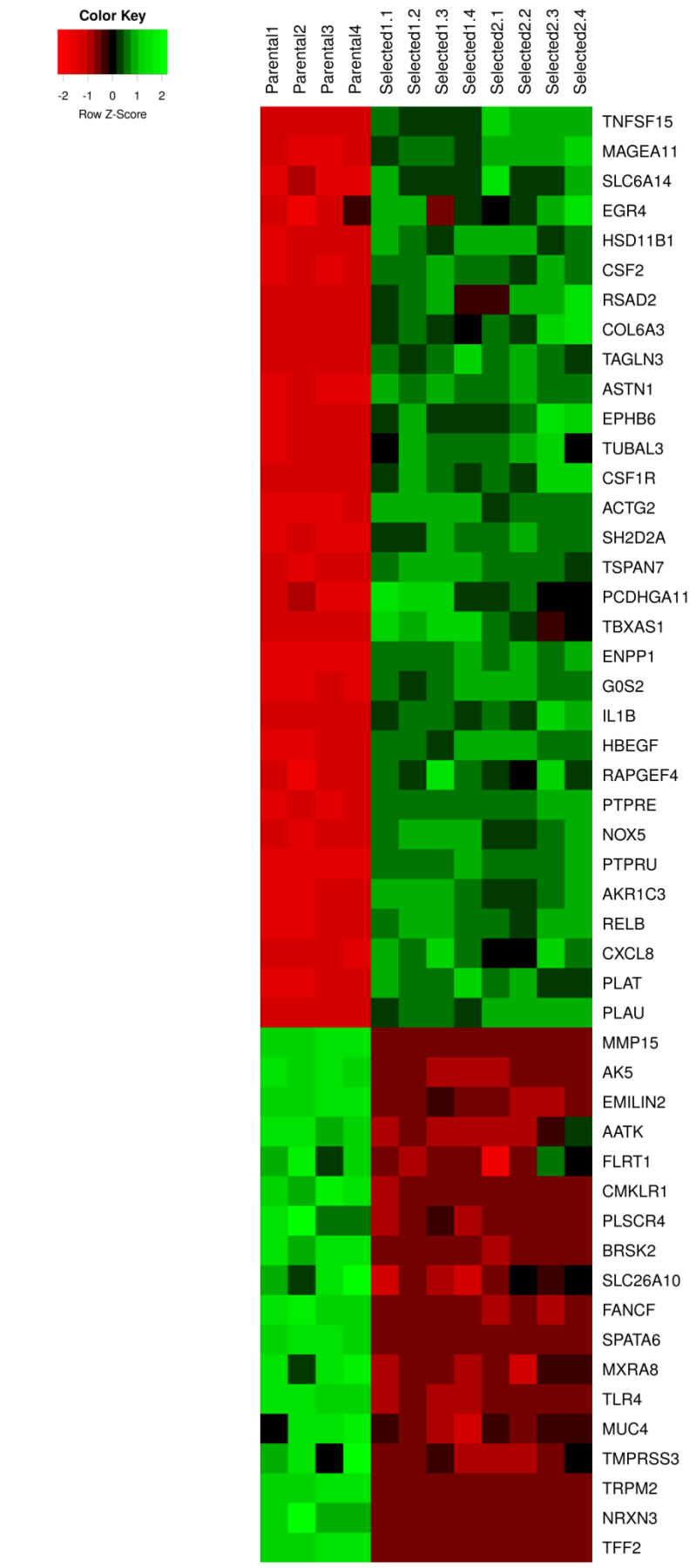

Figure 6-10 Genes identified in "KRAS signatures" for MDA MB 435 cells.
The heatmap represents 49 genes that were associated with KRAS, Raf and MAPK signalling identified by GSEA for MDA MB 435 sub-populations.

6.2.6 Trametinib treatment affects the expression of genes associated with the Ras-Raf-MEK-ERK pathway

Having revealed increased signalling through the Ras-Raf-MEK-ERK mitogen-activated protein kinase (MAPK) pathway by GSEA of RNA sequencing data, next I wanted to investigate whether the MAPK/ERK pathway was responsible for the observed changes in pore-selected MDA MB 231 and MDA MB 435 cells, such as enhanced confined migration, increased motility, disrupted cytoskeleton and decreased stiffness. In order to validate the effect of MAPK/ERK pathway inhibition on observed changes, I decided to use two pharmacologically distinct MEK inhibitors, Trametinib and U0126.

I started the investigation by checking whether the expression of genes that were associated with the KRAS "signature" identified by GSEA, were dependent on the activity of MAPK/ERK pathway. For this purpose, I chose several genes for MDA MB 231 cells, including: *ENPP1*, *HBEGF*, *PTPRU*, *MXRA8*, *HSD11B1* and *TNFSF15*, and the following genes for MDA MB 435 cells: *PLAU*, *PLAT*, *HBEGF*, *PTPRU*, *MXRA8*, *HDS11B1*, and assessed their expression following Trametinib treatment. In brief, the experiment was performed as follows; cells were seeded in a well of 6-well plate. Next day, cells were treated with 0.5 μM of Trametinib or DMSO for 24 hours and kept in standard tissue culture conditions. Subsequently RNA was extracted, cDNA synthesized and qRT-PCR was performed. The expression of genes was normalized to *GAPDH*. In order to assess the percentage inhibition of gene expression upon Trametinib treatment, gene expression levels were normalized to DMSO controls. The analysis revealed that the expression of genes that were upregulated in Parental, Selected and Flow sorted MDA MB 231 cells and Parental, Selected MDA MB 435 cells were decreased after Trametinib treatment. Additionally, genes that were downregulated in Selected MDA MB 231 and MDA MB 435 cells were upregulated following MEK inhibitor treatment (Figure 6-11), consistent with genes identified in the KRAS "signature" were dependent on the activity of MAPK/ERK pathway. These genes could be, through direct or indirect means, responsible for the observed disorganisation of cytoskeletal structures and cell plasticity changes in pore-selected cell lines, which would subsequently affect their confined migratory and invasive capabilities.

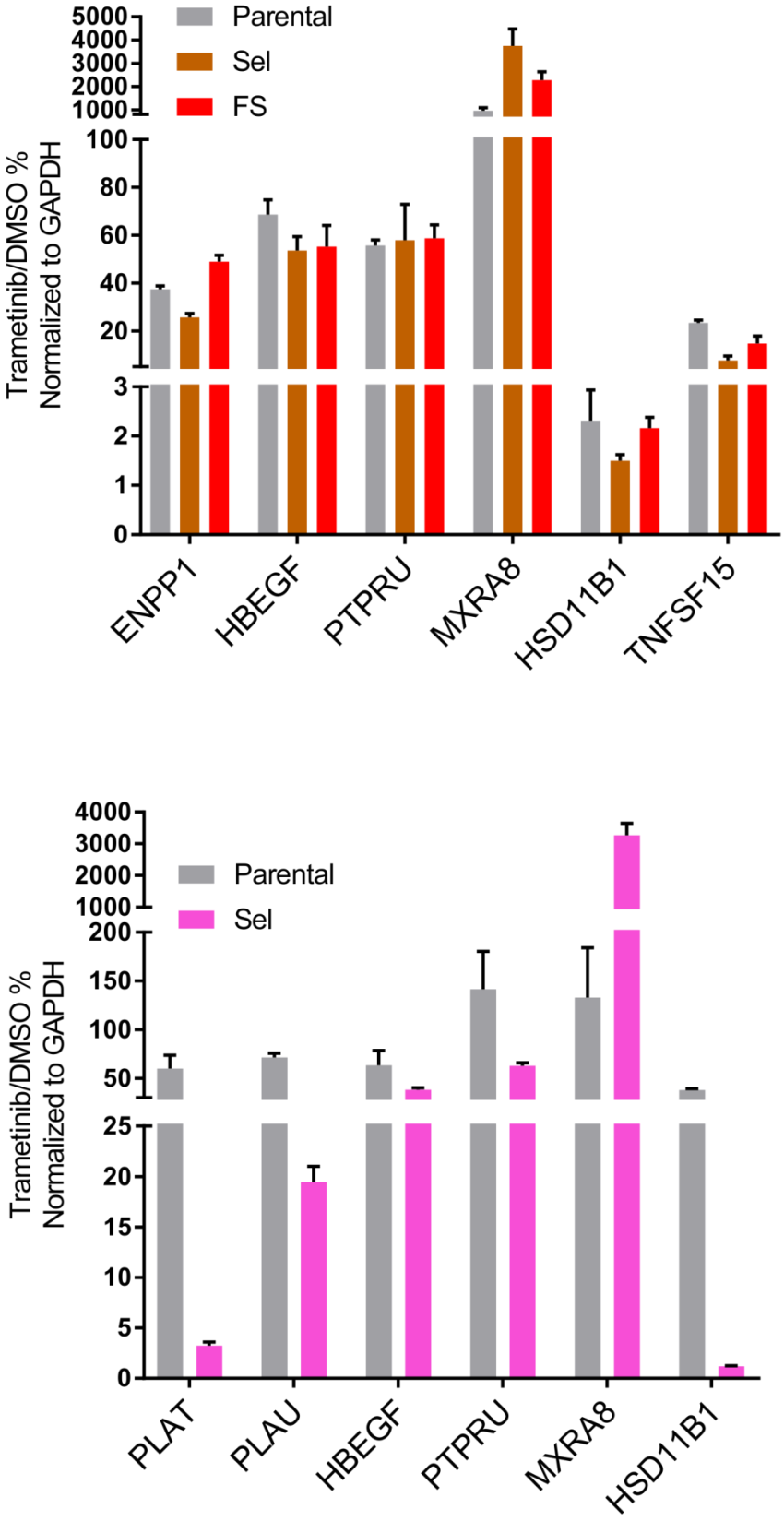

Figure 6-11 Trametinib treatment affects expression of genes associated with the Ras-Raf-MEK-ERK pathway.
The top graph depicts mean percentage (± SEM) of gene expression inhibition upon Trametinib treatment for Parental, Selected and Flow sorted MDA MB 231 cells. Data pooled from n = 3 independent experiments. The bottom graph depicts mean percentage (± SEM) of gene expression inhibition upon Trametinib treatment for Parental and Selected MDA MB 435 cells. Data pooled from n = 3 independent experiments.

6.2.7 MEK inhibition restores actin organisation and focal adhesions in Selected MDA MB 231 and MDA MB 435 cells

Having identified decreased actin cytoskeleton anisotropy and cell rigidity (Young's modulus), as well as an increased signalling through the Ras-Raf-MEK-ERK mitogen-activated protein kinase (MAPK) pathway in pore-selected cells, I decided to inhibit the MAPK pathway to determine whether MAPK signalling contributed to the observed loss of stress fibres and focal contacts in Selected MDA MB 231 and MDA MB 435 cells. In order to evaluate the input of MAPK/ERK pathway on actin organisation, I used two pharmacologically distinct MEK inhibitors, Trametinib or U0126.

In order to image actin by confocal microscopy, samples were prepared as follows. In brief, cells were seeded on coverslips and grown overnight. The next day, they were treated with 0.5 μM Trametinib, 10 μM U0126 or DMSO, and incubated for 24 hours in standard issue culture conditions. After incubation, cells were fixed and stained with phalloidin and anti-pFAK antibody in order to detect focal adhesions. Subsequently, cells were imaged on the Zeiss 710 confocal. The obtained confocal images revealed that following Trametinib or U0126 treatment, Selected MDA MB 231 (Figure 6-12) (Figure 6-13) and MDA MB 435 (Figure 6-16) (Figure 6-17) cells changed their actin organisation from primarily cortical to cytoplasmic fibrillary structures.

In order to quantify actin alignment, the ImageJ plug-in Fibril Tool was utilised. In order to be consistent with the image plane of stained F-actin taken for the anisotropy analysis, Total Internal Reflection Fluorescence microscopy (TIRF) images were used. TIRF microscopy allowed visualisation of fluorescent molecules less than 200 nm from the coverslip surface. Such location corresponded to the ventral cortical actin position. TIRF images revealed diffused actin staining in DMSO-treated pore-selected MDA MB 231 and MDA MB 435 cells, while in Trametinib or U0126-treated pore-selected MDA MB 231 (Figure 6-12) (Figure 6-13) and MDA MB 435 (Figure 6-16) (Figure 6-17) cells, long actin filaments were observed. F-actin anisotropy analysis revealed a significant increase of F-actin anisotropy in Trametinib and U0126-treated pore-selected MDA MB 231 (Figure 6-12) (Figure 6-13) and MDA MB 435 (Figure 6-16) (Figure 6-17) cells relative to DMSO-treated control cells.

Immunofluorescence labelling with anti-pFAK antibody, of Trametinib or U0126-treated pore-selected MDA MB 231 and MDA MB 435 cells revealed assembly of focal adhesions in comparison to DMSO-treated control cells. The pFAK-stained cells images revealed that DMSO-treated pore-selected MDA MB 231 and MDA MB 435 cells had fewer and less pronounced focal complexes, while Trametinib or U0126-treated cells were characterized by more mature and larger focal assemblies. The number of focal adhesions complexes was counted using ImageJ. Number of FA was counted per cell. The average number of focal adhesions per group was counted per cell and then normalized to the cell area, which was determined from Operetta High Content Imaging System. The analysis revealed that DMSO-treated Selected MDA MB 231 (Figure 6-14) (Figure 6-15) and MDA MB 435 (Figure 6-18) (Figure 6-19) cells had fewer focal adhesions per cell and per cell area compared to Trametinib or U0126-treated cells.

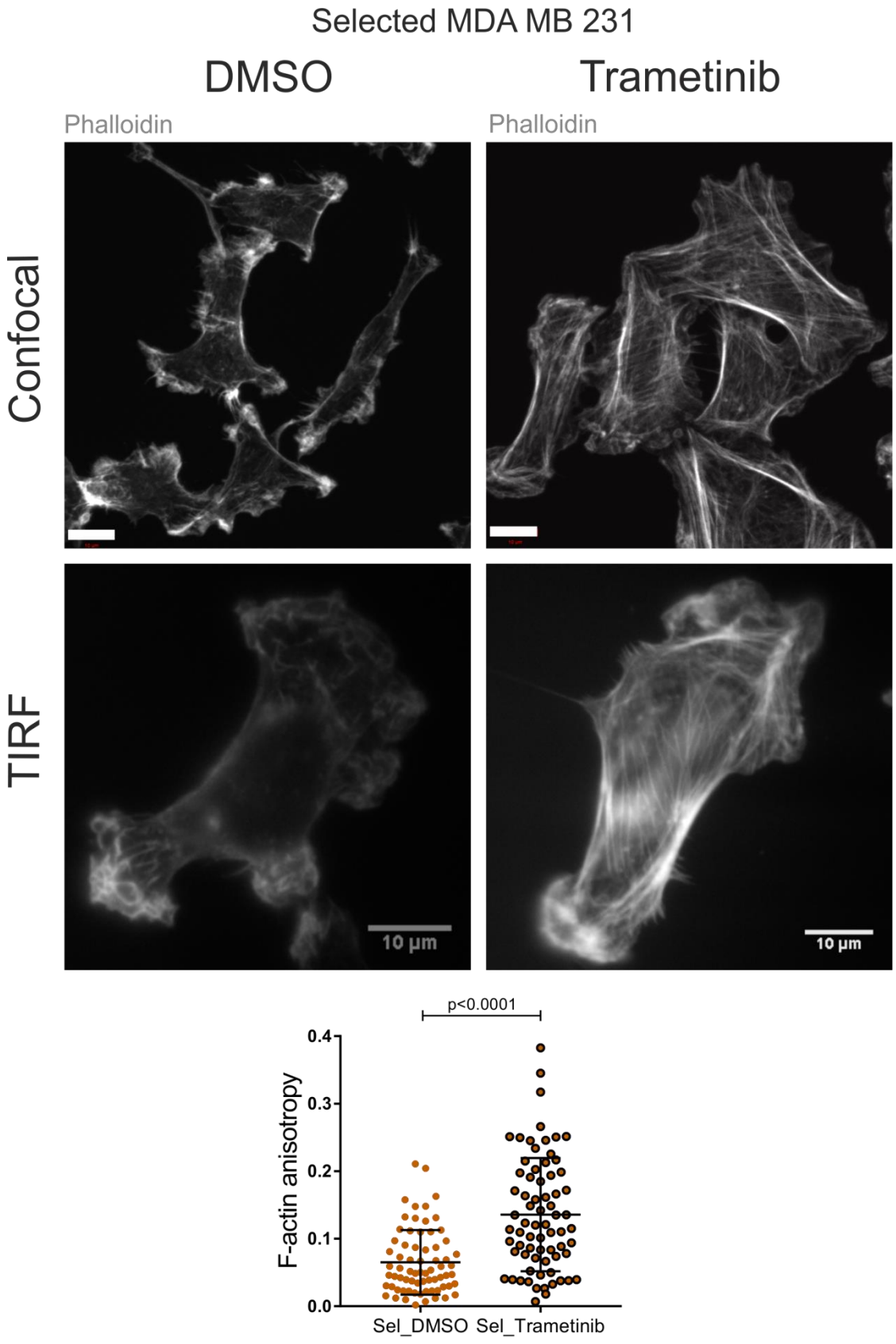

Figure 6-12 Trametinib treatment restores actin structures in Selected MDA MB 231 cells. Top panel – representative maximal projection images of phalloidin-stained Selected MDA MB 231 cells treated with DMSO or Trametinib. Images were acquired on a Zeiss 710 confocal microscope. Bottom panel - representative images of phalloidin-stained Selected MDA MB 231 cells treated with DMSO or Trametinib. Images were acquired on a TIRF microscope. Scale bar = 10 µm. The bottom graph depicts mean (± SD) F-actin anisotropy for DMSO and Trametinib-treated Selected MDA MB 231 cells. Data represent individual cells pooled from n = 3 independent experiments. Statistical significance determined by Mann - Whitney test.

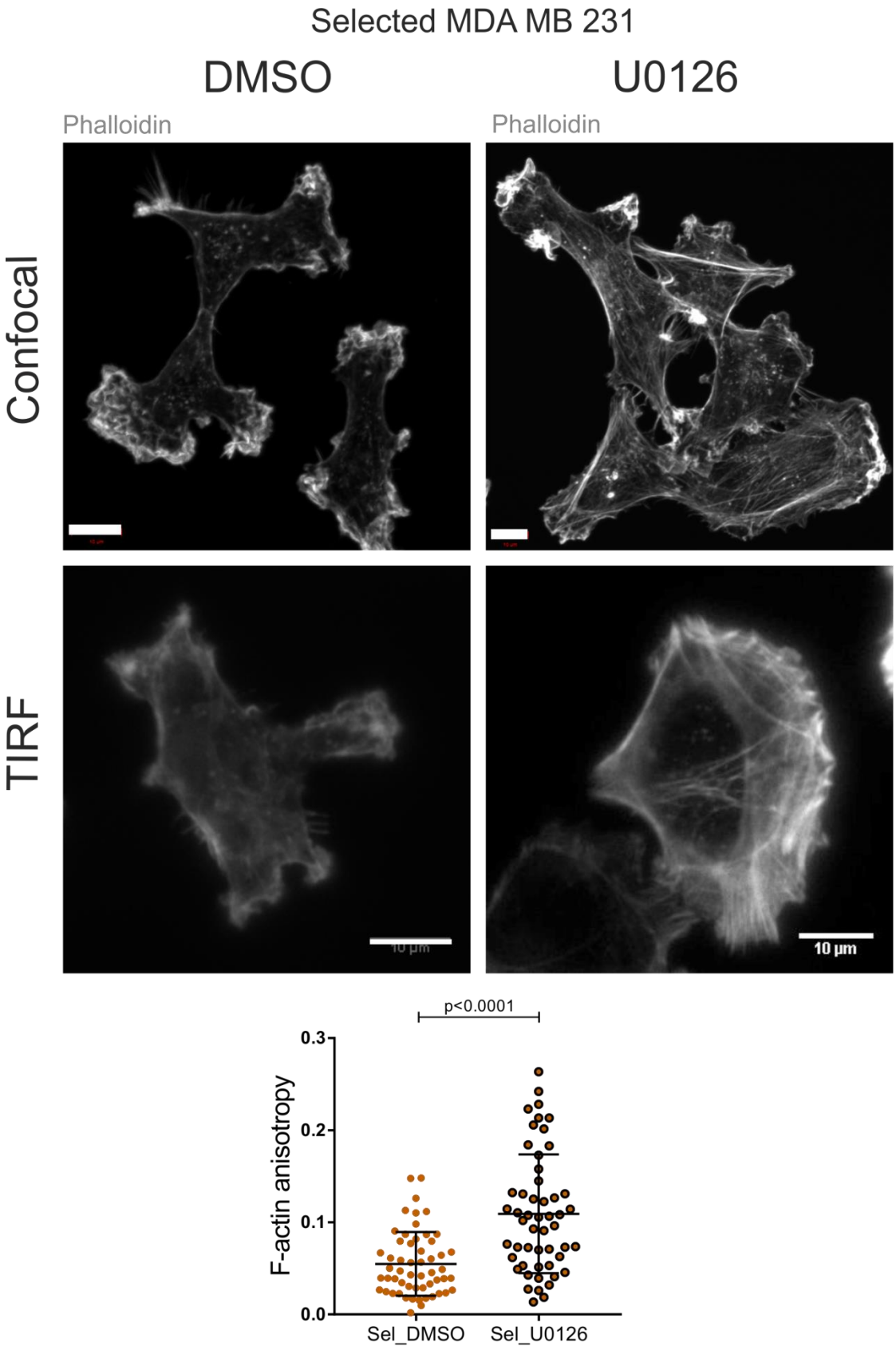

Figure 6-13 U0126 treatment restores actin structures in Selected MDA MB 231 cells.
Top panel – representative maximal projection images of phalloidin-stained Selected MDA MB 231 cells treated with DMSO or U0126. Images were acquired on a Zeiss 710 confocal microscope. Bottom panel - representative images of phalloidin-stained Selected MDA MB 231 cells treated with DMSO or U0126. Images were acquired on a TIRF microscope. Scale bar = 10 µm. The bottom graph depicts mean (± SD) F-actin anisotropy for DMSO and U0126-treated Selected MDA MB 231 cells. Data represent individual cells pooled from n = 3 independent experiments. Statistical significance determined by Mann - Whitney test.

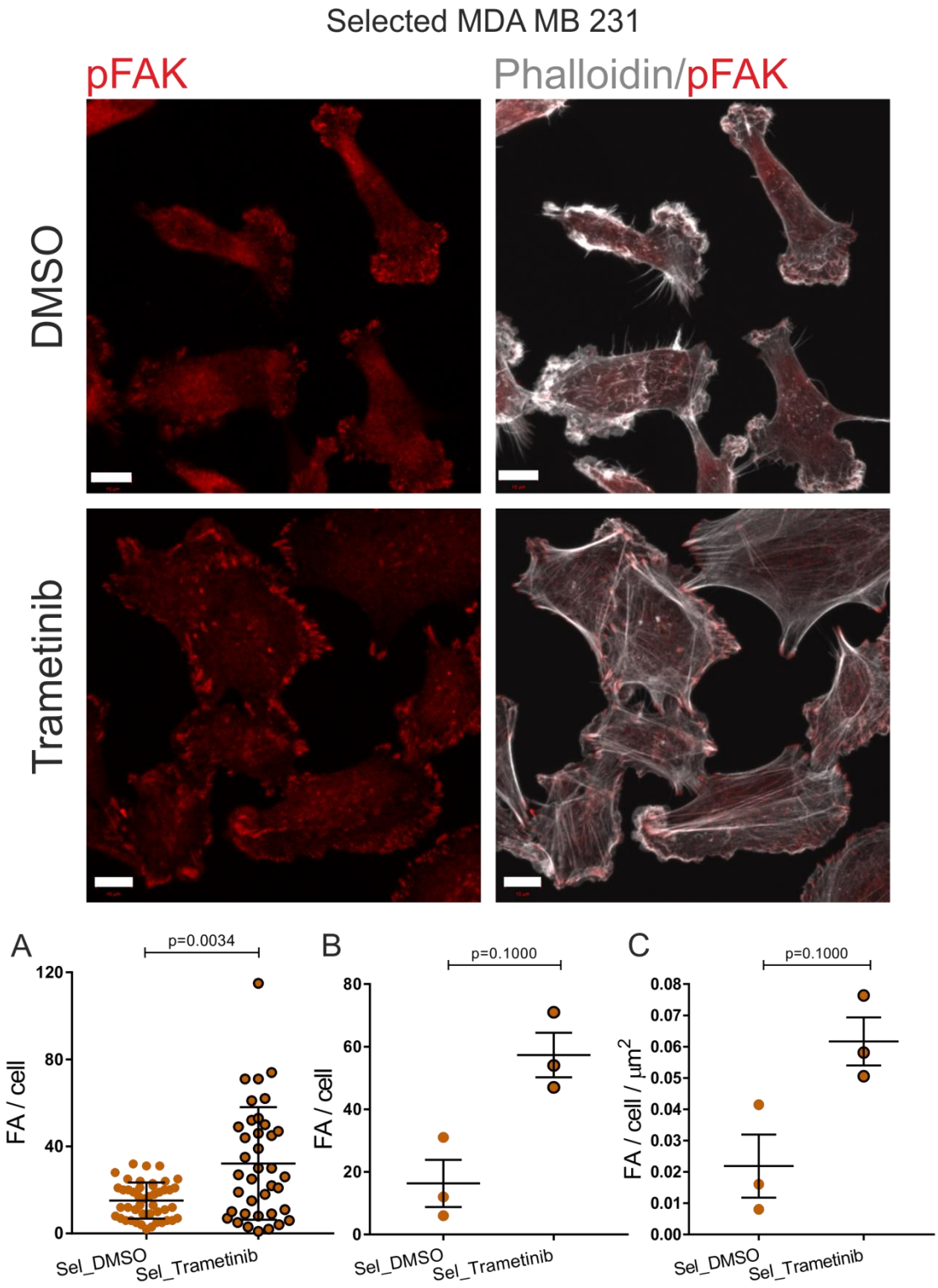

Figure 6-14 Trametinib treatment restores focal adhesions in Selected MDA MB 231 cells. Representative images of pFAK-stained Selected MDA MB 231 cells treated with Trametinib or DMSO. The images were acquired on a Zeiss 710 confocal microscope. Scale bar = 10 µm. A) Graph depicts focal adhesions per individual cell. Data depicts individual cells pooled from n = 3 independent experiments, with mean (± SD) indicated. B) Graph depicts mean (± SEM) focal adhesions per cell (n = 12 – 15 cells per experiment). Data from n = 3 independent experiments. C) Mean (± SEM) focal adhesions per cell per mean cell area (n = 12 – 15 cells per experiment). Data pooled from n = 3 independent experiments. Statistical significance determined by Mann - Whitney test.

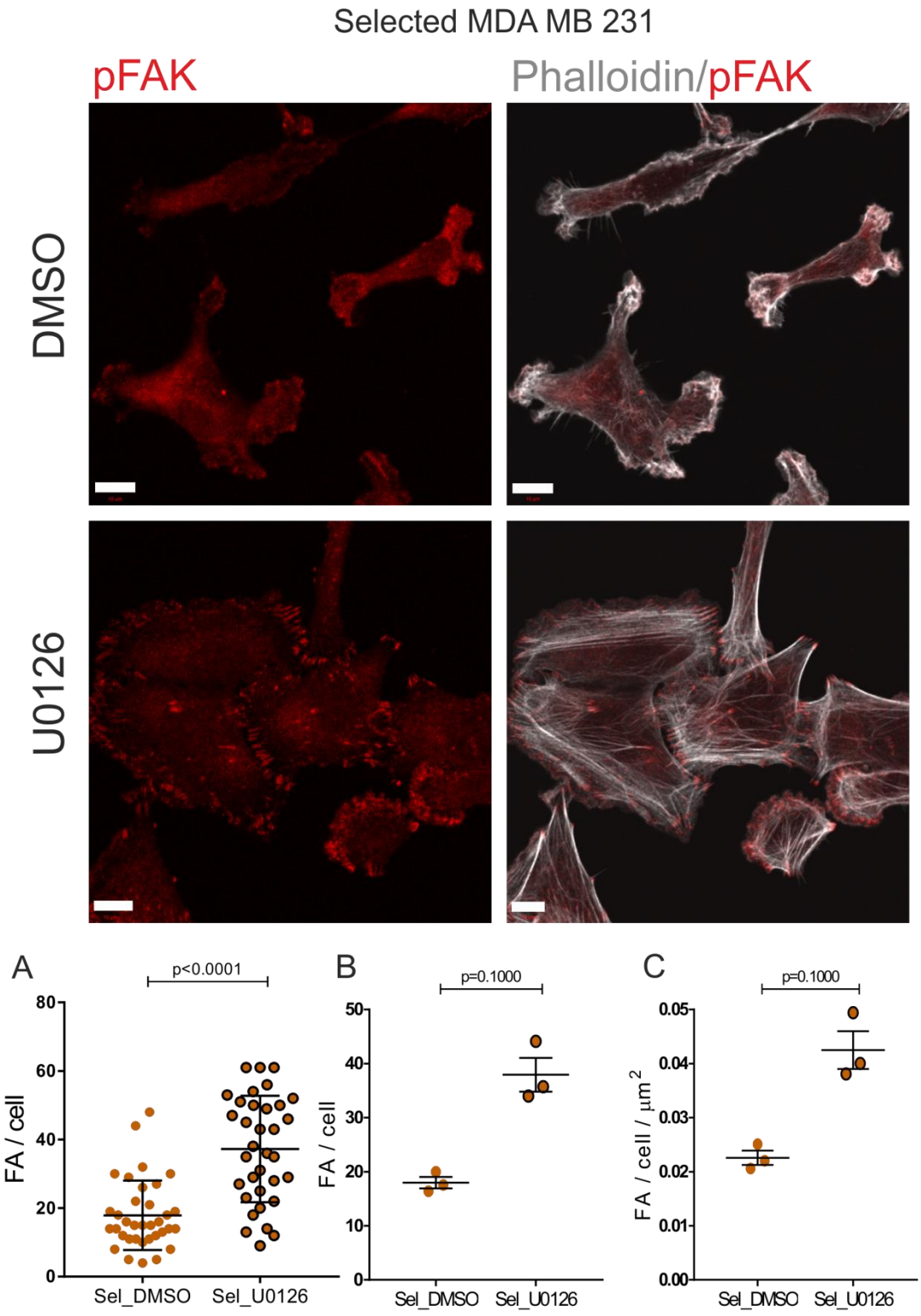

Figure 6-15 U0126 treatment restores focal adhesions in Selected MDA MB 231 cells. Representative images of pFAK-stained Selected MDA MB 231 cells treated with U0126 or DMSO. The images were acquired on a Zeiss 710 confocal microscope. Scale bar = 10 µm. A) Graph depicts focal adhesions per individual cell. Data depicts individual cells pooled from n = 3 independent experiments, with mean (± SD) indicated. B) Graph depicts mean (± SEM) focal adhesions per cell (n = 12 – 15 cells per experiment). Data from n = 3 independent experiments. C) Mean (± SEM) focal adhesions per cell per mean cell area (n = 12 – 15 cells per experiment). Data pooled from n = 3 independent experiments. Statistical significance determined by Mann - Whitney test.

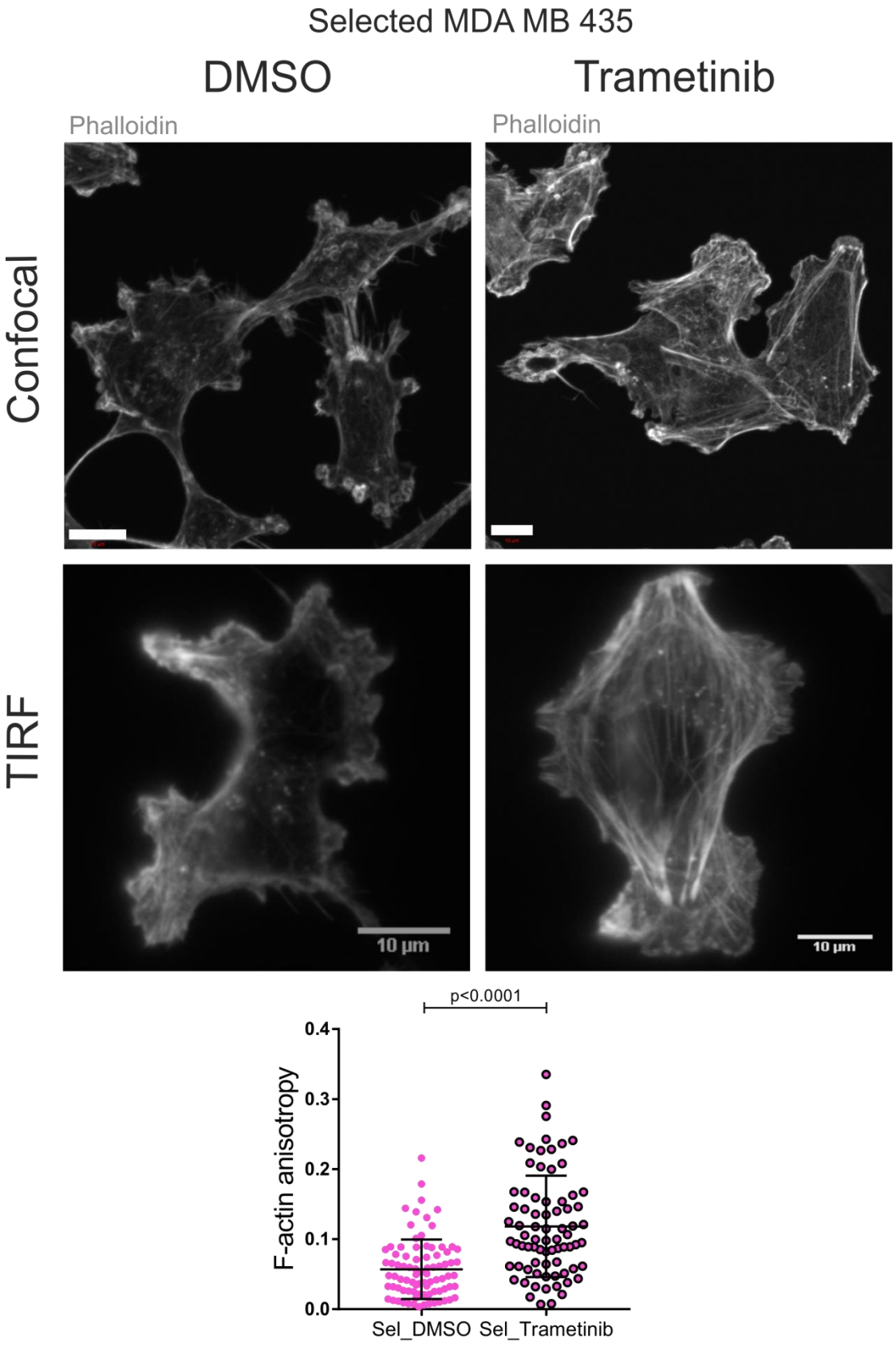

Figure 6-16 Trametinib treatment restores actin structures in Selected MDA MB 435 cells. Top panel – representative maximal projection images of phalloidin-stained Selected MDA MB 435 cells treated with DMSO or Trametinib. Images were acquired on a Zeiss 710 confocal microscope. Bottom panel - representative images of phalloidin-stained Selected MDA MB 435 cells treated with DMSO or Trametinib. Images were acquired on a TIRF microscope. Scale bar = 10 µm. The bottom graph depicts mean (± SD) F-actin anisotropy for DMSO and Trametinib-treated Selected MDA MB 435 cells. Data represent individual cells pooled from n = 3 independent experiments. Statistical significance determined by Mann - Whitney test.

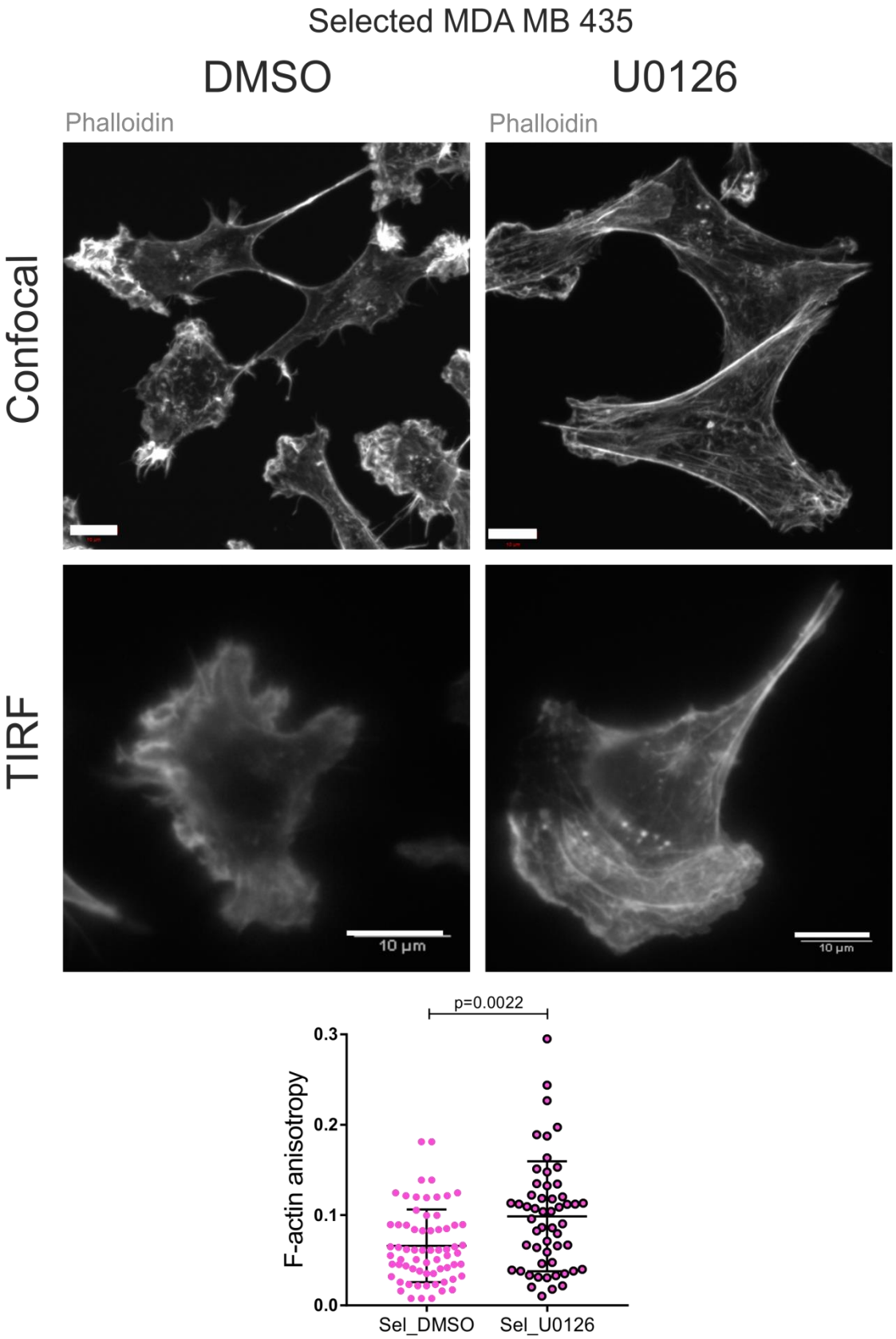

Figure 6-17 U0126 treatment restores actin structure in Selected MDA MB 435 cells.
Top panel – representative maximal projection images of phalloidin-stained Selected MDA MB 435 cells treated with DMSO or U0126. Images were acquired on a Zeiss 710 confocal microscope. Bottom panel - representative images of phalloidin-stained Selected MDA MB 435 cells treated with DMSO or U0126. Images acquired on a TIRF microscope. Scale bar = 10 µm. The bottom graph depicts mean (± SD) F-actin anisotropy for DMSO and U0126-treated Selected MDA MB 435 cells. Data represent individual cells pooled from n = 3 independent experiments. Statistical significance determined by Mann - Whitney test.

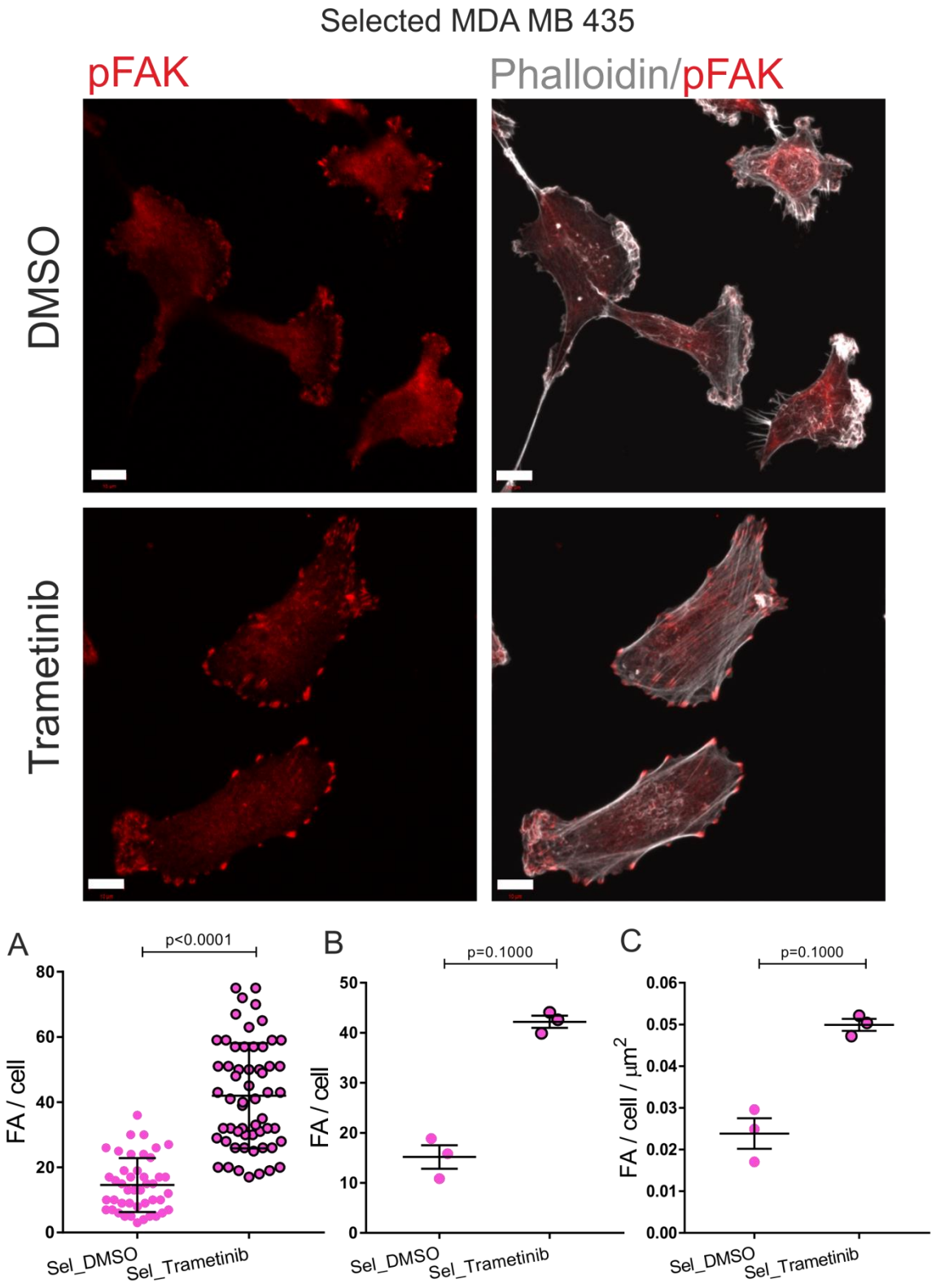

Figure 6-18 Trametinib treatment restores focal adhesions in Selected MDA MB 435 cells. Representative images of pFAK-stained Selected MDA MB 435 cells treated with Trametinib or DMSO. The images were acquired on a Zeiss 710 confocal microscope. Scale bar = 10 µm. A) Graph depicts focal adhesions per individual cell. Data depicts individual cells pooled from n = 3 independent experiments, with mean (± SD) indicated. B) Graph depicts mean (± SEM) focal adhesions per cell (n = 12 – 15 cells per experiment). Data from n = 3 independent experiments. C) Mean (± SEM) focal adhesions per cell per mean cell area (n = 12 – 15 cells per experiment). Data pooled from n = 3 independent experiments. Statistical significance determined by Mann - Whitney test.

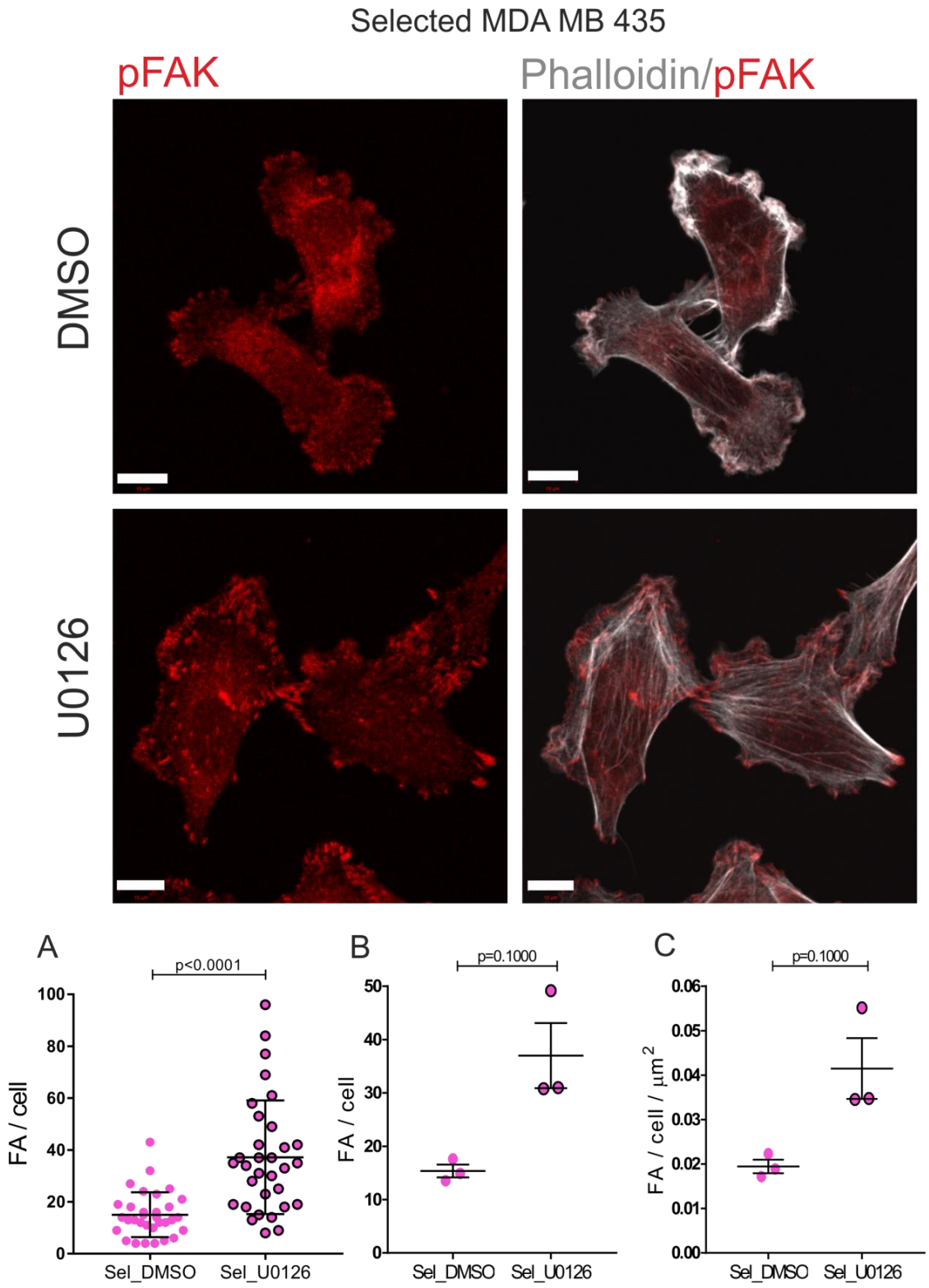

Figure 6-19 U0126 treatment restores focal adhesions in Selected MDA MB 435 cells. Representative images of pFAK-stained Selected MDA MB 435 cells treated with U0126 or DMSO. The images were acquired on a Zeiss 710 confocal microscope. Scale bar = 10 µm. A) Graph depicts focal adhesions per individual cell. Data depicts individual cells pooled from n = 3 independent experiments, with mean (± SD) indicated. B) Graph depicts mean (± SEM) focal adhesions per cell (n = 12 – 15 cells per experiment). Data from n = 3 independent experiments. C) Mean (± SEM) focal adhesions per cell per mean cell area (n = 12 – 15 cells per experiment). Data pooled from n = 3 independent experiments. Statistical significance determined by Mann - Whitney test.

6.2.8 MEK inhibition leads to increased cell stiffness

After establishing that inhibition of the Ras-RAF-MEK-ERK pathway with two MEK inhibitors, Trametinib and U0126, led to F-actin restoration in pore-selected MDA MB 231 and MDA MB 435 cells, next I wanted to investigate whether the MAPK/ERK pathway was involved in cell rigidity modulation. In order to evaluate this relationship, AFM measurements were performed on Trametinib-treated MDA MB 231 and MDA MB 435 cells. AFM measurements were performed in collaboration with the Engineering Department at University of Glasgow. In brief, cells were seeded in 3 cm petri dishes and incubated 24 hours in standard tissue culture conditions. After incubation, cells were treated with 0.5 μM Trametinib or control cells with DMSO, and incubated for 24 hours prior to AFM measurements. During the experiment, cells were kept in culture conditions and 1% HEPES was added to the media to maintain pH levels. Cells were probed with a 4.74 μm diameter spherical bead and force of 3 nN. Five measurements were taken over the nuclear area and an average value of Young's modulus was determined per cell. The analysis revealed that MEK inhibition led to an increase of cell stiffness in all sub-populations of MDA MB 231 and MDA MB 435 cells (Figure 6-20). These results suggested that the MAPK/ERK pathway is not only involved in the regulation of cell cytoskeleton organisation but also in the modulation of cell elasticity.

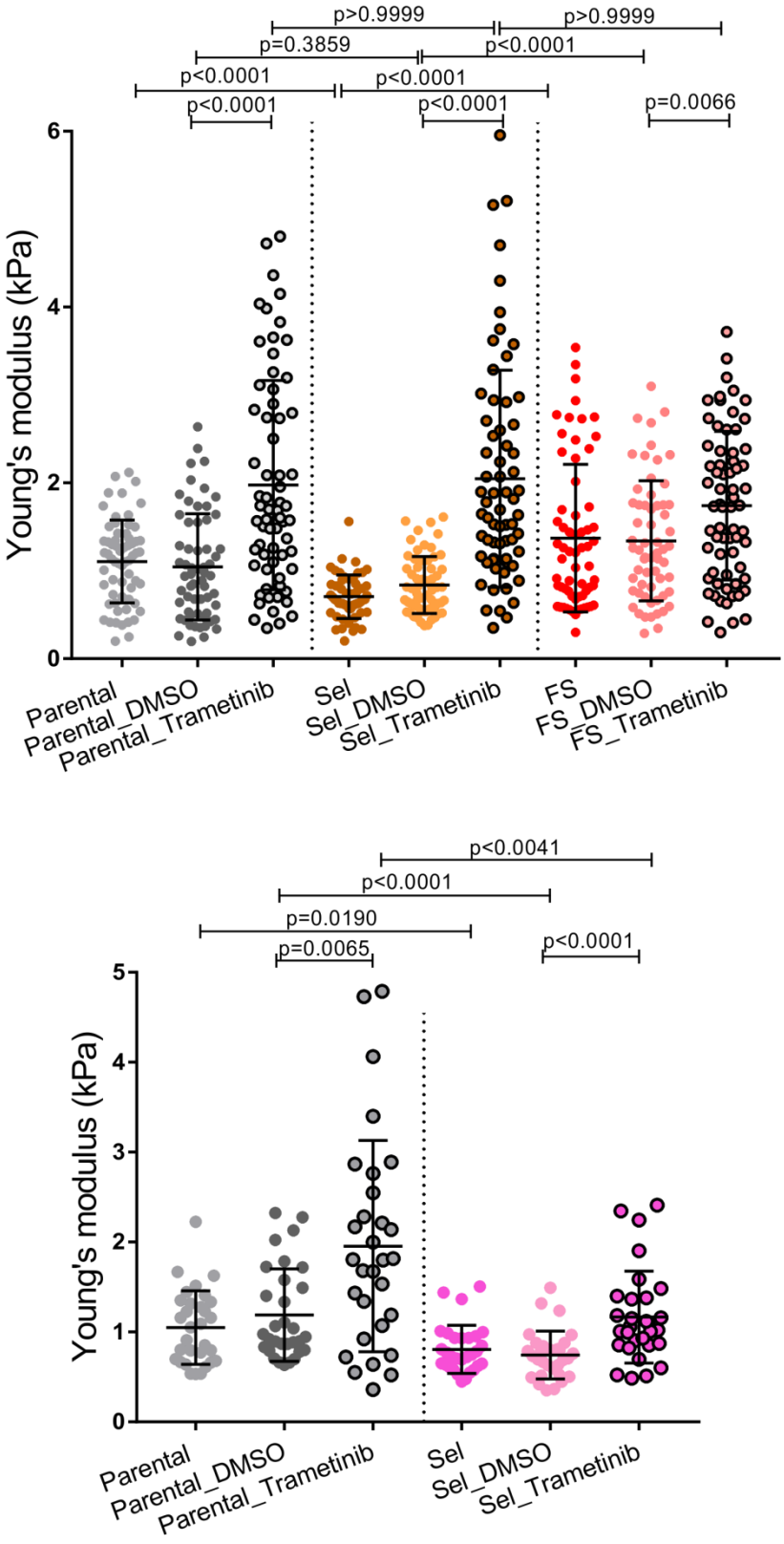

Figure 6-20 MEK inhibition leads to increased cell stiffness.
The top graph represents mean (± SD) Young's modulus of Parental, Selected and Flow sorted MDA MB 231 cells treated with Trametinib or DMSO. Data represent individual cells pooled from n = 2 independent experiments. Statistical significance of multiple comparisons was determined by Kruskal – Wallis followed by Dunn's multiple comparison test. DMSO vs Trametinib-treated cells were compared by Mann - Whitney test. The bottom graph represents mean (± SD) Young's modulus of Parental and Selected MDA MB 435 cells treated with Trametinib or DMSO. Data represent individual cells from n = 1 experiment. Statistical significance determined by Mann - Whitney test.

6.2.9 MEK inhibition restrains invasion by pore-selected MDA MB 231 and MDA MB 435 cells

Having shown that MEK inhibition led to restoration of actin cytoskeleton structures, and increased cell stiffness in pore-selected MDA MB 231 and MDA MB 435 cells, the effect on the collagen invasion assay was next investigated following U0126 treatment. In order to prepare collagen plugs, human primary fibroblasts were mixed with rat tail collagen1 and left for a week to allow conditioning of the collagen. The fibroblasts were then removed by treating the collagen disks with puromycin for 48 hours and subsequently washed twice with PBS. Once the matrices were prepared, cells were seeded on top and allowed to invade the collagen for 8 days. MEM/EBSS complete media containing 10 μM U0126 or DMSO was added to the dishes as indicated. Media was changed every other day. After 8 days of invasion, collagen disks were fixed, paraffin-embedded and stained with H&E, and individual cell invasion distances were quantified using ImageJ. The analysis revealed that upon U0126 treatment, pore-selected MDA MB 231 (Figure 6-21) and MDA MB 435 (Figure 6-22) cells invaded less deeply into the collagen relative to DSMO-treated control cells, suggesting that the rebuilding of actin cytoskeleton structures and increased cell stiffness dictated the invasive ability of pore-selected cells.

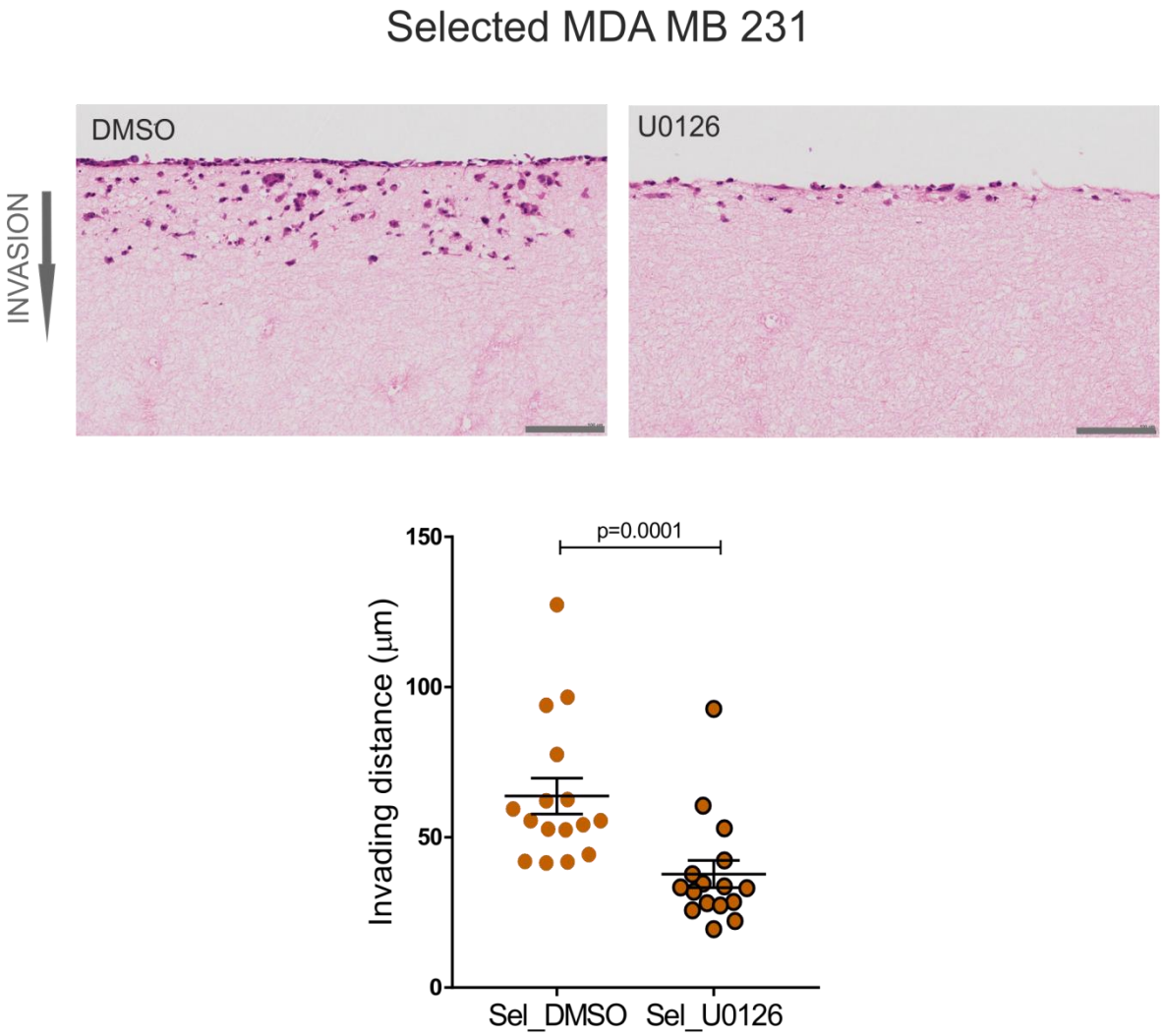

Figure 6-21 U0126 treatment of pore-selected MDA MB 231 cells restrains invasion. Representative images of invading cells into the collagen matrix for pore-selected MDA MB 231 cells treated with DMSO or U0126. Scale bar = 100 µm. Graph depicts mean (± SEM) travelled distance for Selected MDA MB 231 cells treated with DMSO or U0126. Data pooled from n = 3 independent experiments. Statistical significance determined by Mann - Whitney test.

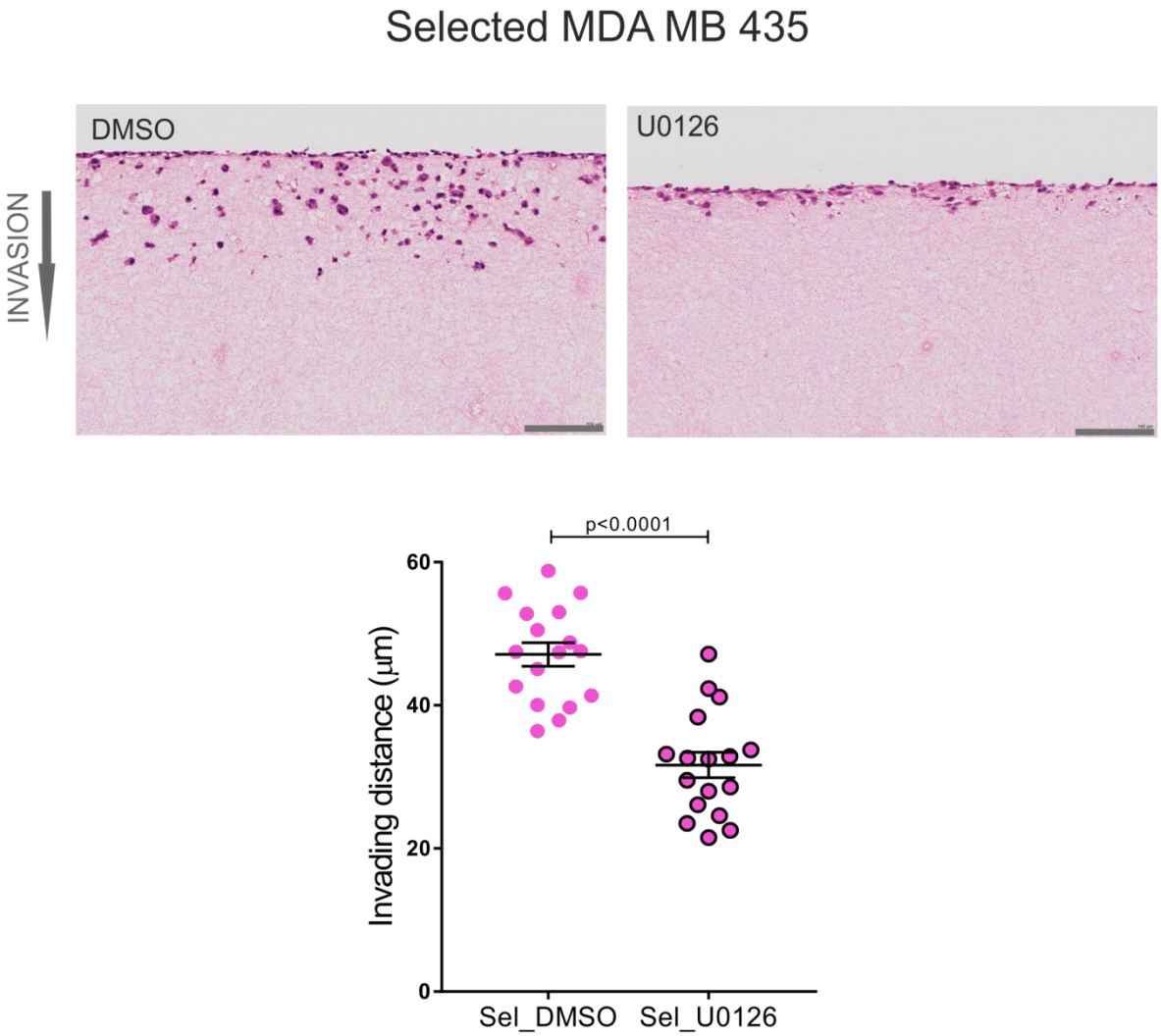

Figure 6-22 U0126 treatment of pore-selected MDA MB 435 cells restrains cell invasion. Representative images of invading cells into the collagen matrix for pore-selected MDA MB 435 cells treated with DMSO or U0126. Scale bar = 100 µm. Graph depicts mean (± SEM) travelled distance for Selected MDA MB 435 cells treated with DMSO or U0126. Data pooled from n = 3 independent experiments. Statistical significance determined by Mann - Whitney test.

6.2.10 Trametinib treated cells migrate slower and shorter distances

Having identified enhanced cell motility of Selected MDA MB 231 and MDA MB 435 cells with an individual cell migration assay, I next wanted to investigate whether MEK inhibition had an effect on cell motility. In order to perform an individual cell migration assay, 5,000 cells were seeded per well in a 24-well plate and subsequently incubated overnight in standard tissue culture conditions. The next day, cells were treated with 0.5 μM Trametinib or 10 μM U0126, control cells with DMSO, for 24 hours and subsequently placed in a Nikon TE 2000 Time Lapse Microscope in which images were acquired every 15 minutes for 22 hours. Individual cells were tracked for 45 frames excluding dividing cells using a Manual tracking tool in ImageJ. Migration velocity, accumulated distance and Euclidean distance were measured using the Chemotaxis plug-in in ImageJ. From this experiment I found that, Trametinib or U0126-treated Parental, Selected and Flow sorted MDA MB 231 cells (Figure 6-23) (Figure 6-24), and Parental and Selected MDA MB 435 cells (Figure 6-25) (Figure 6-26) migrated slower and shorter distance relative to DMSO-treated control cells.

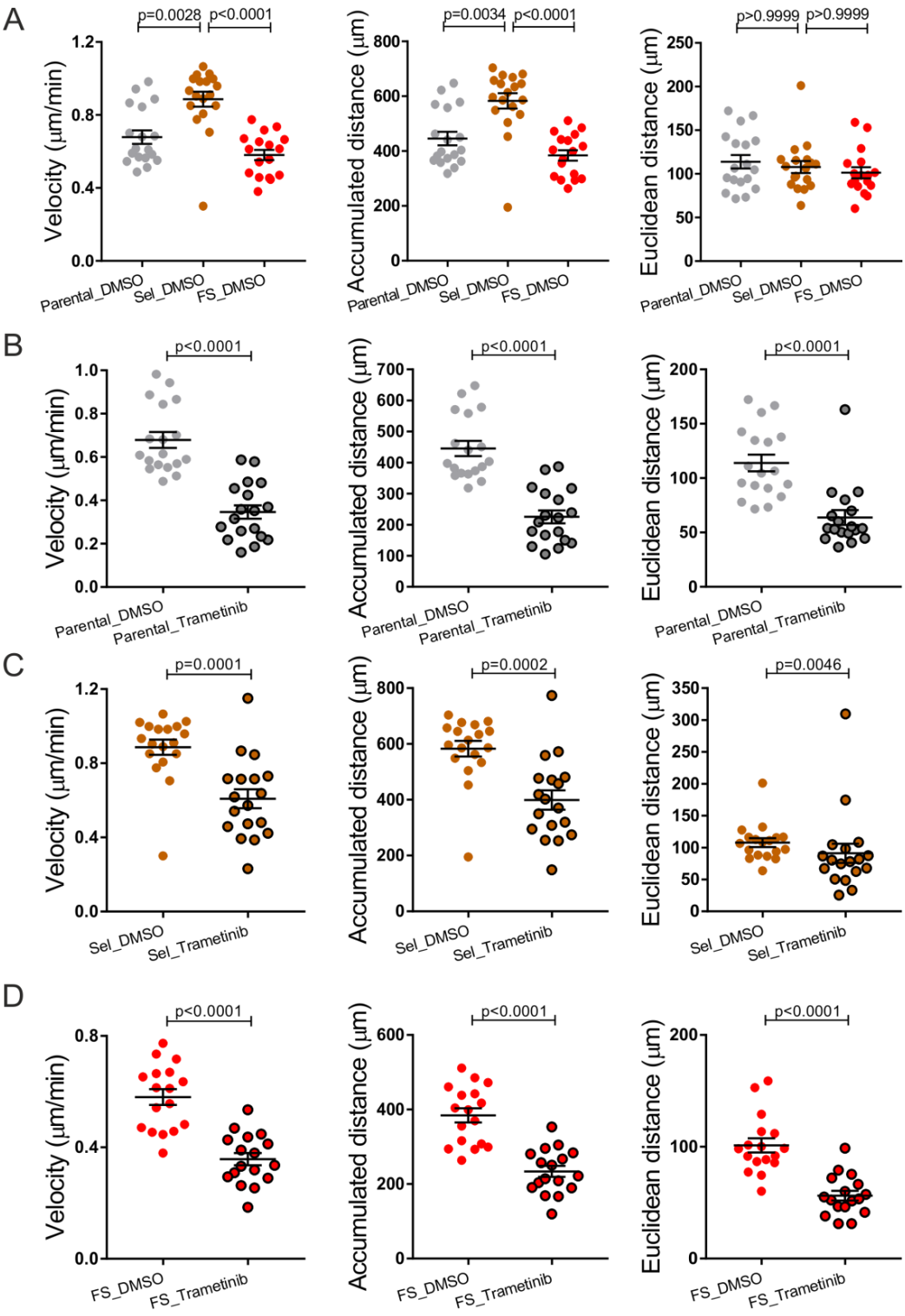

Figure 6-23 MDA MB 231 cells treated with Trametinib migrate slower and shorter distance. A) Graphs represent mean (± SEM) velocity, accumulated distance and Euclidean distance for Parental, Selected and Flow sorted MDA MB 231 cells treated with DMSO. Statistical significance determined by Kruskal – Wallis followed by Dunn's multiple comparison test. B) Graphs represent mean (± SEM) velocity, accumulated distance and Euclidean distance for Parental MDA MB 231 cells treated with 0.5 µM of Trametinib or DMSO. C) Graphs represent mean (± SEM) velocity, accumulated distance and Euclidean distance for Selected MDA MB 231 cells treated with 0.5 µM of Trametinib or DMSO. D) Graphs represent mean (± SEM) velocity, accumulated distance and Euclidean distance for Flow sorted MDA MB 231 cells treated with 0.5 µM of Trametinib or DMSO. Each dot represents a mean of n ≥ 8 tracked cells. Data pooled from n = 3 independent experiments. Statistical significance determined by Mann - Whitney test.

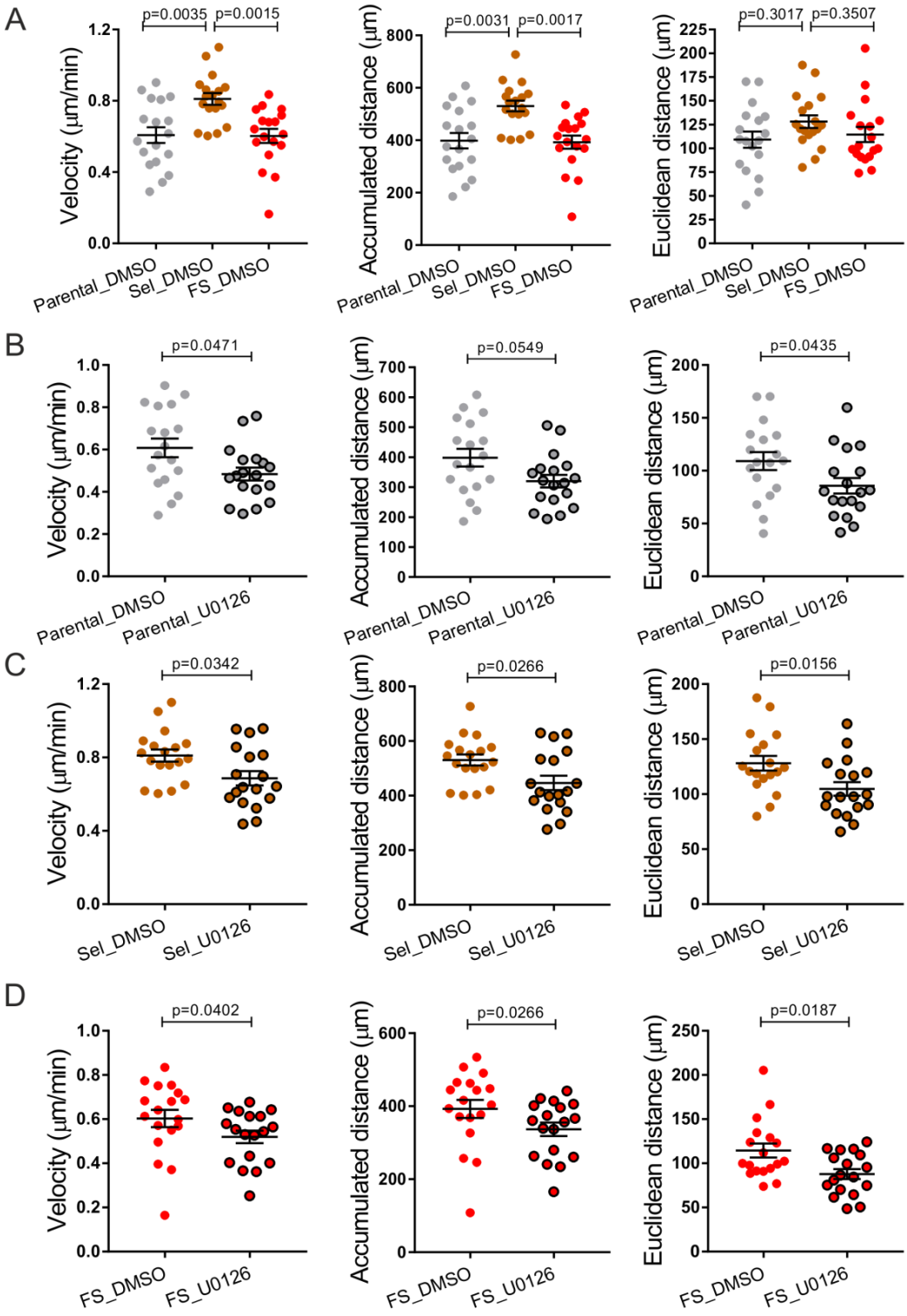

Figure 6-24 MDA MB 231 cells treated with U0126 migrate slower and shorter distance.
A) Graphs represent mean (± SEM) velocity, accumulated distance and Euclidean distance for Parental, Selected and Flow sorted MDA MB 231 cells treated with DMSO. Statistical significance determined by Kruskal – Wallis followed by Dunn's multiple comparison test. B) Graphs represent mean (± SEM) velocity, accumulated distance and Euclidean distance for Parental MDA MB 231 cells treated with 10 µM of U0126 or DMSO. C) Graphs represent mean (± SEM) velocity, accumulated distance and Euclidean distance for Selected MDA MB 231 cells treated with 10 µM of U0126 or DMSO. D) Graphs represent mean (± SEM) velocity, accumulated distance and Euclidean distance for Flow sorted MDA MB 231 cells treated with 10 µM of U0126 or DMSO. Each dot represents a mean of n ≥ 8 tracked cells. Data pooled from n = 3 independent experiments. Statistical significance determined by Mann - Whitney test.

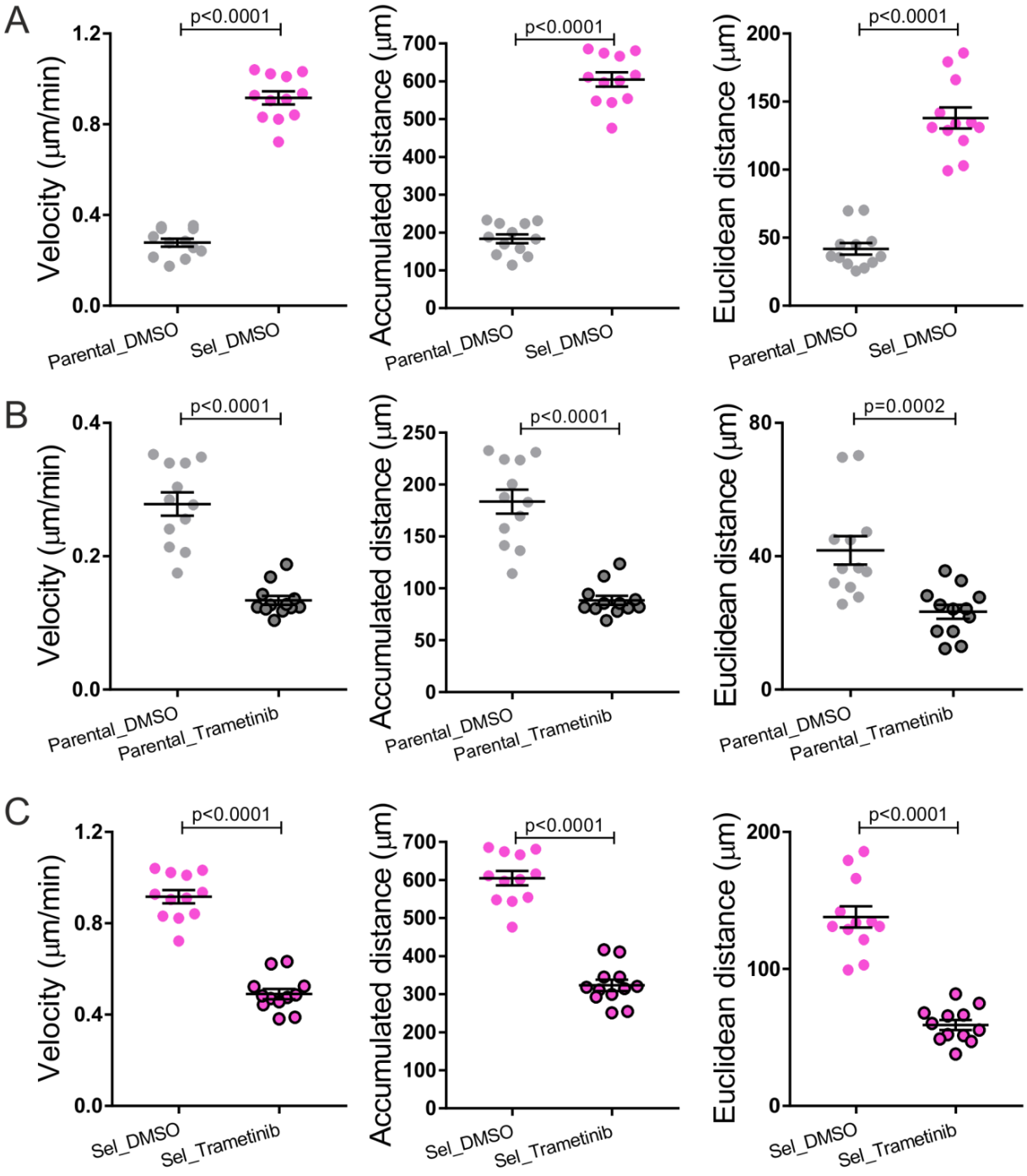

Figure 6-25 MDA MB 435 cells treated with Trametinib migrate slower and shorter distance. A) Graphs represent mean (± SEM) velocity, accumulated distance and Euclidean distance for Parental and Selected MDA MB 435 cells treated with DMSO. B) Graphs represent mean (± SEM) velocity, accumulated distance and Euclidean distance for Parental MDA MB 435 cells treated with 0.5 µM of Trametinib or DMSO. C) Graphs represent mean (± SEM) velocity, accumulated distance and Euclidean distance for Selected MDA MB 435 cells treated with 0.5 µM of Trametinib or DMSO. Data pooled from n = 2 independent experiments. Statistical significance determined by Mann - Whitney test.

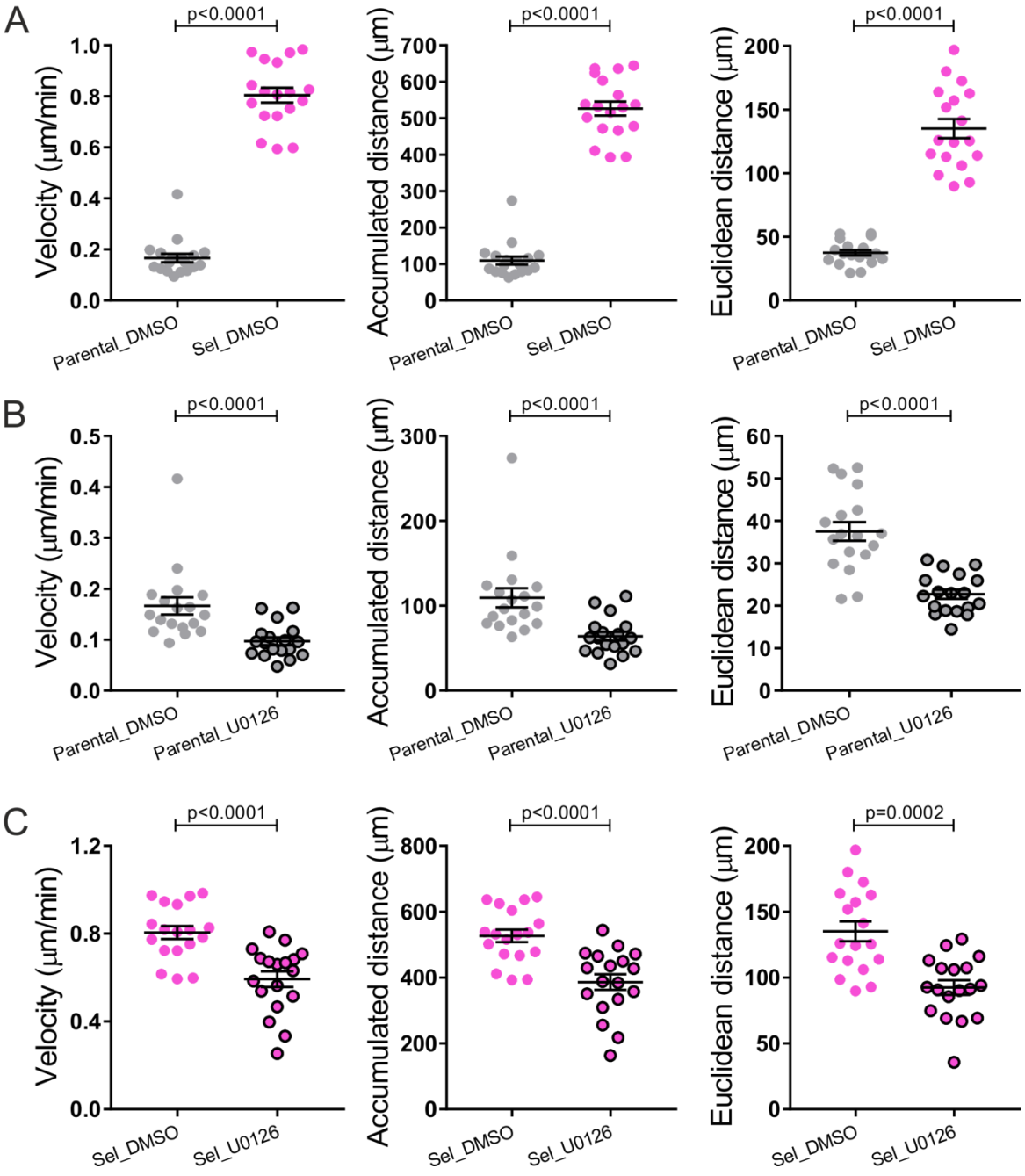

Figure 6-26 MDA MB 435 cells treated with U0126 migrate slower and shorter distance.
A) Graphs represent mean (± SEM) velocity, accumulated distance and Euclidean distance for Parental and Selected MDA MB 435 cells treated with DMSO. B) Graphs represent mean (± SEM) velocity, accumulated distance and Euclidean distance for Parental MDA MB 435 cells treated with 10 µM of U0126 or DMSO. C) Graphs represent mean (± SEM) velocity, accumulated distance and Euclidean distance for Selected MDA MB 435 cells treated with 10 µM of U0126 or DMSO. Data pooled from n = 3 independent experiments. Statistical significance determined by Mann - Whitney test.

6.2.11 Trametinib treated Selected MDA MB 231 spread more relative to Parental and Flow sorted MDA MB 231 cells

Having identified decreased cell spreading of pore-selected MDA MB 231 relative to Parental MDA MB 231 cells, I next wanted to find out whether MEK inhibition had an effect on cell spreading. In order to evaluate this behaviour, I utilised two different approaches. First, I used Operetta High Content Imaging System to quantify the areas of cells treated with Trametinib or DMSO. In the second approach, spreading properties, with and without Trametinib treatment, was investigated using the xCelligence Real-Time Cell Analyzer (RTCA) system.

In order to measure cell area with the Operetta System, 10,000 cells were seeded in black 96-well plates. Following 24-hour incubation, cells were treated with 10 μM Trametinib, or control cells with DMSO, and subsequently incubated for 24 hours in standard tissue culture conditions. After incubation, cells were fixed and stained with DAPI and Whole Cell Stain (WCS). The analysis of cell areas revealed that DMSO-treated Selected MDA MB 231 had smaller cell areas compared to DSMO-treated Parental and Flow sorted MDA MB 231 cells. Upon Trametinib treatment, Selected and Flow sorted MDA MB 231 cells spread significantly more than Parental MDA MB 231 cells (Figure 6-27).

The RTCA system is impendence-based and allows monitoring of cell spreading in real-time. Special plates called E-plates that were used in this assay have micro electrodes integrated at the bottom of the plate which allow measurement of changes in electrical impendence across the plate due to cell spreading. In order to perform the experiment, 10,000 cells were seeded per well, the plates were placed in the machine and scanned every 5 minutes for 5 hours. After 5 hours, 0.5 μM Trametinib was added and scanning was continued for the next 7 hours. The results revealed that DMSO-treated Selected MDA MB 231 cells have decreased spreading relative to DMSO-treated Parental and Flow sorted MDA MB 231 cells, while Trametinib treatment led to an increase of cell spreading only in Selected MDA MB 231 cells (Figure 6-28).

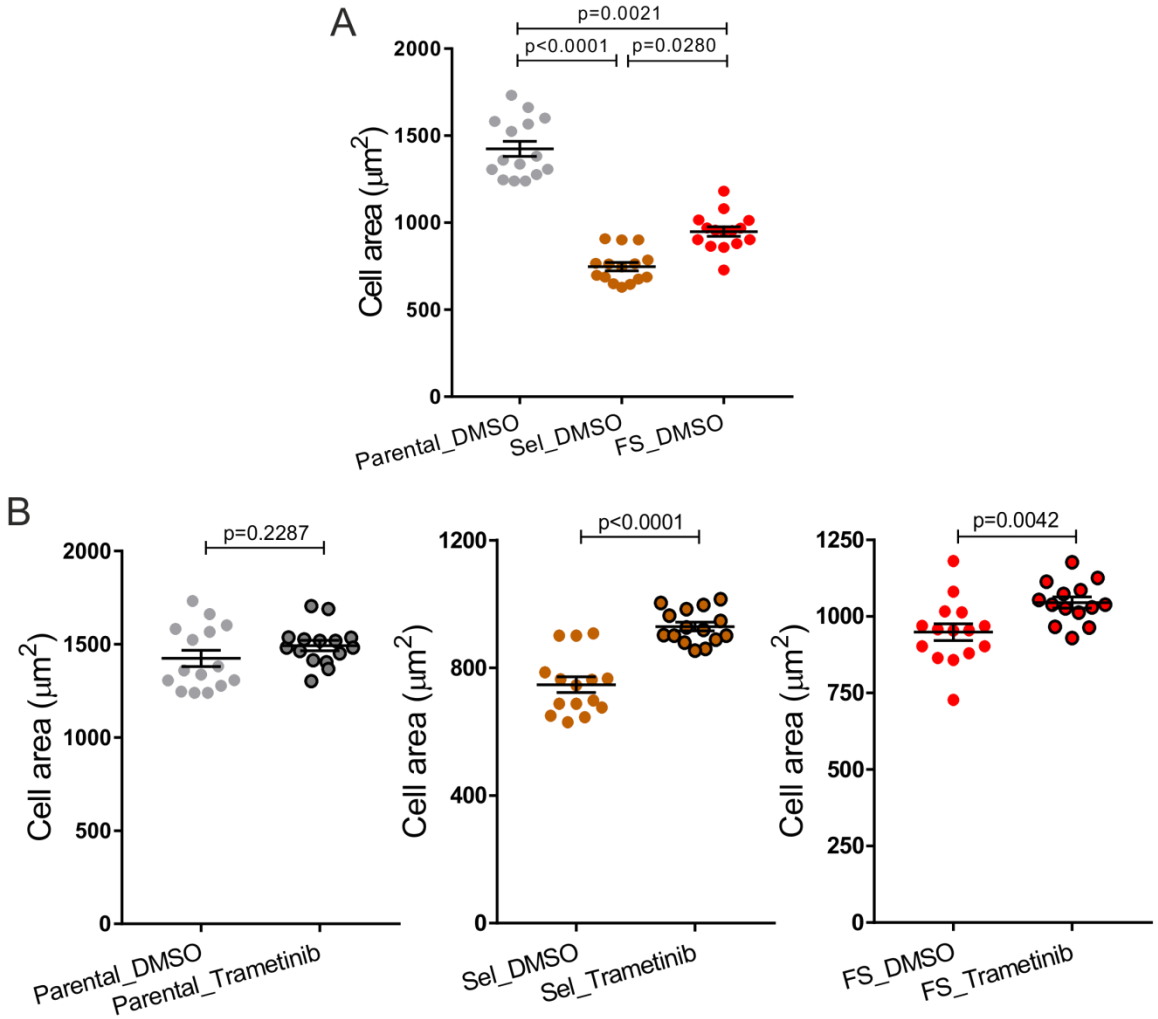

Figure 6-27 Trametinib-treated Selected MDA MB 231 cells spread more relative to Parental and Flow sorted MDA MB 231 cells.
A) Graph depicts mean (± SEM) cell area for Parental, Selected and Flow sorted MDA MB 231 cells treated with DMSO. Statistical significance determined by Kruskal – Wallis followed by Dunn's multiple comparison test. B) Graphs depict mean (± SEM) cell area for Parental, Selected and Flow sorted MDA MB 231 cells treated with DMSO or Trametinib. Each dot represents an average from n = 6 fields per well, from at least 200 cells per field. Data pooled from n = 3 independent experiments. Statistical significance determined by Mann - Whitney test.

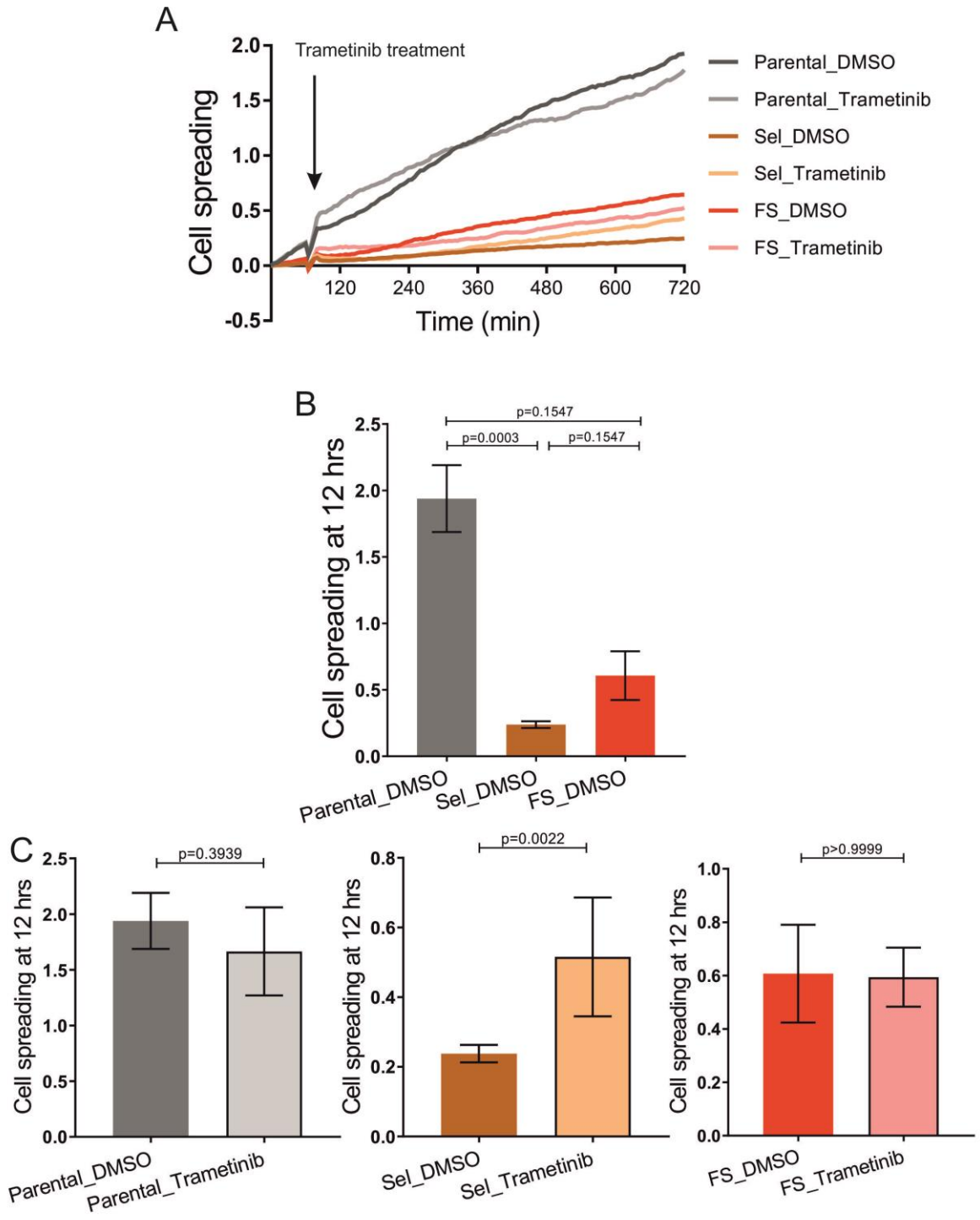

Figure 6-28 Trametinib-treated Selected MDA MB 231 cells spread more than Parental and Flow sorted MDA MB 231 cells.

A) Graph depicts cell spreading for Parental, Selected and Flow sorted MDA MB 231 cells treated with DMSO or Trametinib. B) Graph depicts mean (± SD) cell spreading at 12 hrs for Parental, Selected and Flow sorted MDA MB 231 cells treated with DMSO. Statistical significance determined by Kruskal – Wallis followed by Dunn's multiple comparison test. C) Graphs depict mean (± SD) cell spreading at 12 hrs for Parental, Selected and Flow sorted MDA MB 231 cells treated with DMSO or Trametinib. Data pooled from n = 2 independent experiments. Statistical significance determined by Mann - Whitney test.

6.2.12 Trametinib treated Parental and Selected MDA MB 435 cells spread more relative to DMSO

In order to investigate MDA MB 435 cell spreading properties upon Trametinib treatment, I utilised two different methods as detailed for MDA MB 231 cells. First, I used Operetta High Content Imaging System to quantify cell areas of cells treated with Trametinib or DMSO. In the second approach, spreading properties investigated using xCelligence Real-Time Cell Analyzer (RTCA) system.

Cell area analysis revealed that DMSO-treated Selected MDA MB 231 cells had decreased cell areas in comparison to DMSO-treated Parental cells. Trametinib treatment led to significantly increased cell areas of both Parental and Selected cells MDA MB 435 cells (Figure 6-29).

The analysis of cell spreading from using xCelligence Real-Time Cell Analyzer (RTCA) revealed that DSMO-treated Selected MDA MB 435 cells have decreased spreading relative to DMSO-treated Parental MDA MB 435 cells, while Trametinib treatment led to increased cell spreading of both Parental and Selected MDA MB 435 cells (Figure 6-30).

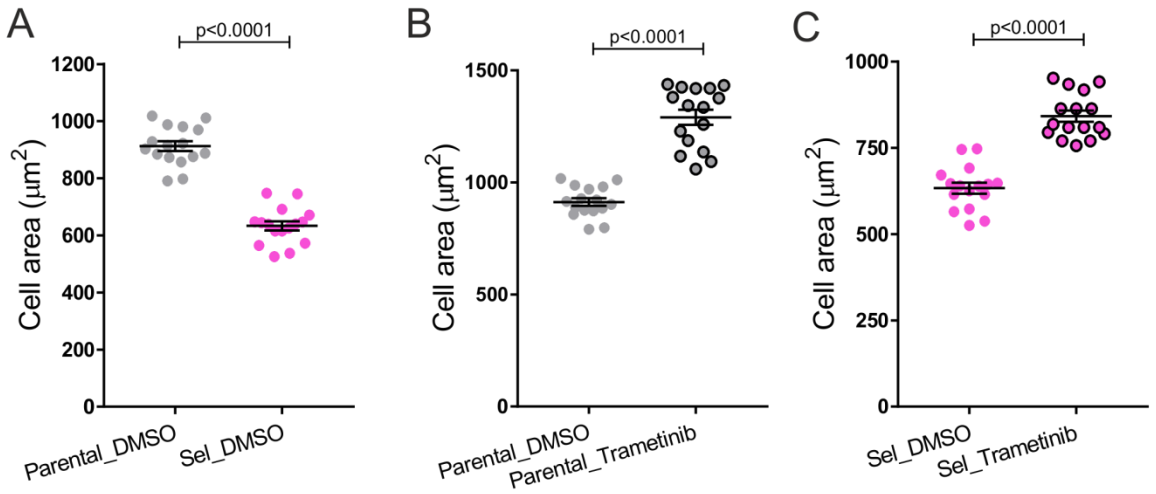

Figure 6-29 Parental and Selected MDA MB 435 cells treated with Trametinib spread more. A) Graph depicts mean (± SEM) of cell area for Parental and Selected MDA MB 435 cells treated with DMSO. B) Graph depicts mean (± SEM) of cell area for Parental MDA MB 435 cells treated with DMSO or Trametinib. C) Graph depicts mean (± SEM) of cell area for Selected MDA MB 435 cells treated with DMSO or Trametinib. Each dot represents an average from n = 6 fields per well, from at least 200 cells per field. Data pooled from n = 3 independent experiments. Statistical significance determined by Mann - Whitney test.

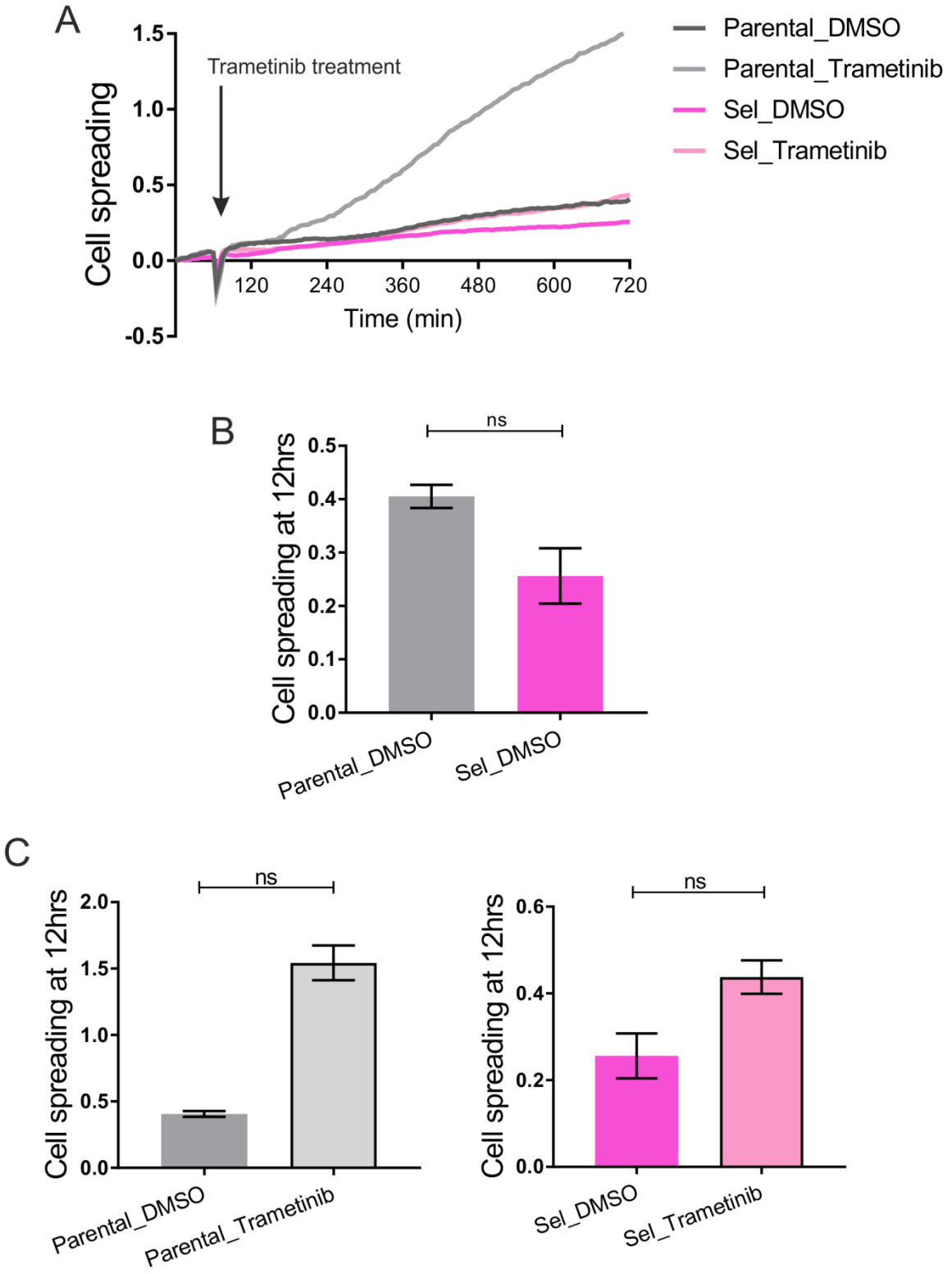

Figure 6-30 Trametinib-treated Parental and Selected MDA MB 435 cells spread more.
A) Graph depicts cell spreading for Parental and Selected MDA MB 435 cells treated with DMSO or Trametinib. B) Graph depicts mean (± SD) cell spreading at 12 hrs for Parental and Selected MDA MB 435 cells treated with DMSO. C) Graphs depicts mean (± SD) cell spreading at 12 hrs for Parental and Selected MDA MB 435 cells treated with DMSO or Trametinib. Data from n = 1 experiment. Statistical significance determined by Mann - Whitney test (ns = not significant).

6.3 Conclusions

To identify signalling pathways that influenced cytoskeletal and cell stiffness changes observed in pore-selected MDA MB 231 and MDA MB 435 cells, an RNA Sequencing experiment was performed. In this chapter, I have presented data showing that analysis of RNA - Seq by utilising Gene Set Enrichment Analysis (GSEA) allowed me to identify increased signalling through the Ras-Raf-MEK-ERK mitogen-activated protein kinase (MAPK) pathway in pore-selected MDA MB 231 and MDA MB 435 cells. Due to the fact that this pathway plays an important role in controlling many fundamental cellular processes, I decided to interrogate whether the observed alterations in the activity of the MAPK/ERK pathway were causally related to the cytoskeletal and stiffness changes in pore-selected cell lines. For this purpose, I decided to block the MAPK/ERK pathway by applying two different MEK inhibitors, Trametinib and U0126. I found that upon Trametinib or U0126 treatment, the actin organisation changed from primarily cortical to cytoplasmic fibrillary structures in pore-selected MDA MB 231 and MDA MB 435 cells. Additionally, pore-selected MDA MB 231 and MDA MB 435 cells were characterized by more mature and larger focal adhesion assemblies after MEK inhibitor treatment. Moreover, I found that MEK inhibition led to increased cell stiffness of all sub-populations of MDA MB 231 and MDA MB 435 cells. By utilising the collagen invasion assay, I found that blocking MEK restrained pore-selected cell invasion into the collagen. Furthermore, I found that MEK inhibition diminished cell motility and altered spreading of all sub-populations of MDA MB 231 and MDA MB 435 cells *in vitro*.

The results described above showed that MEK inhibition had an effect on all sub-populations of MDA MB 231 and MDA MB 435 cells in various experimental assays. Such an effect was not unexpected due to the fact that signalling through the MAPK/ERK pathway is maintained at a basal level in Parental and Flow sorted MDA MB 231, and Parental MDA MB 435 cells. Therefore blocking it with Trametinib or U0126 completely abolished its activity in all treated cell lines, as a consequence changes in different cell properties were observed.

7 Discussion

Cancer metastasis is a major problem in cancer. It is responsible for 90% of patient mortality, and yet it remains an incompletely understood process. The metastatic cascade involves multiple steps, such as invasion of surrounding tissue, intravasation, transit through blood or lymphatic vessels and extravasation to secondary organs (Mehlen and Puisieux 2006). Within primary tumours, due to highly selective processes, sub-populations of cancer cells gain traits which enable them to invade the tumour associated stroma through confined spaces, and subsequently survive the complex "journey" from the primary neoplasm to foreign tissues (Vanharanta and Massague 2013; Nguyen, Yoshida et al. 2016). During the metastatic "journey", cancer cells must invade through epithelial cell layers and dense extracellular matrix which, as detailed in the introduction, is composed of tunnel-like tracks or pores which range in size from 0.1 - 30 μm. Hence, a common feature of some of the steps in the metastatic cascade is the ability of cancer cells to squeeze through confined spaces. It is known that some cancer cells are more deformable than other cells, and have the ability to squeeze through available spaces, move to secondary sites and colonize the foreign tissue. However the pathways/factors leading to such phenotypes are still unknown. Therefore, acquiring detailed understanding of the molecular mechanisms that contribute to cancer cell constrained migration will help to identify potential drug targets to block tumour cell dissemination and improve patient outcomes. In order to identify factors associated with cytoskeletal and elasticity changes that subsequently contribute to enhanced constrained cell migration and invasive abilities, I utilized an *in vitro* selection strategy through 3 μm pores. I was able to select for cells with enhanced confined migration ability *in vitro*. Properties that were unique to both pore-selected cell lines were disorganized cell cytoskeleton and decreased cell stiffness. To pinpoint factors or signalling pathways responsible for such phenotypes, I applied an unbiased method - RNA Sequencing and was able to identify, for the first time, that Ras-Raf-MEK-ERK mitogen-activated protein kinase (MAPK) pathway was the modulator of cytoskeleton organization and stiffness, and subsequently involved in the enhanced invasive phenotype.

7.1 *In vitro* selection of cancer cells through 3 µm pores using cell culture inserts

The purpose of this part of the project was to separate invasive cancer cells with constrained migration capabilities from the parental tumour cell lines, and to apply a holistic approach to identify potential confined migration contributors. I chose the breast cancer (MDA MB 231-luc-D3H2LN) and melanoma cancer (MDA MB 435) cell lines as they are known to be highly heterogeneous, and because breast and melanoma tumours may be highly metastatic. In order to enrich for such cell sub-populations, I adopted a stringent selection strategy in which invasive cells were selected from MDA MB 231-luc-D3H2LN or MDA MB 435 cell populations based on their passage through 3 µm diameter constrictions in cell culture inserts that mimic gaps in dense extracellular matrix (ECM) or between cells. After three rounds, populations were selected that were significantly more migratory through 3 µm pores *in vitro* relative to Parental cells. Keeping in mind that cell size might have an impact on cell migration in 3D environments, I decided to test the hypothesis that cells with smaller volumes might have enhanced ability to migrate through physical hindrances. Having observed the smaller relative cell size of pore-selected cells, an additional selection strategy was employed. Using flow cytometry sorting, I was able to enrich Parental MDA MB 231 cells for as equivalently small as pore-selected MDA MB 231 cells. Having obtained the necessary control for cell size, I found that pore-selected MDA MB 231 cells were significantly more migratory *in vitro* through 3 µm pores relative to Parental and Flow sorted MDA MB 231 cells. This experimental set up allowed me to make an important conclusion that constrained migration capability was not entirely dependent on cell size. In fact, this finding can be supported by Lautscham *et al. (*Lautscham, Kammerer *et al. 2015).* They reported that cells' ability to migrate through narrow pores did not depend on cytoplasmic volume (total cell volume with subtracted nuclear volume). By utilising microfluidic devices with decreasing microchannels cross sections with an average pore size of 3 µm pores, they tested four different cancer cell lines of varying cell size, stiffness and adhesiveness on their ability to migrate through narrow channels and found that nuclear volume and cell adhesiveness were the main factors influencing constrained migration, but not cell size.

The next step was to find out whether the sub-populations of pore-selected cells exhibited invasive properties in more physiological relevant environments. It was first tested by using an *in vitro* 3D collagen invasion assay, and secondly, their growth and metastatic abilities were assessed *in vivo*. From these experiments, I found that pore-selected cells were not only characterized with constrained migration abilities but also they were more invasive in the 3D collagen assay *in vitro*. They were also more aggressive *in vivo* as shown by increased tumour volumes and weights for pore-selected MDA MB 231 cells, and by increased number of lung tumours in mice injected with pore-selected MDA MB 435 cells. These results revealed that the selection strategy enabled me to successfully separate invasive cancer cells with constrained migration ability, which is the key finding of this chapter, and to my knowledge this is the first described *in vitro* 3 μm pore selection strategy for invasive cancer cells. In the literature, there are studies describing *in vitro* selection of invasive sub-clones from varying cancer cell lines such as human breast cancer, human lung adenocarcinoma, primary human melanoma, human glioblastoma and human gastric cancer cell lines (Jacob, Bosserhoff et al. 1995; Chu, Yang et al. 1997; Peng, Ran et al. 2009; Abdelkarim, Vintonenko et al. 2011; Koo, Martin et al. 2012) using the Transwell invasion (also referred as Boyden chamber) method to study cancer cell metastatic process. However, these studies were focused on investigating different aspects of the metastatic cascade, typically the contribution of the extracellular matrix on the cancer progression. Therefore, researchers used Transwell membrane inserts with 8 μm pores coated with the basement-membrane gels, such as laminin-2, matrigel or basement membrane type-IV collagen. The investigators were able to successfully select invasive sub-cell lines from parental cells. In addition, these selected cell-lines also exhibited enhanced metastatic potential *in vivo*, consistent with my own results. This indicated that Transwell assay can be used as an *in vitro* strategy for selection of more invasive cancer cells.

There are numerous studies employing *in vivo* selection of highly metastatic cells from cancer cell lines, such as human pancreatic adenocarcinoma, human breast cancer, human melanoma and human lung adenocarcinoma (Bruns, Harbison et al. 1999; Clark, Golub et al. 2000; Gumireddy, Sun et al. 2007; Cai, Luo et al. 2015). In these studies, the investigators injected parental cancer cells into

immune-compromised mice subcutaneously, orthotopically or into the tail vein. The metastases were harvested and the tumour cells were re-injected into mice. After several rounds of selection, highly metastatic cells were obtained and their gene expression profiles were compared to parental cells. Such an *in vivo* selection model constitutes a relevant selection strategy due to the fact that it resembles the human situation. Moreover, the orthotopic injection of cancer cells necessitates the entire metastatic process for distant lesions to occur, consequently it provides a good approach for identifying genes associated with metastatic tropism. Nonetheless, due to the lack of a fully functional immune system in immune-compromised mice, the input of the immune system to metastatic progression cannot be evaluated. Moreover, such a selection strategy does not allow for studying a particular step of the metastatic cascade. This demonstrates that a variety of approaches can be useful for answering distinct scientific questions about different aspects of the metastatic process.

7.1.1 Nuclear properties in constrained cell migration

There are many *in vivo* studies demonstrating that nuclear deformation plays an important role during cancer cell dissemination (Yamauchi, Yang et al. 2005; Alexander, Koehl et al. 2008; Beadle, Assanah et al. 2008) as well as transendothelial migration (Voisin, Woodfin et al. 2009). Nuclear properties such as size, shape, and rigidity may impact the cells' ability to migrate through confined spaces in the extracellular environment. Wolf *et al.* (Wolf, Te Lindert et al. 2013) demonstrated that cells which size exceeded the diameter of the pore cross-section, and which were not able to proteolytically widen the pore size, experienced nuclear arrest and immobilization in the pore opening. Lautscham *et al.* (Lautscham, Kammerer et al. 2015) reported that the main obstacle for cancer cells to overcome the physical hindrance is the large nuclear volume, by comparing different cancer cell lines with varying nuclear size. In contrast to these papers, I found that the equivalently smaller nuclei size of pore-selected and flow sorted cells did not explain the enhanced confined migratory ability of pore-selected cells, which suggested that there were additional factors contributing to the confined migration capability of Selected MDA MB 231 cells.

The ability of the nucleus to deform depends on nuclear rigidity, which can be dictated by lamin A/C expression, chromatin content or chromatin condensation. Mutation in the *LMNA* gene coding for lamin A cause more than 300 diseases, referred to as laminopathies (Worman, Fong et al. 2009). Additionally, lamin A/C expression has been observed to be deregulated in many cancer types (Hutchison 2014). Cells derived from mice deficient for lamin A/C (*lamina*$^{-}$/$^{-}$*)* had significantly softer and fragile nuclei (Lammerding, Schulze et al. 2004). Many studies have reported that the deregulation of lamin A/C expression impaired cell migration in 2D environments. Furthermore low levels of lamin A/C facilitated 3 μm pore migration (Harada, Swift et al. 2014), while increased lamin A/C expression resulted in cell migration impairment (Rowat, Jaalouk et al. 2013). In order to reveal potential determinants of enhanced confined migration capability of pore-selected cells, the mechanical properties of the nucleus were investigated. The results revealed that pore-selected and flow-sorted MDA MB 231 cells had stiffer nuclei compared to Parental MDA MB 231 cells, in spite of the fact that lamin A/C expression was diminished in those cell-types. First, it revealed that the augmented nuclear stiffness of pore-selected cells did not explain its enhanced confined migration. Second, the possible explanation for the discrepancy between enhanced nuclei stiffness and decreased lamin A/C expression could be that lamin A/C are not the only determinants of nuclear rigidity. In fact, it is unclear whether lamin A/C or chromatin content/condensation is most responsible for changes in nuclei stiffness. In the study conducted by Pajerowski *et al*. (Pajerowski, Dahl et al. 2007), they showed that the nucleus of embryonic stem cells is more pliable due to an open and less condensed chromatin structure than nuclei of differentiated cells in which chromatin is more compacted. However, during cell differentiation not only does the compaction level of chromatin increase, but also the expression of lamins A and C. Besides lamins, chromatin content may also impact nuclear rigidity. As an example, the nuclear interior increases in stiffness when it becomes compressed exhibiting sponge-like properties (Dahl, Engler et al. 2005; Rowat, Lammerding et al. 2008). Cells aspirated into narrow micropipettes first showed decreases in nuclear size, but then reached a plateau where chromatin could be no longer shrunk. Chromatin in the nucleus exists in two states; heterochromatin, which is the more condensed form; and euchromatin, which is the lightly condensed and transcriptionally active form.

The level of chromatin compaction may depend on post-translational histone modifications.

Chromatin compaction may have a big impact on nuclear stiffness and translocation. For example, some studies reported that alterations of chromatin, by divalent cations or upregulation of heterochromatin proteins, led to enhanced chromatin compaction and nuclear stiffness, while treatment of nuclei with chelating agents resulted in chromatin decondensation and reduction in nuclear rigidity (Dahl, Engler et al. 2005). Furthermore, condensed forms of chromatin may facilitate directed cell migration. With this in mind, I speculated whether chromatin condensation was altered and may have facilitated the confined migration ability of pore-selected MDA MB 231 cells. In order to assess it, I first investigated the chromatin content which revealed that Parental cells had significantly more chromatin relative to Selected and Flow sorted MDA MB 231 cells. In order to assess chromatin condensation, I stained cells for the heterochromatin marker H3K27me^3 as a starting point. Immunostaining revealed larger patches in pore-selected and Flow sorted MDA MB 231 cells, suggesting enhanced chromatin compaction in comparison to Parental cells. Next, to use a more quantitative approach of chromatin condensation detection, I utilised a method described by Lleres *et al.* (Lleres, James et al. 2009). They presented a quantitative analysis of chromatin compaction in live cells using a FLIM-FRET-based assay. As a control experiment, to validate whether differences in chromatin compaction could be detected, I treated cells with 2-deoxyglucose (2-DG) and sodium azide, and observed chromatin compaction in pore-selected and Parental MDA MB 231 cells regardless of differences in DNA content. This was consistent with the data reported by Lleres *et al.* who also showed that treatment of cells with 2-DG and sodium azide led to extensive chromatin compaction. Having validated the method, I continued with the assay and revealed that pore-selected and flow sorted cells had more compacted chromatin relative to Parental cells, which may explain the increased nuclear stiffness of these cell lines.

Together, my findings revealed that nuclear size, stiffness and chromatin condensation did not determine the pore-selected cells' ability to migrate through confined pores. However, the findings of this chapter indicated that the

reduction in chromosome number correlated with decreased nuclear and cell volume; additionally the decreased chromosome number correlated with more condensed chromatin.

7.2 Cell mechanical properties

There is a plethora of studies showing that malignant cancer cells are softer than corresponding normal cells, and that such plasticity may facilitate cancer cell invasion and metastasis (Cross, Jin et al. 2008; Faria, Ma et al. 2008; Li, Lee et al. 2008). These reports are supported by my own experimental data showing that pore-selected MDA MB 231 and MDA MB 435 cells, which were more migratory through confined spaces as well as more invasive *in vivo*, had reduced cell stiffness that might have facilitated their confined migration ability. As detailed in the introduction, the main determinant of cellular mechanics is the network of cytoplasmic actin filaments that bestow individual cells with the ability to overcome external mechanical forces (Moeendarbary and Harris 2014). Moreover, it has been shown that mechanical properties of purified cytoskeletal components such as actin, microtubules and intermediate filaments exhibited viscoelastic properties similar to whole cells (Gittes, Mickey et al. 1993; Janmey, Hvidt et al. 1994). Actin filaments, together with actin crosslinkers and polymerizing factors, create a mesh of 200 nm thickness located below the apical plasma membrane called actin cortex which shapes and provides a structural support for cancer cells, and which contributes to cell mechanical rigidity (Kumar, Maxwell et al. 2006). In addition, Gupta *et al.* (Gupta, Sarangi et al. 2015) reported that cells with well-developed stress fibres (nematic organization) were characterized with solid-like mechanical properties, while cells with more disorganized, (orthoradial) pattern of actin filaments around the nucleus (isotropic organization) were characterized with fluid like mechanical properties. To address the question of what might be responsible for the observed differences in cell stiffness between Parental, Selected and Flow sorted MDA MB 231 and Parental and Selected MDA MB 435, the organization of the actin cytoskeleton was investigated. Confocal, as well as TIRF, imaging of phalloidin-stained cytoplasmic and cortical F-actin revealed that pore-selected MDA MB 231 and MDA MB 435 cells had more ruffled actin organization, marked by fewer distinct cytoplasmic and cortical F-actin fibres compared to Parental or Flow sorted MDA MB 231, as well as Parental MDA MB 435. Quantification of actin

fibre alignment revealed a significant decrease in F-actin anisotropy in both pore-selected cell lines relative to other sub-populations from each cell line. Furthermore, when I disrupted F-actin by treating cells with Cytochalasin D, I observed a marked decrease of cortical stiffness in Parental MDA MB 231 cells, which can be supported by (Rotsch and Radmacher 2000; Wakatsuki, Schwab et al. 2001), suggesting that the cell mechanical properties are dependent on organization of the cortical F-actin. These results are consistent with a role of cytoskeleton mechanical properties in confined cell migration.

The cell cytoskeleton connects with the ECM via membrane-associated macromolecular assemblies called focal adhesions. Despite the fact that cells can utilize different migration modes that are more or less dependent on integrin–mediated adhesion, the general picture of cell migration points out that focal adhesions play an important role in the cell migration process by helping cells to convert contractile forces into traction forces to move cells forward and retract the cell body tail. Focal adhesions are assembled during stress fibre polymerization, which drives the formation of extending protrusions (filopodia, lamellipodia) (Nagano, Hoshino et al. 2012). Nonetheless, there is conflicting data in the literature describing the role of increased adhesion as supporting (Rolli, Fransvea et al. 2003) or preventing tumour cell migration (Rodriguez Fernandez, Geiger et al. 1992). Due to observed changes in cytoskeleton organization between Parental and pore-selected MDA MB 231 and MDA MB 435 cells, I decided to interrogate whether the observed cytoskeleton organization in pore-selected cells had an effect on focal adhesion assembly and subsequently on cell adhesiveness and motility. By staining cells with anti pFAK antibody, I found that pore-selected cells had a significantly reduced number of focal adhesions relative to Parental cells. However, despite the difference in number of focal complexes, the MDA MB 231 sub-populations did not differ in substrate adhesiveness. To determine whether the observed disparity in focal adhesion had an effect on cell motility, I utilized a random motility assay. The results revealed that pore-selected MDA MB 231 and MDA MB 435 cells migrated with increased speed and further distance. These results supported previously reported data showing that rapidly moving cells such as neutrophils and *Dictyostelium discoideum* (Nagasaki, Kanada et al. 2009) exhibit very small focal

adhesions while cells with pronounced focal complexes such as fibroblasts move slowly.

Apart from the cytoskeleton being a known cell rigidity determinant, it has also been reported that lipid bilayers possess bending and compression elasticity. Plasma membrane stiffness and fluidity depend on the plasma membrane composition of lipids and proteins, as well as cholesterol content (Byfield, Aranda-Espinoza et al. 2004; Zhao, Prijic et al. 2016). Membrane fluidity is an indication of the movement of molecules in the membrane. Some studies have reported that decreased membrane fluidity correlated with increased metastatic potential of breast cancer cells, and such effect could be reversed by depletion of cholesterol upon antimetastatic drug treatment (Sherbet 1989; Sok, Sentjurc et al. 2002). In order to inspect whether the observed changes in cell rigidity might have been due to changes in membrane fluidity, I utilized a previously described method (Klein, Pillot et al. 2003). The lateral membrane diffusion of NBD-C6-sphingomyelin-treated cells was measured using a Fluorescence Recovery after Photobleaching method (FRAP). The results revealed that there were no differences in $t_{1/2}$ and mobile fraction between all the sub-populations of MDA MB 231 and MDA MB 435, suggesting that there was no difference in membrane fluidity. As a result, membrane fluidity did not appear to be a cell property that dictated the ability of pore-selected cells to migrate through constrained pores, again pinpointing a significant role of cytoskeleton mechanical properties in confined cell migration.

Altogether, these results indicated that cytoskeletal rigidity plays a significant role in confined cell migration of pore-selected MDA MB 231 and MDA MB 435 cells. Moreover, dysregulated cytoskeletal organization in both pore-selected cell lines imposed less pronounced focal adhesion assembly, which was reflected in their increased motility.

7.3 RNA Sequencing analysis reveals increased signalling through the Ras-Raf-MEK-ERK mitogen-activated protein kinase (MAPK) pathway in pore-selected MDA MB 231 and MDA MB 435 cells

The purpose of this part of the project was to identify factors or signalling pathways associated with the observed changes in pore-selected MDA MB 231 and MDA MB 435 cells. For this reason, RNA Sequencing experiments were conducted. In order to unveil factors or signalling pathways, Gene Set Enrichment Analysis (GSEA) algorithms were applied. GSEA allows for the identification of enriched sets of genes based on previously published data. The GSEA analysis revealed increased signalling through the Ras-Raf-MEK-ERK mitogen-activated protein kinase (MAPK) pathway in pore-selected cells. The MAPK/ERK pathway plays important roles in the regulation of many fundamental cellular processes, such as proliferation, migration, angiogenesis and survival (Chong, Vikis et al. 2003; Wellbrock, Karasarides et al. 2004; Meloche and Pouyssegur 2007; Mebratu and Tesfaigzi 2009). Due to the fact that many components of this pathway have been found to be either mutated or overexpressed in many human cancers, it has been a subject of intense research, therefore there have been already many inhibitors developed to block some of the cascade's kinases. For example, Vemurafenib and Sorafenib block the activity of B-Raf kinase, and Trametinib and U0126 block MEK1/2 kinases (Roberts and Der 2007; Burotto, Chiou et al. 2014; Holderfield, Nagel et al. 2014; Tran, Cheng et al. 2016).

In order to assess the impact of the MAPK/ERK pathway on the observed changes in pore-selected cells, I decided to block this pathway by applying two selective MEK inhibitors, Trametinib or U0126. I started the investigation by assessing whether expression of genes that were associated with the KRAS "signature", identified by GSEA, was dependent on the activity of the MAPK/ERK pathway. To address this, I treated MDA MB 231 and MDA MB 435 cells with Trametinib and performed qRT-PCR. From this experiment, I determined that expression of the chosen genes was dependent on MAPK/ERK pathway activity, suggesting that these genes could be responsible for the observed disorganisation of cytoskeletal structures and cell plasticity changes in pore-selected cell lines and subsequently affect their confined migratory and invasive capabilities.

In order to validate an effect of MAPK/ERK pathway inhibition on actin organisation and focal adhesion assembly, I treated pore-selected MDA MB 231 and MDA MB 435 cells with Trametinib or U0126. I found that MEK inhibitor treatment led to the appearance of long actin filaments and more focal adhesions in comparison to the more disorganised actin organisation and fewer focal complexes in DMSO-treated control cells. These results suggested that the MAPK/ERK pathway played an important role in stress fibre assembly. These results can be supported by Choi and Helfman (Choi and Helfman 2014). They showed that MDA MB 231 LM2 cells, which were selected based on their ability to metastasise to the lungs, had poorly organized stress fibres in comparison to their Parental cells, and interestingly LM2 cells had higher level of K-Ras expression and increased levels of pERK. Additionally, they showed that knock-down of K-Ras or inhibition of MAPK/ERK pathway with U0126 inhibitor led to actin fibre restoration.

In the next step of the project, I wanted to interrogate whether inhibition of the MAPK/ERK pathway had an effect on cell stiffness. Cell stiffness was significantly decreased in pore-selected cells, and following treatment with Trametinib cells became stiffer in comparison to DMSO-treated cells. In order to assess how MAPK/ERK pathway inhibition affected cell invasion and motility *in vitro*, collagen invasion and individual cell migration assays were conducted. I found that upon U0126 treatment invasion of pore-selected MDA MB 231 and MDA MB 435 cells through fibroblast-conditioned collagen was restrained. Additionally, all the sub-populations of MDA MB 231 and MDA MB 435 cells migrated more slowly and moved shorter distances upon MEK inhibition, again suggesting that elevated signalling through the MAPK/ERK pathway in pore-selected MDA MB 231 and MDA MB 435 cells was responsible for the enhanced invasive capabilities and motility *in vitro*.

These results suggested that elevated signalling through the MAPK/ERK pathway was responsible for actin disruption and cell stiffness determination in pore-selected MDA MB 231 and MDA MB 435 cells, and to my knowledge, this is the first time that the MAPK/ERK pathway has been shown to be involved in the cell elasticity modulation.

Before going into the possible mechanisms of how the MAPK/ERK pathway might alter actin filament organization, I will briefly describe how actin filaments and stress fibres are formed. F-actin filaments are formed by polymerization of globular monomeric actin (G-actin) subunits in a process called actin treadmilling, as described in the introduction. Moreover, the assembly and disassembly of actin filaments is regulated by many actin binding proteins, at least 100 (Dominguez and Holmes 2011). Bundled actin filaments, together with myosin II and the actin cross-linking protein α-actinin create structures called stress fibres (Burridge and Wittchen 2013). Stress fibre formation is dependent on actomyosin contractility, which can be regulated by several kinases that have the potential to phosphorylate myosin regulatory light chain 2 and cofilin. Initiation of stress fibre and focal adhesion formation is regulated by the well-characterized small GTPase RhoA (Hanna and El-Sibai 2013). RhoA, when bound to GTP, has the ability to activate Rho-associated coiled-coil kinases (ROCK). ROCK kinases phosphorylate many downstream substrates, such as myosin light chain (MLC), regulatory subunit of MLC phosphatase (MYPT1) and LIM kinases. Phosphorylation of MLC activates it and increases its interaction with actin, which results in cell contractility. Phosphorylation of MYPT1 inhibits its activity and increases levels of phosphorylated MLC. Phosphorylation of LIM kinases activates them, which in turn leads to the phosphorylation and inhibition of the F-actin depolymerizing activity of cofilin (Rath and Olson 2012). There have been many studies showing that the Ras/ERK pathway has the capacity to modulate cell cytoskeletal organisation, and one mechanism by which Ras modifies actin filament assembly is by altering RhoA/ROCK pathway. For example, active ERK diminished the activity of ROCK by post translational modification (Pawlak and Helfman 2002), or through regulation of $p21^{Cip1}$ which is involved in Ras-induced inhibition of the ROCK/LIMK/Cofilin pathway (Besson, Gurian-West et al. 2004). Furthermore, RhoA activity could be diminished by ERK via regulation of Fra-1 (Vial, Sahai et al. 2003). Based on the above, it is valid to speculate that the increased signalling through the MAPK/ERK pathway in pore-selected cells might affect the activity of RhoA/ROCK signalling directly by decreasing the activity of RhoA, ROCK or LIMK, or by affecting their activity through an uncharacterized indirect mechanism.

An additional possibility for how the MAPK/ERK pathway might be involved in the dysregulation of actin cytoskeleton and cell elasticity changes in pore-selected cells is through the action of KRAS "signature" genes. By applying GSEA analysis, I was able to pinpoint some genes that were described by being activated by oncogenic KRAS based on previously published data. Therefore, it is possible to speculate that the coordinated action of some of the products of these genes, or a product of a single gene, might affect the activity of proteins involved in the complex mechanisms of the actin polymerization/depolymerization process, leading to cytoskeleton disorganisation. One of the genes which would require further investigation is Trangelin 3 (also called NP22). Transgelins are actin-binding proteins belonging to the calponin protein family and have been shown to gel and stabilise actin gels *in vitro* (Assinder, Stanton et al. 2009). The precise role of these proteins is unknown, however it has been reported that they play roles in many biological activities, including regulating muscle fibre contractility, cell differentiation, tissue invasion, and tumour suppression (Assinder, Stanton et al. 2009). Expression of transgelins has been found to be decreased in breast, colon and prostate cancers (Shields, Rogers-Graham et al. 2002; Wulfkuhle, Sgroi et al. 2002; Yang, Chang et al. 2007). In terms of the role of transgelins in stress fibre formation, it has been reported that depletion of Transgelin 2 (also known as SM22β) in REF52 fibroblasts led to disrupted cell cytoskeleton and changes in cell motility (Thompson, Moghraby et al. 2012). Additionally, Na *at al*. showed that Transgelin 2 stabilized cortical F-actin at the immunological synapse by blocking the activity of cofilin (Na, Kim et al. 2015). In addition, Mori *et al*. reported that Transgelin 3 co-localized with F-actin on stress fibres (Mori, Muto et al. 2004). Therefore, due to the increased expression of Translegin 3 in pore-selected cells and its ability to bind to actin, it is reasonable to speculate that it might play a significant role in the regulation of actin polymerization/depolymerization machinery or the stress fibre formation process leading to actin filament disruption and consequently decreased cell stiffness.

7.4 Final conclusions and future directions

In conclusion, I showed that using Transwell assay with 3 μm pore membranes I was able to select for cells with enhanced constrained migration properties, enhanced motility and upregulated invasion capabilities *in vitro*. Additionally, I demonstrated that confined migration did not solely depend on cell or nuclei size, or nuclear rigidity. By investigating cell mechanical features, I found that pore-selected cells were significantly softer, which was due to disrupted actin cytoskeletal organization. Pore-selected MDA MB 231 and MDA MB 435 cells had more ruffled-like F-actin with short actin filaments in comparison to longer and more aligned actin stress fibre organisation in Parental cells. Moreover, by applying RNA Sequencing, I was able to identify that increased signalling through the MAPK/ERK pathway was responsible for the disrupted actin cytoskeleton and decreased cell stiffness, and consequently for increased cell motility and invasive capacity *in vitro* and *in vivo*.

I therefore propose that increased signalling through the MAPK/ERK pathway leads to an upregulation of genes, which in turn, through a direct or indirect manner, contribute to altered cell cytoskeletal organization and focal adhesions, and subsequently diminished cell stiffness. Changes in cell elasticity facilitate cancer cell confined migration and invasion capabilities, and finally support their metastatic capabilities *in vivo*. Blocking the MAPK/ERK pathway with Trametinib or U0126 led to changes in gene expression, which might have contributed to actin cytoskeleton stabilization. Restoration of the actin cytoskeleton made cells stiffer and in consequence contributed to a reduction in cancer cell invasion and motility (Figure 7-1).

There are still some questions that should be addressed; whether activating the MAPK/ERK pathway in Parental cells, for example through overexpressing oncogenic Ras or B-Raf, would disrupt actin organisation, reduce cell stiffness and subsequently promote their confined migration and invasion abilities *in vitro* and *in vivo*. In addition to that, it would be interesting to characterize whether the effect of the Ras/MAPK pathway on actin structures is due to acute or sustained signalling. To address this question, Parental MDA MB 231 and MDA MB 435 cells could be transfected/transduced with estrogen-receptor hormone binding domain fusions with Ras (ER-Ras) or B-Raf (BRaf-ER), which allow for the

specific and conditional activation of these proteins upon the addition of estrogen analogues such as 4-hdroxytamoxifen (4-HT). Cells could be stimulated with 4-HT to activate Ras or B-Raf, and the time course of MAPK activation monitored by western blotting of MAPK component phosphorylation. F-actin structures could be examined in fixed cells over time. In parallel, Selected MDA MB 231 and MDA MB 435 cells could be treated with the MEK inhibitors U0126 or Trametinib, which restored actin structures and increased F-actin anisotropy, at intervals ranging from minutes to hours to determine the time course of cytoskeleton recovery. In addition, cells could be transfected with GFP-tagged LifeAct, which is a 17 amino acid peptide that enables F-actin visualization in live cells (Riedl, Crevenna et al. 2008), and the effects of MEK inhibition and Ras/B-Raf overexpression on F-actin structures monitored by time-lapse fluorescence microscopy. AFM measurements of cell elasticity would determine the temporal relationships between MAPK activation, cytoskeleton disruption and mechanical properties. Moreover, it would be interesting to interrogate which of the genes that were identified by GSEA could be directly involved in the alteration of actin organisation and cell stiffness modulation. Such candidates could be potential drug targets.

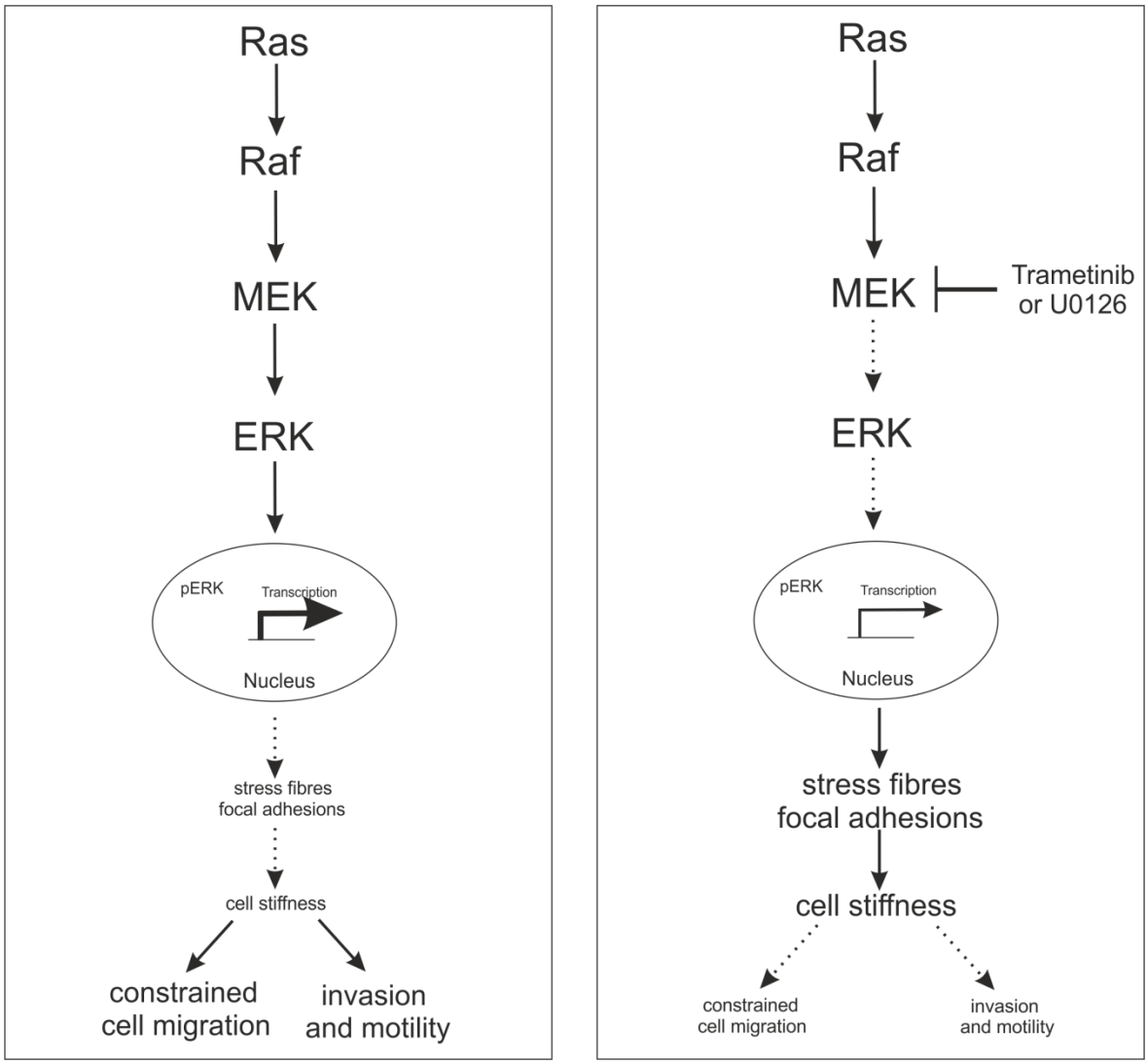

Figure 7-1 Proposed model for the MAPK/ERK pathway in actin cytoskeleton and cell stiffness regulation.

(Left panel) Increased signalling through the MAPK/ERK pathway leads to changes in gene expression, which in turn contribute to cell cytoskeleton disorganisation and changes in cell stiffness. Subsequently, decreased cell stiffness facilitates cancer cell constrained and invasive capabilities. (Right panel) Inhibition of the MAPK/ERK pathway leads to decreased expression of genes associated with cytoskeletal alteration and contributes to stress fibre and focal adhesion restoration. The rebuilt cell cytoskeleton recovers cell stiffness and diminishes constrained cell migration and invasion abilities.

List of References

Abdelkarim, M., N. Vintonenko, et al. (2011). "Invading basement membrane matrix is sufficient for MDA-MB-231 breast cancer cells to develop a stable in vivo metastatic phenotype." PLoS One **6**(8): e23334.

Addae-Mensah, K. A. and J. P. Wikswo (2008). "Measurement techniques for cellular biomechanics in vitro." Exp Biol Med (Maywood) **233**(7): 792-809.

Al-Mehdi, A. B., K. Tozawa, et al. (2000). "Intravascular origin of metastasis from the proliferation of endothelium-attached tumor cells: a new model for metastasis." Nat Med **6**(1): 100-102.

Alexander, S., G. E. Koehl, et al. (2008). "Dynamic imaging of cancer growth and invasion: a modified skin-fold chamber model." Histochem Cell Biol **130**(6): 1147-1154.

Alizadeh, E., S. M. Lyons, et al. (2016). "Measuring systematic changes in invasive cancer cell shape using Zernike moments." Integr Biol (Camb) **8**(11): 1183-1193.

Allinen, M., R. Beroukhim, et al. (2004). "Molecular characterization of the tumor microenvironment in breast cancer." Cancer Cell **6**(1): 17-32.

Allis, C. D. and T. Jenuwein (2016). "The molecular hallmarks of epigenetic control." Nat Rev Genet **17**(8): 487-500.

Assinder, S. J., J. A. Stanton, et al. (2009). "Transgelin: an actin-binding protein and tumour suppressor." Int J Biochem Cell Biol **41**(3): 482-486.

auf dem Keller, U., M. Huber, et al. (2006). "Nrf transcription factors in keratinocytes are essential for skin tumor prevention but not for wound healing." Molecular and cellular biology **26**(10): 3773-3784.

Bamburg, J. R. and B. W. Bernstein (2010). "Roles of ADF/cofilin in actin polymerization and beyond." F1000 Biol Rep **2**: 62.

Bartek, J., J. Lukas, et al. (2007). "DNA damage response as an anti-cancer barrier - Damage threshold and the concept of 'conditional haploinsufficiency'." Cell Cycle **6**(19): 2344-2347.

Beadle, C., M. C. Assanah, et al. (2008). "The role of myosin II in glioma invasion of the brain." Mol Biol Cell **19**(8): 3357-3368.

Belletti, B., M. S. Nicoloso, et al. (2008). "Stathmin activity influences sarcoma cell shape, motility, and metastatic potential." Mol Biol Cell **19**(5): 2003-2013.

Bentolila, L. A., R. Prakash, et al. (2016). "Imaging of Angiotropism/Vascular Co-Option in a Murine Model of Brain Melanoma: Implications for Melanoma Progression along Extravascular Pathways." Sci Rep **6**: 23834.

Besson, A., M. Gurian-West, et al. (2004). "p27Kip1 modulates cell migration through the regulation of RhoA activation." Genes Dev **18**(8): 862-876.

Bhaumik, S. R., E. Smith, et al. (2007). "Covalent modifications of histones during development and disease pathogenesis." Nat Struct Mol Biol **14**(11): 1008-1016.

Bissell, M. J. and W. C. Hines (2011). "Why don't we get more cancer? A proposed role of the microenvironment in restraining cancer progression." Nat Med **17**(3): 320-329.

Blanchoin, L., R. Boujemaa-Paterski, et al. (2014). "Actin dynamics, architecture, and mechanics in cell motility." Physiol Rev **94**(1): 235-263.

Bockhorn, M., R. K. Jain, et al. (2007). "Active versus passive mechanisms in metastasis: do cancer cells crawl into vessels, or are they pushed?" Lancet Oncol **8**(5): 444-448.

Bordeleau, F., T. A. Alcoser, et al. (2014). "Physical biology in cancer. 5. The rocky road of metastasis: the role of cytoskeletal mechanics in cell migratory response to 3D matrix topography." Am J Physiol Cell Physiol **306**(2): C110-120.

Breitsprecher, D. and B. L. Goode (2013). "Formins at a glance." Journal of cell science **126**(1): 1-7.

Bruns, C. J., M. T. Harbison, et al. (1999). "In vivo selection and characterization of metastatic variants from human pancreatic adenocarcinoma by using orthotopic implantation in nude mice." Neoplasia **1**(1): 50-62.

Burotto, M., V. L. Chiou, et al. (2014). "The MAPK pathway across different malignancies: a new perspective." Cancer **120**(22): 3446-3456.

Burridge, K. and C. Guilluy (2016). "Focal adhesions, stress fibers and mechanical tension." Exp Cell Res **343**(1): 14-20.

Burridge, K. and E. S. Wittchen (2013). "The tension mounts: stress fibers as force-generating mechanotransducers." J Cell Biol **200**(1): 9-19.

Bustin, M., F. Catez, et al. (2005). "The dynamics of histone H1 function in chromatin." Mol Cell **17**(5): 617-620.

Byfield, F. J., H. Aranda-Espinoza, et al. (2004). "Cholesterol depletion increases membrane stiffness of aortic endothelial cells." Biophys J **87**(5): 3336-3343.

Cai, X., J. Luo, et al. (2015). "In vivo selection for spine-derived highly metastatic lung cancer cells is associated with increased migration, inflammation and decreased adhesion." Oncotarget **6**(26): 22905-22917.

Carlier, M. F. and S. Shekhar (2017). "Global treadmilling coordinates actin turnover and controls the size of actin networks." Nat Rev Mol Cell Biol **18**(6): 389-401.

Carmeliet, P. and R. K. Jain (2011). "Principles and mechanisms of vessel normalization for cancer and other angiogenic diseases." Nat Rev Drug Discov **10**(6): 417-427.

Cavallaro, U. and G. Christofori (2001). "Cell adhesion in tumor invasion and metastasis: loss of the glue is not enough." Biochim Biophys Acta **1552**(1): 39-45.

Cavallaro, U. and G. Christofori (2004). "Cell adhesion and signalling by cadherins and Ig-CAMs in cancer." Nat Rev Cancer **4**(2): 118-132.

Chambers, A. F., A. C. Groom, et al. (2002). "Dissemination and growth of cancer cells in metastatic sites." Nat Rev Cancer **2**(8): 563-572.

Choi, C. and D. M. Helfman (2014). "The Ras-ERK pathway modulates cytoskeleton organization, cell motility and lung metastasis signature genes in MDA-MB-231 LM2." Oncogene **33**(28): 3668-3676.

Chong, H., H. G. Vikis, et al. (2003). "Mechanisms of regulating the Raf kinase family." Cell Signal **15**(5): 463-469.

Chu, Y. W., P. C. Yang, et al. (1997). "Selection of invasive and metastatic subpopulations from a human lung adenocarcinoma cell line." Am J Respir Cell Mol Biol **17**(3): 353-360.

Clark, E. A., T. R. Golub, et al. (2000). "Genomic analysis of metastasis reveals an essential role for RhoC." Nature **406**(6795): 532-535.

Condeelis, J. and J. E. Segall (2003). "Intravital imaging of cell movement in tumours." Nat Rev Cancer **3**(12): 921-930.

Conklin, M. W., J. C. Eickhoff, et al. (2011). "Aligned collagen is a prognostic signature for survival in human breast carcinoma." Am J Pathol **178**(3): 1221-1232.

Cory, G. O. and P. J. Cullen (2007). "Membrane curvature: the power of bananas, zeppelins and boomerangs." Curr Biol **17**(12): R455-457.

Costa-Silva, B., N. M. Aiello, et al. (2015). "Pancreatic cancer exosomes initiate pre-metastatic niche formation in the liver." Nat Cell Biol **17**(6): 816-826.

Cross, S. E., Y. S. Jin, et al. (2008). "AFM-based analysis of human metastatic cancer cells." Nanotechnology **19**(38): 384003.

Cuddapah, V. A., S. Robel, et al. (2014). "A neurocentric perspective on glioma invasion." Nat Rev Neurosci **15**(7): 455-465.

Dahl, K. N., A. J. Engler, et al. (2005). "Power-law rheology of isolated nuclei with deformation mapping of nuclear substructures." Biophys J **89**(4): 2855-2864.

Davidson, P. M., C. Denais, et al. (2014). "Nuclear deformability constitutes a rate-limiting step during cell migration in 3-D environments." Cell Mol Bioeng **7**(3): 293-306.

Davies, H., G. R. Bignell, et al. (2002). "Mutations of the BRAF gene in human cancer." Nature **417**(6892): 949-954.

Dhillon, A. S., S. Hagan, et al. (2007). "MAP kinase signalling pathways in cancer." Oncogene **26**(22): 3279-3290.

Ding, S., W. Zhang, et al. (2013). "Induction of an EMT-like transformation and MET in vitro." J Transl Med **11**: 164.

Dirat, B., L. Bochet, et al. (2011). "Cancer-associated adipocytes exhibit an activated phenotype and contribute to breast cancer invasion." Cancer Res **71**(7): 2455-2465.

Doerschuk, C. M., N. Beyers, et al. (1993). "Comparison of neutrophil and capillary diameters and their relation to neutrophil sequestration in the lung." J Appl Physiol (1985) **74**(6): 3040-3045.

Doerschuk, C. M., R. K. Winn, et al. (1990). "CD18-dependent and -independent mechanisms of neutrophil emigration in the pulmonary and systemic microcirculation of rabbits." J Immunol **144**(6): 2327-2333.

Dominguez, R. and K. C. Holmes (2011). "Actin structure and function." Annu Rev Biophys **40**: 169-186.

Eden, S., R. Rohatgi, et al. (2002). "Mechanism of regulation of WAVE1-induced actin nucleation by Rac1 and Nck." Nature **418**(6899): 790-793.

Egeblad, M. and Z. Werb (2002). "New functions for the matrix metalloproteinases in cancer progression." Nat Rev Cancer **2**(3): 161-174.

Espinosa, G., I. Lopez-Montero, et al. (2011). "Shear rheology of lipid monolayers and insights on membrane fluidity." Proc Natl Acad Sci U S A **108**(15): 6008-6013.

Faria, E. C., N. Ma, et al. (2008). "Measurement of elastic properties of prostate cancer cells using AFM." Analyst **133**(11): 1498-1500.

Feinberg, A. P., R. Ohlsson, et al. (2006). "The epigenetic progenitor origin of human cancer." Nat Rev Genet **7**(1): 21-33.

Fidler, I. J. (2003). "The pathogenesis of cancer metastasis: the 'seed and soil' hypothesis revisited." Nat Rev Cancer **3**(6): 453-458.

Fischer, K. R., A. Durrans, et al. (2015). "Epithelial-to-mesenchymal transition is not required for lung metastasis but contributes to chemoresistance." Nature **527**(7579): 472-476.

Friedl, P. (2004). "Prespecification and plasticity: shifting mechanisms of cell migration." Curr Opin Cell Biol **16**(1): 14-23.

Friedl, P. and K. Wolf (2003). "Tumour-cell invasion and migration: diversity and escape mechanisms." Nat Rev Cancer **3**(5): 362-374.

Friedl, P. and K. Wolf (2008). "Tube Travel: The Role of Proteases in Individual and Collective Cancer Cell Invasion." Cancer Res **68**(18): 7247-7249.

Fu, Y., L. K. Chin, et al. (2012). "Nuclear deformation during breast cancer cell transmigration." Lab Chip **12**(19): 3774-3778.

Gaggioli, C., S. Hooper, et al. (2007). "Fibroblast-led collective invasion of carcinoma cells with differing roles for RhoGTPases in leading and following cells." Nat Cell Biol **9**(12): 1392-1400.

Gauthier, N. C., M. A. Fardin, et al. (2011). "Temporary increase in plasma membrane tension coordinates the activation of exocytosis and contraction during cell spreading." Proc Natl Acad Sci U S A **108**(35): 14467-14472.

Gerlitz, G. and M. Bustin (2010). "Efficient cell migration requires global chromatin condensation." Journal of Cell Science **123**(Pt 13): 2207-2217.

Gerlitz, G., I. Livnat, et al. (2007). "Migration cues induce chromatin alterations." Traffic **8**(11): 1521-1529.

Giampieri, S., C. Manning, et al. (2009). "Localized and reversible TGF[beta] signalling switches breast cancer cells from cohesive to single cell motility." Nat Cell Biol **11**(11): 1287-1296.

Gittes, F., B. Mickey, et al. (1993). "Flexural rigidity of microtubules and actin filaments measured from thermal fluctuations in shape." J Cell Biol **120**(4): 923-934.

Goddette, D. W. and C. Frieden (1986). "Actin polymerization. The mechanism of action of cytochalasin D." J Biol Chem **261**(34): 15974-15980.

Goley, E. D. and M. D. Welch (2006). "The ARP2/3 complex: an actin nucleator comes of age." Nat Rev Mol Cell Biol **7**(10): 713-726.

Grady, M. E., R. J. Composto, et al. (2016). "Cell elasticity with altered cytoskeletal architectures across multiple cell types." J Mech Behav Biomed Mater **61**: 197-207.

Gritsenko, P. G., O. Ilina, et al. (2012). "Interstitial guidance of cancer invasion." J Pathol **226**(2): 185-199.

Grivennikov, S. I., F. R. Greten, et al. (2010). "Immunity, inflammation, and cancer." Cell **140**(6): 883-899.

Gruenbaum, Y., A. Margalit, et al. (2005). "The nuclear lamina comes of age." Nat Rev Mol Cell Biol **6**(1): 21-31.

Guelen, L., L. Pagie, et al. (2008). "Domain organization of human chromosomes revealed by mapping of nuclear lamina interactions." Nature **453**(7197): 948-951.

Gumireddy, K., F. Sun, et al. (2007). "In vivo selection for metastasis promoting genes in the mouse." Proc Natl Acad Sci U S A **104**(16): 6696-6701.

Gupta, G. P. and J. Massague (2006). "Cancer metastasis: building a framework." Cell **127**(4): 679-695.

Gupta, G. P., D. X. Nguyen, et al. (2007). "Mediators of vascular remodelling co-opted for sequential steps in lung metastasis." Nature **446**(7137): 765-770.

Gupta, M., B. R. Sarangi, et al. (2015). "Adaptive rheology and ordering of cell cytoskeleton govern matrix rigidity sensing." Nat Commun **6**: 7525.

Gupton, S. L. and F. B. Gertler (2007). "Filopodia: the fingers that do the walking." Sci STKE **2007**(400): re5.

Hanahan, D. and R. A. Weinberg (2011). "Hallmarks of cancer: the next generation." Cell **144**(5): 646-674.

Hancock, J. F. (2003). "Ras proteins: different signals from different locations." Nat Rev Mol Cell Biol **4**(5): 373-384.

Hanna, S. and M. El-Sibai (2013). "Signaling networks of Rho GTPases in cell motility." Cell Signal **25**(10): 1955-1961.

Harada, T., J. Swift, et al. (2014). "Nuclear lamin stiffness is a barrier to 3D migration, but softness can limit survival." J Cell Biol **204**(5): 669-682.

Harari, P. M. (2004). "Epidermal growth factor receptor inhibition strategies in oncology." Endocr Relat Cancer **11**(4): 689-708.

Harris, A. L. (2002). "Hypoxia--a key regulatory factor in tumour growth." Nat Rev Cancer **2**(1): 38-47.

Hartmann, S., A. J. Ridley, et al. (2015). "The Function of Rho-Associated Kinases ROCK1 and ROCK2 in the Pathogenesis of Cardiovascular Disease." Front Pharmacol **6**: 276.

Hegerfeldt, Y., M. Tusch, et al. (2002). "Collective cell movement in primary melanoma explants: plasticity of cell-cell interaction, beta1-integrin function, and migration strategies." Cancer Res **62**(7): 2125-2130.

Hiratsuka, S., S. Goel, et al. (2011). "Endothelial focal adhesion kinase mediates cancer cell homing to discrete regions of the lungs via E-selectin up-regulation." Proc Natl Acad Sci U S A **108**(9): 3725-3730.

Ho, C. Y. and J. Lammerding (2012). "Lamins at a glance." J Cell Sci **125**(Pt 9): 2087-2093.

Holderfield, M., T. E. Nagel, et al. (2014). "Mechanism and consequences of RAF kinase activation by small-molecule inhibitors." Br J Cancer **111**(4): 640-645.

Huang, Y., N. Song, et al. (2009). "Pulmonary vascular destabilization in the premetastatic phase facilitates lung metastasis." Cancer Res **69**(19): 7529-7537.

Hussain, S. P., L. J. Hofseth, et al. (2003). "Radical causes of cancer." Nat Rev Cancer **3**(4): 276-285.

Hutchison, C. J. (2014). "Do lamins influence disease progression in cancer?" Adv Exp Med Biol **773**: 593-604.

Jacob, K., A. K. Bosserhoff, et al. (1995). "Characterization of selected strongly and weakly invasive sublines of a primary human melanoma cell line and isolation of subtractive cDNA clones." Int J Cancer **60**(5): 668-675.

Janmey, P. A., S. Hvidt, et al. (1994). "The mechanical properties of actin gels. Elastic modulus and filament motions." J Biol Chem **269**(51): 32503-32513.

Jenkins, D. E., Y. S. Hornig, et al. (2005). "Bioluminescent human breast cancer cell lines that permit rapid and sensitive in vivo detection of mammary tumors and multiple metastases in immune deficient mice." Breast cancer research : BCR **7**(4): R444-454.

Johnson, G. L. and R. Lapadat (2002). "Mitogen-activated protein kinase pathways mediated by ERK, JNK, and p38 protein kinases." Science **298**(5600): 1911-1912.

Jonkers, J. and P. W. Derksen (2007). "Modeling metastatic breast cancer in mice." J Mammary Gland Biol Neoplasia **12**(2-3): 191-203.

Jordan, P., R. Brazao, et al. (1999). "Cloning of a novel human Rac1b splice variant with increased expression in colorectal tumors." Oncogene **18**(48): 6835-6839.

Joyce, J. A. and J. W. Pollard (2009). "Microenvironmental regulation of metastasis." Nat Rev Cancer **9**(4): 239-252.

Kang, Y. and K. Pantel (2013). "Tumor cell dissemination: emerging biological insights from animal models and cancer patients." Cancer Cell **23**(5): 573-581.

Kessenbrock, K., V. Plaks, et al. (2010). "Matrix metalloproteinases: regulators of the tumor microenvironment." Cell **141**(1): 52-67.

Ketene, A. N., E. M. Schmelz, et al. (2012). "The effects of cancer progression on the viscoelasticity of ovarian cell cytoskeleton structures." Nanomedicine **8**(1): 93-102.

Khanna, C. and K. Hunter (2005). "Modeling metastasis in vivo." Carcinogenesis **26**(3): 513-523.

Khatau, S. B., R. J. Bloom, et al. (2012). "The distinct roles of the nucleus and nucleus-cytoskeleton connections in three-dimensional cell migration." Sci Rep **2**: 488.

Kim, H. J. and D. Bar-Sagi (2004). "Modulation of signalling by Sprouty: a developing story." Nat Rev Mol Cell Biol **5**(6): 441-450.

Klein, C., T. Pillot, et al. (2003). "Determination of plasma membrane fluidity with a fluorescent analogue of sphingomyelin by FRAP measurement using a standard confocal microscope." Brain Res Brain Res Protoc **11**(1): 46-51.

Kocaturk, B. and H. H. Versteeg (2015). "Orthotopic injection of breast cancer cells into the mammary fat pad of mice to study tumor growth." J Vis Exp(96).

Kojima, H., A. Ishijima, et al. (1994). "Direct measurement of stiffness of single actin filaments with and without tropomyosin by in vitro nanomanipulation." Proc Natl Acad Sci U S A **91**(26): 12962-12966.

Koo, S., G. S. Martin, et al. (2012). "Serial selection for invasiveness increases expression of miR-143/miR-145 in glioblastoma cell lines." BMC Cancer **12**: 143.

Kouzarides, T. (2007). "Chromatin modifications and their function." Cell **128**(4): 693-705.

Kumar, S., I. Z. Maxwell, et al. (2006). "Viscoelastic retraction of single living stress fibers and its impact on cell shape, cytoskeletal organization, and extracellular matrix mechanics." Biophys J **90**(10): 3762-3773.

Kunda, P., A. E. Pelling, et al. (2008). "Moesin controls cortical rigidity, cell rounding, and spindle morphogenesis during mitosis." Curr Biol **18**(2): 91-101.

Kusch, T. and J. L. Workman (2007). "Histone variants and complexes involved in their exchange." Subcell Biochem **41**: 91-109.

Kuznetsova, T. G., M. N. Starodubtseva, et al. (2007). "Atomic force microscopy probing of cell elasticity." Micron **38**(8): 824-833.

Kyriakis, J. M. and J. Avruch (2001). "Mammalian mitogen-activated protein kinase signal transduction pathways activated by stress and inflammation." Physiol Rev **81**(2): 807-869.

Lambert, A. W., D. R. Pattabiraman, et al. (2017). "Emerging Biological Principles of Metastasis." Cell **168**(4): 670-691.

Lammerding, J. (2011). "Mechanics of the nucleus." Compr Physiol **1**(2): 783-807.

Lammerding, J., L. G. Fong, et al. (2006). "Lamins A and C but not lamin B1 regulate nuclear mechanics." J Biol Chem **281**(35): 25768-25780.

Lammerding, J., P. C. Schulze, et al. (2004). "Lamin A/C deficiency causes defective nuclear mechanics and mechanotransduction." J Clin Invest **113**(3): 370-378.

Lautscham, L. A., C. Kammerer, et al. (2015). "Migration in Confined 3D Environments Is Determined by a Combination of Adhesiveness, Nuclear Volume, Contractility, and Cell Stiffness." Biophys J **109**(5): 900-913.

Lavoie, H. and M. Therrien (2015). "Regulation of RAF protein kinases in ERK signalling." Nat Rev Mol Cell Biol **16**(5): 281-298.

Lee, G. Y. H. and C. T. Lim (2007). "Biomechanics approaches to studying human diseases." Trends in Biotechnology **25**(3): 111-118.

Leung, E., A. Xue, et al. (2016). "Blood vessel endothelium-directed tumor cell streaming in breast tumors requires the HGF/C-Met signaling pathway." Oncogene.

Li, J., Z. Jia, et al. (2016). "Carcinoma-Associated Fibroblasts Lead the Invasion of Salivary Gland Adenoid Cystic Carcinoma Cells by Creating an Invasive Track." PLoS One **11**(3): e0150247.

Li, Q. S., G. Y. H. Lee, et al. (2008). "AFM indentation study of breast cancer cells." Biochemical and Biophysical Research Communications **374**(4): 609-613.

Lleres, D., J. James, et al. (2009). "Quantitative analysis of chromatin compaction in living cells using FLIM-FRET." J Cell Biol **187**(4): 481-496.

Lugassy, C., S. Zadran, et al. (2014). "Angiotropism, pericytic mimicry and extravascular migratory metastasis in melanoma: an alternative to intravascular cancer dissemination." Cancer Microenviron **7**(3): 139-152.

Luger, K., A. W. Mader, et al. (1997). "Crystal structure of the nucleosome core particle at 2.8 A resolution." Nature **389**(6648): 251-260.

Martins, R. P., J. D. Finan, et al. (2012). "Mechanical regulation of nuclear structure and function." Annu Rev Biomed Eng **14**: 431-455.

Maurer, G., B. Tarkowski, et al. (2011). "Raf kinases in cancer-roles and therapeutic opportunities." Oncogene **30**(32): 3477-3488.

McAllister, S. S., A. M. Gifford, et al. (2008). "Systemic endocrine instigation of indolent tumor growth requires osteopontin." Cell **133**(6): 994-1005.

McPhee, G., M. J. Dalby, et al. (2010). "Can common adhesion molecules and microtopography affect cellular elasticity? A combined atomic force microscopy and optical study." Med Biol Eng Comput **48**(10): 1043-1053.

Mebratu, Y. and Y. Tesfaigzi (2009). "How ERK1/2 activation controls cell proliferation and cell death: Is subcellular localization the answer?" Cell Cycle **8**(8): 1168-1175.

Mehlen, P. and A. Puisieux (2006). "Metastasis: a question of life or death." Nat Rev Cancer **6**(6): 449-458.

Meloche, S. and J. Pouyssegur (2007). "The ERK1/2 mitogen-activated protein kinase pathway as a master regulator of the G1- to S-phase transition." Oncogene **26**(22): 3227-3239.

Meng, S., D. Tripathy, et al. (2004). "Circulating tumor cells in patients with breast cancer dormancy." Clin Cancer Res **10**(24): 8152-8162.

Michaelson, D., J. Silletti, et al. (2001). "Differential localization of Rho GTPases in live cells: regulation by hypervariable regions and RhoGDI binding." J Cell Biol **152**(1): 111-126.

Mitchell, M. J., C. Denais, et al. (2015). "Lamin A/C deficiency reduces circulating tumor cell resistance to fluid shear stress." Am J Physiol Cell Physiol **309**(11): C736-746.

Moeendarbary, E. and A. R. Harris (2014). "Cell mechanics: principles, practices, and prospects." Wiley Interdiscip Rev Syst Biol Med **6**(5): 371-388.

Mori, K., Y. Muto, et al. (2004). "Neuronal protein NP25 interacts with F-actin." Neurosci Res **48**(4): 439-446.

Morton, W. M., K. R. Ayscough, et al. (2000). "Latrunculin alters the actin-monomer subunit interface to prevent polymerization." Nat Cell Biol **2**(6): 376-378.

Na, B. R., H. R. Kim, et al. (2015). "TAGLN2 regulates T cell activation by stabilizing the actin cytoskeleton at the immunological synapse." J Cell Biol **209**(1): 143-162.

Nabeshima, K., T. Inoue, et al. (1999). "Cohort migration of carcinoma cells: differentiated colorectal carcinoma cells move as coherent cell clusters or sheets." Histol Histopathol **14**(4): 1183-1197.

Nabeshima, K., T. Inoue, et al. (2002). "Matrix metalloproteinases in tumor invasion: role for cell migration." Pathol Int **52**(4): 255-264.

Nagano, M., D. Hoshino, et al. (2012). "Turnover of focal adhesions and cancer cell migration." Int J Cell Biol **2012**: 310616.

Nagasaki, A., M. Kanada, et al. (2009). "Cell adhesion molecules regulate contractile ring-independent cytokinesis in Dictyostelium discoideum." Cell Res **19**(2): 236-246.

Nagrath, S., L. V. Sequist, et al. (2007). "Isolation of rare circulating tumour cells in cancer patients by microchip technology." Nature **450**(7173): 1235-1239.

Nash, G. F., L. F. Turner, et al. (2002). "Platelets and cancer." Lancet Oncol **3**(7): 425-430.

Nejedla, M., S. Sadi, et al. (2016). "Profilin connects actin assembly with microtubule dynamics." Mol Biol Cell **27**(15): 2381-2393.

Nguyen, A., M. Yoshida, et al. (2016). "Highly variable cancer subpopulations that exhibit enhanced transcriptome variability and metastatic fitness." Nat Commun **7**: 11246.

O'Connor, K. and M. Chen (2013). "Dynamic functions of RhoA in tumor cell migration and invasion." Small GTPases **4**(3): 141-147.

Olson, M. F. and E. Sahai (2009). "The actin cytoskeleton in cancer cell motility." Clin Exp Metastasis **26**(4): 273-287.

Orimo, A. and R. A. Weinberg (2006). "Stromal fibroblasts in cancer: a novel tumor-promoting cell type." Cell Cycle **5**(15): 1597-1601.

Oser, M. and J. Condeelis (2009). "The cofilin activity cycle in lamellipodia and invadopodia." J Cell Biochem **108**(6): 1252-1262.

Padua, D., X. H. Zhang, et al. (2008). "TGFbeta primes breast tumors for lung metastasis seeding through angiopoietin-like 4." Cell **133**(1): 66-77.

Pajerowski, J. D., K. N. Dahl, et al. (2007). "Physical plasticity of the nucleus in stem cell differentiation." Proc Natl Acad Sci U S A **104**(40): 15619-15624.

Palmieri, V., D. Lucchetti, et al. (2015). "Mechanical and structural comparison between primary tumor and lymph node metastasis cells in colorectal cancer." Soft Matter **11**(28): 5719-5726.

Pantel, K., R. H. Brakenhoff, et al. (2008). "Detection, clinical relevance and specific biological properties of disseminating tumour cells." Nat Rev Cancer **8**(5): 329-340.

Paszek, M. J., N. Zahir, et al. (2005). "Tensional homeostasis and the malignant phenotype." Cancer Cell **8**(3): 241-254.

Paul, C. D., P. Mistriotis, et al. (2017). "Cancer cell motility: lessons from migration in confined spaces." Nat Rev Cancer **17**(2): 131-140.

Pawlak, G. and D. M. Helfman (2002). "Post-transcriptional down-regulation of ROCKI/Rho-kinase through an MEK-dependent pathway leads to cytoskeleton disruption in Ras-transformed fibroblasts." Mol Biol Cell **13**(1): 336-347.

Pellegrin, S. and H. Mellor (2007). "Actin stress fibres." J Cell Sci **120**(Pt 20): 3491-3499.

Peng, L., Y. L. Ran, et al. (2009). "Secreted LOXL2 is a novel therapeutic target that promotes gastric cancer metastasis via the Src/FAK pathway." Carcinogenesis **30**(10): 1660-1669.

Polacheck, W. J. and C. S. Chen (2016). "Measuring cell-generated forces: a guide to the available tools." Nat Methods **13**(5): 415-423.

Pollard, T. D. and G. G. Borisy (2003). "Cellular motility driven by assembly and disassembly of actin filaments." Cell **112**(4): 453-465.

Pollock, C. B., S. Shirasawa, et al. (2005). "Oncogenic K-RAS Is Required to Maintain Changes in Cytoskeletal Organization, Adhesion, and Motility in Colon Cancer Cells." Cancer Res **65**(4): 1244-1250.

Prasad, V. V. and R. O. Gopalan (2015). "Continued use of MDA-MB-435, a melanoma cell line, as a model for human breast cancer, even in year, 2014." NPJ Breast Cancer **1**: 15002.

Provenzano, P. P., K. W. Eliceiri, et al. (2006). "Collagen reorganization at the tumor-stromal interface facilitates local invasion." BMC Med **4**(1): 38.

Psaila, B. and D. Lyden (2009). "The metastatic niche: adapting the foreign soil." Nat Rev Cancer **9**(4): 285-293.

Rath, N. and M. F. Olson (2012). "Rho-associated kinases in tumorigenesis: re-considering ROCK inhibition for cancer therapy." EMBO Rep **13**(10): 900-908.

Ridley, A. J. (2015). "Rho GTPase signalling in cell migration." Curr Opin Cell Biol **36**: 103-112.

Ridley, A. J., M. A. Schwartz, et al. (2003). "Cell migration: integrating signals from front to back." Science **302**(5651): 1704-1709.

Riedl, J., A. H. Crevenna, et al. (2008). "Lifeact: a versatile marker to visualize F-actin." Nat Methods **5**(7): 605-607.

Roberts, P. J. and C. J. Der (2007). "Targeting the Raf-MEK-ERK mitogen-activated protein kinase cascade for the treatment of cancer." Oncogene **26**(22): 3291-3310.

Rodriguez Fernandez, J. L., B. Geiger, et al. (1992). "Suppression of tumorigenicity in transformed cells after transfection with vinculin cDNA." J Cell Biol **119**(2): 427-438.

Rolli, M., E. Fransvea, et al. (2003). "Activated integrin alphavbeta3 cooperates with metalloproteinase MMP-9 in regulating migration of metastatic breast cancer cells." Proc Natl Acad Sci U S A **100**(16): 9482-9487.

Rotsch, C. and M. Radmacher (2000). "Drug-induced changes of cytoskeletal structure and mechanics in fibroblasts: an atomic force microscopy study." Biophys J **78**(1): 520-535.

Rowat, A. C., D. E. Jaalouk, et al. (2013). "Nuclear envelope composition determines the ability of neutrophil-type cells to passage through micron-scale constrictions." J Biol Chem **288**(12): 8610-8618.

Rowat, A. C., J. Lammerding, et al. (2008). "Towards an integrated understanding of the structure and mechanics of the cell nucleus." Bioessays **30**(3): 226-236.

Rowat, A. C., J. Lammerding, et al. (2006). "Mechanical properties of the cell nucleus and the effect of emerin deficiency." Biophys J **91**(12): 4649-4664.

Rudzka, D. A., J. M. Cameron, et al. (2015). "Reactive oxygen species and hydrogen peroxide generation in cell migration." Commun Integr Biol **8**(5): e1074360.

Rudzka, D. A., W. Clark, et al. (2017). "Transcriptomic profiling of human breast and melanoma cells selected by migration through narrow constraints." Sci Data **4**: 170172.

Rudzka, D. A. and M. F. Olson (2015). "Microtrack migration: insights into 3D cell motility. Focus on "Comparative mechanisms of cancer cell migration through 3D matrix and physiological microtracks"." Am J Physiol Cell Physiol **308**(6): C434-435.

Sabeh, F., R. Shimizu-Hirota, et al. (2009). "Protease-dependent versus -independent cancer cell invasion programs: three-dimensional amoeboid movement revisited." J Cell Biol **185**(1): 11-19.

Sahai, E. and C. J. Marshall (2003). "Differing modes of tumour cell invasion have distinct requirements for Rho/ROCK signalling and extracellular proteolysis." Nat Cell Biol **5**(8): 711-719.

Sahai, E., M. F. Olson, et al. (2001). "Cross-talk between Ras and Rho signalling pathways in transformation favours proliferation and increased motility." Embo J **20**(4): 755-766.

Sahai, E., J. Wyckoff, et al. (2005). "Simultaneous imaging of GFP, CFP and collagen in tumors in vivo using multiphoton microscopy." BMC Biotechnol **5**: 14.

Santarpia, L., S. M. Lippman, et al. (2012). "Targeting the MAPK-RAS-RAF signaling pathway in cancer therapy." Expert Opin Ther Targets **16**(1): 103-119.

Sanz-Moreno, V. and C. J. Marshall (2009). "Rho-GTPase signaling drives melanoma cell plasticity." Cell Cycle **8**(10): 1484-1487.

Sherbet, G. V. (1989). "Membrane fluidity and cancer metastasis." Exp Cell Biol **57**(4): 198-205.

Shields, J. M., K. Rogers-Graham, et al. (2002). "Loss of transgelin in breast and colon tumors and in RIE-1 cells by Ras deregulation of gene expression through Raf-independent pathways." J Biol Chem **277**(12): 9790-9799.

Shimi, T., K. Pfleghaar, et al. (2008). "The A- and B-type nuclear lamin networks: microdomains involved in chromatin organization and transcription." Genes Dev **22**(24): 3409-3421.

Sok, M., M. Sentjurc, et al. (2002). "Cell membrane fluidity and prognosis of lung cancer." Ann Thorac Surg **73**(5): 1567-1571.

Solovei, I., A. S. Wang, et al. (2013). "LBR and lamin A/C sequentially tether peripheral heterochromatin and inversely regulate differentiation." Cell **152**(3): 584-598.

Steeg, P. S. (2006). "Tumor metastasis: mechanistic insights and clinical challenges." Nature Medicine **12**(8): 895-904.

Stetler-Stevenson, W. G., S. Aznavoorian, et al. (1993). "Tumor cell interactions with the extracellular matrix during invasion and metastasis." Annu Rev Cell Biol **9**: 541-573.

Stewart, M. P., J. Helenius, et al. (2011). "Hydrostatic pressure and the actomyosin cortex drive mitotic cell rounding." Nature **469**(7329): 226-230.

Swaminathan, V., K. Mythreye, et al. (2011). "Mechanical stiffness grades metastatic potential in patient tumor cells and in cancer cell lines." Cancer Res **71**(15): 5075-5080.

Swift, J. and D. E. Discher (2014). "The nuclear lamina is mechano-responsive to ECM elasticity in mature tissue." J Cell Sci **127**(Pt 14): 3005-3015.

Swift, J., Ivanovska, I. L., et al. (2013). " Nuclear lamin-A scales with tissue stiffness and enhances matrix-directed differentiation." Science **341**(6249): 1240104-1 - 1240104-15.

Tang, L. and X. Han (2013). "The urokinase plasminogen activator system in breast cancer invasion and metastasis." Biomed Pharmacother **67**(2): 179-182.

Tao, J., Y. Li, et al. (2017). "Cell mechanics: a dialogue." Rep Prog Phys **80**(3): 036601.

Thiery, J. P., H. Acloque, et al. (2009). "Epithelial-mesenchymal transitions in development and disease." Cell **139**(5): 871-890.

Thomas, C. M., C. Monturo, et al. (2011). "Experiences of Faculty and Students Using an Audience Response System in the Classroom." Cin-Computers Informatics Nursing **29**(7): 396-400.

Thompson, O., J. S. Moghraby, et al. (2012). "Depletion of the actin bundling protein SM22/transgelin increases actin dynamics and enhances the tumourigenic phenotypes of cells." BMC Cell Biol **13**: 1.

Timpson, P., E. J. Mcghee, et al. (2011). "Organotypic Collagen I Assay: A Malleable Platform to Assess Cell Behaviour in a 3-Dimensional Context." Jove-Journal of Visualized Experiments(56).

Tong, Z. Q., E. M. Balzer, et al. (2012). "Chemotaxis of Cell Populations through Confined Spaces at Single-Cell Resolution." PLoS One **7**(1).

Tran, K. A., M. Y. Cheng, et al. (2016). "MEK inhibitors and their potential in the treatment of advanced melanoma: the advantages of combination therapy." Drug Des Devel Ther **10**: 43-52.

Van Troys, M., L. Huyck, et al. (2008). "Ins and outs of ADF/cofilin activity and regulation." Eur J Cell Biol **87**(8-9): 649-667.

Vanharanta, S. and J. Massague (2013). "Origins of metastatic traits." Cancer Cell **24**(4): 410-421.

Vargas-Pinto, R., H. Gong, et al. (2013). "The effect of the endothelial cell cortex on atomic force microscopy measurements." Biophys J **105**(2): 300-309.

Vial, E., E. Sahai, et al. (2003). "ERK-MAPK signaling coordinately regulates activity of Rac1 and RhoA for tumor cell motility." Cancer Cell **4**(1): 67-79.

Voisin, M. B., A. Woodfin, et al. (2009). "Monocytes and neutrophils exhibit both distinct and common mechanisms in penetrating the vascular basement membrane in vivo." Arterioscler Thromb Vasc Biol **29**(8): 1193-1199.

Wakatsuki, T., B. Schwab, et al. (2001). "Effects of cytochalasin D and latrunculin B on mechanical properties of cells." J Cell Sci **114**(Pt 5): 1025-1036.

Wang, W., S. Goswami, et al. (2004). "Identification and testing of a gene expression signature of invasive carcinoma cells within primary mammary tumors." Cancer Res **64**(23): 8585-8594.

Wang, X. Q., H. Li, et al. (2009). "Oncogenic K-Ras regulates proliferation and cell junctions in lung epithelial cells through induction of cyclooxygenase-2 and activation of metalloproteinase-9." Mol Biol Cell **20**(3): 791-800.

Weigelin, B., G.-J. Bakker, et al. (2012). "Intravital third harmonic generation microscopy of collective melanoma cell invasion." Intravital **1**(1): 32-43.

Weis, S., J. Cui, et al. (2004). "Endothelial barrier disruption by VEGF-mediated Src activity potentiates tumor cell extravasation and metastasis." J Cell Biol **167**(2): 223-229.

Wellbrock, C., M. Karasarides, et al. (2004). "The RAF proteins take centre stage." Nat Rev Mol Cell Biol **5**(11): 875-885.

Wolf, K., I. Mazo, et al. (2003). "Compensation mechanism in tumor cell migration: mesenchymal-amoeboid transition after blocking of pericellular proteolysis." J. Cell Biol. **160**(2): 267-277.

Wolf, K., M. Te Lindert, et al. (2013). "Physical limits of cell migration: control by ECM space and nuclear deformation and tuning by proteolysis and traction force." J Cell Biol **201**(7): 1069-1084.

Wolf, K., Y. I. Wu, et al. (2007). "Multi-step pericellular proteolysis controls the transition from individual to collective cancer cell invasion." Nat Cell Biol **9**(8): 893-904.

Worman, H. J., L. G. Fong, et al. (2009). "Laminopathies and the long strange trip from basic cell biology to therapy." J Clin Invest **119**(7): 1825-1836.

Wu, X., F. Quondamatteo, et al. (2006). "Cdc42 expression in keratinocytes is required for the maintenance of the basement membrane in skin." Matrix Biol **25**(8): 466-474.

Wulfkuhle, J. D., D. C. Sgroi, et al. (2002). "Proteomics of human breast ductal carcinoma in situ." Cancer Res **62**(22): 6740-6749.

Wyckoff, J. B., Y. Wang, et al. (2007). "Direct visualization of macrophage-assisted tumor cell intravasation in mammary tumors." Cancer Res **67**(6): 2649-2656.

Yamauchi, K., M. Yang, et al. (2005). "Real-time in vivo dual-color imaging of intracapillary cancer cell and nucleus deformation and migration." Cancer Res **65**(10): 4246-4252.

Yang, Z., Y. J. Chang, et al. (2007). "Transgelin functions as a suppressor via inhibition of ARA54-enhanced androgen receptor transactivation and prostate cancer cell growth." Mol Endocrinol **21**(2): 343-358.

Yoshimura, T., T. Hamada, et al. (2016). "PCP4/PEP19 promotes migration, invasion and adhesion in human breast cancer MCF-7 and T47D cells." Oncotarget **7**(31): 49065-49074.

Zhao, W., S. Prijic, et al. (2016). "Candidate Antimetastasis Drugs Suppress the Metastatic Capacity of Breast Cancer Cells by Reducing Membrane Fluidity." Cancer Res **76**(7): 2037-2049.

Zheng, X., J. L. Carstens, et al. (2015). "Epithelial-to-mesenchymal transition is dispensable for metastasis but induces chemoresistance in pancreatic cancer." Nature **527**(7579): 525-530.